

**DOKUZ EYLUL UNIVERSITY  
GRADUATE SCHOOL OF NATURAL AND APPLIED  
SCIENCES**

**DEVELOPMENT OF NANO MATERIAL  
BASED SENSORS FOR DETERMINATION OF  
SOME-CATION/ANION IN GROUNDWATER  
AND COMPLEMENTARY USAGE OF  
ION CHROMATOGRAPHY**

**by**

**Merve ZEYREK ONGUN**

**July, 2013**

**İZMİR**

**DEVELOPMENT OF NANO MATERIAL  
BASED SENSORS FOR DETERMINATION OF  
SOME-CATION/ANION IN GROUNDWATER  
AND COMPLEMENTARY USAGE OF  
ION CHROMATOGRAPHY**

**A Thesis Submitted to the  
Graduate School of Natural and Applied Sciences of Dokuz Eylül University  
In Partial Fulfillment of the Requirements for the Degree of Doctor of  
Philosophy in Chemistry, Analytical Chemistry Program**

**by  
Merve ZEYREK ONGUN**

**July, 2013  
İZMİR**

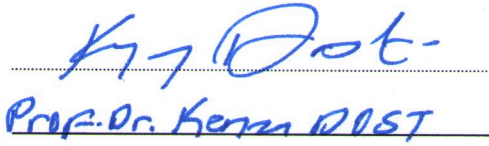
## Ph.D. THESIS EXAMINATION RESULT FORM

We have read the thesis entitled “**DEVELOPMENT OF NANO MATERIAL BASED SENSORS FOR DETERMINATION OF SOME-CATION/ANION IN GROUNDWATER AND COMPLEMENTERY USAGE OF ION CHROMATOGRAPHY**” completed by **MERVE ZEYREK ONGUN** under supervision of **PROF. DR. KADRIYE ERTEKİN** and we certify that in our opinion it is fully adequate, in scope and in quality, as a thesis for the degree of Doctor of Philosophy.



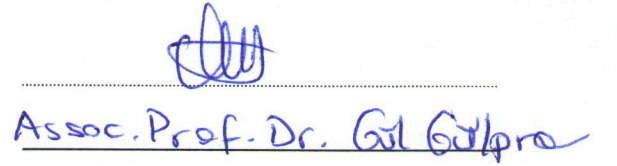
Prof. Dr. Kadriye Ertekin

Supervisor



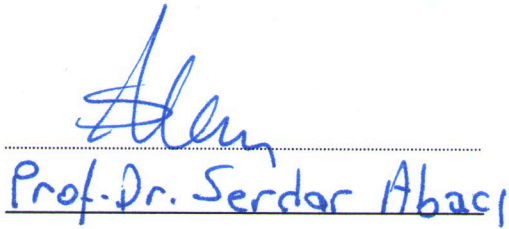
Prof. Dr. Kemal DOST

Thesis Committee Member



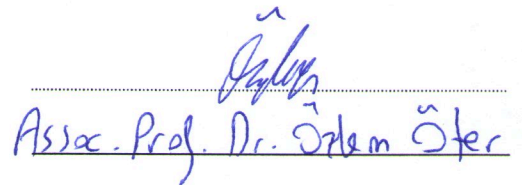
Assoc. Prof. Dr. Gül Güllüoğlu

Thesis Committee Member



Prof. Dr. Serdar Abacı

Examining Committee Member



Assoc. Prof. Dr. Özlem Öter

Examining Committee Member



Prof. Dr. Ayşe OKUR

Director

Graduate School of Natural and Applied Sciences

## ACKNOWLEDGMENTS

I would like to express my sincere gratitude to my supervisor Prof. Dr. Kadriye ERTEKİN for providing the fascinating subject, for her valuable support during this thesis and for the great working conditions at our laboratory.

I gratefully acknowledge that my personal funding was provided by the Scientific and Technological Research Council of Turkey (TUBITAK) and TUBITAK-BIDEB.

I gratefully acknowledge the extensive helps of my colleagues Özlem Öter.

Finally, I would like to thank to my mother Özlem ZEYREK, my father Erol ZEYREK, my grandmother Filiz CİHANBEĞENDİ and especially to my husband Erim Refik ONGUN, for their tolerant attitude to my working effort during the elaboration of this dissertation and for their incessant support and understanding during all the years of my studies.

Merve ZEYREK ONGUN

# **DEVELOPMENT OF NANO MATERIAL BASED SENSORS FOR DETERMINATION OF SOME-CATION/ANION IN GROUNDWATER AND COMPLEMENTARY USAGE OF ION CHROMATOGRAPHY**

## **ABSTRACT**

In this thesis, novel materials using electrospun nano-scale polymeric fibers has been proposed as a promising material for sensing trace amounts of cations in water and groundwater systems. The offered sensors operate by detecting fluorescence intensity changes of fluoroionophore embedded in polymer matrices. The spectral characterization and sensor properties of seven different ionophores were described.

Some of the exploited dyes were newly synthesized and used for the first time for sensing purposes. Highly sensitive emission based nano-scale sensors for Copper(II), Mercury (II), Iron (III) and Tin (II) were fabricated. We performed spectral characterizations of the ionophores in conventional solvents and in solid matrices. Then, we investigated the selectivity and following the sensor performances of the ionophores into detail in terms of sensitivity, selectivity, working range, short-term stability and response time. We checked accuracies of the offered sensors exploiting recovery tests and used them in real groundwater samples.

A great effort has also been made for development of a sensor to detect the conventional anions throughout the studies. We observed a significant response only for bicarbonate and hydroxyl ions with ODC-3 and ODC-5 dyes. The observed response was not a selective response for bicarbonate but rather, a response to pH in the alkaline range of the pH scale.

Throughout the thesis, for each fluoroionophore, we compared results of thin films and electrospun nanofibers and revealed the advantages of the nano-scale materials over existing thin films.

Here, we performed coupling of electrospun nanomaterials with fluorescence based measurement techniques without scattering and other side effects. By this way, we attained detection limits extending to sub-picomolar levels. Further efforts will focus on exploring new sensing materials and polymer compositions, controlling the nanoscale size of the electrospun membranes, and optimizing the sensitivities for the detection of a variety of analyses.

**Keywords:** Sensor, nanosensor, optical chemical sensor, fluorescence, Hg (II), Fe(III), Cu (II), Sn (II).

**YER ALTI SULARINDA BULUNAN BAZI KATYON/ANYON TAYİNİNE  
YÖNELİK NANO MALZEME ESASLI SENSÖR GELİŞTİRİLMESİ VE  
ANALİZLERİN İYON KROMATOĞRAFİSİ KULLANIMIYLA  
TAMAMLANMASI**

**ÖZ**

Bu tezde, su ve yeraltı suyu sistemlerindeki katyonların eser miktarlarının algılanması için yeni malzemeler olarak nano-ölçekli polimerik liflerin kullanılması önerilmiştir. Önerilen sensörler polimer matrikse gömülü floroionoforun floresans şiddetindeki değişiklikleri algılayarak çalışır. Yedi farklı iyonoforun spektral karakterizasyonları ve sensör özellikleri tanımlanmıştır.

Yararlanan boyaların bazıları yeni sentezlenmiş olup sensor amacıyla ilk kez kullanılmıştır. Bakır (II), Civa (II), Demir (III) ve Kalay (II) için çok hassas emisyon esaslı nano ölçekli sensörler üretilmiştir. İyonoforların alışımlı çözücüler ve katı matrislerde spektral karakterizasyonu yapılmıştır. Ardından, duyarlılık, seçicilik, çalışma aralığı, kısa vadeli stabilitesi ve cevap süresi açısından iyonoforların sensor performansları detaylıca araştırılmıştır. Sunulan sensörlerin doğrulukları geri kazanım testlerinden yararlanarak kontrol edilmiş ve gerçek yeraltı suyu örneklerinde kullanılmıştır.

Çalışmalar boyunca alışımlı anyonları tespit eden bir sensör geliştirilmesi için büyük bir çaba da harcanmıştır. Sadece ODC-3 ve ODC-5 boyalarında, bikarbonat ve hidroksit anyonları için anlamlı bir yanıt görülmüştür. Bikarbonat iyonu için gözlemlenen yanıt çok hassastır ancak, bikarbonata seçimli bir cevap olmaktan çok pH skalasının alkali bölgesindeki değişmelere bir cevap şeklindedir.

Tez boyunca, her floroionofor için, ince film ve elektroegirme tekniği ile hazırlanmış nanofiberlerin sonuçları karşılaştırıldı ve mevcut ince filmler üzerinde nano ölçekli malzemelerin avantajları ortaya çıkarıldı.

Burada, saçılma ve diđer yan etkiler olmadan floresansa dayalı ölçüm teknikleri ile elektroęirilmiş nanomalzemeler üzerinden ölçümler gerçekleştirildi. Bu arada, pikomolar altı seviyelerine uzanan tayin limitlerine ulaşılmıştır. İleri çalışmalarda, yeni algılama malzemelerinin ve polimer kompozisyonlarının keşfedilmesi, elektroęirilmiş membranların nano boyutlarının kontrolleri ve çeşitli analitlerin hassasiyetlerinin tespiti için optimizasyonları üzerinde durulacaktır.

**Anahtar Sözcükler:** Sensör, nanosensör, optik kimyasal sensör, floresans, Hg (II), Fe (III), Cu (II), Sn (II).



## CONTENTS

	<b>Page</b>
THESIS EXAMINATION RESULT FORM .....	ii
ACKNOWLEDGMENTS .....	iii
ABSTRACT.....	iv
ÖZ .....	vi
LIST OF FIGURES .....	xvi
LIST OF TABLES .....	xxvii
<b>CHAPTER ONE - INTRODUCTION .....</b>	<b>1</b>
1.1 Dissolved Constituents in Groundwater.....	1
1.1.1 Major Ions .....	1
1.1.2 Minor Ions.....	2
1.1.3 Trace Ions.....	3
1.2 Chemical Analysis Techniques of Water.....	4
1.3 Chemical Sensors .....	5
1.3.1 Optical Chemical Sensors .....	6
1.3.1.1 Principles of Optical Chemical Sensors.....	7
1.3.1.2 Classification of Optical Chemical Sensors.....	8
1.3.2 Fiber Optic Sensors .....	8
1.3.2.1 Sensing Modes and Fiber-Optic Assemblies .....	12
1.3.3 A Short View to the Optical Chemical Sensors .....	14
1.4 Luminescence.....	16
1.4.1 Mechanism of Luminescence.....	16
1.4.1.1 Fluorescence and Phosphorescence (Photoluminescence) .....	17

1.5 Stoke's Shift.....	19
1.6 Quantum Yield.....	19
1.7 Fluorescence Lifetime.....	20
1.8 Time Correlated Single Photon Counting (TCSPC) Method.....	23
1.9 Towards Design of an Optical Sensor.....	24
1.9.1 Indicators.....	24
1.9.1.1 Indicators Exploited For Cation Sensing .....	24
1.9.1.2 Indicators Exploited For Anion Sensing .....	29
1.9.2 Polymer Matrix Materials .....	29
1.9.2.1 Polymers Used In Optical Sensor Design .....	30
1.9.3 Immobilization of Indicator Chemistry in Polymers .....	33
1.9.3.1 Hydrophobic Interactions.....	34
1.9.3.2 Exploiting Attraction of Opposite Charges.....	35
1.9.3.3 Covalent Immobilization.....	36
1.10 Ionic Liquids .....	36
<b>CHAPTER TWO - ELECTROSPINNING AND NANOFIBER .....</b>	<b>38</b>
2.1 Nanotechnology and Nanomaterials .....	38
2.2 Electrospinning of Polymeric Nanofibers .....	40
2.3 Theory of Electrospinning.....	41
2.3.1 Parameters of Electrospinning Process .....	42
2.4 Electrospun Nanofibrous Membranes for Sensors Design.....	42

**CHAPTER THREE- EXPERIMENTAL METHOD AND INSTRUMENTATION ..... 43**

3.1 Reagents ..... 43

3.2 Preparation of the Buffer Solutions ..... 44

    3.2.1 Preparation of 0.005 M H<sub>3</sub>PO<sub>4</sub> Buffer..... 44

    3.2.2 Preparation of 0.01 M Acetic Acid / Acetate Buffer ..... 44

    3.2.3 Preparation of 0.005 M Acetic Acid / Acetate Buffer ..... 44

    3.2.4 Preparation of 0.005 M NaH<sub>2</sub>PO<sub>4</sub>/ Na<sub>2</sub>HPO<sub>4</sub> Buffer ..... 45

3.3 Structural Specification of the Exploited Ionophores ..... 45

3.4 Preparation of Electrospun Nano-Fibers and Thin Films..... 50

    3.4.1 Fabrication of Electrospun Nanofibers ..... 50

    3.4.2 Thin Film Fabrication ..... 52

3.5 Apparatus and Experimental Setup..... 52

    3.5.1 Spectrophotometer and Spectrofluorometer Apparatus..... 52

    3.5.2 Electrospinning Apparatus..... 54

    3.5.3 Time Correlated Single Photon Counting (TCSPC) Apparatus ..... 54

    3.5.4 Experimental Method and Instrumentation for Ion Chromatographic Studies ..... 55

**CHAPTER FOUR - EMISSION BASED SUB-NANOMOLAR Cu (II) SENSING WITH ELECTROSPUN NANOFIBERS..... 59**

4.1 Introduction ..... 59

4.2 Spectral Characterization of Fluoroionophore ..... 62

    4.2.1 Emission Spectra Related Characteristics and Quantum Yield Calculations ..... 62

4.3 SEM Images of Electrospun Membranes .....	65
4.4 Detection of pK <sub>a</sub> for DPAINH .....	67
4.5 Copper Ion Sensing Studies: Cu (II) Uptake into the Membrane and Fluorescence Based Response .....	70
4.6 Stern–Volmer Analysis .....	75
4.7 Sensor Dynamics and Analytical Figures of Merit .....	78
4.8 Recovery and Selectivity Studies, Tests With Real Samples.....	79
4.9 Conclusion.....	80
<b>CHAPTER FIVE - DETERMINATION OF Hg (II) EXPLOITING DIFFERENT IONOPHORES.....</b>	<b>82</b>
5.1 A Short View to Sensing of Ionic Mercury.....	82
5.2 Determination of Mercury (II) Ions Using Luminescent Carbazole Derivative at Femtomolar Levels .....	84
5.2.1 Photocharacterization of Fluoroionophore and Quantum Yield Calculations .....	85
5.2.2 SEM Images of Electrospun Membranes .....	88
5.2.3 Effect of pH .....	89
5.2.4 Response to Hg (II) Ions.....	90
5.2.5 Stern-Volmer Analysis .....	93
5.2.6 Lifetime Analysis.....	95
5.2.7 Selectivity Studies .....	99
5.2.8 Recovery and Regeneration Studies with Real Groundwater Samples.....	101
5.2.9 Conclusion .....	101

5.3 Sensing of Hg (II) Ions with Embedded Carbazole Derivative.....	102
5.3.1 The Photophysical Properties and Quantum Yield Calculations of the Indicator Dye .....	103
5.3.2 SEM Images of Electrospun Membranes.....	106
5.3.3 Dynamic Working Range and Hg (II) Response .....	107
5.3.4 Stern-Volmer Analysis .....	112
5.3.5 Lifetime Analysis.....	114
5.3.6 Selectivity Studies .....	117
5.3.7 Recovery and Regeneration Studies With Real Groundwater Samples.....	119
5.3.8 Conclusion .....	119
5.4 A Fluorescent Probe; Chlorophenyl Imino Molecule in Form of Nanofibers for Sensing of Hg (II) Ions .....	120
5.4.1 The Spectral Assessment and Quantum Yield Calculations of Newly Synthesized DMK-1A Dye.....	120
5.4.2 SEM Images.....	123
5.4.3 Effect of pH .....	124
5.4.4 Dynamic Working Range and Response of Mercuric Ions .....	126
5.4.5 Lifetime Analysis.....	134
5.4.6 Selectivity Characteristics and Interference Effect.....	136
5.4.7 Recovery and Regeneration Studies with Real Groundwater Samples.....	137
5.4.8 Conclusion .....	138

**CHAPTER SIX - FLUORESCENT Fe (III) SENSING AT NANO/SUB-NANO MOLAR LEVEL WITH OPTICAL CHEMICAL SENSORS..... 139**

6.1 Introduction .....	139
6.2 Sensing of Fe (III) Ions with Embedded Carbazole Derivative .....	141
6.2.1 The Photophysical Properties of the Indicator Dye in Different Solvents and Quantum Yield Calculations.....	142
6.2.2 SEM Images of Electrospun Membranes .....	145
6.2.3 Effect of pH .....	146
6.2.4 Dynamic Working Range and Response for Fe (III).....	147
6.2.5 Stern-Volmer Analysis .....	150
6.2.6 Lifetime Analysis.....	151
6.2.7 Selectivity Studies .....	153
6.2.8 Recovery and Regeneration Studies in Real Groundwater Samples.....	155
6.2.9 Conclusion .....	155
6.3 Response of ODC-3 to Fe (III) Ions .....	156
6.3.1 Dynamic Working Range and Response for Fe (III).....	156
6.3.2 Stern-Volmer Analysis .....	160
6.3.3 Lifetime Analysis.....	162
6.3.4 Recovery and Regeneration Studies in Real Groundwater Samples.....	163
6.3.5 Conclusion .....	163
6.4 Response of ODC-5 to Fe (III) Ions .....	164
6.4.1 Dynamic Working Range and Response for Fe (III).....	164
6.4.2 Stern-Volmer Analysis .....	168
6.4.3 Lifetime Analysis.....	170

6.4.4 Recovery and Regeneration Studies in Real Groundwater Samples.....	170
6.4.5 Conclusion.....	171
6.5 Design of a Fluorescent Optical Sensor Using Nanofibers for Fe (III) .....	171
6.5.1 Spectral Evaluation of the Newly Synthesized Dye .....	172
6.5.2 SEM Images of Electrospun Membranes .....	174
6.5.3 Effect of pH .....	175
6.5.4 Dynamic Working Range and Response for Fe (III) Ions .....	176
6.5.5 Stern-Volmer Analysis .....	180
6.5.6 Lifetime Analysis.....	181
6.5.7 Interference Effects.....	183
6.5.8 Recovery and Regeneration Studies .....	185
6.5.9 Conclusion.....	185

**CHAPTER SEVEN -A SENSITIVE DETERMINATION OF Sn (II) WITH FLUORESCENCE SPECTROSCOPY EXPLOITING ELECTROSPUN FIBERS ..... 186**

7.1 Introduction.....	186
7.2 Sensor Design.....	188
7.2.1 Spectral Evaluation of Newly Synthesized Dye and Quantum Yield Calculations .....	188
7.2.2 SEM Images of Electrospun Membranes .....	191
7.2.3 Effect of pH .....	192
7.2.4 Dynamic Working Range and Response for Sn (II) Ions .....	193
7.2.5 Stern-Volmer Analysis .....	196
7.2.6 Lifetime Analysis.....	197

7.2.7 Interference Effects.....	199
7.2.8 Recovery and Regeneration Studies .....	201
7.2.9 Conclusion .....	201
<b>CHAPTER EIGHT - CONCLUSIONS .....</b>	<b>202</b>
<b>REFERENCES.....</b>	<b>204</b>



## LIST OF FIGURES

	<b>Page</b>
Figure 1.1 Basic structure of an optical fiber .....	9
Figure 1.2 Total internal reflections in an optical fiber .....	10
Figure 1.3 Different types of optical fibers .....	12
Figure 1.4 Bifurcated fiber-optic cable assembly .....	13
Figure 1.5 The electronic states of organic molecules .....	17
Figure 1.6 Jablonski diagram with the reciprocal rates of transition in [s].....	18
Figure 1.7 Simulated time domain traces for a fluorophore that exhibits a 1, 5, or 10 ns excited-state lifetime .....	22
Figure 1.8 The main components for signal processing in TCSPC .....	23
Figure 1.9 Valinomycin .....	25
Figure 1.10 Examples of crown ether containing molecular probes I: Oxygen II: Sulphur containing crown ether moieties .....	26
Figure 1.11 Examples of chelating sensors .....	26
Figure 1.12 Calixarene based fluorescent probes .....	27
Figure 1.13 Fluorescent probes working on principle of excimer formation .....	27
Figure 1.14 Dimerization of crown ether bearing phthalocyanine structures upon exposure to K <sup>+</sup> ions .....	28
Figure 1.15 Potassium sensing with bis[4-N-(1-aza-4,7,10,13,16 pentaoxacyclo octadecyl)-3,5-dihydroxyphenyl] squaraine .....	29
Figure 2.1 The most frequently used electrospinning set-up. ....	41
Figure 3.1 Structure of the copper sensitive fluoroionophore, N <sup>3</sup> -3 (4(dimethyl amino) phenyl)allylidene)isonicotinohydrazide (DPAINH) .....	45
Figure 3.2 Schematic structures of the mercury, iron and silver sensitive fluoro ionophore; 2-(9-methyl-9H-carbazol-3yl)-5-(pyridin-4-yl)-1,3,4oxadiazole dye (ODC-3). ....	46

Figure 3.3 Structure of the mercury and iron sensitive fluoroionophore; 2-(9-hexyl-9H-carbazol-3-yl)-5-(pyridin-4-yl)-1,3,4-oxadiazole (ODC-5) .....	47
Figure 3.4 Structure of mercury sensitive molecule, 2-{(E)-[(4-chlorophenyl)imino] methyl} phenol (DMK-1A) .....	47
Figure 3.5 Structures of the iron sensitive fluoroionophore 9-hexyl-9H-carbazole-3-carbonitrile (ODC 1) .....	48
Figure 3.6 Structure of iron sensitive molecule, 2-{[(4-bromo-2,6dimethylphenyl) imino] methyl} phenol (MS-4) .....	49
Figure 3.7 Structure of tin sensitive molecule, 3-(2,4,6-trimethoxybenzyl)-3,4-dihydroquinazoline (MS-3) .....	49
Figure 3.8 Structures of PMMA, EC, DOP, PTCPB and RTIL .....	51
Figure 3.9 Instrumental set-up used for dye-doped nanofiber measurements .....	54
Figure 4.1 Structure of the copper sensitive fluoroionophore, N'-3-(4-(dimethyl amino) phenyl) allylidene) isonicotinohydrazide (DPAINH) .....	62
Figure 4.2 I: Excitation and emission spectra of the fluoroinophore in (a) EtOH, (b) THF, (c) DMF, (d) DCM. II: (a) in embedded form in EC, (b) in PMMA .....	63
Figure 4.3 The integrated fluorescence intensities vs absorbance values of Quinine Sulfate in H <sub>2</sub> SO <sub>4</sub> , DPAINH dye in EC and DPAINH dye in THF .....	64
Figure 4.4 SEM images of electrospun membranes; (a) and (b); PMMA based nanofibers at different magnifications such as ×1000, ×20 000 .....	66
Figure 4.5 SEM images of electrospun membranes; (c) and (d); EC based nanofibers at different magnifications such as ×500 and ×20 000 .....	67
Figure 4.6 pH induced emission characteristics and sigmoidal calibration curve of DPAINH doped EC membrane in the pH range of 7.0–3.0. (a) pH=7.0, (b) pH=6.5, (c) pH= 6.0, (d) pH= 5.5, (e) pH= 5.0, (f) pH= 4.5, (g) pH= 4.0, (h) pH= 3.5, (j) pH= 3.0, (pKa=4.77) .....	69

Figure 4.7 pH induced emission characteristics and sigmoidal calibration curve DPAINH doped PMMA membrane after exposure to buffer solutions in the pH range of 7.0–11.0 (a) pH=7.0, (b) pH= 7.5, (c) pH= 8.0, (d) pH= 8.5, (e) pH= 9.0, (f) pH= 9.5, (g) pH= 10.0, (h) pH= 10.5, (j) pH= 11.0, (pKa=8.60) ..... 69

Figure 4.8 I: Fluorescence response of the dye doped PMMA thin film to Cu (II) ions at pH 4.0. (a) Cu-free buffer, (b)  $10^{-12}$  M, (c)  $10^{-11}$ , (d)  $10^{-10}$ , (e)  $10^{-9}$ , (f)  $10^{-8}$ , (g)  $10^{-7}$ , (h)  $10^{-6}$ , (i)  $10^{-5}$ , (j)  $10^{-4}$ , (k)  $10^{-3}$  M Cu(II). Inset: Linearized calibration plot for the concentration range of  $10^{-12}$ - $10^{-5}$  M Cu(II). II: Response of the PMMA based nanofiber to Cu (II) ions at pH 4.0. (a) Cu-free buffer, (b)  $10^{-12}$  M, (c)  $10^{-11}$ , (d)  $10^{-10}$ , (e)  $10^{-9}$ , (f)  $10^{-8}$ , (g)  $10^{-7}$ , (h)  $10^{-6}$ , (i)  $10^{-5}$ , (j)  $10^{-4}$ , (k)  $10^{-3}$ , (l)  $10^{-2}$ , (m)  $10^{-1}$  M Cu(II). Inset: Linearized calibration plot for the concentration range of  $10^{-12}$ - $10^{-2}$  M Cu(II)..... 72

Figure 4.9 I: Fluorescence response of the dye doped EC thin film to Cu(II) ions at pH 4.0. (a) Cu-free buffer, (b)  $10^{-12}$  M, (c)  $10^{-11}$ , (d)  $10^{-10}$ , (e)  $10^{-9}$ , (f)  $10^{-8}$ , (g)  $10^{-7}$ , (h)  $10^{-6}$  (i)  $10^{-5}$ , (j)  $10^{-4}$ , (k)  $10^{-3}$  M Cu (II). Inset: Linearized calibration plot for the concentration range of  $10^{-9}$ - $10^{-4}$  M Cu (II). II: Response of the EC based nanofiber to Cu (II) ions at pH 4.0. (a) Cu-free buffer, (b)  $10^{-12}$  M, (c)  $10^{-11}$ , (d)  $10^{-10}$ , (e)  $10^{-9}$ , (f)  $10^{-8}$ , (g)  $10^{-7}$ , (h)  $10^{-6}$ , (i)  $10^{-5}$ , (j)  $10^{-4}$ , (k)  $10^{-3}$  M Cu (II). Inset: Linearized calibration plot for the concentration range of  $10^{-12}$ - $10^{-3}$  M Cu (II) ..... 73

Figure 4.10 Absorption spectra of the fluoroionophore in the absence (a) and presence (b) of the quencher; Cu (II) ..... 75

Figure 4.11 Gathered Stern Volmer plots of the electrspun nano-fibers and continuous thin films in PMMA (I) and in EC (II). ..... 77

Figure 4.12 I: Response of DPAINH to  $10^{-5}$  M of different metal cations in acetic acid/acetate buffer solutions at pH 4.0. II: Response of the dye to  $10^{-5}$  M of the major anions in near neutral waters..... 80

Figure 5.1 Schematic structures of the mercury sensitive fluoroionophore;2-(9-methyl-9H-carbazol-3yl) -5-(pyridin-4-yl)-1,3,4oxadiazole dye (ODC-3) ..... 84

Figure 5.2 Absorption spectra of the ODC -3 dye ( $10^{-5}$  M dye or 2 mM dye/kg polymer). (a) THF, (b) DMF, (c) Toluene: EtOH, (d) DCM, (e) Toluene ..... 85

Figure 5.3 Excitation and corrected emission spectra of the ODC -3 dye ( $10^{-5}$ M dye or 2 mM dye/kg polymer). (a) THF, (b) DCM, (c) Toluene, (d)To: EtOH, (e)DMF.....	86
Figure 5.4 The integrated fluorescence intensities vs absorbance values of Quinine Sulfate in $H_2SO_4$ , ODC-3 dye in EC and ODC-3 dye in THF .....	87
Figure 5.5 SEM images of EC based electrospun nanofibers (a), (b) and (c); EC based nanofibers at different magnifications such as $\times 500$ , $\times 1000$ and $\times 30\ 000$ .....	89
Figure 5.6 The pH dependency of ODC-3 dye in presence of Hg (II) ions between pH 4.0-10.0 using the EC based thin films. ....	90
Figure 5.7 Fluorescence response of the EC based thin film to Hg (II) ions at pH 5.0. (a) Hg-free buffer, (b) $10^{-9}$ M Hg (II), (c) $10^{-8}$ , (d) $10^{-7}$ , (e) $10^{-6}$ , (f) $10^{-5}$ , (g) $10^{-4}$ , (h) $10^{-3}$ M Hg(II), and linearized calibration plot for the concentration range of $10^{-9}$ - $10^{-3}$ M Hg (II).....	91
Figure 5.8 Fluorescence response of the EC based nanofibers to Hg (II) ions at pH 5.0. (a) Hg-free buffer, (b) $10^{-11}$ M Hg (II), (c) $10^{-10}$ , (d) $10^{-9}$ , (e) $10^{-8}$ , (f) $10^{-7}$ , (g) $10^{-6}$ , (h) $10^{-5}$ , (i) $10^{-4}$ , (j) $10^{-3}$ , (k) $10^{-2}$ M Hg (II), and linearized calibration plot for the concentration range of $10^{-11}$ - $10^{-3}$ M Hg (II) .....	92
Figure 5.9 I: The Stern Volmer plots of EC based thin films, II: electrospun nanofibers in presence of the quencher .....	95
Figure 5.10 Decay curves of the exploited dye in THF, in thin film form and in form of nanofiber, respectively. In all cases a and b shows quencher free and quencher containing decay profiles. The dye excited at 367 nm with a picoseconds pulsed laser and intensity decay data acquisition was performed at 415 nm.....	97
Figure 5.11 Absorption spectra of the fluoroionophore (a) in the absence and (b) in presence of the quencher; Hg (II).....	98
Figure 5.12 I: Metal-ion response of mercury sensitive ODC-3 at pH 5.0. Inset: Response to Hg (II) ions when Fe (III) suppressed with masking agent; citrate. I: Response to the anions of the same composition at near neutral pH. Results were plotted as relative fluorescence changes; $(I-I_0)/I_0$ .....	100

Figure 5.13 Schematic structures of the mercury sensitive fluoroionophore;2-(9-hexyl-9Hcarbazol -3-yl)-5-(pyridin-4-yl)-1,3,4-oxadiazole (ODC-5).....	102
Figure 5.14 Absorption spectra of the ODC -5 dye ( $10^{-5}$ M dye or 2 mM dye/kg polymer).(a) THF, (b) DCM, (c) Toluene: EtOH, (d) Toluene, (e) DMF, (f) EtOH .....	103
Figure 5.15 Excitation and corrected emission spectra of the ODC-5 dye ( $10^{-5}$ M dye or 2 mM dye/kg polymer). (a)THF, (b) Toluene, (c) DCM, (d) To: EtOH, (e) DMF, (f) EtOH .....	104
Figure 5.16 The integrated fluorescence intensities vs absorbance values of Quinine Sulfate in $H_2SO_4$ , ODC-5 dye in EC and ODC-5 dye in THF .....	105
Figure 5.17 SEM images of EC based electrospun nanofibers (a), (b) and (c); EC based nanofibers at different magnifications such as $\times 1000$ , $\times 5000$ , $\times 10\ 000$ .....	107
Figure 5.18 Absorption spectrum of the ODC-5 dye in THF (a) Hg (II) free, (b) in presence of $5 \times 10^{-5}$ M Hg (II) .....	108
Figure 5.19 The pH dependency of ODC-5 dye in presence of Hg (II) ions between pH 4.0-10.0 using the EC based thin films. ....	109
Figure 5.20 Fluorescence response of the ODC-5-doped EC based nanofiber to Hg (II) ions at pH 5.0. (a) Hg-free buffer (b) $10^{-9}$ M, (c) $10^{-8}$ , (d) $10^{-7}$ , (e) $10^{-6}$ , (f) $10^{-5}$ , (g) $10^{-4}$ , (h) $10^{-3}$ , (i) $10^{-2}$ mol/L Hg(II), and linearized calibration plot for the concentration range of $10^{-9}$ - $10^{-2}$ M Hg (II) .....	110
Figure 5.21 Fluorescence response of the ODC-5-doped EC based nanofiber to Hg (II) ions at pH 5.0. (a) Hg-free buffer (b) $10^{-11}$ M, (c) $10^{-10}$ , (d) $10^{-9}$ , (e) $10^{-8}$ , (f) $10^{-7}$ , (g) $10^{-6}$ , (h) $10^{-5}$ , (i) $10^{-4}$ , (j) $10^{-3}$ , (k) $10^{-2}$ mol/L Hg(II) and linearized calibration plot for the concentration range of $10^{-11}$ - $10^{-2}$ M Hg (II) .....	111
Figure 5.22 The Stern Volmer plot of EC based I: thin films and II: electrospun nanofibers .....	113

Figure 5.23 Decay curves of the exploited dye in THF, in thin film form and in form of nanofiber, respectively. In all cases a and b shows quencher free and quencher containing decay profiles. The dye excited at 367 nm with a picoseconds pulsed laser and intensity decay data acquisition was performed at 412 nm.....	115
Figure 5.24 I: Metal-ion response of mercury sensitive ODC-5 at pH 5.0. Inset: Response to ionic mercury in presence of Fe (III). Fe (III) ions has been suppressed with citrate buffer. II: Response to the anions of the same composition at near neutral pH. Results were plotted as relative fluorescence changes; $(I-I_0)/I_0$ .....	118
Figure 5.25 Structure of mercury sensitive molecule, 2-{(E)-[(4-chlorophenyl)imino] methyl} phenol (DMK-1A) .....	120
Figure 5.26 Absorption spectra of the DMK-1A dye ( $10^{-5}$ M dye or 2 mM dye/kg polymer). (a) DCM, (b) EtOH, (c) DMF, (d) Toluene: EtOH .....	121
Figure 5.27 Excitation and corrected emission spectra of the DMK-1A dye ( $10^{-5}$ M dye or 2 mM dye/kg polymer). (a) DCM, (b) EtOH, (c) DMF), (d) To: EtOH .....	122
Figure 5.28 The integrated fluorescence intensities vs absorbance values of Quinine Sulfate in $H_2SO_4$ , DMK-1A dye in EC and DMK-1A dye in THF .....	122
Figure 5.29 SEM images of EC based electrospun nanofibers (a) and (b); EC based nanofibers at different magnifications such as $\times 500$ and $\times 15\ 000$ .....	124
Figure 5.30 The pH dependency of DMK-1A dye in presence of Hg (I) ions between pH 3.5-6.5 using the EC and PMMA based nanofibers, respectively.....	125
Figure 5.31 The pH dependency of DMK-1A dye in presence of Hg (II) ions between pH 3.5-6.5 using the EC and PMMA based nanofibers, respectively.....	126
Figure 5.32 Physical aspect of the ion-exchange pathway scheme .....	126
Figure 5.33 Absorption spectrum of the DMK-1A dye in THF (a) Hg (I) free, (b) in presence of $5 \times 10^{-5}$ M Hg (I) .....	127
Figure 5.34 Absorption spectrum of the DMK-1A dye in THF (a) Hg (II) free, (b) in presence of $5 \times 10^{-5}$ M Hg (II) .....	128

Figure 5.35 Fluorescence response of the EC based thin film to Hg (II) ions at pH 6.0. (a) Hg-free buffer, (b) $10^{-11}$ M Hg (II), (c) $10^{-10}$ , (d) $10^{-9}$ , (e) $10^{-8}$ , (f) $10^{-7}$ , (g) $10^{-6}$ , (h) $10^{-5}$ , (i) $10^{-4}$ , (j) $10^{-5}$ M Hg(II), and linearized calibration plot for the concentration range of $10^{-11}$ - $10^{-3}$ M Hg (II) .....	129
Figure 5.36 Fluorescence response of the EC based nanofiber to Hg (II) ions at pH 6.0. (a) Hg-free buffer, (b) $10^{-13}$ M Hg (II), (c) $10^{-12}$ , (d) $10^{-11}$ , (e) $10^{-10}$ , (f) $10^{-9}$ , (g) $10^{-8}$ , (h) $10^{-7}$ (i) $10^{-6}$ , (j) $10^{-5}$ , (k) $10^{-4}$ , (l) $10^{-3}$ M Hg(II), and linearized calibration plot for the concentration range of $10^{-13}$ - $10^{-4}$ M Hg (II) .....	130
Figure 5.37 Fluorescence response of the EC based thinfilm to Hg (I) ions at pH 5.5. (a) Hg-free buffer, (b) $10^{-9}$ M Hg (I), (c) $10^{-8}$ , (d) $10^{-7}$ , (e) $10^{-6}$ , (f) $10^{-5}$ , (g) $10^{-4}$ , (h) $10^{-3}$ M Hg (I), and linearized calibration plot for the concentration range of $10^{-9}$ - $10^{-4}$ M Hg (I) .....	131
Figure 5.38 Fluorescence response of the EC based nanofiber to Hg (I) ions at pH 5.5. (a) Hg-free buffer, (b) $10^{-10}$ M Hg (I), (c) $10^{-9}$ , (d) $10^{-8}$ , (e) $10^{-7}$ , (f) $10^{-6}$ , (g) $10^{-5}$ , (h) $10^{-4}$ , (j) $10^{-3}$ M Hg (I), and linearized calibration plot for the concentration range of $10^{-10}$ - $10^{-3}$ M Hg (I) .....	132
Figure 5.39 Decay curves of the exploited dye in THF and in thin film form, respectively. In all cases a and b shows quencher free and quencher containing decay profiles. The dye excited at 367 nm with a picoseconds pulsed laser.....	135
Figure 5.40 I: Metal ion response of EC based nanofibers at pH 6.0. II: Response to the anions of the same composition at near neutral pH. Results were plotted as relative fluorescence changes; $(I-I_0)/I_0$ .....	137
Figure 6.1 Structures of the iron sensitive fluoroionophore-,9-hexyl-9H-carbazole-3-carbonitrile (ODC 1) .....	141
Figure 6.2 Absorption spectra of the ODC -1 dye ( $10^{-5}$ M dye or 2 mM dye/kg polymer).(a) EtOH, (b) To: EtOH (80:20), (c) DCM, (d) THF, (e) Toluene, (f) DMF .....	142
Figure 6.3 Excitation and corrected emission spectra of the ODC -1 dye ( $10^{-5}$ M dye or 2 mM dye/kg polymer). (a)THF, (b)DCM, (c)Toluene, (d)To: EtOH, (e) DMF.....	143

Figure 6.4 The integrated fluorescence intensities vs absorbance values of Quinine Sulfate in H <sub>2</sub> SO <sub>4</sub> , ODC-1 dye in EC and ODC-1 dye in THF.....	144
Figure 6.5 SEM images of EC based electrospun nanofibers (a), and (b); EC based nanofibers at different magnifications such as ×1000 and ×10 000 .....	145
Figure 6.6 The pH dependency of ODC-1 dye in presence of Fe (III) ions between pH 4.0-10.0 using the EC based thin films .....	146
Figure 6.7 Absorption spectrum of the ODC-1 dye in THF (a) Fe (III)free, (b) in presence of 5×10 <sup>-5</sup> M Fe (III).....	147
Figure 6.8 Fluorescence response of the ODC-1-doped EC based thin film to Fe (III) ions at pH 5.5. (a) Fe-free buffer (b) 10 <sup>-7</sup> , (c) 10 <sup>-6</sup> , (d) 10 <sup>-5</sup> , (e) 10 <sup>-4</sup> , (f) 10 <sup>-3</sup> M Fe (III), and linearized calibration plot for the concentration range of 10 <sup>-7</sup> -10 <sup>-3</sup> M Fe (III) .....	148
Figure 6.9 Fluorescence response of the ODC-1-doped EC based nanofiber to Fe (III) ions at pH 5.5. (a) Fe-free buffer (b) 10 <sup>-10</sup> , (c) 10 <sup>-9</sup> , (d) 10 <sup>-8</sup> , (e) 10 <sup>-7</sup> , (f) 10 <sup>-6</sup> , (g) 10 <sup>-5</sup> , (h) 10 <sup>-4</sup> , (i) 10 <sup>-3</sup> , (j) 10 <sup>-2</sup> M Fe (III), and linearized calibration plot for the concentration range of 10 <sup>-10</sup> -10 <sup>-3</sup> M Fe (III) .....	149
Figure 6.10 I: The Stern Volmer plots of EC based thin films, II: electrospun nanofibers in presence of the quencher.....	151
Figure 6.11 Decay curves of the exploited dye in THF, in thin film form and in form of nanofiber, respectively. In all cases a and b shows quencher free and quencher containing decay profiles. The dye excited at 367 nm with a picoseconds pulsed laser and intensity decay data acquisition was performed at 370 nm.....	153
Figure 6.12 I: Metal-ion response of ODC-1 at pH 5.50. II: Response to the anions of the same composition at near neutral pH. Results were plotted as relative fluorescence changes; (I-I <sub>0</sub> )/I <sub>0</sub> .....	154
Figure 6.13 Absorption spectrum of the ODC-3 dye in THF (a) Fe (III) free, (b) in presence of 5x10 <sup>-5</sup> M Fe (III) .....	156
Figure 6.14 The pH dependency of ODC-3 dye in presence of Fe (III) ions between pH 4.0-6.0 using the EC based thin films .....	157



Figure 6.15 Excitation - emission spectra of thin film. Emission based response of the ODC-3 doped EC fiber to different concentrations of Fe (III) and linearized calibration curve at pH=5.0. (a) Buffer, (b) $10^{-9}$ , (c) $10^{-8}$ , (d) $10^{-7}$ , (e) $10^{-6}$ , (f) $10^{-5}$ , (g) $10^{-4}$ , (h) $10^{-3}$ mol/L. Inset: Response to Fe (III) when the potential interferent ionic mercury has been suppressed with thiocyanate. ....	158
Figure 6.16 Excitation and emission spectra of electrospun fibers. Emission based response of the ODC-3 doped EC fiber to different concentrations of Fe (III) and linearized calibration curve at pH=5.0. (a) buffer, (b) $10^{-10}$ , (c) $10^{-9}$ , (d) $10^{-8}$ , (e) $10^{-7}$ , (f) $10^{-6}$ , (g) $10^{-5}$ , (h) $10^{-4}$ , (i) $10^{-3}$ , (j) $10^{-2}$ mol/L.....	159
Figure 6.17 I: The Stern Volmer plots of EC based thin films, II: electrospun nanofibers in presence of the quencher .....	161
Figure 6.18 Absorption spectrum of the ODC-5 dye in THF (a) Fe (III) free, (b) in presence of $5 \times 10^{-5}$ M Fe (III).....	165
Figure 6.19 The pH dependency of ODC-5 dye in presence of Fe (III) ions between pH 4.0-6.0 using the EC based thin films .....	165
Figure 6.20 Fluorescence response of the ODC-5-doped EC based thin film to Fe (III) ions at pH 5.0. (a) Fe-free buffer, (b) $10^{-9}$ , (c) $10^{-8}$ , (d) $10^{-7}$ , (e) $10^{-6}$ , (f) $10^{-5}$ , (g) $10^{-4}$ , (h) $10^{-3}$ mol/L Fe (III) and linearized calibration plot for the concentration range of $10^{-9}$ - $10^{-3}$ M Fe (III). Inset: Response to Fe (III) when the potential interferent ionic mercury has been suppressed with thiocyanate. ....	166
Figure 6.21 Fluorescence response of the ODC-5-doped EC based nanofiber to Fe (III) ions at pH 5.0. (a) Fe-free buffer, (b) $10^{-11}$ , (c) $10^{-10}$ , (d) $10^{-9}$ , (e) $10^{-8}$ , (f) $10^{-7}$ , (g) $10^{-6}$ , (h) $10^{-5}$ , (i) $10^{-4}$ , (j) $10^{-3}$ mol/L Fe(III), and linearized calibration plot for the concentration range of $10^{-11}$ - $10^{-3}$ M Fe (III) .....	167
Figure 6.22 I: The Stern Volmer plots of EC based thin films, II: electrospun nanofibers in presence of the quencher.....	169
Figure 6.23 Structure of iron sensitive molecule, 2-([(4-bromo-2,6dimethylphenyl) imino] methyl} phenol (MS-4) .....	172
Figure 6.24 Absorption spectra of the MS-4 dye ( $10^{-5}$ M dye or 2 mM dye/kg polymer). (a) EtOH, (b)THF, (c) DMF, (d) DCM, (e) To: EtOH(80:20) .....	172

Figure 6.25 Excitation and corrected emission spectra of the MS-4 dye ( $10^{-5}$ M dye or 2 mM dye/kg polymer). (a)THF, (b) EtOH, (c) To: EtOH(80:20), (d) DCM, (e) DMF.....	173
Figure 6.26 SEM images of PMMA based electrospun nanofibers (a) and (b); PMMA based nanofibers at different magnifications such as $\times 500$ , $\times 10000$ .....	175
Figure 6.27 pH dependent response of MS-4 dye doped PMMA membran to Fe (III) ions at pH 4.0-10.0.....	176
Figure 6.28 Absorption spectrum of the MS-4 dye in THF (a) Fe (III) free, (b) in presence of $5 \times 10^{-5}$ M Fe (III).....	177
Figure 6.29 Response of the MS 4 doped PMMA based thin film to Fe (III) ions at pH 5.5. (a) Fe (III)-free, (b) $10^{-8}$ , (c) $10^{-7}$ , (d) $10^{-6}$ , (e) $10^{-5}$ , (f) $10^{-4}$ , (g) $10^{-3}$ , (h) $10^{-2}$ Mol/L, and linearized calibration plot for the concentration range of $10^{-8}$ - $10^{-2}$ M Fe (III) .....	178
Figure 6.30 Fluorescence response of the MS 4 doped PMMA based nanofiber to Fe (III) ions at pH 5.5. (a) Fe (III) -free buffer, (b) $10^{-12}$ , (c) $10^{-11}$ , (d) $10^{-10}$ , (e) $10^{-9}$ , (f) $10^{-8}$ , (g) $10^{-7}$ , (h) $10^{-6}$ , (i) $10^{-5}$ , (j) $10^{-4}$ , (k) $10^{-3}$ Mol/L, and linearized calibration plot for the concentration range of $10^{-12}$ - $10^{-5}$ M Fe (III).....	179
Figure 6.31 I: The Stern Volmer plots of PMMA based thin films, II: electrospun nanofibers in presence of the quencher .....	181
Figure 6.32 Decay curves of the exploited dye in THF, in thin film form and in form of nanofiber, respectively. In all cases a and b shows quencher free and quencher containing decay profiles. The dye excited at 367 nm with a picoseconds pulsed laser. ....	183
Figure 6.33 I: Metal-ion response of MS-4 at pH 5.50. II: Response to the anions of the same composition at near neutral pH. Results were plotted as relative fluorescence changes; $(I-I_0)/I_0$ .....	184
Figure 7.1 Structure of tin sensitive molecule, 3-(2,4,6-trimethoxybenzyl)-3,4-dihydroquinazoline (MS-3) .....	188

Figure 7.2 Absorption spectra of the MS-3 dye ( $10^{-5}$ M dye or 2 mM dye/kg polymer). (a)THF, (b) DCM, (c) EtOH, (d) To: EtOH(80:20), (e) DMF .....	189
Figure 7.3. Excitation and corrected emission spectra of the MS-3 dye ( $10^{-5}$ M dye or 2 mM dye/kg polymer). (a) THF, (b) EtOH, (c) To: EtOH, (d) DCM, (e) DMF.....	190
Figure 7.4 SEM images of PMMA based electrospun nanofibers (a) and (b); PMMA based nanofibers at different magnifications such as $\times 500$ and $\times 10000$ .....	191
Figure 7.5 pH dependent response of MS-3 dye doped PMMA membran to Sn (II) ions at pH 4.0-10.0.....	192
Figure 7.6 Absorption spectrum of the MS-3 dye in THF (a) Sn (II) free, (b) in presence of $5 \times 10^{-5}$ M Sn (II) .....	193
Figure 7.7 Fluorescence response of the MS-3 doped PMMA based thin film to Sn (II) ions at pH 4.0. (a) Sn (II) -free buffer, (b) $10^{-8}$ , (c) $10^{-7}$ , (d) $10^{-6}$ , (e) $10^{-5}$ , (f) $10^{-4}$ , (g) $10^{-3}$ , (h) $10^{-2}$ , (i) $10^{-1}$ Mol/L, and linearized calibration plot for the concentration range of $10^{-8}$ - $10^{-2}$ M Sn (II).....	194
Figure 7.8 Response of the PMMA based nanofiber to Sn (II) ions at pH 4.0. (a) Sn (II) free, (b) $10^{-10}$ , (c) $10^{-9}$ , (d) $10^{-8}$ , (e) $10^{-7}$ , (f) $10^{-6}$ , (g) $10^{-5}$ , (h) $10^{-4}$ , (i) $10^{-3}$ , (j) $10^{-2}$ , (k) $10^{-1}$ Mol/L, and linearized calibration plot for the concentration range of $10^{-10}$ - $10^{-3}$ M Sn (II) .....	195
Figure 7.9 I: The Stern Volmer plots of PMMA based thin films, II: electrospun nanofibers in presence of the quencher.....	197
Figure 7.10 Decay curves of the exploited dye in THF, in thin film form and in form of nanofiber, respectively. In all cases a and b shows quencher free and quencher containing decay profiles. The dye excited at 367 nm with a picoseconds pulsed laser. ....	199
Figure 7.11 I: Metal-ion response of MS-3 at pH 5.50. II: Response to the anions of the same composition at near neutral pH. Results were plotted as relative fluorescence changes; $(I-I_0)/I_0$ .....	200

## LIST OF TABLES

	<b>Page</b>
Table 1.1 Dissolved major constituents in natural water .....	2
Table 1.2 Dissolved trace constituents in natural water .....	3
Table 1.3 Hydrophobic polymers .....	31
Table 1.4 Hydrophilic polymers .....	32
Table 1.5 Unpolar polymers .....	32
Table 1.6 Ionic polymers .....	33
Table 1.7 Hydrophobic molecules .....	34
Table 1.8 Lipophilic molecules .....	35
Table 1.9 Ion-exchange molecules .....	35
Table 3.1 Operating Conditions .....	56
Table 3.2 The simultaneous determination of common anions and cations in the mineral water of Sarikiz using ion chromatography method .....	57
Table 3.3 The result of the heavy metal analysis of Sarikiz .....	58
Table 4.1 The excitation–emission spectra related characteristics of the DPAINH acquired in conventional solvents, and in thin film form of PMMA and EC .....	65
Table 4.2 The Stern-Volmer plots related data of PMMA and EC based electrospun nanofibers and thin films. ....	76
Table 4.3 Calibration related characteristics of PMMA and EC based electrospun nanofibers and thin films .....	78
Table 5.1 UV-Vis spectra related data of ODC -3 in the solvents of EtOH, DCM, THF, Toluene, Toluene/ Ethanol mixture (80:20) and DMF. ....	85
Table 5.2 Emission and excitation spectra related data of ODC-3 in the solvents of EtOH, DCM, THF, Toluene, Toluene/Ethanol mixture (80:20), DMF and in solid matrix of EC. ....	87
Table 5.3 Calibration related characteristics of ODC-3 doped EC based electrospun nanofibers and thin films for Hg (II) ions. ....	93

Table 5.4 $K_{sv}$ Constant of EC based electrospun nanofibers and thin films for Hg (II) ions.....	95
Table 5.5 Florescence lifetimes of the carbazole derivative in THF, EC based thin films and electrospun nanofibers in the presence and absence of the quencher. ....	96
Table 5.6 UV-Vis spectra related data of ODC -5 in the solvents of EtOH, DCM, THF, Toluene/ Ethanol mixture (80:20), DMF and Toluene.....	103
Table 5.7 Emission and excitation spectra related data of ODC-5 in the solvents of EtOH, DCM, THF, Toluene, Toluene/Ethanol mixture (80:20), DMF and in solid matrices of EC.....	105
Table 5.8 Calibration characteristics of EC based electrospun nanofibers and thin films. ....	112
Table 5.9 The Stern Volmer plot and $K_{sv}$ Constant of EC based electrospun nanofibers and thin films.....	113
Table 5.10 Florescence lifetimes of the carbazole derivative in THF, EC based thin films and electrospun nanofibers in the presence and absence of the quencher .....	114
Table 5.11 UV-Vis spectra related data of DMK-1A in the solvents of EtOH, DCM, Toluene/ Ethanol mixture (80:20) and DMF .....	121
Table 5.12 Emission and excitation spectra related data of DMK-1A in the solvents of EtOH, DCM, Toluene/ Ethanol mixture (80:20), DMF and in solid matrices of EC and PMMA.....	123
Table 5.13 Calibration characteristics of EC based electrospun nanofibers and thin films .....	133
Table 5.14 Florescence lifetimes of the carbazole derivative in THF, PMMA based thin films and electrospun nanofibers in the presence and absence of the quencher .....	134
Table 6.1 UV-Vis spectra related data of ODC -1in the solvents of EtOH, DCM, THF, Toluene, Toluene/ Ethanol mixture (80:20) and DMF.....	143

Table 6.2 Emission and excitation spectra related data of ODC-1 in the solvents of EtOH, DCM, THF, Toluene, Toluene/ Ethanol mixture (80:20), DMF and in solid matrices of EC and PMMA.....	144
Table 6.3 Calibration characteristics of EC based electrospun nanofibers and thin films .....	150
Table 6.4 $K_{sv}$ Constant of EC based electrospun nanofibers and thin films for Fe (III) ions .....	151
Table 6.5 Florescence lifetimes of the carbazole derivative in THF, EC based thin films and electrospun nanofibers in the presence and absence of the quencher .....	152
Table 6.6 Calibration characteristics of EC based electrospun nanofibers and thin films .....	160
Table 6.7 $K_{sv}$ Constant of EC based electrospun nanofibers and thin films for Fe (III) ions .....	161
Table 6.8 Florescence lifetimes of the carbazole derivative in THF, EC based thin films and electrospun nanofibers in the presence and absence of the quencher .....	162
Table 6.9 Calibration characteristics of EC based electrospun nanofibers and thin films .....	168
Table 6.10 $K_{sv}$ Constant of EC based electrospun nanofibers and thin films for Fe (III) ions .....	169
Table 6.11 Florescence lifetimes of the carbazole derivative in THF, EC based thin films and electrospun nanofibers in the presence and absence of the quencher .....	170
Table 6.12 UV-Vis spectra related data of MS-4 in the solvents of THF, EtOH, To: EtOH (toluene/ethanol mixture (80:20)), DCM and DMF.....	173
Table 6.13 Emission and excitation spectra related data of MS-4 in the solvents of EtOH, DCM, THF, Toluene, Toluene/ Ethanol mixture (80:20), DMF and in solid matrices of EC and PMMA.....	174
Table 6.14 Calibration related characteristics of PMMA based electrospun nanofibers and thin films .....	180

Table 6.15 $K_{sv}$ Constant of PMMA based electrospun nanofibers and thin films for Fe (III) ions .....	181
Table 6.16 Florescence lifetimes of the carbazole derivative in THF, PMMA based thin films and electrospun nanofibers in the presence and absence of the quencher .....	182
Table 7.1 UV-Vis spectra related data of MS-3 in the solvents of THF, EtOH, To: EtOH (80:20), DCM and DMF.....	189
Table 7.2 Emission and excitation spectra related data of MS-3 in the solvents of EtOH, DCM, THF, To: EtOH (80:20), DMF and in solid matrices of EC and PMMA .....	190
Table 7.3 Calibration related characteristics of PMMA based electrospun nanofibers and thin films .....	196
Table 7.4 $K_{sv}$ Constant of PMMA based electrospun nanofibers and thin films for Sn (II) ions .....	197
Table 7.5 Florescence lifetimes of the carbazole derivative in THF, PMMA based thin films and electrospun nanofibers in the presence and absence of the quencher .....	198

# CHAPTER ONE

## INTRODUCTION

### 1.1 Dissolved Constituents in Groundwater

Water is the most convenient solvent for geochemical species and plays the main role in their continuous cycle in the environment, below, at and above the earth's surface. This enormous effect of water is due to the unique structure of the water molecule, its polarity and solubility considerations.

Groundwater constitutes an important portion of hydrologic cycle or movement of water between oceans, atmosphere and earth's crust. Groundwater contains a wide variety of dissolved cations and anions in various concentrations, because of physical, chemical and biochemical interactions. Sometimes they are hot systems and may be enriched in H<sub>2</sub>S, CO<sub>2</sub>, NH<sub>3</sub> reduced phosphorous compounds such as hypophosphite (PO<sub>2</sub><sup>3-</sup>) and/or phosphite (PO<sub>3</sub><sup>3-</sup>) as well as metal cation and, anions (Prasanna, 2010).

#### 1.1.1 Major Ions

Major cations and anions in groundwater are detected in concentrations ranging from 1 to 1000 ppm ((milligrams per liter) (mg/L)). The major cations include Na<sup>+</sup>, K<sup>+</sup>, Ca<sup>2+</sup>, Mg<sup>2+</sup> and Li<sup>+</sup>. The corresponding major anions can be listed as Cl<sup>-</sup>, HCO<sub>3</sub><sup>-</sup> and SO<sub>4</sub><sup>2-</sup>. The chemical equilibrium equation between bicarbonate and carbonate is as follows;



Because bicarbonate and carbonate are pH dependent species and have been on opposite sides of the equilibrium, they are not often detected in the same groundwater sample. However, they can be found altogether at certain temperatures, pressures, and hydrogen ion concentrations (pHs) (Abbott, 2007).



The major cations consist of 11.4 percent (%) by mass of the elements in the earth's crust, while oxygen (46.6%), silicon (27.7%), alumina (8.1%), and iron (5.0%) made-up nearly the rest (Abbott, 2007). Table 1.1 shows dissolved major constituents of groundwater samples and their sources.

Table 1.1 Dissolved major constituents in natural water (Hydrologyproject, 2012).

<b>Cations</b>	<b>Sources</b>
Sodium (Na <sup>+</sup> )	Feldspars, clays, halite, mirabilite, industrial wastes
Calcium (Ca <sup>2+</sup> )	Amphiboles, feldspars, gypsum, aragonite, calcite, pyroxenes, dolomite, clay minerals
Magnesium (Mg <sup>2+</sup> )	Amphiboles, olivine, pyroxenes, dolomite, magnesite, clay minerals
Potassium (K <sup>+</sup> )	Feldspars, feldspathoids, some micas, clays
<b>Anions</b>	<b>Sources</b>
Bicarbonate (HCO <sub>3</sub> <sup>-</sup> )	Limestone, dolomite
Sulfate (SO <sub>4</sub> <sup>2-</sup> )	Oxidation of sulphide ores, gypsum, anhydrite
Chloride (Cl <sup>-</sup> )	Sedimentary rock, igneous rock
Silica	

### ***1.1.2 Minor Ions***

Potential minor ions found in groundwater have concentrations typically ranging from 0.01 to 10 mg/L. These ions include Fe<sup>2+</sup>, Fe<sup>3+</sup>, Mn<sup>2+</sup>, Cu<sup>+</sup>, Cu<sup>2+</sup>, Br<sup>-</sup>, I<sup>-</sup>, F<sup>-</sup>, BO<sub>2</sub><sup>-</sup>, HPO<sub>4</sub><sup>2-</sup>, SO<sub>3</sub><sup>2-</sup>, HSO<sub>4</sub><sup>-</sup>, S<sub>2</sub>O<sub>3</sub><sup>2-</sup>, HS<sup>-</sup>, HSiO<sub>3</sub><sup>-</sup> and HSO<sub>3</sub><sup>-</sup> (Hydrologyproject, 2012).

### 1.1.3 Trace Ions

Elements shown on the entire periodic table can presently occur in ground waters at low concentrations (< 0.01 mg/L). The levels of some of these trace cations (e.g., Ag, Fe, Pb, and Zn) in ground waters are controlled by concentration of the sulfide ( $S^{2-}$ ). Trace elements that form simple large anions or oxy-anions in solution may exhibit high mobility (Br, I, As, Mo, W) (See Table 1.2).

Table 1.2 Dissolved trace constituents in natural water (Hydrologyproject, 2012).

Dissolved trace constituents in natural water (< 0.1 ppm)			
Aluminum	Antimony	Arsenic	Barium
Beryllium	Bismuth	Bromide	Cadmium
Cerium	Cesium	Chromium	Cobalt
Copper	Gallium	Germanium	Gold
Indium	Iodide	Lanthanum	Lead
Lithium	Manganese	Molybdenum	Nickel
Niobium	Phosphate	Platinum	Radium
Rubidium	Ruthenium	Scandium	Selenium
Silver	Thallium	Thorium	Tin
Titanium	Tungsten	Uranium	Vanadium
Yttrium	Zinc		Zirconium

Acidity is an important factor on mineral content of waters and generally formed by passage of strong acids or acidogenic species like HCl and  $SO_2$  or  $CO_2$  from the magmatic region to the circulating water. The groundwater can be considered as a complex matrix rich in metal cations and anions. Many metals (Ag, Au, Cu, Mo, Pb,

Sn, W, Zn) may form complexes with anionic constituents such as  $\text{Cl}^-$ ,  $\text{HS}^-$  and/or  $\text{OH}^-$  at high temperatures (Smith, Bisiar, Putra, & Blackwood, n.d.).

## 1.2 Chemical Analysis Techniques of Water

Chemical analysis of water is carried out to identify and quantify the chemical species and properties of certain water. This includes pH, major cations ( $\text{Na}^+$ ,  $\text{K}^+$ ,  $\text{Ca}^{2+}$ ,  $\text{Mg}^{2+}$ ,  $\text{NH}_4^+$ ) and anions ( $\text{Cl}^-$ ,  $\text{F}^-$ ,  $\text{SO}_4^{2-}$ ,  $\text{PO}_4^{3-}$ ,  $\text{NO}_3^-$ ,  $\text{NO}_2^-$ ,  $\text{HCO}_3^-$ ), trace elements and isotopes, unstable volatiles such as  $\text{CO}_2$ ,  $\text{H}_2\text{S}$  and  $\text{O}_2$ , organic material and nutrients (Wikipedia, 2012).

Depending on the content of the subjective sample, different methods can be applied to quantify the components. While some techniques can be performed exploiting simple laboratory equipment, others require sophisticated devices; like inductively coupled plasma emission or mass spectrometry (ICP-MS) (Zoriy, Ostapczuk, Halicz, Hille, & Becker, 2005; Bednar, Kirgan, & Jones, 2009), high performance liquid chromatography (HPLC) (D'Archivio, Fanelli, Mazzeo, & Ruggieri, 2007; V'azquez, Mughari, & Galera, 2008), inductively coupled plasma (ICP) (Kova'cs, Nagy, Borsze'ki, & Halmos, 2009), graphite furnace atomic absorption spectroscopy (GFAAS) (González, Firmino, Nomura, Rocha, Oliveira, & Gaubeur, 2009), flame atomic absorption spectrophotometry (Manzoor, Shah, Shaheen, Khalique, & Jaffar, 2006). For the samples in form of steam, gas chromatography can be used to determine the quantities of methane, carbon dioxide, oxygen and nitrogen.

Saturated calomel electrode and glass electrode are often used in conjunction to determine the pH of water (Parga, Cocke, Valenzuela, Gomes, Kesmez, Irwin, Moreno, & Weir, 2005).

Dissolved oxygen and  $\text{H}_2\text{S}$  are most commonly measured by titration (Sasamoto, Yui, & Arthur, 2004).

Recently, ion chromatography appeared as a sensitive and stable alternative technique that can measure major cations ( $\text{Li}^+$ ,  $\text{NH}_4^+$ ,  $\text{Na}^+$ ,  $\text{K}^+$ ,  $\text{Ca}^{2+}$  and  $\text{Mg}^{2+}$ ) and anions easily ( $\text{F}^-$ ,  $\text{Cl}^-$ ,  $\text{NO}_2^-$ ,  $\text{Br}^-$ ,  $\text{NO}_3^-$ ,  $\text{PO}_4^{3-}$  and  $\text{SO}_4^{2-}$ ) (Zeyrek, Ertekin, Kacmaz, Seyis, & Inan, 2010).

Most of these techniques are generally requiring sophisticated and expensive equipment, sometimes sample pretreatment, and/or analyte pre-concentration steps. Analytical chemists still need practical as well as accurate sensitive and selective detection techniques for analysis of ion rich samples. In this context, scientists offered chemical sensors for analysis or continuous monitoring of waters in last two decades. Today, there are a huge number of optical chemical sensors working in this field extensively and successfully. With respect to above-mentioned techniques, chemical sensors provide many advantages such as being simple, rapid, inexpensive, selective and sensitive. Because of these advantages, studies on chemical sensor design are still one of the most popular fields of analytical chemistry.

In this work, we will focus on development of optical chemical sensors for analysis of some cations and anions in difficult matrices such as groundwater.

### **1.3 Chemical Sensors**

A chemical sensor is mostly a small device that gives a signal because of a chemical interaction or process between the analyte and the sensor device and can be used for the qualitative or quantitative determination of the analyte of interest.

Chemical sensors have widely been used in applications like process control, product quality controls, in critical care units, homeland security, safety, industrial hygiene controls, engineering controls, monitoring of air pollutants, human comfort controls, medical diagnostics and home safety alarms. With these widespread applications, chemical sensors provided economic and social benefits (Stetter, Penrose, & Yao, 2003).

The chemical sensors can simply be classified as electrochemical, optical, mass sensitive and heat-sensitive, considering to the type of transducer (Cattrall, 1997). Electrochemical devices transform the electrochemical signal arising from the analyte within the electrode to a useful signal. Very sensitive devices, magnetic devices, thermometric devices and devices working on other physical properties for example  $\alpha$ ,  $\beta$ , or  $\gamma$  radiation may form the basis for chemical sensors.

### ***1.3.1 Optical Chemical Sensors***

There are different definitions and classifications for chemical sensors. Among them, definition of the International Union of Pure and Applied Chemistry (IUPAC) attracts the attention. According to the IUPAC, a chemical sensor is;

“A device, that transforms chemical information, ranges from the concentration of a specific sample component to total composition analysis, into an analytically useful signal. The chemical information, mentioned above, may originate from a chemical reaction of the analyte or from a physical property of the system investigated. Chemical sensors contain two basic functional units: a receptor and a transducer part. Some sensors may include a separator which is, for example a membrane (IUPAC, 1997)” (EPA, 2012).

The receptor part of a sensor is defined by IUPAC as;

“The chemical information is transformed in it into a form of energy, which maybe measured by the transducer. The receptor part maybe based upon various principles: physical, chemical or biochemical (IUPAC, 1997).”

The transducer part of a sensor is defined by IUPAC as;

“Device capable of transforming energy carrying the chemical information about the sample into a useful analytical signal (IUPAC 1997)” (EPA, 2012).

The optical chemical sensors mainly use the optical components like light sources of xenon lamps, lasers or LEDs (Light Emitting Diodes), fiber optics, photo diodes and/or photo multiplier tubes, and amplifiers. The resulting target in an optical chemical design is miniaturization. In such kind of designs, small components take the place of large ones. If the equipments are appropriate for measurement of either absorption or emission, the intensity and wavelength of the characteristic light provide the analytical signal for quantitative and/or qualitative analysis. Sometimes other optical properties like refractive index, diffraction, reflection etc. may provide the analytical signal. All these things consist of pieces of the equipments of the device. The other aspect of an optical chemical sensor is the 'indicator chemistry'. In this part, a chromophore, an ionophore or sometimes a fluoroionophore is encapsulated (or covalently bonded) in an appropriate matrix material, which selectively recognizes the analyte. The choice of correct ionophore and appropriate matrix material is probably the most important issue in the design of an optical chemical sensor (Mayr, 2002). Ideally, a sensor should provide adequate sensitivity, large working range, and high selectivity towards the analyte of interest, a corresponding signal output to the amount of analyte, fast response, high signal-to-noise ratio and long-term stability (Mayr, 2002).

#### *1.3.1.1 Principles of Optical Chemical Sensors*

An optical chemical sensor normally consists of the following components:

1. A recognition unit, where indicator chemistry works, a specific interaction between the recognition element and the analyte takes place;
2. The transducer unit that converts the recognition process into a measurable optical signal;
3. Optical components, which consists of a light source (a LED or a laser), fiber optics; lenses, filters;
4. A detector (in its simplest form a photodiode or a photo multiplier tube), which detects and converts the change of the measured optical property;
5. Signal amplification, signal processing (conversion from optical to digital) and readout.

### *1.3.1.2 Classification of Optical Chemical Sensors*

Optical chemical sensors may be classified according to the operating principle of the transducer. If the fiber optics were exploited in the design of the sensor, they called as fiber optic chemical sensors. In another approach, they can be classified according to their application area like gas sensors, cation sensors, anion sensors, biosensors etc. In most of the optical chemical sensors, one of the listed parameters was measured to provide a significant analytical signal.

- a) Absorbance should be measured in a transparent medium, caused by the absorptivity of the analyte itself or by an indirect reaction with some proper chromophore or chromoionophore.
- b) Fluorescence, is the emission of light in a different wavelength by the fluorescent molecule that has absorbed light or other electromagnetic radiation
- c) Reflectance can be measured in non-transparent moieties.
- d) Luminescence, is the intensity of light emitted after an excitation process
- e) Refractive index, measured as the result of a change in solution composition.
- f) Optothermal effect, the thermal effect observed after absorption of the light.
- g) Light scattering, scattering of the light by a particle in solution or in vacuum.

### *1.3.2 Fiber Optic Sensors*

An optical fiber is mainly a flexible, transparent material made of glass or plastic. It works as a waveguide to transmit the light between the two ends of the fiber. Prior to the analysis, in the beginning, optical fibers were widely used in field of communication. Later, fibers were used for illumination, and produced in bundles so that they used to carry the light, allowing viewing in confined spaces. Today, specially designed fibers have been used for a variety of other applications, including optical chemical sensors.

An optical fiber typically consists of a transparent core surrounded by a transparent cladding material with a lower refraction index. Light is kept within the

core by means of total internal reflections. This causes the fiber to act as a waveguide.

In sensor design, optical fiber can be used to deliver light from a remote source to a detector, or it can serve as the sensor itself to measure properties such as light intensity, radiation, displacement, temperature, pressure, strain, magnetic and/or electric fields, flow rate, and vibration. An understanding of the working principles of optical fiber is necessary to perform the best use of the technology (Cohen, Digby, & Miller, 1997).

An optical fiber consists of three principal units, named the core, the cladding and the coating, respectively, as shown in the Figure 1.1.

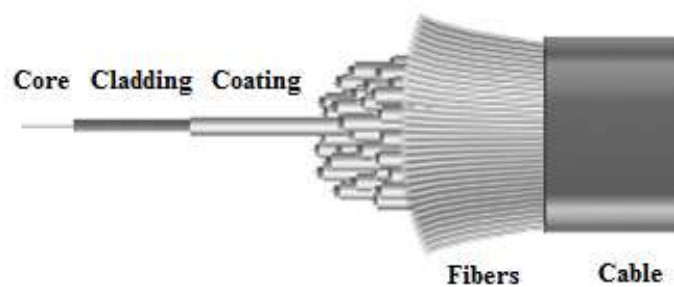


Figure 1.1 Basic structure of an optical fiber (Fidanboyly, & Efendioglu, 2009).

Core is the central section of the fiber and is generally, made up of silica. This part is the light-transmitting region of the fiber.

Cladding is the first optical layer surrounding the core, which acts as an optical waveguide that confines the light. It is also usually made up of silica with a different refractive index than that of the index of the core.

The coating is the first non-optical layer surrounding the cladding, typically consists of one or more layers of a polymer that protects the silica against physical forces or environmental effects.



As mentioned earlier, refractive indices of the core and cladding should be different  $n_1$ , and  $n_2$ , respectively. The refractive index of the core,  $n_1$ , should always be greater than the index of the cladding,  $n_2$ . Therefore, light propagates through the core, and the fiber acts as an optical waveguide (Cohen, Digby, & Miller, 1997).

The core can be concluded as a cylindrical rod of dielectric material and is generally made up of glass. Light propagates mainly along the core of the fiber. The cladding layer is made of a dielectric material (glass or plastic) with an index of refraction less than that of the core. Functions of this part are decrease loss of light propagating through the core, scattering loss, protecting the fiber and supporting the mechanical strength. The coating is an additional layer used to protect the optical fiber from physical effects. The coating is mainly made up of plastics (Jones, 1998; Fidanboyly, & Efendioglu, 2009).

Propagating of the light along the fiber is based on the “total internal reflection”. The critical angle of incidence is the angle at which total internal reflection occurs. At any angle of incidence, greater than the critical angle, light is totally reflected within the glassy medium (See Figure 1.2) (Jones, 1998; Fidanboyly, & Efendioglu, 2009).

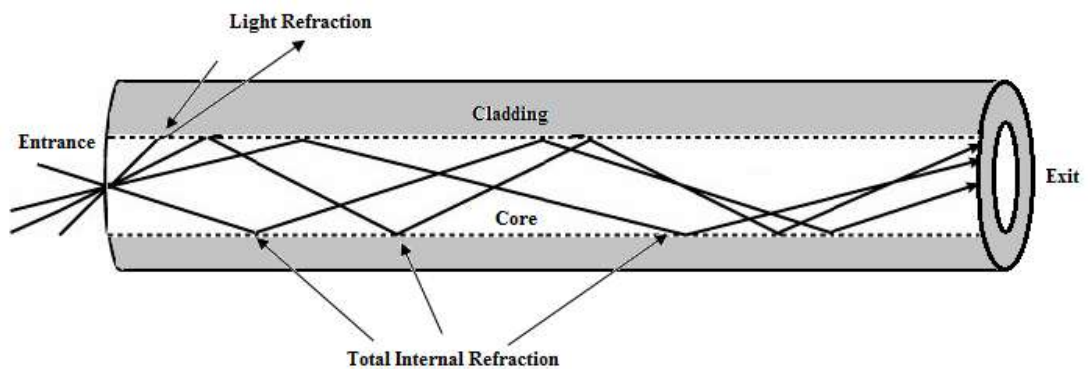


Figure 1.2 Total internal reflections in an optical fiber.

The critical angle of incidence is determined by using Snell's Law (See Equation 1.1).

$$n_i \sin I = n_r \sin R \quad (1.1)$$

where:

$n_i$  = index of refraction of the medium in which the light is initially traveling

$n_r$  = index of refraction of the second medium

$I$  = angle between the incident ray and the normal to the interface

$R$  = angle between the refracted ray and the normal to the interface (Cohen, Digby, & Miller, 1997).

An optical fiber is a good example of an electromagnetic surface (Jones, 1998; Fidanboylu, & Efendioglu, 2009).

An optical fiber also characterized with numerical aperture (NA) which defines the angle of acceptance, or the maximum angle for which light rays entering the core could be guided (See Equation 1.2). It is also a measure of how strongly the fiber guides light and thus resists bending-induced losses. It is calculated with the equation:

$$NA = \sqrt{\left(\frac{2}{n_1}\right)^2 - \left(\frac{2}{n_2}\right)^2} = \sin \theta \quad (1.2)$$

$n_1$  and  $n_2$  = core and cladding indices of refraction

$\theta$  = half-acceptance angle (Cohen, Digby, & Miller, 1997).

Optical fibers can be classified into two groups named single mode and multimode. In classifying the index of refraction profile, we differentiate between step index and gradient index. Step index fibers have a constant index profile over the whole cross section. Gradient index fibers have a nonlinear, rotationally symmetric index profile, which falls off from the center of the fiber outwards. (Jenny, 2000; Fidanboylu, & Efendioglu, 2009). Figure 1.3 shows the different types of fibers.

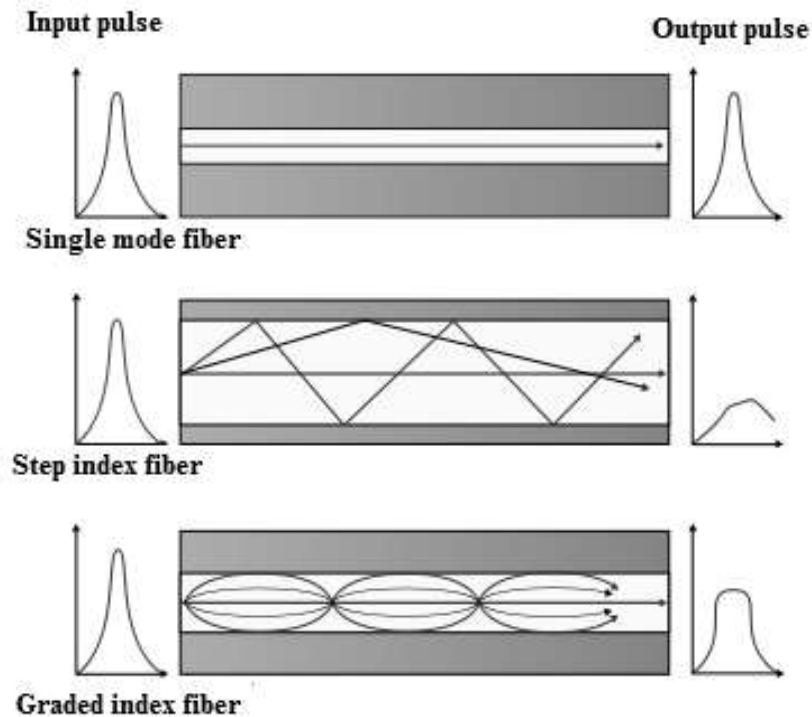


Figure 1.3 Different types of optical fibers (Fidanboylu, & Efendioglu, 2009).

### 1.3.2.1 Sensing Modes and Fiber-Optic Assemblies

Because fiber-optic sensor systems are a component of sensor technology, different sensing modes (diffuse reflective, through-beam, retro reflective) are also available for fiber optics. The two types of fiber-optic assemblies that address these sensing modes are *individual* and *bifurcated*.

Fiber-optic through-beam mode, as shown in Figure 1.4, consists of two cables. One is interfaced to the light source and is used to guide the light energy towards the sensing location. The other tip is interfaced with the detector or receiver of the remote sensor and is used to guide the light beam from the sensing location to the detector (Biala, 2001).

A bifurcated fiber-optic assembly can be used for both, diffuse reflective and retro reflective sensing.



Figure 1.4 Bifurcated fiber-optic cable assemblies (Biala, 2001).

In general, the FOSs uses optical fibers either as the sensing element "intrinsic sensors", where fiber body is used as the main sensing moiety, or as a means of waveguide from a remote sensor to the electronics of an instrument or a device that process the signals "extrinsic sensors" (Wikipedia, 2012).

In the intrinsic sensors, the measurement directly acts on the optical fiber and changes the properties of the light intensity, phase, polarization, and wavelength or transit time. Applications of intrinsic sensors can be listed as temperature, displacement, pressure, pH, smoke etc. Analyte dependent variations can be measured effectively by observing variations in the refractive index (Annamdas, 2011).

In the extrinsic sensors, mostly multimode optical fibers are used to transmit modulated light. The fiber only carries the light from the source to the sensing part and from the sensing part to the demodulation system. Extrinsic sensors are used to measure chemical variables, vibration, rotation, displacement, velocity, acceleration etc. (Annamdas, 2011).

### ***1.3.3 A Short View to the Optical Chemical Sensors***

Optical chemical sensors can utilize various optical parameters (absorbance, reflectance, luminescence, fluorescence), covering different regions of the electromagnetic spectrum (from UV, to NIR) allowing the measurement not only of the intensity of light, but also of other variables, such as lifetime, refractive index, scattering, diffraction and polarization (Lobnik, Turel, & Urek, 2012).

Optical chemical sensors have numerous advantages over other sensing techniques such as selectivity, ease of miniaturization, being inexpensive, non-destructive, immunity to electromagnetic interference etc. (Lobnik, Turel, & Urek, 2012).

As mentioned earlier, an optical chemical sensor is a device that measures a physical quantity or the concentration of a chemical or biochemical species and converts it into a signal, which can be read by an observer or by an instrument. The most widely used basic measuring techniques in optical chemical sensors are optical absorption and luminescence, but sensors based on other optical parameters, such as refractive index and dispersion, have been developed. However, sometimes the term “sensor” is being used to refer to a cation or anion-selective molecular probe or a pH indicator.

On the other hand, the alternative use of optical fibers in various applications has grown, especially during the past 10-15 years. Optical fibers can be used as sensors to measure temperature, pressure and other physical quantities by modifying a fiber so that the quantity to be measured modulates a light related parameter such as intensity, phase, polarization, and wavelength or transit time of light throughout the fiber. Extrinsic fiber optic sensors use an optical fiber, usually a multimode one, to transmit modulated light from either an electronic design or a non-fiber optical sensor. A major benefit of extrinsic sensors is their ability to reach places like, high temperature, corrosive nature, strong gamma radiation etc. (Wikipedia, 2012).

Optical fibers have many uses in remote sensing. In some applications, the instrumentation can be designed independently, simply containing a proper light source, bifurcated optical fibers, a detector and a signal processor. Sometimes the sensor may be itself an optical fiber. In other cases, fiber is used to connect a non-fiber optic sensor platform to a measurement system. Depending on the application, optical fiber may be used because of its small size or the fact that no electrical power is needed at the remote location (Chinaopticcable, 2012).

In recent designs, the fiber optic probes were incorporated with spectroscopic instruments, which eliminate the need for traditional cuvettes for measurements. The probe can be immersed in a beaker, water bath, and enclosed pipe or can be interfaced with any suitable platform containing solid sample. In such kind of designs, light source and detector systems of the conventional spectroscopic instruments are being used together with fiber optics.

Conceptual basis of optical sensor design relies on absorption and emission based spectroscopic techniques. Therefore results of the huge number of absorption or emission based experimental studies can be beneficial in early stages of optical sensor design.

Except that of instrumentation, optical chemical sensors are mainly composed of a polymer matrix material, an ion carrier and an indicator dye or a combined form of the carrier and dye; chromoionophore or more specifically fluoroionophore; that acts as a fluorescent probe.

Aside from instrumentation, probably, the most challenging aspect of an optical chemical sensor design is the planning of the indicator chemistry, which covers proper choice of analyte-specific indicator, and compatible matrix material where the reagent dye can be adsorbed, covalently or electrostatically immobilized, or simply encapsulated that is also permeable to the analyte.

In order to perform an efficient immobilization of the indicator in the support matrix, the indicator must be soluble and stable in the chosen material. Commonly used polymer based matrix materials in optical chemical sensor design include polystyrene, polyvinyl chloride, polymethyl methacrylate, polydimethyl siloxanes, polytetrafluoroethylenes, polymers for molecular imprinting, organic conductive polymers, hydro gel-plasticizer emulsions and cellulose derivatives such as ethyl cellulose. The sol-gel process and different types of glassy materials also provide relatively suitable support matrix for the immobilization of analyte-sensitive reagents.

Recently, with advances in materials fabrication and better understanding of the characteristics of the ionic liquids (IL), these substances are being used in optical sensor design as matrix material or additive. Understanding of the availability of ionic liquids is a novel development in this area and future applications ILs looks promising.

The reagent-immobilized materials (sensitive layers) can be fabricated into several configurations, such as thin films, gels, to be interfaced with optical fibers, in nanoparticles, etc. The most common types are thin polymer films, membranes and recently nano-scale materials (Lobnik, Turel, & Urek, 2012).

In this thesis, we focused on fluorescence-based measurements during optical chemical sensor development efforts. In the following chapter, short information will be given on theoretical bases of luminescence. Additionally, steady-state and lifetime based measurements techniques will be mentioned.

## **1.4 Luminescence**

### ***1.4.1 Mechanism of Luminescence***

Luminescence is the light emission by the electronically excited atoms or molecules. Electronic excitation requires the supply of energy. Different types of luminescence, depending on the source of energy can be mentioned.

Electroluminescence, chemiluminescence, thermo luminescence and photoluminescence, are known (Lakowicz, 1983; Parker, 1968; Schmidt, 1994).

Luminescence occurs when an electron returns to the electronic ground state from an excited state and loses its excess energy as a photon.

#### 1.4.1.1 Fluorescence and Phosphorescence (Photoluminescence)

The electronic states of the molecules having conjugated systems may exhibit two different states; singlet and triplet.

*Singlet state:* All electrons in the molecule are in opposite spin (spin-paired).

*Triplet state:* One set of electron spins is unpaired (See Figure 1.5).

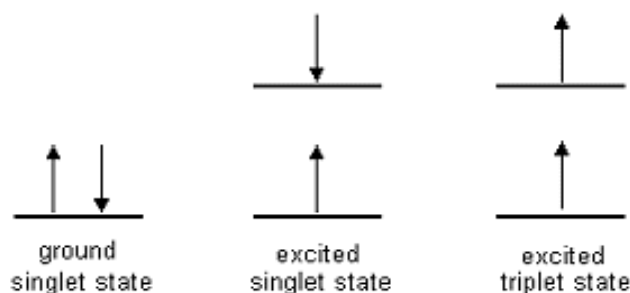


Figure 1.5 The electronic states of organic molecules (Teaching, 2012).

#### Fluorescence

Absorption of UV or visible radiation by a molecule, (especially molecules containing conjugated systems) results with excitation from the vibrational levels of the ground state to one of the vibrational levels of the first excited singlet state. Occasionally, the excitation can occur to the second or third levels of the singlet-excited states (Frohne, 2004).

The excited electron will quickly fall to the lowest vibrational level by losing its energy through collisions. The molecule may also transfer the excess energy by means of vibrational or rotational movements. When the molecule returns to the ground state, from the singlet excited, by emitting of photon, this is called



‘Fluorescence’. A light absorbing molecule may lose its energy some other ways. Total of these processes are called ‘*radiation less energy transfer*’ (Frohne, 2004).

Intra-molecular redistribution of energy between possible electronic and vibrational states can be performed by reorientation of the molecule itself in ways, which help the internal transfer of energy.

### Phosphorescence

The spin of an excited electron can be reversed, when the molecule in an excited *triplet* state; this is called *intersystem crossing*. A molecule in the excited triplet state does not always use intersystem crossing to return to the ground state. It can lose its energy by emitting a photon. A triplet/singlet transition is much less possible than that of a singlet/singlet transition. The lifetime of the excited triplet state (phosphorescence) can be extending to seconds or 100 seconds. Emission from triplet/singlet transitions can continue after irradiation stopped. Phosphorescence is usually measured at low temperatures or alternatively in highly viscous media (Frohne, 2004). The electronic transitions during absorption and emission of light are illustrated by Jablonski level diagram, shown in Figure 1.6.

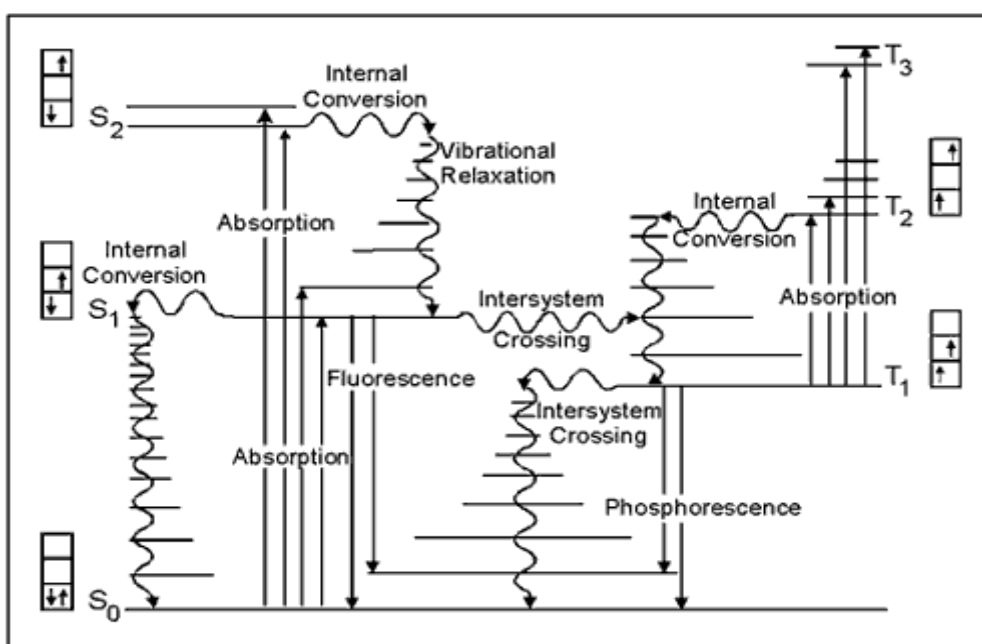


Figure 1.6 Jablonski diagram with the reciprocal rates of transition in [s] (Photobiology, 2012).

## 1.5 Stoke's Shift

Stokes shift can be define as the difference between positions of the band maxima of the absorption and emission spectra of the same electronic transition in terms of wavelength or wave number. It is named by Irish physicist, Sir George G. Stokes (Lakowicz, 1983).

When a molecule or an atom absorbs a photon, it gains energy and becomes in the excited state. One way for the molecule or the atom is to emit a photon to relax, losing its energy. Another method would be to loss the energy in form of heat. The energy difference between the emitted photon and the absorbed photon is called as the Stokes shift. The difference is generally stated in terms of wavelength. If the emitted photon has more energy, in this time the difference in energy is called as *anti-Stokes shift*; this excess energy comes from consumption of thermal phonons in a crystal lattice, cooling the crystal in the process. Yttrium oxysulfide doped with gadolinium oxysulfide can be mentioned as a good example of anti-Stokes pigments, absorbing in the near infrared and emitting in the visible region of the electromagnetic spectrum (Lakowicz, 1983).

## 1.6 Quantum Yield

The fluorescence quantum yield is a specific property of a fluorophore and depends upon microenvironment of the molecule. It is especially important for the characterization of novel fluorescent probes. The fluorescence quantum yield can simply be defined as the ratio of photons absorbed to photons emitted through the fluorescence process (See Equation 1.3) (Allen, 2010).

$$Q = \frac{\textit{photons}_{em}}{\textit{photons}_{abs}} \quad (1.3)$$

The quantum yield  $Q$  can also be formulated by exploiting the rate constants of the radiative ( $k_r$ ) and non-radiative ( $k_{nr}$ ) relaxation pathways (See Equation 1.4).

$$Q = \frac{k_r}{k_r + \sum k_{nr}} \quad (1.4)$$

Today measurement of the absolute quantum yield can be performed exploiting extra equipment on conventional spectrofluorometers. However, this approach is quite new and not so much convenient. It is more convenient to determine the relative quantum yield of a fluorophore by comparison to a reference fluorophore with a well-known quantum yield. There are two approaches for measurement of relative quantum yield: single-point measurement comparative method and multi-point measurement comparative methods, respectively.

The single-point method compares the integrated emission intensities from a single sample and a reference at same concentration. While this method is fast and easy, it may not always be reliable. The second approach; the comparative method described by Williams et al.; which involves the use of different concentrations of well characterized references with known fluorescence quantum yields (Allen, 2010).

In this thesis, the comparative William's method has been exploited during quantum yield calculations.

## 1.7 Fluorescence Lifetime

Fluorescence lifetime is an average time for a molecule to remain in the excited state before emitting a photon. It is not easy to give a distinct fluorescence lifetime for a molecule. Each molecule emits randomly after excitation. Many excited molecules will fluoresce earlier than the average lifetime, whereas some fluoresce long after the average lifetime. Fluorescence lifetimes for most of the molecules are generally approximately 1-10 nsec. However, they also can range from microseconds to the sub-nanoseconds.

Measurement of the fluorescence lifetime is different from measurement of steady-state fluorescence and requires specific equipment, light sources and detectors (Princetoninstruments, 2012).

Information taken by normal fluorescence spectroscopy is different than that of the information can be obtained by using time-resolved fluorescence method. Time-resolved fluorescence measurements provide information about the microenvironment of the molecule.

When a fluorescent molecule and an analyte interfaced and reacted a number of processes can occur reducing fluorescence intensity. These processes can be listed as collisional quenching, dynamic quenching, energy transfer (intermolecular, intramolecular or resonance), charge transfer reactions or formation of complexes in the ground state.

These events occur on the same time scale as the fluorescence decay. Thus, measurement of the fluorescence lifetimes (by means of time-resolved fluorescence spectroscopy) can be used to investigate these processes and gain insight into the chemical surroundings of the fluorophore (Princetoninstruments, 2012).

One can record the time-dependent decays of fluorescence (lifetimes) in the time or frequency domains. In the time domain measurements, one measures the sample emission following pulsed excitation by using detectors with high temporal resolution (e.g. streak cameras) or time-sampling circuits (e.g. time correlated single photon counting approach; TCSPC). In the frequency domain measurements, one measures the emission phase angle.

In a single fluorescence decay process, when the sample is excited with an optically short pulse of light, the excited-state decays as it is depleted of excited fluorophores.

The time course of this process can be described by an exponential decay Equation 1.5;

$$Fl(t) = Fl_0 e^{-t/\tau} \quad (1.5)$$

where;  $Fl_0$  is the fluorescence intensity at the time excitation is terminated and  $\tau$  is the excited-state fluorescence lifetime. In many cases, the intensity decay cannot be accurately defined by a single exponential decay equation (Bright, & Munson, 2003).

In these situations, the observed intensity decay (See Equation 1.6) is often given by a sum of exponential terms:

$$Fl(t) = \sum_{i=1}^n a_i e^{-t/\tau_i} \quad (1.6)$$

where  $\alpha_i$  is the pre-exponential factor denoting the contribution to the total time-resolved decay of the component with lifetime  $\tau_i$ .

Simple time domain decay curves arise only if the sample is excited with an infinitely short pulse of light. Figure 1.7 illustrates a set of time-resolved decay curves exhibiting 1, 5, and 10 ns excited-state lifetimes (Bright, & Munson, 2003).

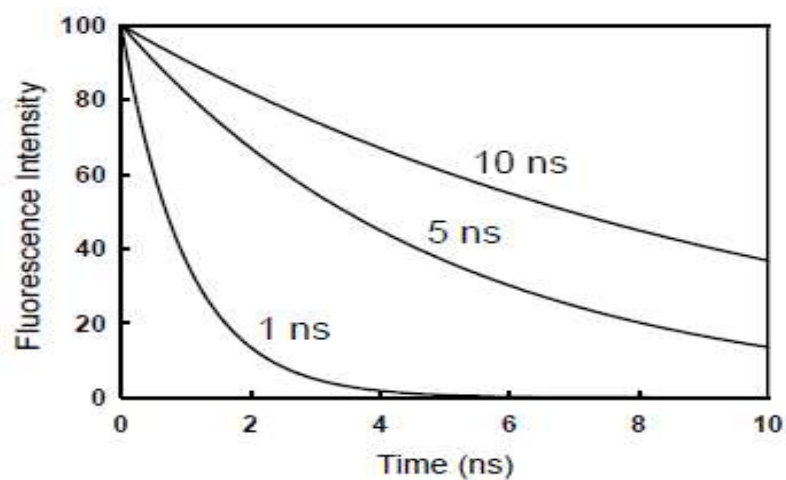


Figure 1.7 Simulated time domain traces for a fluorophore that exhibits a 1, 5, or 10 ns excited-state lifetime (Bright, & Munson, 2003).

## 1.8 Time Correlated Single Photon Counting (TCSPC) Method

Time correlated single photon counting (TCSPC) is a digital photon counting technique, which is time correlated in relation to a pulsed excitation light. The main components for signal processing in TCSPC are;

1. Constant fraction discriminators (CFD) is used to extract precise timing information from the detector pulse output.
2. Electrical delays (DEL),
3. Time-to-Amplitude Converter (TAC),
4. Amplifier (between the TAC and ADC),
5. Analogue to Digital Converter (ADC),
6. Digital memory (Mem) (See in Figure 1.8).

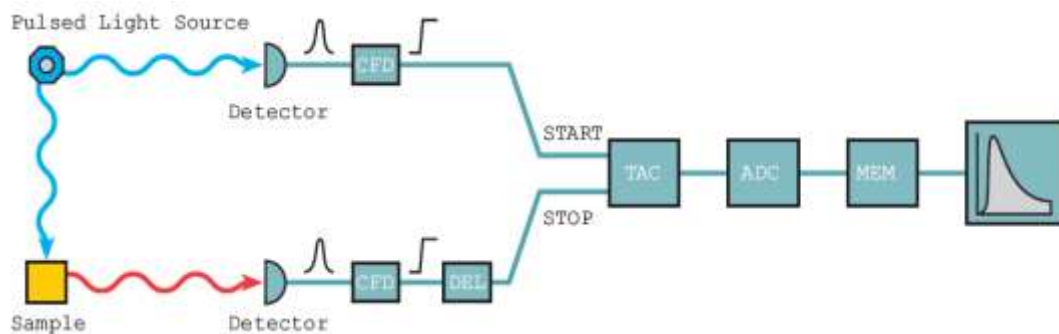


Figure 1.8 The main components for signal processing in TCSPC (Edinburghphotonics, 2012).

In TCSPC technique, the sample is excited many times using a pulsed light source. The acquired data forms a probability histogram correlating the time between an excitation pulse (START) and the observation of the first photon coming from fluorescence (STOP).

In TCSPC technique, the time at which a photon is incident on the detector should be defined at least with a picosecond resolution to obtain a high precision (Edinburghphotonics, 2012).

## **1.9 Towards Design of an Optical Sensor**

There are two aspects of the sensor design. The light source, transducer, the sensing layer, data-acquisition electronics (detectors and amplifiers) and software consists of the components of a sensor system. The choice of appropriate indicator, support materials, and immobilization techniques consists of the indicator chemistry (Lobnik, Turel, & Urek, 2012).

In the following chapters, potential indicator molecular probes, polymeric and glassy support materials and immobilization techniques will be mentioned.

### ***1.9.1 Indicators***

#### *1.9.1.1 Indicators Exploited For Cation Sensing*

Probably the key point of the indicator chemistry in an optical chemical sensor design is the transformation of the measured concentration of the analyte into a measurable analytical signal. Up to now, various types of colorimetric indicators (ionophores) have been used in optical chemical sensor design. The term ionophore describes ligands that selectively bind ions. Mainly they are macro-cyclic molecules with an appropriate ion-binding cavity. In such cases, selectivity depends on the degree of fit between of the analyte ion and the ion-binding site of the ionophore (Wolfbeis, 2004).

There are huge numbers of ionophores responding to cations and/or anions. Some of them are commercialized and some of them are newly synthesized ones. They may be lipophilic or hydrophilic. They may respond to the analyte in solution moiety or in solid state, in immobilized forms. However, in order to say an optical chemical sensor, preferably the indicator should be immobilized in an appropriate solid matrix.

Cation sensing exploiting chromogenic ionophores may work on directly or indirectly. Upon metal ion binding a loss of proton from the reagent may occur. In such cases, the response is pH dependent Chromogenic crown ether structures may be used for selective sensing of  $\text{Ca}^{2+}$  and  $\text{Ba}^{2+}$ .

Valinomycin, (See in Figure 1.9) (potassium-selective neutral ionophore) and a neutral  $\text{H}^+$  selective chromoionophore have been used together in selective detection of potassium ions (Wolfbeis, 1991).

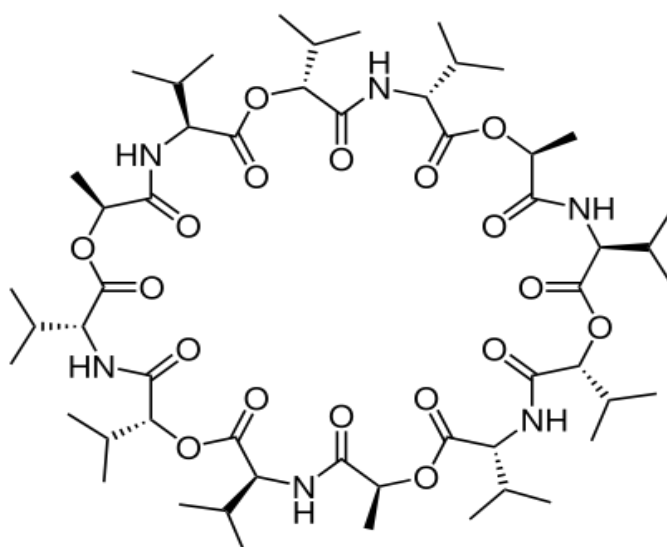
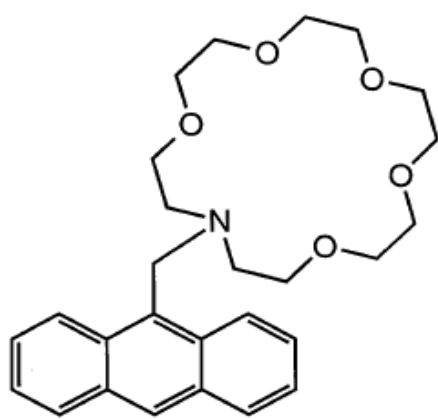


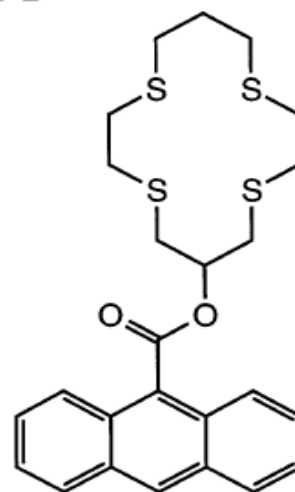
Figure 1.9 Valinomycin (Wikipedia, 2012).

Many cations such as  $\text{Co}^{2+}$ ,  $\text{Cr}^{3+}$ ,  $\text{Fe}^{3+}$ ,  $\text{Cu}^{2+}$ ,  $\text{Ni}^{2+}$  and  $\text{Hg}^{2+}$  quench or enhance fluorescence upon exposure to the ionophore encapsulated within the matrix. In order to design an optical chemical sensor, selectively responding compounds should be chosen, and immobilized in sufficiently permeable matrices. In the elegant work of Valeur, sensors for cation recognition were classified and explained into detail. According to Valeur, Fluorescent photo induced electron transfer (PET) based cation sensors can be classified as Crown containing, Cryptand-based, Podand-based, Chelating and Calixarene based, PET sensors involving excimer formation and sensors involving energy transfer. Same author has been made a similar structural classification also for photo induced charge transfer (PCT) cation sensors (Valeur, & Leray, 2000) (See Figure 1.10-15).



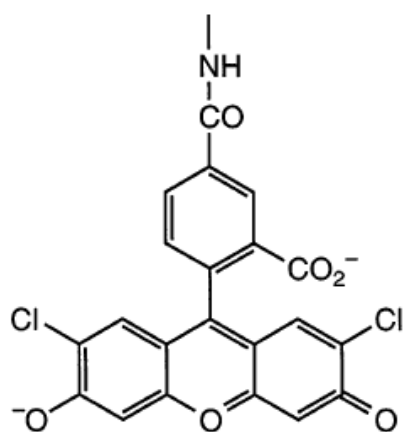


I

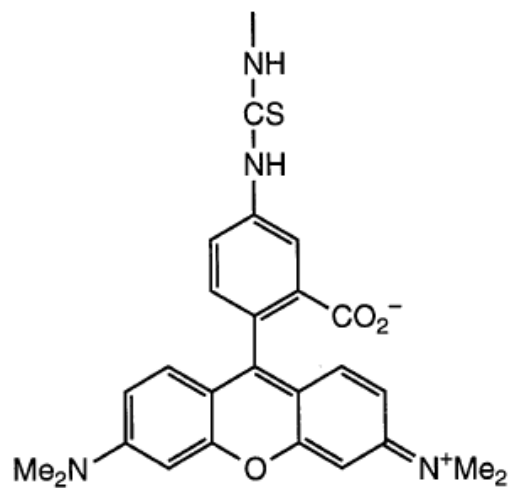


II

Figure 1.10 Examples of crown ether containing molecular probes I: Oxygen II: Sulphur containing crown ether moieties (Valeur, & Leray, 2000).



Calcium Green



Calcium Orange

Figure 1.11 Examples of chelating sensors (Valeur, & Leray, 2000).



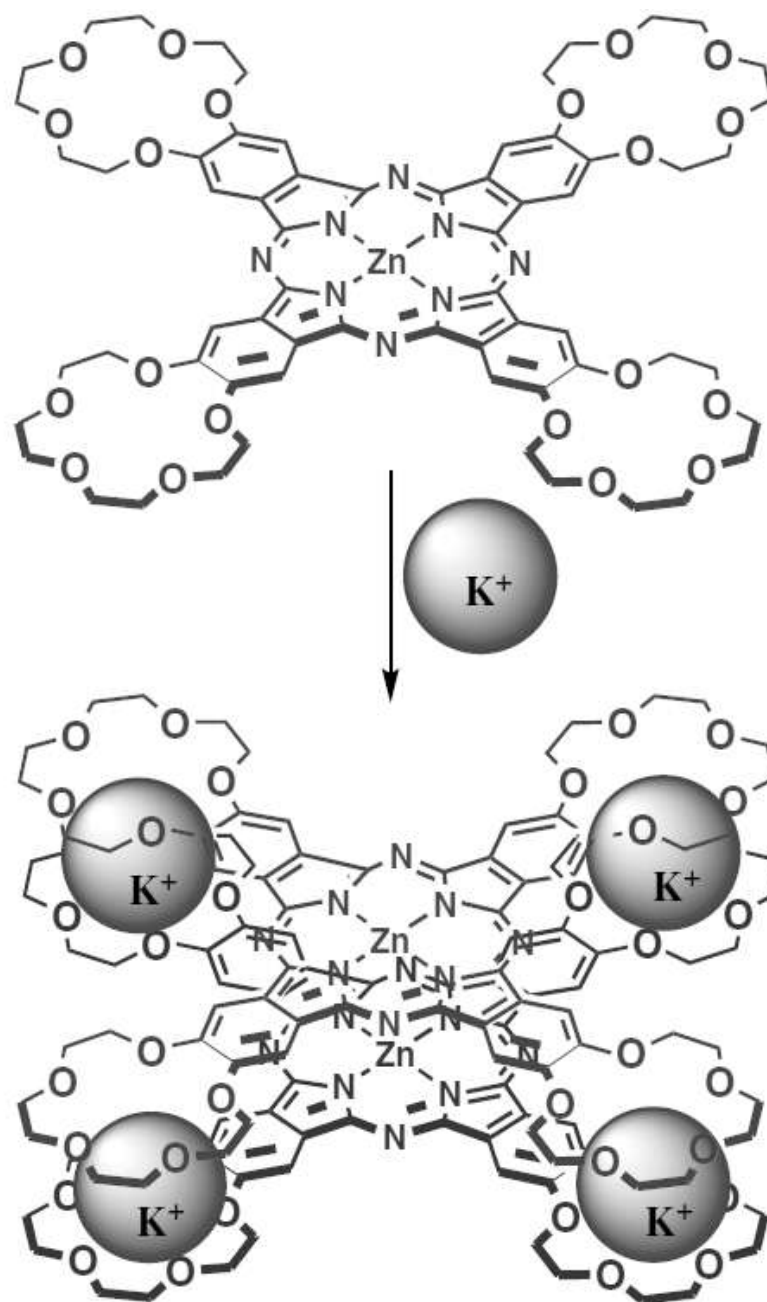


Figure 1.14 Dimerization of crown ether bearing phthalocyanine structures upon exposure to  $K^+$  ions (Topal, Atilla, Ertekin, Tommasino, Luneau, & Gürek, 2012).

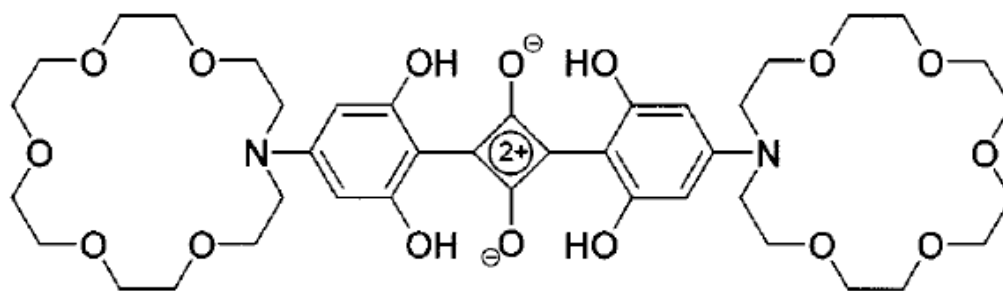


Figure 1.15 Potassium sensing with bis[4-N-(1-aza-4,7,10,13,16-pentaoxacyclooctadecyl)-3,5-dihydroxyphenyl]suaraine (Ertekin, Yenigül, & Akkaya, 2002).

Examples of fluorescent molecules recognizing metal cations are numerous. Understanding of sensing mechanism, cation-induced photo physical changes and their relationship with matrix, is very important and would be helpful for the investigators. Another alternative way in anion sensing is ligand exchange. Sulphide can be determined depending on its ability to rely dithiofluorescein from complexes with silver nitrate and with o-hydroxymercuribenzoic acid.

#### *1.9.1.2 Indicators Exploited For Anion Sensing*

Anion sensing with this kind of indicator dyes is not convenient. Paramagnetic anions and anions having high atomic number atoms are potential quenchers for fluorophores. Anions can also be sensed an indirect way exploiting their oxidizing or reducing properties via their effect on chromic dyes (Wolfbeis, 1997).

#### *1.9.2 Polymer Matrix Materials*

In a sensor design, the exploited polymeric matrix materials are expected to satisfy different requirements to perform optical chemical sensing. Probably one of the most important of them is the one regarding solubility considerations. The indicator dye and all other additives have to be soluble and stable enough within the polymeric matrix without leaching. The analyte also has to be diffusible into the polymer. The chosen polymeric material has to be chemically and physically stable in order to provide long operational lifetime and shelf-life requirements.

Furthermore, swelling, crack formation, crystallization, migration or reorientation of neither the indicator dye nor the other additives within the polymeric matrix must occur. The chosen polymer must be resistant to heat, ambient light, convenient chemicals (acids, bases, oxidants) and if it is possible it should be non-toxic or biocompatible. The polymer preferably should not have any intrinsic color/luminescence, and it should be optically transparent in the whole spectral range (Mohr, 2002). Finally, the material should have good mechanical stability.

#### *1.9.2.1 Polymers Used In Optical Sensor Design*

Chose of appropriate polymer is an extremely important part of optical sensor design. The microenvironment of the immobilized dye has a strong effect on its spectral properties,  $pK_a$  value, luminescence lifetime, binding constant, etc. In the choice of polymer, the permeability for the analyte, stability, availability for immobilization of the indicator dye, compatibility with other materials and optical properties should be considered. Structure of the polymeric material has a considerable effect on the performance of the sensor and its characteristics. Selectivity, sensitivity, working range, calibration performance, and response time and short-long term stability can be listed among them.

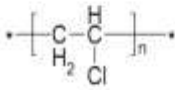
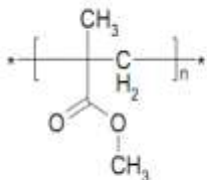
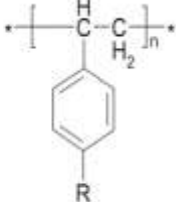
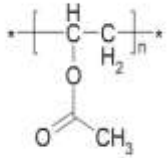
Polymers having a high glass transition temperature ( $T_g$ ) are brittle. Addition of plasticizers make possible of diffusion of ions and gases through the polymeric matrix material. Therefore, the plasticizer contents extending to 66% have been used for the preparation of sensor layers (Lobnik, Turel, & Urek, 2012).

Polymers can be classified in four categories.

**a) Hydrophobic polymers:** Such kind of polymers is not soluble in water. While poly (vinyl chloride) is soluble in tetrahydrofuran and cyclopentanone, polymers such as poly (methyl methacrylate), polystyrene and poly (vinyl acetate) are also soluble in ethyl acetate, ethylmethylketone, or dichloromethane (See Table 1.6). It is possible to use the plasticizers in such hydrophobic polymers. By the addition of the

different plasticizers, polarity, lipophilicity, selectivity and sensitivity of the polymer can be tuned. Immobilization of the neutral indicator dye usually is performed by encapsulation (Mohr, 2002).

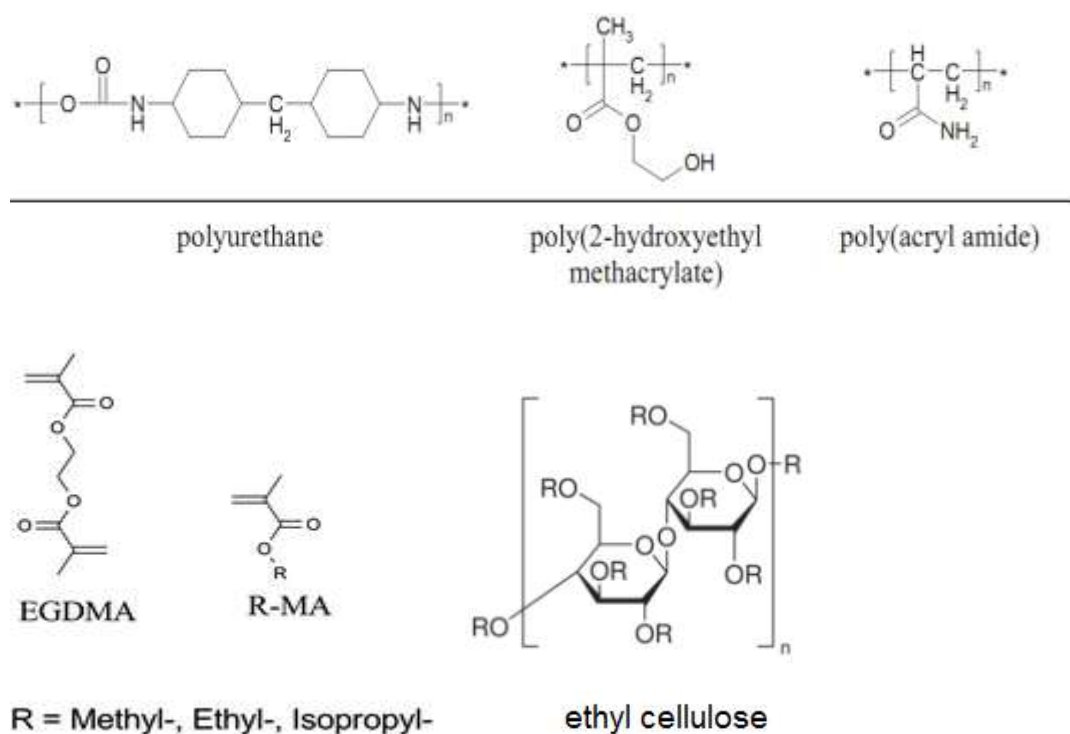
Table 1.6 Hydrophobic polymers (Personal.uni-jena, 2012).

			
poly(vinyl chloride) (Tg ~90 °C)	poly(methyl methacrylate) (Tg ~100 °C)	polystyrene- derivatives (Tg 100-140 °C)	poly(vinyl acetate) (Tg ~30 °C)

**b) Hydrophilic polymers:** Hydrophilic polymers (See Table 1.7) provide a matrix, which is compatible with aqueous environments. Ion diffusion is quite good but possible water uptake extending from 10 to 1000% is an important disadvantage of this kind of polymers and can cause significant swelling. Swelling is an undesired property of the matrix and affects the optical properties of the sensors. Immobilization of the indicator dye can be performed by electrostatic interactions and/or covalent bonding to the polymer (Mohr, 2002).

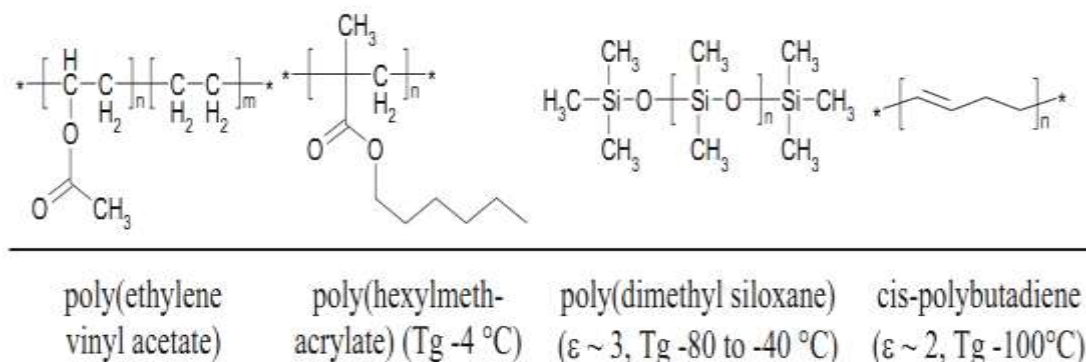
Functional groups (hydrogen-bonding structures) such as hydroxyl, amino, or carboxamide characterize the hydrophilic polymers. Typical examples can be listed as the polysaccharides (cellulose), polyacrylates, polyacrylamides, polyimines, polyglycols, and variety of so-called hydro gels (Lobnik, Turel, & Urek, 2012).

Table 1.7 Hydrophilic polymers (Personal.uni-jena, 2012).



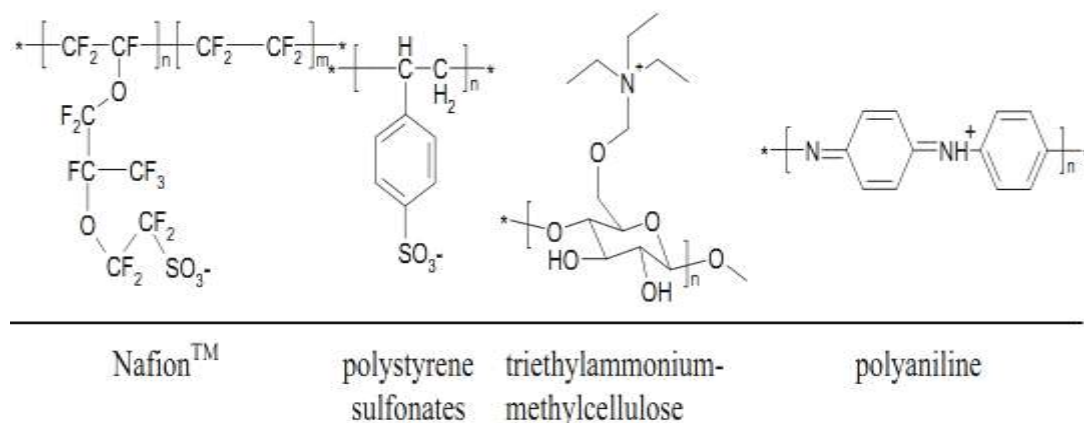
**c) Unpolar/soft polymers:** Polymers with low glass transition do not require plasticizers. They are appropriate matrix materials for molecules without electrical dipole. These compounds are often non-polar (See Table 1.8) and, consequently, they are not appropriate solvents for polar species, ionophores, cation or anion forms of the dyes and the analytes (Mohr, 2002).

Table 1.8 Unpolar polymers (Personal.uni-jena, 2012).



**d) Ionic Polymers (Polyelectrolytes):** Ionic polymers are positively or negatively charged structures. They are good candidates for the immobilization of the cationic or anionic dyes. Polyelectrolytes (See Table 1.9) exhibit a large amount of dissociable groups. In sensor design, they can be used to exchange their counter ions with indicator ions (Mohr, 2002).

Table 1.9 Ionic polymers (Personal.uni-jena, 2012).



### 1.9.3 Immobilization of Indicator Chemistry in Polymers

Method chosen for immobilization of indicator into a polymer matrix also has an important effect on the sensing characteristics. Encapsulation, impregnation, covalent bonding and doping are usually applied. Doping is one of the most effectively used immobilization technique as it is not restricted with certain indicators a/or polymers. When the doping is applied, the sensor stability is better compared to the other techniques (Lobnik, Turel, & Urek, 2012).

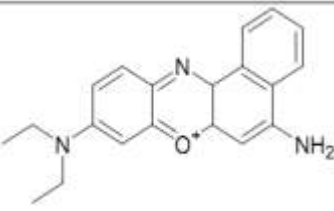
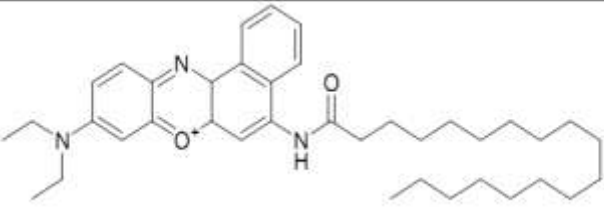
Recently, the immobilization of indicators in tiny beads rather than the polymer layers has also been applied. Nano-particles that can be placed into the cell, allowed the measurement of analytes within the living cells.



### 1.9.3.1 Hydrophobic Interactions

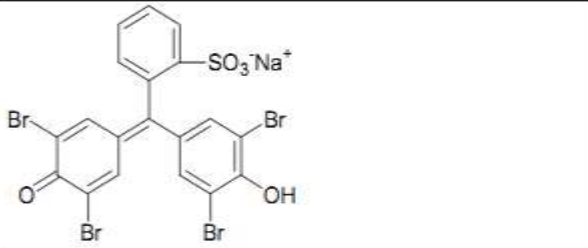
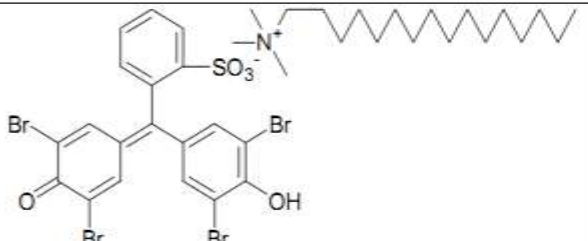
Today, the indicator chemistry is mainly valid for aqueous solutions. Therefore, the molecules are water-soluble and are not proper indicators to dissolve in lipophilic polymers. In order to make dyes, ionophores and ligands soluble in polymers and to avoid leaching of the components, they have to be made lipophilic by appropriate synthetic approaches (Mohr, 2002) (See Table 1.10).

Table 1.10 Hydrophobic molecules (Personal.uni-jena, 2012).

	<b>Nile Blue</b>  pH indicator (red to blue upon protonation, pK ~11.6)  water-soluble
	<b>Octadecyl Nile Blue</b>  pH indicator  polymer/plasticizer-soluble

Lipophilic molecules can be prepared by integrating long alkyl chains to the molecule. Another possibility is to prepare the lipophilic compounds by ion-pairing approach by simple synthetic treatment. The ion pair formation between bromophenolblue and hexadecyltrimethylammonium is shown below (Mohr, 2002) (See Table 1.11).

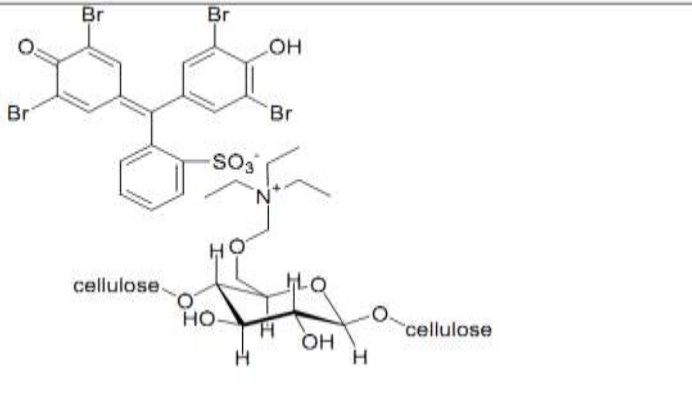
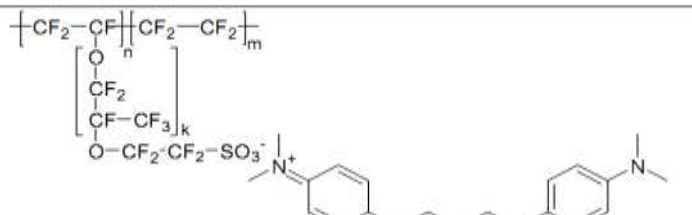
Table 1.11 Lipophilic molecules (Personal.uni-jena, 2012).

	<p><b>Bromophenol Blue</b></p> <p>pH indicator (yellow to blue upon deprotonation, pK ~3.8)</p> <p>water soluble</p>
	<p><b>Hexadecyltrimethylammonium Bromophenol Blue Ion Pair</b></p> <p>pH indicator</p> <p>lipophilic and polymer/plasticizer-soluble</p>

### 1.9.3.2 Exploiting Attraction of Opposite Charges

Positively or negatively charged indicator dyes can also be directly immobilized on the polymers bearing opposite charges. This kind of immobilization is not tedious. Solutions or suspensions of the polymers are usually mixed with aqueous or alcoholic solutions of the dyes (Mohr, 2002) (See Table 1.12).

Table 1.12 Ion-exchange molecules (Personal.uni-jena, 2012).

	<p><b>Bromophenol Blue</b></p> <p>immobilized on triethylammonium methylcellulose</p>
	<p><b>[1,5-Bis(<i>p</i>-dimethylamino-phenyl)-2,4-pentadienyl]-carbenium ion</b></p> <p>immobilised on Nafion™</p>

### *1.9.3.3 Covalent Immobilization*

Covalent immobilization of the indicator to the polymer matrix is probably one of the strongest of all immobilization methods. In covalent immobilization, the operational stability and shelf life is superior with respect to other immobilization techniques. However, to design the indicator chemistry and polymers with functional groups requires significant synthetic effort (Mohr, 2002).

Chemical modifications on ionophores may affect their sensing abilities. There may be two different approaches in immobilization: to bind the functional dye to an appropriate polymer matrix or to polymerize a reactive dye with conventional monomers to give a copolymer. Some molecules with reactive groups (such as isothiocyanate, sulfonyl, vinylsulfonyl, chloride, or succinimidyl) can be covalently attached to polymers bearing special groups like amino, aminoethylcellulose, etc. (Personal.uni-jena, 2012).

## **1.10 Ionic Liquids**

Recent years, ionic liquids appeared as new matrix materials for sensor design. Unlike conventional solvents, ionic liquids consist of ions. Their unique properties such as non-volatility, non-flammability and excellent chemical and thermal stability has become an attractive alternative to the environment compared to their conventional organic solvents (Yang, & Pan, 2005).

Ionic liquids typically comprise an organic, primarily nitrogen-containing but alternatively phosphorus-containing, mainly heterocyclic cation and an inorganic anion. The structural and task-specific tenability of both the cations and anions suggest great flexibility in the potential applications of ionic liquids. The nature of anion is very critical because it largely controls the physical and chemical properties, miscibility with water and other solvents or matrix materials, viscosity, as well as thermal and photo stability. The most common cations employed in ionic liquids are N-alkylpyridinium N,N'-dialkylimidazolium and tetraalkylphosphonium. The large

phosphonium cations can combine with relatively large anions to make viscous but flowing liquids (Del Sesto, Corley, Robertson, & Wilkes, 2005).

Due to the strong Coulomb attractions between the ions of these liquids they exhibit no measurable vapor pressure up to their thermal decomposition point;  $>300\text{ }^{\circ}\text{C}$ . This lack of vapor pressure make these materials highly attractive for gas processing and they may be considered as “liquid solids” incorporating some of the most useful physical properties of both phases. Although there have been numerous details concerning their properties, probably the most important one is that room-temperature ionic liquids have been utilized as “clean solvents” and “catalysts” for green chemistry. Additionally, their gas sorption–desorption dynamic is very fast and desorption by vacuuming is completely reversible. These characteristics make the RTILs exceptionally promising (Fuller, Carlin, Delong, & Haworth, 1994; Bonhote, Dias, Armand, Papageorgiou, & Gratzel, 1996; Welton, 1998; Holbrey, & Seddon, 1999; Lau, Van Rantwijk, Seddon, & Sheldon, 2000; Sweeny, & Peters, 2001; Cadena, Anthony, Shah, Morrow, Brennecke, & Maginn, 2004; Blanchard, Gu, & Brennecke, 2001; Anthony, Maginn, & Brennecke, 2002; Bates, Mayton, Ntai, & Davis, 2002; Kamps, Tuma, Xia, & Maurer, 2003; Camper, Scovazzo, Koval, & Noble, 2004).

As mentioned earlier, understanding of spectral behaviors of RTILs and preliminary experimental results regarding their employment in absorption and molecular fluorescence spectrometry is important. In order to understand the feasibility of design of a RTIL employing optical chemical sensor, the computability of this group of chemicals with water, other conventional solvents and even with polymers should be well understood.

Therefore, results of the absorption and emission based spectral studies exploiting chromophores or fluorophores performed in ionic liquids or ionic liquid-solvent mixtures are expected to be enlightening for optical sensor designers. In this work, we have aimed to incorporate most of the advantages of RTILs with sensor applications.

## **CHAPTER TWO**

### **ELECTROSPINNING AND NANOFIBER**

#### **2.1 Nanotechnology and Nanomaterials**

Nanomaterials and nanotechnology are extremely new fields of science and technology. According to Korotcenkov, nanotechnology can be defined as manipulating and making materials at the atomic and molecular levels. It has been found that with reduction in size, novel electrical, mechanical, chemical, catalytic, and optical properties can be introduced (Korotcenkov, 2010).

Nanotechnology has been found wide applications in fields of information, materials science, advanced materials technology, biology, medicine, engineering, electronics, physics, fiber-optic communication networks, chemistry, computer simulations, aerospace technology, and chemical engineering (Korotcenkov, 2010).

According to the International Union of Pure and Applied Chemistry (IUPAC), nano-materials are defined as materials having sizes smaller than 100 nanometers ( $1 \text{ nm} = 10^{-9} \text{ m}$ ) along at least one dimension (length, width, or height) (Wikipedia, 2012).

Two main reasons enforce the materials exhibit different properties at the nanoscale. First, nanomaterials have a relatively larger surface area when compared to the same mass of material produced in an ordinary form. This can make materials more chemically reactive (in some cases materials that are inert in their larger form are reactive when produced in their nanoscale form), and affect their strength or electrical properties. Second, quantum effects can begin to dominate the behavior of matter at the nanoscale affecting the optical, electrical and magnetic behavior of materials (Royalsociety, 2012)

Nanomaterial is a term used to explain an “intentionally made nanomaterial”. A nanomaterial is an object that has at least one dimension in the nanometer scale. Nanomaterials are categorized according to their dimensions (Barry, n.d.). According to this classification;

- 0-D nanomaterials
- 1-D nanomaterials
- 2-D nanomaterials

For example, a nanomaterial with three dimensions and less than 100 nm are nanoparticles, quantum dots etc. nanomaterials with two dimensions and less than 100 nm, are nanotubes, fibers, and nanowires. Nanomaterials with one dimension and less than 100 nm are thin fibers, layers and surface coatings (Barry, n.d.).

As a result, it has been concluded that one-dimensional structures will be of benefit for developing new generation chemical sensors that can achieve high performance. Therefore, in the last decade, the study of 1-D materials has become a primary focus in the field of chemical sensor design. Synthesis of new nano-objects and exploitation of their extraordinary properties is the goal and dream of many researchers engaged in the field of sensor design. In addition, it has also been established that 1-D structures may be ideal systems in which to study the nature of chemical sensing effects (Korotcenkov, 2010).

In this work, we fabricated nanomaterials in form of nanofibers exploiting electrospinning technique for sensor preparation purposes. In the following chapter, preparation of the polymeric nanofibers by this technique is explained into detail

## 2.2 Electrospinning of Polymeric Nanofibers

There are various technologies for fabrication of nanofibers. Each of these methods results with fiber formation with different physical properties. They can be listed as drawing technology for producing micro or nanofibers by using a micropipette; synthesis of carbon nanotubes, nanofibre arrays and electronically conductive polymeric nanostructures and thermal phase separation method for producing nanoporous nanofibres. Electrospinning is probably most convenient way to produce nanomaterials (Haghi, & Zaikov, 2011; He, Liu, Mo, Wan, & Xu, 2008).

This technique allows the fabrication of polymeric fibers with diameters ranging from 3 nm to 5  $\mu\text{m}$ . Potential applications of electrospinning technique can be listed as production of filtration membranes, catalytic nanofibers, sensors, and in scaffold design for tissue engineering. Experimental setup of the electrospinning system is simple and inexpensive. A typical electrospinning setup consists of a programmable syringe pump, a high voltage source, and a collecting substrate (See Figure 2.1). During the electrospinning process, a polymer solution is field in the syringe, which acts as a reservoir and holds at needle tip by surface tension (Pham, Sharma, & Mikos, 2006).

The system uses a high static voltage to draw the fiber from the liquid polymer. As a jet of charged fluid polymer sprays out the bottom of the needle, an electric field forces the stream to spin, stretching the fiber lengthwise so its diameter becomes as little as nanometer scale. After a while, the collected fibers form a thin membrane as it hits the electrically conductive substrate. These electrospun membranes have a unique combination of stretchiness and strength, and are easy to handle, making them suitable for a wide variety of applications. Electrospun nano-fibrous membranes can have approximately 1 to 2 orders of magnitude more surface area than that found in continuous thin films (Reneker, & Chun, 1996; Gibon, Schreuder-Gibson, & Rivin, 2001).

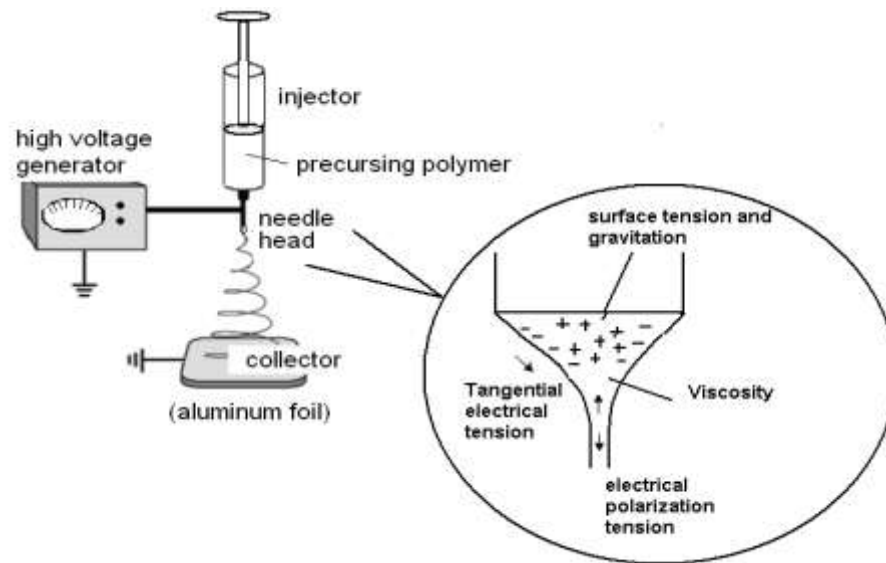


Figure 2.1 The most frequently used electrospinning set-up.

### 2.3 Theory of Electrospinning

Electrospinning is a technique used to prepare functional nanostructured surfaces exploiting electrostatic forces. The basic principle of electrospinning is the usage of a high voltage power supply (in the range of kV) which is able to charge the polymer drop pending at the tip of the syringe, and upon exposure the high voltage, to overcome the surface tension. When the high voltage applied between the needle of the syringe (filled with the polymer) and the grounded substrate, the drop of the polymers becomes charged, reoriented depending on the electric field, formed a Taylor cone, and then eventually suddenly ejected. In order to provide a charged jet the polymeric solution should have an electrical conductivity. Electric forces then accelerate and stretch the fiber lengthwise causing the diameter to decrease. Additionally, volatile solvents may begin a rapid evaporation, causing a decrease in jet diameter and velocity. During spinning process, as the fiber formed, it becomes deposited continuously and randomly on the grounded collector. As the process occurs, new fibers are accumulated and nonwoven nanofibrous membranes (NFM) are formed (Scampicchio, Bulbarello, Arecchi, Cosio, Benedetti, & Mannino, 2012).



### ***2.3.1 Parameters of Electrospinning Process***

The electrospinning process can be manipulated changing a number of variables. Doshi and Reneker classified these parameters as solution properties, controlled variables, and ambient parameters. Solution dependent properties can be listed as the viscosity, conductivity, surface tension, molecular weight of the polymer, dipole moment, and dielectric constant. Controlled variables include the flow rate, strength of the electric field, distance between the tip and the collector, design of the needle tip, and geometry and material of the collector. Ambient parameters are temperature, humidity, and velocity of the accumulating air (Pham, Sharma, & Mikos, 2006).

### **2.4 Electrospun Nanofibrous Membranes for Sensors Design**

In recent years, the importance of the electrospinning techniques for sensor design has been well understood. In some of these works, the nanofibers produced through the electrospinning process. Because of the higher surface area electrospun, nano materials have found applications as sensors and catalysts.

It is expected that this large amount of functional surface area has the potential to provide enhanced sensitivity, selectivity, good response time, stability, durability, reproducibility, and reversibility. So far, a few examples of electrospun polymer nanofibers have been reported as gas sensors (Ding, Wang, Yu, & Sun, 2009), chemical sensors, optical sensors (Wang, Drew, Lee, Senecal, Kumar, & Samuelson, 2002) and biosensors (Scampicchio, Bulbarello, Arecchi, Cosio, Benedetti, & Mannino, 2012; Manesh, Santhosh, Gopalan, & Lee, 2008). The principle of nanofiber sensors is to utilize the chemical or physical interaction between the analyte and the sensing material. Due to the promising properties, the electrospun nanofibers may find large application in sensor design.

## CHAPTER THREE

### EXPERIMENTAL METHOD AND INSTRUMENTATION

#### 3.1 Reagents

In this thesis, the polymers ethyl cellulose (EC) and poly (methyl methacrylate) (PMMA) were used as support materials and were purchased from Across and Aldrich, respectively. The plasticizer, dioctyl phthalate (DOP) and lipophilic ionic additive; potassium tetrakis-(chlorophenyl) borate (PTCPB) were supplied from Aldrich. Room temperature ionic liquid (RTIL), 1-ethyl-3-methylimidazolium tetrafluoroborate (EMIMBF<sub>4</sub>) was provided from Fluka. Absolute ethanol (EtOH), tetrahydrofuran (THF), dichloromethane (DCM), dimethylformamide (DMF) and chloroform (CH<sub>3</sub>Cl) were of analytical grade and purchased from Merck, Fluka, and Riedel. Solvents for the spectroscopic studies were used without further purification.

Buffer components; acetic acid/acetate, phosphate and metal salts were of reagent grade (Merck and Fluka). Aqueous solutions were prepared with freshly deionized ultra pure water (specific resistance >18.2 MΩcm, pH 5.5) from a Millipore reagent grade water system.

The calibration and metal sensing studies were performed by using atomic absorption spectroscopy (AAS) certified reference standard solutions of Ag<sup>+</sup>, Al<sup>3+</sup>, Ba<sup>2+</sup>, Ca<sup>2+</sup>, Co<sup>2+</sup>, Cr<sup>3+</sup>, Cu<sup>2+</sup>, Fe<sup>3+</sup>, Fe<sup>2+</sup>, Hg<sub>2</sub><sup>2+</sup>, Hg<sup>2+</sup>, Li<sup>+</sup>, K<sup>+</sup>, Mn<sup>2+</sup>, Mg<sup>2+</sup>, Na<sup>+</sup>, NH<sub>4</sub><sup>+</sup>, Ni<sup>2+</sup>, Pb<sup>2+</sup>, Sn<sup>2+</sup> and Zn<sup>2+</sup>.

All standards were diluted with 0.01 M acetic acid/acetate buffer of pH 5.0 and were prepared in polyethylene measuring flask to avoid adsorption of metal ions. All of the experiments were carried out at room temperature; 25 ± 1 °C.

The pH of the solutions were monitored by use of a digital pH-meter (ORION) calibrated with standard buffers of pH 12.00, 7.00 and 4.00 at  $25 \pm 1$  °C. All of the experiments were carried out at room temperature; 25 °C.

### **3.2 Preparation of the Buffer Solutions**

Deionized water, generated by a Milli-Q deionized water unit, which had a resistance better than 18.2 MΩcm, was used for the preparation of all of the watery solutions.

#### ***3.2.1 Preparation of 0.005 M $H_3PO_4$ Buffer***

0.285 mL ( $d=1.71$  and 14.83 Molar) of phosphoric acid were dissolved in 950 mL ultra pure water. The solution was titrated to pH 2.0 at the lab temperature of 20°C either with 0.1 M  $HNO_3$  or 0.1 M NaOH as needed. The resulting solution was completed to 1000 mL with ultra pure water in a volumetric flask. The buffer solutions in the range of pH 2.0-3.0, were prepared by the same way by adjusting to the desired pH.

#### ***3.2.2 Preparation of 0.01 M Acetic Acid / Acetate Buffer***

0.572 mL of acetic acid ( $d=1.05$  and 17.48 Molar) were dissolved in 950 mL ultra pure water. The solution was titrated to pH 5.0 at the lab temperature of 20 °C either with 0.1 M  $HNO_3$  or 0.1 M NaOH as needed. The resulting solution was made up to 1000 mL with ultra pure water in a volumetric flask. The buffer solutions in the range of pH 4.0-7.0 were prepared by the same way by adjusting to the desired pH.

#### ***3.2.3 Preparation of 0.005 M Acetic Acid / Acetate Buffer***

0.286 mL of acetic acid ( $d=1.05$  and 17.48 Molar) were dissolved in 950 mL ultra pure water. The solution was titrated to pH 5.0 at the lab temperature of 20°C either with 0.1 M  $HNO_3$  or 0.1 M NaOH as needed. The resulting solution was made up to 1000 mL with ultra pure water in a volumetric flask. The buffer solutions in the range of pH 4.0-7.0 were prepared by the same way by adjusting to the desired pH.

### 3.2.4 Preparation of 0.005 M NaH<sub>2</sub>PO<sub>4</sub>/ Na<sub>2</sub>HPO<sub>4</sub> Buffer

0.78 g of NaH<sub>2</sub>PO<sub>4</sub>·2H<sub>2</sub>O (MA=156.01) and 1.79 g of Na<sub>2</sub>HPO<sub>4</sub>·12H<sub>2</sub>O (MA=358.14) were dissolved in 950 mL ultra pure water. The solution was titrated to pH 7.0 at the lab temperature of 20 °C either with 0.1 M HNO<sub>3</sub> or 0.1 M NaOH as needed. The resulting solution was made up to 1000 ml with ultra pure water in a volumetric flask. The buffer solutions in the range of pH 7.0-9.0 and 10-12 were prepared by the same way by adjusting to the desired pH.

### 3.3 Structural Specification of the Exploited Ionophores

The copper sensitive fluorescent ionophore (explained into detail in chapter 4), N<sup>3</sup>-3-(4-(dimethylamino) phenyl) allylidene) isonicotinohydrazide (DPAINH) (See Figure 3.1) was synthesized in our laboratories by Professor Y. ERGUN according to the literature method and characterized with <sup>1</sup>H NMR and IR based data (Sinha, Jain, Tilekar, Upadhyaya, Kishore, Jana, & Arora, 2005).

m.p.: 252°C IR(KBr): 3302 (NH), 1664 (C=O), 1595 (C=N)

<sup>1</sup>H-NMR (400 MHz, CDCl<sub>3</sub>): δ 3.01 (s, 6H, N(CH<sub>3</sub>)<sub>2</sub>), 6.67 (d, 2H, J=7.2 Hz, ArH), 6.81-6.91 (m, 1H, =CH), 7.36 (d, 2H, J=7.4 Hz, ArH), 7.67 (d, 2H, J= 7.8 Hz, ArH), 7.75-7.82 (m, 1H, =CH), 7.97-8.01 (m, 1H, N=CH), 8.74 (d, 2H, J= 7.6 Hz, ArH), 8.92 (bs, 1H, NH).

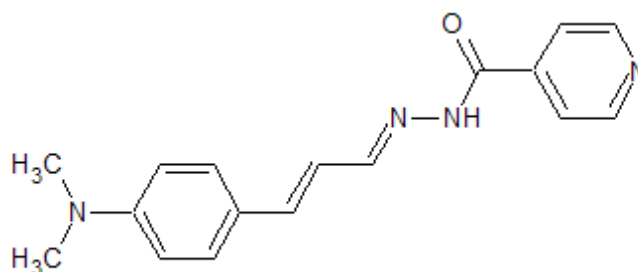


Figure 3.1 Structure of the copper sensitive fluoroionophore, N<sup>3</sup>-3-(4(dimethylamino) phenyl)allylidene)isonicotinohydrazide (DPAINH).

The mercury and iron sensitive fluorescent ionophore (explained into detail in chapter 5 and 6), 2-(9-methyl-9H-carbazol-3-yl)-5-(pyridin-4-yl)-1,3,4-oxadiazole dye (ODC-3) (See Figure 3.2) has been synthesized in our laboratories by Professor Y. ERGUN according to the literature information and characterized with  $^1\text{H}$  NMR and IR based data (Shin, Wong, Lin, Chen, & Yeh, 2006). The  $^1\text{H}$  NMR and IR based measurements were performed by Professor Y. ERGUN.

m.p.: 277°C; Yield: 86%.IR (KBr):  $\nu$  3182 (NH), 3003 (CH), 2850 (CH), 1645 (C=O)  $\text{cm}^{-1}$ .

$^1\text{H}$ -NMR (DMSO- $d_6$ , 400 MHz):  $\delta$  3.85 (s, 3H,  $\text{CH}_3$ ), 7.22 (t, 1H,  $J=6.8$  Hz, ArH), 7.41 (t, 1H,  $J=7.6$  Hz, ArH), 7.56 (d, 1H,  $J=7.6$  Hz, Ar-H), 7.64 (d, 1H,  $J=8.4$  Hz, ArH), 7.83 (d, 2H,  $J=4.4$  Hz, Pyridine-H), 7.92 (d, 1H,  $J=8.4$  Hz, ArH), 8.21 (d, 1H,  $J=7.6$  Hz, ArH), 8.49 (s, 1H, ArH), 8.65 (s, 1H, N=CH), 8.79 (d, 2H,  $J=4.2$  Hz, Pyridine-H), 11.98 (s, 1H, NH).

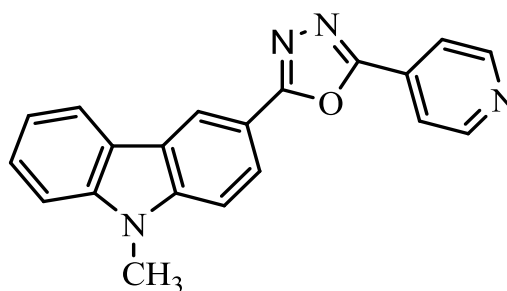


Figure 3.2 Schematic structures of the mercury, iron and silver sensitive fluoroionophore;2-(9-methyl-9H-carbazol-3-yl)-5-(pyridin-4-yl)-1,3,4oxadiazole dye (ODC-3).

The other mercury and iron sensitive fluorescent ionophore was also obtained from Professor Y. ERGUN (Explained into detail in Chapter 5 and 6). The 2-(9-hexyl-9H-carbazol-3-yl)-5-(pyridin-4-yl)-1,3,4-oxadiazole (ODC-5) (See Figure 3.3) dye was synthesized in our laboratories according to the literature method and characterized with  $^1\text{H}$  NMR and IR based data (Shin, et al. 2006).

The  $^1\text{H}$  NMR and IR based measurements were performed by Professor Y. ERGUN. IR (KBr): 2909 (C-H), 1598 (C=N)  $\text{cm}^{-1}$ .  $^1\text{H}$ -NMR (400 MHz,  $\text{d}_6$ -DMSO):  $\delta$  2.97 (s, 12H, 4xCH<sub>3</sub>), 6.66 (d, 4H,  $J=8.4$  Hz, 4x ArH), 7.57 (d, 4H,  $J=8.8$  Hz, 4x ArH), 8.41 (s, 2H, -N=CH), GC-MS [M]<sup>+</sup>= 294.3, mp=265.2  $^\circ\text{C}$ .

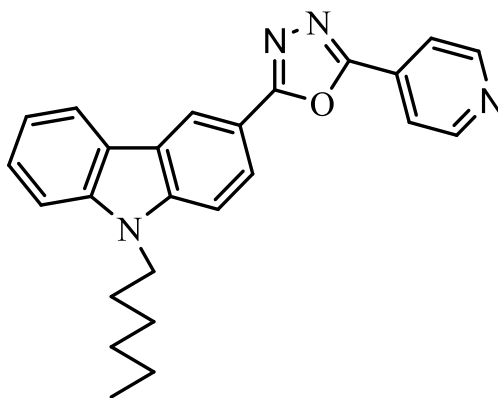


Figure 3.3 Structure of the mercury and iron sensitive fluoroionophore; 2-(9-hexyl-9H-carbazol-3-yl)-5-(pyridin-4-yl)-1,3,4-oxadiazole (ODC-5).

The other mercury sensitive fluorescent ionophore (explained in chapter 5), 2-*{(E)-[(4-chlorophenyl)imino]methyl}phenol* (DMK-1A); (See Figure 3.4) was provided by Prof. Dr. Engin ÇETİNKAYA, University of Ege, department of chemistry. DMK-1A was synthesized by following literature information (Usharani, Akila, & Rajavel, 2012).

mp: 104-108  $^\circ\text{C}$ . Yield: 70 %  $\nu(\text{C}=\text{N})$ : 1642  $\text{cm}^{-1}$ .  $^1\text{H}$  NMR of DMK-1A ( $\text{CDCl}_3$ , 400 MHz,  $\delta$ ), 12.85 (s, 1H, OH); 8.57 (s, 1H, CH=N); Aromatic CH: 7.36 (t,  $J$  8 Hz, 4H); 7.20 (d,  $J$  8 Hz, 2H); 7.00 (d,  $J$  8 Hz, 1H); 6.92 (t,  $J$  8 Hz, 1H);  $^{13}\text{C}$  NMR of DMK-1A ( $\text{CDCl}_3$ , 100 MHz,  $\delta$ ), 163.2 (C=N); 161.3; 147.3; 133.6; 132.7; 132.6; 129.7; 122.7; 119.4; 119.3; 117.5 ( $\text{C}_{\text{aromatics}}$ ).

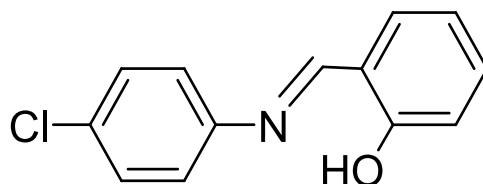


Figure 3.4 Structure of mercury sensitive molecule, 2-*{(E)-[(4-chlorophenyl)imino] methyl} phenol* (DMK-1A).

The iron sensitive fluorescent ionophore (explained into detail in chapter 6), 9-hexyl-9H-carbazole-3-carbonitrile (ODC 1) (See Figure 3.5) was synthesized in our laboratories by Professor Y. ERGUN in a similar way to the literature (Bottari, Maccari, Monferto, Ottana, Rotondo, & Vigorita, 2000), and characterized with  $^1\text{H}$  NMR and IR based data.

mp: 253°C, IR(KBr): 3479 (NH), 2222 (CN), 1663 (C=O), 1607 (C=N)  $\text{cm}^{-1}$

$^1\text{H}$ -NMR (400 MHz,  $d_6$ -DMSO):  $\delta$  7.74 (d, 2H,  $J=8.0$  Hz, ArH), 7.84 (d, 2H,  $J=7.4$  Hz, ArH), 8.03 (d, 2H,  $J=8.0$  Hz, ArH), 8.1 (bs, 1H, NH), 8.57 (s, 1H, N=CH), 8.92 (d, 2H,  $J=7.6$  Hz, ArH).

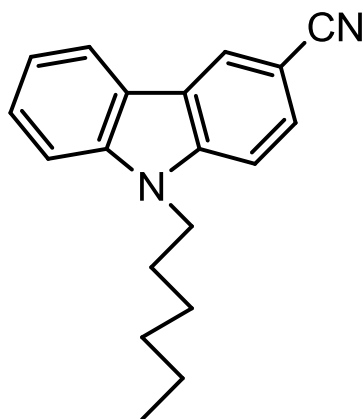


Figure 3.5 Structure of the iron sensitive fluoroionophore 9-hexyl-9H-carbazole-3-carbonitrile (ODC 1).

The other iron sensitive fluorescent ionophore (explained into detail in chapter 6), 2-{[(4-bromo-2,6-dimethylphenyl)imino]methyl}phenol (MS-4) (See Figure 3.6) was synthesized by Prof. Dr. Engin ÇETİNKAYA, in the University of Ege, department of chemistry by following literature (De Clercq, & Ugent, 2002)

mp: 107-109°C Yield:86%  $\nu(\text{C}=\text{N})$ : 1623  $\text{cm}^{-1}$

$^1\text{H}$ NMR of DMA-2 ( $\text{CDCl}_3$ , 400 MHz,  $\delta$ ), 12.68 (s, 1H, OH); 8.28 (s, 1H, CH=N); Aromatic CH: 7.39 (t,  $J$  8.8 Hz, 1H); 7.32 (d,  $J$  7.2 Hz, 1H); 7.22 (s, 2H); 7.04 (d,  $J$  8.4 Hz, 1H); 6.94 (t,  $J$  8.8 Hz, 1H); 2.15 (s, 6H,  $\text{CH}_3$ ).  $^{13}\text{C}$  NMR of DMA-2 ( $\text{CDCl}_3$ , 100 MHz,  $\delta$ ), 167.4 (C=N), 161.5; 147.6; 133.7; 132.6; 131.2; 130.7; 119.4; 118.9; 117.9; 117.6 ( $\text{C}_{\text{aromatics}}$ ).

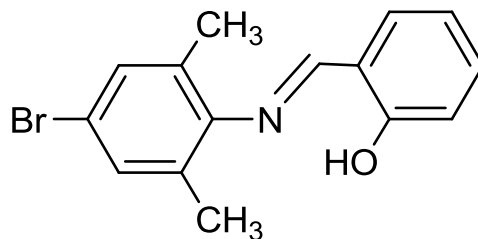


Figure 3.6 Structure of iron sensitive molecule, 2-([(4-bromo-2,6-dimethylphenyl) imino] methyl) phenol (MS-4).

The Sn (II) sensitive fluorescent ionophore (explained into detail in chapter 7), 3-(2,4,6-trimethoxybenzyl)-3,4-dihydroquinazoline (MS-3) (See Figure 3.7) was synthesized by Prof. Dr. Engin ÇETİNKAYA, in the University of Ege, department of chemistry by following literature (Mercan, Çetinkaya, & Sahin, 2013).

mp: 148-150°C Yield: 96%  $\nu(\text{C}=\text{N})$ : 1612  $\text{cm}^{-1}$

$^1\text{H}$  NMR of MS-3 ( $\text{CDCl}_3$ , 400 MHz,  $\delta$ ) 7.18 (s, 1H, NCHN), [7.05 (t,  $J$  8.8 Hz, 1H), 6.94 (d,  $J$  8 Hz, 1H), 6.86 (t,  $J$  7.2 Hz, 1H), 6.73 (d,  $J$  7.2 Hz, 1H) ( $\text{NC}_6\text{H}_4\text{CH}_2\text{N}$ )], 6.09 (s, 2H,  $\text{C}_6\text{H}_2(\text{OCH}_3)_3$ -2,4,6), 4.38 (s, 2H,  $\text{NC}_6\text{H}_4\text{CH}_2\text{N}$ ), 4.25 (s, 2H,  $\text{CH}_2\text{C}_6\text{H}_2(\text{OCH}_3)_3$ -2,4,6), 3.82, 3.79 (s, 9H,  $\text{C}_6\text{H}_2(\text{OCH}_3)_3$ -2,4,6).  $^{13}\text{C}$  NMR of MS-3 ( $\text{CDCl}_3$ , 100 MHz,  $\delta$ ), 151.2 (NCHN), 142.3, 128.1, 125.7, 124.4, 124.1, 121.1 ( $\text{NC}_6\text{H}_4\text{CH}_2\text{N}$ ), 161.7, 160.1, 103.9, 90.6 ( $\text{C}_6\text{H}_2(\text{OCH}_3)_3$ -2,4,6), 55.8, 55.4 ( $\text{C}_6\text{H}_2(\text{OCH}_3)_3$ -2,4,6), 46.2 ( $\text{CH}_2\text{C}_6\text{H}_2(\text{OCH}_3)_3$ -2,4,6), 44.7 ( $\text{NC}_6\text{H}_4\text{CH}_2\text{N}$ ).

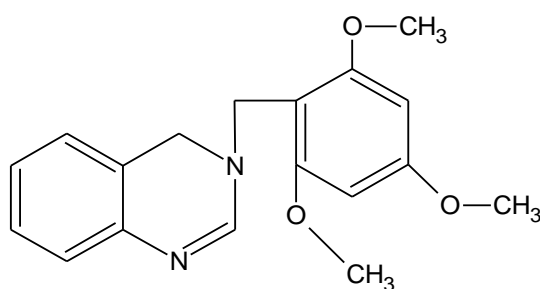


Figure 3.7 Structure of tin sensitive molecule, 3-(2,4,6-trimethoxybenzyl)-3,4-dihydroquinazoline (MS-3).



### **3.4 Preparation of Electrospun Nano-Fibers and Thin Films**

#### ***3.4.1 Fabrication of Electrospun Nanofibers***

Electrospinning was used to fabricate PMMA (Poly (methylmethacrylate) or EC (Ethyl cellulose) based continuous nanofibers. Experimental conditions were optimized to form bead-free nanofibers varying concentrations of plasticizer, PMMA and/or EC and RTIL (1-Ethyl-3-methylimidazolium tetrafluoroborate) in the precursor polymer solution. The concentration of RTIL was varied from 5% up to 50% (w/w) with respect to the PMMA or EC content. We find that the presence of the RTIL in the polymer solutions facilitates the production of bead-free nanofibers from the lower polymer concentrations. This result can be attributed to the ionic conductivity and proper viscosity of the RTIL doped precursor polymer solutions (Uyar, Balan, Toppare, & Besenbacher, 2009).

In most of the sensor composites, we preferred the optimum matrix composition, which contains 50% PMMA or EC, 40% plasticizer and 10% IL by weight. The resulting composites were prepared by mixing 240 mg of polymer (PMMA or EC), 192 mg of plasticizer (Dioctyl phthalate, DOP), 1 to 5 mg of ionophore, equivalent amount of potassium tetrakis (4-chlorophenyl) borate (PTCPB) in 2.0 mL of THF or DCM: EtOH (25:75) solvent systems, then, mixed properly under magnetic stirring. Chemical structures of the exploited polymers, plasticizers, lipophilic anionic additive, and RTIL were shown in Figure 3.8. (Ongun, Ertekin, Gocmenturk, Ergun, & Suslu, 2012).

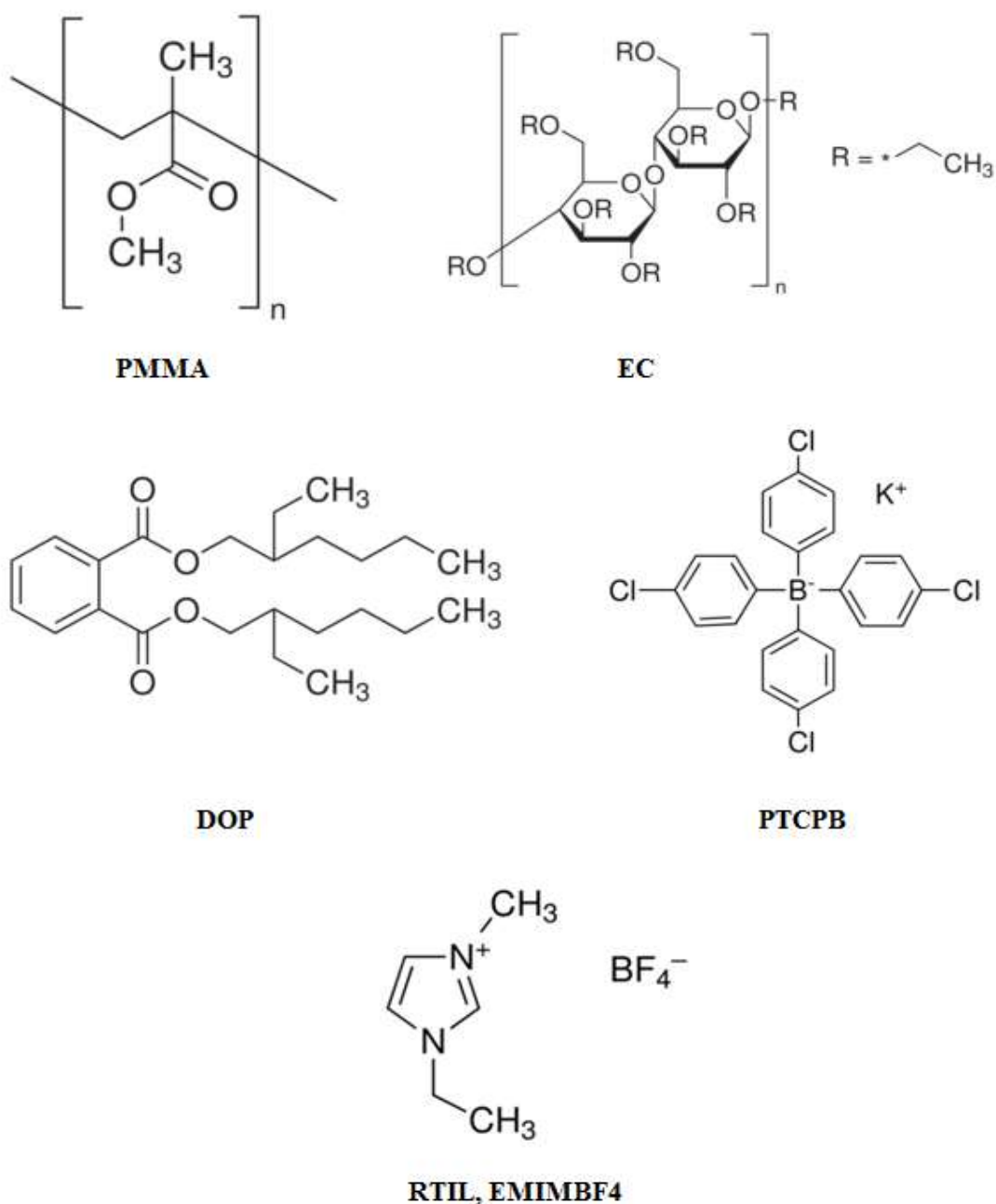


Figure 3.8 Structures of PMMA, EC, DOP, PTCPB and RTIL.

For the fabrication of nanofibers, the polymer solution was taken in a 10 mL hypodermic syringe and an electric potential of 25 kV was applied between the needle and the substrate in the form of an aluminum sheet. The distance between the needle and the electrode was 10 cm while the diameter of the needle was 0.40 mm. The solution flow rate was maintained at 1 mL/h. When high voltage is applied, the electrically charged polymeric solution produces a spray like stream. Meanwhile, the

solvent evaporates and nanoscale fibers were deposited on the aluminum sheet. The surface morphology of the fabricated nanofibers was studied using the scanning electron microscope (SEM) instrument (6060-JEOL JSM). The nanofibers deposited on aluminum substrate were cut into proper size, fixed in the cuvette or flow cell and the excitation or emission spectra were recorded (Wang, Drew, Lee, Senecal, Kumar, & Samuelson, 2002; Ongun, et al. 2012).

### ***3.4.2 Thin Film Fabrication***

The thin films were prepared using the same composites indicated for the electrospun nanofibres. The resulting mixtures were spread onto a 125  $\mu\text{m}$  polyester support (Mylar TM type) with a spreading device. Thickness of the films was measured using Tencor Alpha Step 500 Prophyloimeter and was found to be  $5.11 \pm 0.081 \mu\text{m}$  ( $n = 8$ ). Each sensing film was cut to 1.2 cm diameter, fixed in the cuvette or flow cell, and the excitation and/or emission spectra were recorded (Ongun, et al. 2012).

## **3.5 Apparatus and Experimental Setup**

### ***3.5.1 Spectrophotometer and Spectrofluorometer Apparatus***

The absorption spectra of the solutions and sensor films were recorded by using a Shimadzu 1801 UV-Visible (Japan) spectrophotometer. Steady state fluorescence emission and excitation spectra were measured using Varian Cary Eclipse Spectrofluorometer with a xenon flash lamp as the light source (Ongun, et al. 2012).

The data acquired with fiber optics were provided with the commercial accessories of Varian Cary Eclipse Spectrofluorometer: Eclipse Fibre optic coupler, Fluorescence remote read probe (2 metres), Probe tip for solid measurements and probe tips for liquid measurements (10 mm and 20 mm length tips). This method also allows the examination of samples remote from the instrument. The components and installation steps are; (Oter, 2007).

- **The fibre optic coupler** is an accessory that enables the use of a fiber optic probe with spectrofluorometer. After the removal of the conventional sample compartment of the spectrofluorometer, the fibre optic coupler was stabilized to the same position by the help of the screws.
- **The fiber optic probe** was connected to the coupler accessory by inserting the two connector ends into the two key holds.
- **The probe tips** were screwed onto the end of the probe. Depending on the phase of sample (solid or liquid), either a solid sample probe tip or a liquid sample probe tip were used (Oter, 2007).

To ensure that the fibre optic system operates at maximum performance, it is necessary to optimize the efficiency with which light passes through the coupling device before experiment begins. The alignment was done by using the software of the instrument (Oter, 2007).

Spectral measurements were carried out either in conventional cuvette of the fluorometer or with fiber optic probe (2m long). For instrumental control, data acquisition and processing, the software package of the spectrofluorometer was used. The tip of the bifurcated fiber optic probe was interfaced with the sensing thin films and/or nanofibers in a buffer containing homemade 300  $\mu\text{L}$  flow cell, which is made from polytetrafluoroethylene (PTFE) in the atelier of University of Ege. The flow cell was equipped with a four-channel Ismatec Reglo Analog peristaltic pump. Flow rate of the peristaltic pump was kept at 2.4  $\text{mL min}^{-1}$ . Analyte solutions or buffers were transported via tygon tubing of 2.06 mm i.d. Instrumental set-up used for dye-doped thin film and nanofiber measurements was shown in Figure 3.9 (Ongun, et al. 2012).

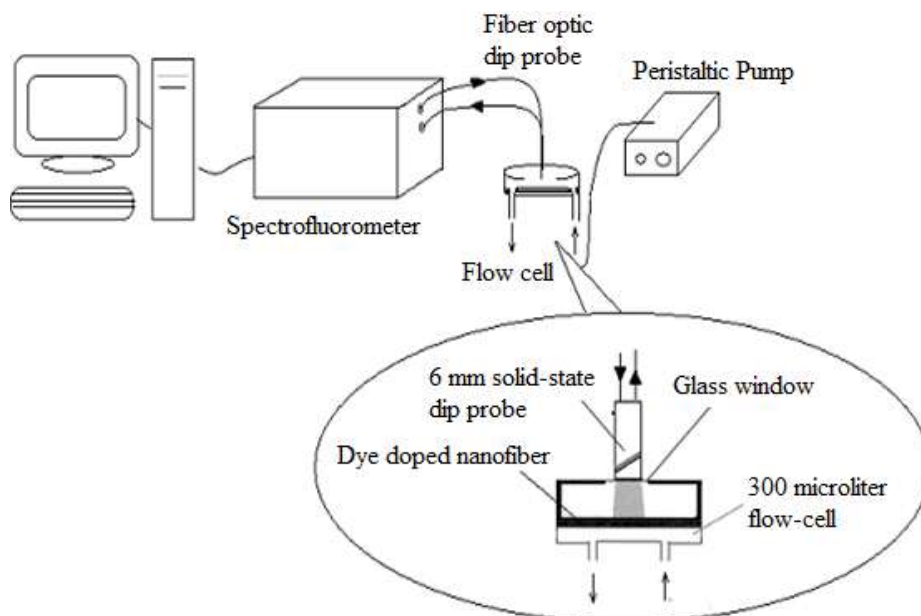


Figure 3.9 Instrumental set-up used for dye-doped nanofiber measurements.

### 3.5.2 *Electrospinning Apparatus*

The homogeneous PMMA or EC solutions were placed in a 10 mL plastic syringe fitted with a metallic needle of 0.4mm of inner diameter. The syringe is fixed vertically on the syringe pump (Top Syringe Pump Top-5300) and the electrode of the high voltage power supply (Gamma High Voltage ES30) was clamped to the metal needle tip. Schematic structure of the electrospinning apparatus is shown earlier in Figure 2.1.

### 3.5.3 *Time Correlated Single Photon Counting (TCSPC) Apparatus*

Fluorescence lifetimes were recorded using a Time Correlated Single Photon Counting (TCSPC) system that was from Edinburgh Instruments (UK). The instrument was equipped with a 367 nm pulsed laser (pulse width: 79 picoseconds) as the excitation source. During measurements, the Instrument Response Function (IRF) was obtained from a non-fluorescing suspension of a colloidal silica (LUDOX 30 %, Sigma Aldrich) in water, held in 10 mm path length quartz cell and was considered to be wavelength independent. All lifetimes were fit to a  $\chi^2$  value of less than 1.1 and with residuals trace symmetrically distributed around the zero axes (Ongun, Ertekin, Hizliates, Oter, Ergun, & Celik, 2013).

### ***3.5.4 Experimental Method and Instrumentation for Ion Chromatographic Studies***

An ion chromatography method for the simultaneous determination of common anions (fluoride, chloride, nitrite, bromide, nitrate, phosphate, and sulfate) and cations (lithium, sodium, ammonium, potassium, magnesium, and calcium) in the mineral water of Sarikiz has been employed using an anion-exchange column, a cation-exchange column and the suppressed conductivity detector.

Deionized water, generated by a Milli-Q deionized water unit that had a resistance better than 18.2 M $\Omega$ cm, was used for the preparation of all the solutions. Certified reference anion standard solution of Dionex (Fluoride 20 mg/L, Chloride 30 mg/L, Nitrite 100 mg/L, Bromide 100 mg/L, Nitrate 100 mg/L, Phosphate 150 mg/L, Sulfate 150 mg/L) and certified reference cations standard (CRS) solution of Dionex (Lithium 49.9 mg/L, Sodium 203 mg/L, Ammonium 251 mg/L, Potassium 506 mg/L, Magnesium 252 mg/L, Calcium 509 mg/L) were used throughout the study.

All systems and components for ionic analysis were from Dionex (Sunnyvale, CA, USA). The hardware used for these analyses consisted of an ICS-1000 ion chromatograph equipped with an isocratic pump, a conductivity detector, a self-regenerating suppressor (ASRS ultra II 4mm), an AS40 auto sampler and a column heater. Eluent flow rates were set at 1 mL/min with an injection volume of 25 $\mu$ L. An Ion Pac<sup>®</sup> AG9-HC (50mm $\times$ 4mm I.D.) guard column and an Ion Pac<sup>®</sup> AS9-HC Analytical (250mm $\times$ 4mm I.D) analytical column were used to separate the anions. The current of the suppressor was set at 45 mA to give a background conductivity of 25.5-26.5  $\mu$ s. A self-regenerating cation suppressor (CSRS ultra II 4mm), an Ion Pac<sup>®</sup> CG12A (50mm $\times$ 4mm I.D.) guard column and an Ion Pac<sup>®</sup> CS12A (250mm $\times$ 4mm I.D) analytical column were used to separate the cations. The current of the suppressor was set at 59 mA to give a background conductivity of 1.5-2  $\mu$ s. Other parameters were same as that of stated in the analysis of the anions. The complete operating conditions and the composition of the eluents used by the ion chromatographic system during the chromatographic runs were summarized in Table 3.1.

Table 3.1 Operating conditions

<b>IC Operating Conditions</b>		
	<b>Anion-exchange</b>	<b>Cation-exchange</b>
Ion-chromatographic unit	Dionex ICS-1000 IC	Dionex ICS-1000 IC
Pump	GP50 gradient pump	GP50 Gradient Pump
Guard column	IonPac® AG9-HC Guard, 50mm×4mm I.D	IonPac® CG12A Guard, 50mm×4mm I.D
Column	IonPac® AS9-HC Analytical, 250mm×4mm I.D	IonPac® CS12A Analytical, 250mm×4mm I.D
Column temperature	30 °C	30 °C
Suppressor	ASRS Ultra II 4mm	CSRS Ultra II 4mm
Suppressor current	45 mA	59 mA
Eluent	9mM Sodium Carbonat	20mM Methanesulfonic acid
Eluent source	Dionex EluGen® EGC-KOH cartridge	Dionex EluGen® EGC Cartridge
Flow-rate	1 mL/min	1 mL/min
Detector	Dionex CD20 conductance detector	Dionex DS6 Heated Conductivity Cell
Cell temperature	35 °C	35 °C
Injection volume	25µL	25µL
Run time	30 min	12.5 min
Background conductance	≈25.5-26.5mS	≈1.5-2 mS
Back pressure	≈2000 psi	≈1050 psi
Data management	Chromeleon® 6.5 chromatography workstation	Chromeleon® 6.5 Chromatography Workstation
Auto sampler	AS-40	AS-40

In this work, we studied simulated and real groundwater samples. The mineral water of Sarikiz (Sarikiz, Manisa; Turkey; Latitude: 38° 44' 83 N, Longitude: 28° 04' 84 E) has been used for tests throughout the thesis. The temperature of the water from well was remarkably constant and was 16.9 °C. The water samples were kept in polyethylene bottles at 4 °C or at room temperature. Then they were filtered with Pionex/Millipore/Sartorius through a filter with a pore diameter 0.45 µm to polyethylene bottles at 25 °C. The major cation and anion constituent of the samples were tested with ion chromatographic approach.

In this study, the 5-groundwater samples from Manisa/Sarikiz region were analyzed with ion chromatography instrument in terms of six major cations and seven anions before and after column treatment. The groundwater samples contain certain heavy metals (iron, copper, zinc, nickel, lead, cadmium, chromium, antimony, arsenic, silver, selenium etc.) as well as typical major groundwater cations (magnesium, calcium, potassium) and anions (chloride, sulphate, phosphate and bicarbonate) (See Table 3.2).

Table 3.2 The simultaneous determination of common anions and cations in the mineral water of Sarikiz using ion chromatography method

<b>Cations</b>	<b>Values (mg/L)</b>	<b>Anions</b>	<b>Values (mg/L)</b>
Lithium	0.20	Fluoride	0.20
Sodium	37.60	Chloride	15.08
Ammonium	<LOD	Nitrite	<LOD
Potassium	5.77	Bromide	<LOD
Magnesium	69.09	Nitrate	<LOD
Calcium	109.00	Phosphate	<LOD
		Sulfate	105.42



The result of the heavy metal analysis was taken from web site of Sarikiz (Sarikiz, 2013) and was performed in the laboratories of Ministry of Health according to regulations of the Institute of Turkish Standards (See Table 3.3).

Table 3.3 The result of the heavy metal analysis of Sarikiz (Sarikiz, 2013).

<b>Cations</b>	<b>Values (mg/L)</b>	<b>Cations</b>	<b>Values (mg/L)</b>
Copper	0.018	Antimony	<LOD
Iron	<LOD	Boron	0.010
Mercury	<LOD	Chrome	0.015
Cadmium	<LOD	Lead	<LOD
Aluminum	0.024	Manganese	0.077
Arsenic	0.001	Nickel	0.005
Barium	0.069	Selenium	<LOD

Prior to the analysis pH, temperature and total conductivity of the water were reported as  $5.98 \pm 0.13$  (n=6),  $18.2$  °C (n=6) and  $1205 \pm 15.6$   $\mu$ S (n=6), respectively. Analysis of the  $\text{CO}_3^{2-}$  and  $\text{HCO}_3^-$  was performed in the field exploiting titrimetric method. 0.1 M of standard solution of HCl was used as titrant. Phenolphthalein and Methyl orange were used as indicators. The carbonate and bicarbonate content of the water samples were found to be 0.0 and  $600 \pm 20.8$  mg/L respectively (n=3).

## CHAPTER FOUR

### EMISSION BASED SUB-NANOMOLAR Cu (II) SENSING WITH ELECTROSPUN NANOFIBERS

#### 4.1 Introduction

Copper is the third most abundant element in the human body and is essential in several biological pathways including electron transport, oxygen metabolism and enzymatic catalysis. Copper is on one side essential for life but on the other hand, depending on the dose, it may be highly toxic for organism. A high level of Cu (II) concentration is not necessary to produce toxicity in the human body. Over time, the heavy metal can reach toxic concentration levels. Therefore, monitoring of trace amounts of Cu (II) levels in water and food samples is quite important. In recent years, a number of chemosensors detecting Cu (II) ions either in biologically relevant species or in aqueous solutions were proposed (Luo, Li, Lv, Zhou, Xiao, & Choi, 2009; Rahimi, Goulding, Shrestha, Mirpuri, & Deo, 2008; Lai, Chang, & Fu, 2009; Cody, & Fahrni, 2004; Kim, & Choi, 2001; Gholivand, Niroomandi, Yari, & Joshagani, 2005; Aksuner, Henden, Yilmaz, & Cukurovali, 2008; Yari, & Afshari, 2006; Oter, Ertekin, Kirilmis, & Koca, 2007; Turel, Duerkop, Yegorova, Scripinets, Lobnik, & Samec, 2009; Chen, Liang, Wang, Liu, & Qian, 2009). In these sensing approaches absorption and/or emission, responses of the chromophore molecules resulting from interaction with Cu (II) ions were recorded as analytical signal.

These investigations provided valuable information for chemosensing of copper ions. Sometimes, indicators proposed for detection of Cu (II) exhibited weak responses to other cations within stated tolerance limits (Kim, & Choi, 2001). Over the last two decades, researchers mainly used the chemosensing agent in embedded form (Gholivand, et al. 2005; Aksuner, et al. 2008; Yari, & Afshari, 2006; Oter, et al. 2007).

In most of these designs optical chemical sensing of Cu(II) ions is mainly performed with a chromoinophore immobilized in polymer membranes such as

polyvinylchloride (PVC) (Gholivand, et al. 2005; Aksuner, et al. 2008; Yari, & Afshari, 2006) or ethyl cellulose (EC) (Oter, et al. 2007) in thin film form. That kind of sensing films display analyte dependent optical properties such as absorbance, fluorescence or reflectance. Mostly, such sensors provided enhanced stability, reversibility and sensitivity with respect to the solution based sensing. However, development of new technologies toward highly sensitive detection techniques is still very important for the researchers working in the field of analytical chemistry.

Sumner et al. (2006), used DsRed and the reference dye Alexa Fluor 488 in a polyacrylamide matrix and produced spherical, ratiometric, 80 nm-sized sensors. They detected copper ions, in the nanomolar (ppb) regime, in biologically relevant samples. Wang et al. (2002), compared performance of thin films and nanomaterials in terms of sensitivity, and revealed the advantage of nanoscale membranes over continuous thin films. In spite of these few examples, usage of nanomaterials in optical chemical sensing is very rare. In the light of the above discussion, usage of polymeric nanomaterials is expected to offer good results in comparison to the sensing films prepared with the same composition.

In this report, we have successfully combined nanoscale electrospun fiber materials with optical sensing technology for Cu (II) ion detection. We conceive of making electrospun fibers from a relatively novel solvent system containing room temperature ionic liquids (RTILs). Here we have demonstrated that it is possible to electrospun the EC and PMMA based composite fibers in presence of non-volatile RTIL; EMIMBF<sub>4</sub>.

The employed RTIL was chosen as polymer electrolyte due to its high ionic conductivity, low vapor pressure, low melting point, high thermal stability, low toxicity and recyclability (Sheldon, 2001; Welton, 1999). The successful application of RTILs in electrospinning could enhance the number and types of materials from which the fibers can be made.

On the other hand, electrospinning has recently gained much attention as a unique technique to fabricate high surface area and highly responsive nanofibrous materials

(Schreuder-Gibson, Gibson, Senecal, Sennett, Samuelson, Walker, Yeomans, Ziegler, Huang, Wang, Yang, Wen, Ren, Hill, Boring, Klabunde, Cheng, & Yin, 2001; Senecal, Ziegler, Auerbach, Schreuder-Gibson, & Samuelson, 2001; Wang, Drew, Lee, Senecal, Kumar, & Samuelson 2002; Drew, Wang, Senecal, Gibson, He, Tripathy, & Samuelson, 2000; Macdiarmid, Norris, Jones, El-sherif, Yuan, Han, & Ko, 2000; Reneker, & Chun, 1996).

In electrospinning, when a sufficiently large electric voltage is applied to the precursor solution in a capillary, it becomes tensioned because of the effect of the electrostatic repulsion forces within the polymer and attraction to a grounded electrode. As the strength of the electric field is increased, the charge overcomes the surface tension and at a critical voltage, a fine jet is sprayed from the tip of the cone. These jets dry to form very thin polymer fibers, which are collected on a substrate as nanofibers. The diameters of electrospun fibers can range from several micrometers to nanometers depending on the nature of precursor polymer and other experimental conditions; such as temperature, flow rate, voltage, and the distance between precursor solution, substrate, and humidity. As a result, electrospun nanofibrous membranes can have a large surface area. It is expected that this functional surface area have the potential to create high sensitivity and fast response in sensing applications.

In this part of the thesis, matrix materials of poly (methyl methacrylate) and ethyl cellulose were used together with ionic liquids. Optical nano-fibrous membrane chemical sensors were fabricated by both thin film and electrospinning technique. The N'-3-(4-(dimethylamino phenyl) allylidene) isonicotinohydrazide dye (DPAINH) was exploited as the Cu (II) selective fluoroionophore (See Figure 4.1). The electrospun nanofibers were characterized using scanning electron microscopy (SEM) and their average diameters were evaluated. To our knowledge this is the first using the fluoroionophore-doped electrospun nano-fibrous materials for copper sensing at sub-nanomolar level (Ongun et al., 2012).

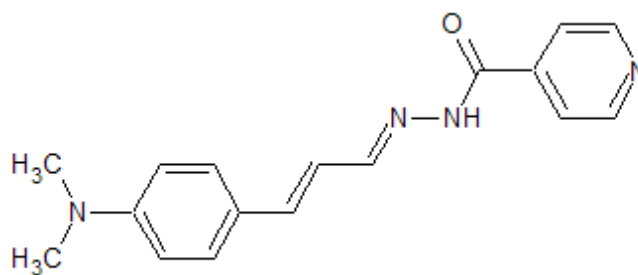


Figure 4.1 Structure of the copper sensitive fluoroionophore, N'-3-(4-(dimethylamino) phenyl) allylidene) isonicotinohydrazide (DPAINH).

## 4.2 Spectral Characterization of Fluoroionophore

### 4.2.1 Emission Spectra Related Characteristics and Quantum Yield Calculations

Photocharacterization of the ionophore was performed in diluted solutions of EtOH, DCM, THF and DMF and in solid matrices of EC and PMMA. Solution phase excitation and emission spectra of the ionophore were shown in Figure 4.2 The ionophore; DPAINH yielded two distinct emission peaks in the exploited solutions, between 300–340 nm and 560–600 nm, depending on the solvent. The exploited Cu (II) sensitive fluoroionophore exhibits strong absorption and bright fluorescence due to the intramolecular charge transfer (ICT) in the excited state. The ICT is continuous along with 9 covalent bonds throughout the molecule from electron donating N,N-dimethylamino group to the nitrogen atoms around carbohydrazide moiety. Immobilization of the molecule in polymers resulted with dramatic spectral changes. Upon immobilization, the emission maxima recorded in diluted solutions around 300 nm were disappeared. Interestingly, the excitation wavelength was shifted to the visible end of the electromagnetic spectrum and the emission efficiency was only appeared at longer wavelengths; around 500 nm (See Table 2 and Figure 4(II)). When doped in EC and PMMA the Stoke's shifts of DPAINH exhibited an enhancement with respect to the solution phase (See Table 2). Therefore when immobilized, the DPAINH dye could be excited at further wavelengths with respect to the solution phase. This result can be attributed to the restricted vibrational rotational motions in solid states.

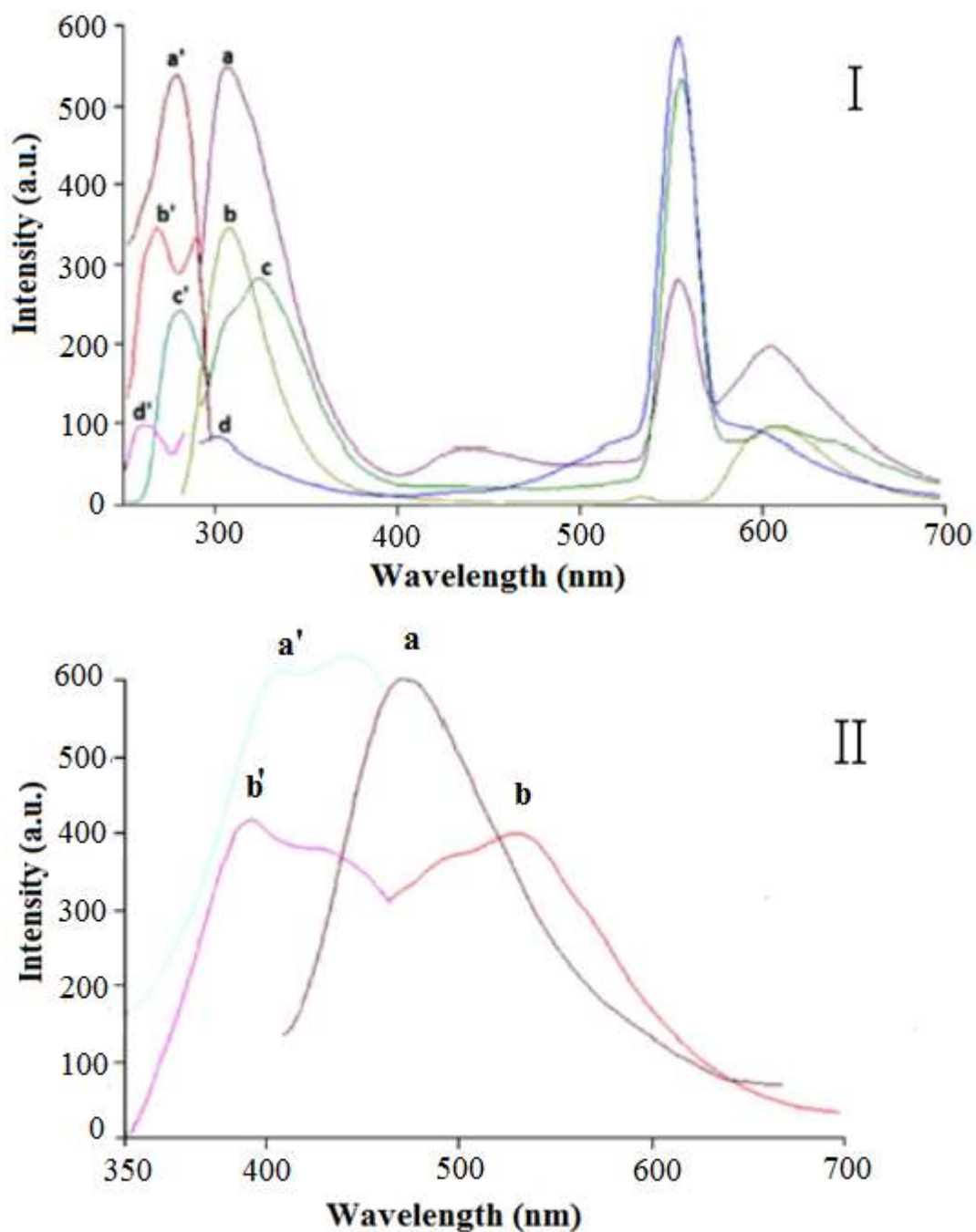


Figure 4.2 I: Excitation and emission spectra of the fluoroinophore in (a) EtOH, (b) THF, (c) DMF, (d) DCM. II: (a) in embedded form in EC, (b) in PMMA.

Fluorescence quantum yield values, ( $\Phi_F$ ) were calculated employing comparative William's method (Williams, Winfield, & Miller, 1983). Quinine Sulphate was used as reference standard whose fluorescence quantum yield is  $\phi_F=0.546$  in  $0.05M H_2SO_4$ . For this purpose, absorbance and emission spectra of five different concentrations of

reference standard and the employed N'-3-(4-(dimethylaminophenyl) allylidene) isonicotinohydrazide dye were recorded. The integrated fluorescence intensities were plotted vs. absorbance for reference and employed dye. The ratio of the gradients of the plots is proportional to the quantum yield. Equation 4.1 was used to calculate fluorescence quantum yields ( $\Phi_F$ ). In the following equation ST and X are denote standard and sample, respectively, and also Grad and  $n$  are the gradient of the plot and refractive index of the solvent or polymer matrix material, respectively.

$$\Phi_F = \Phi_{ST} \left( \frac{Grad_x}{Grad_{ST}} \right) \left( \frac{n_x^2}{n_{ST}^2} \right) \quad (4.1)$$

$$\Phi_F = 0.54 \times \left( \frac{90348}{491185} \right) \times \left( \frac{1.407^2}{1.33^2} \right) \quad (\text{In EC based matrix})$$

$$\Phi_F = 0.54 \times \left( \frac{23490}{491185} \right) \times \left( \frac{1.47^2}{1.33^2} \right) \quad (\text{In THF})$$

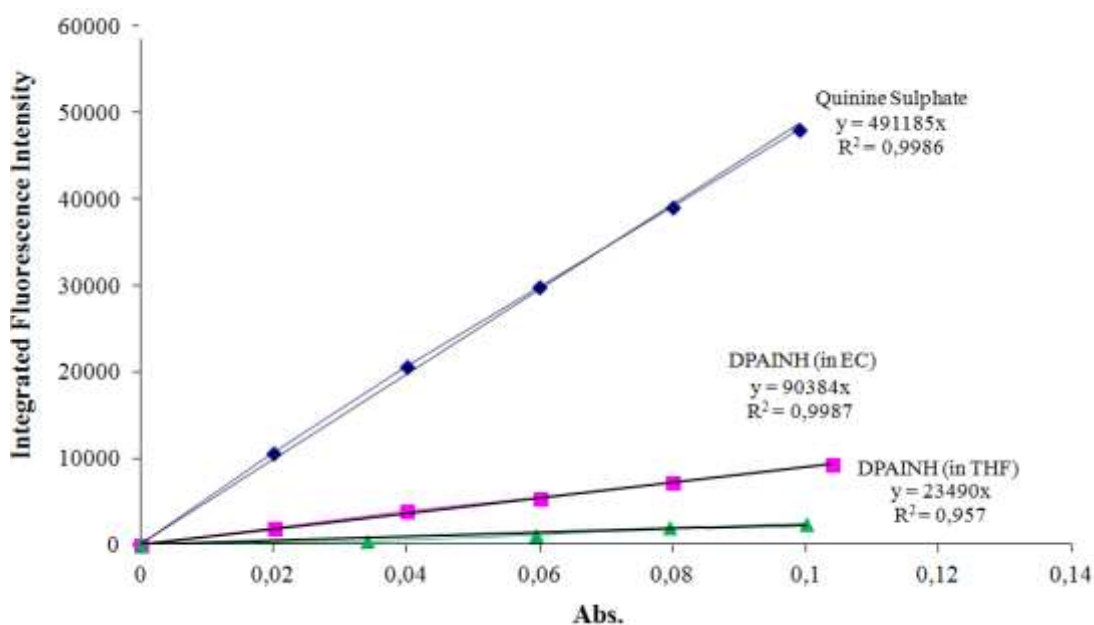


Figure 4.3 The integrated fluorescence intensities vs absorbance values of Quinine Sulfate in  $H_2SO_4$  DPAINH dye in EC and DPAINH dye in THF.

Table 4.1 The excitation–emission spectra related characteristics of the DPAINH acquired in conventional solvents, and in thin film form of PMMA and EC.

Compound	Matrix	$\lambda_{\max}^{em}$	$\lambda_{\max}^{ex}$	$\Delta\lambda_{ST}$ (Stoke's shift)	$\phi_F$ (Quantum yield)
DPAINH	EtOH	285	315	30	0.03
	THF	270	310	40	
	DMF	285	335	50	
	DCM	255	305	50	0.11
	PMMA	395	535	140	
	EC	405	490	85	
	PVC	315	390	75	

Quantum yield of the DPAINH dye in EC was approximately four fold of the quantum yield efficiency observed in THF (See Figure 4.3 and Table 4.1). This can be attributed to the hindered motion of the molecule around single bond within the polymeric matrix material.

### 4.3 SEM Images of Electrospun Membranes

The electrospun nanofibers were characterized using scanning electron microscopy (SEM) and their average diameters were evaluated. SEM images of electrospun membranes of the PMMA and EC at various magnifications are shown in Figure 4.4 and 4.5, respectively. It is observed that the membrane has a 3-D structure with a random fiber orientation that is evenly distributed on the substrate. Average fiber diameters were calculated as  $536 \pm 76$  and  $360 \pm 82$  nm for PMMA and EC based electrospun fibers, respectively. When conditions of the electrospinning process such as solvent composition, viscosity, concentration, temperature, humidity and working distance were kept constant reproducibility in the preparation of electrospun membranes was quite good.



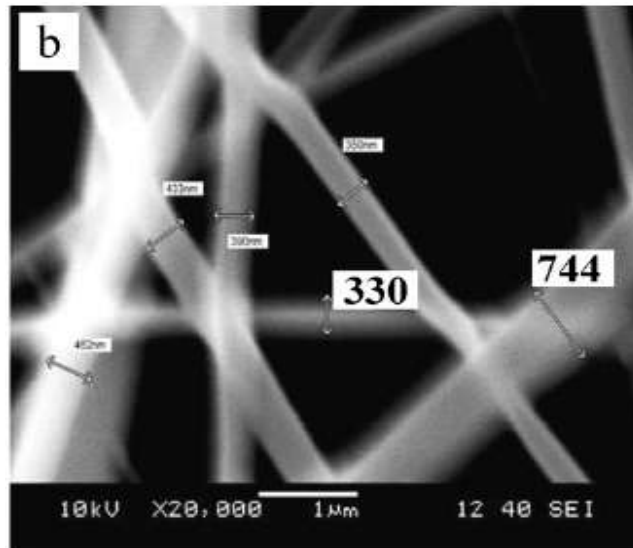
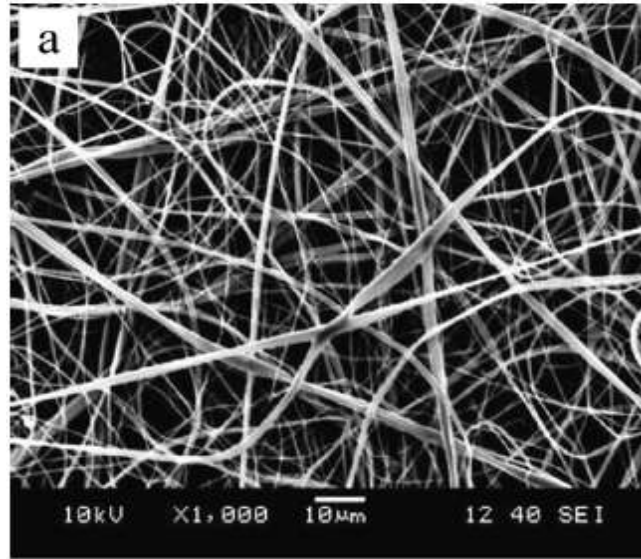


Figure 4.4 SEM images of electrospun membranes; (a) and (b); PMMA based nanofibers at different magnifications such as  $\times 1000$ ,  $\times 20\,000$ .

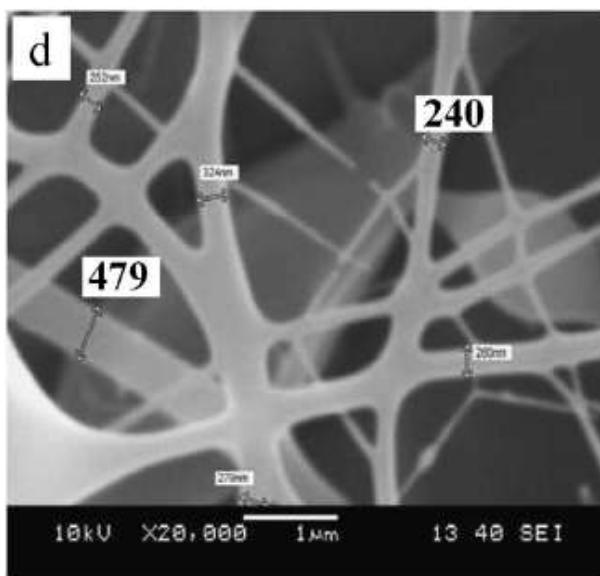
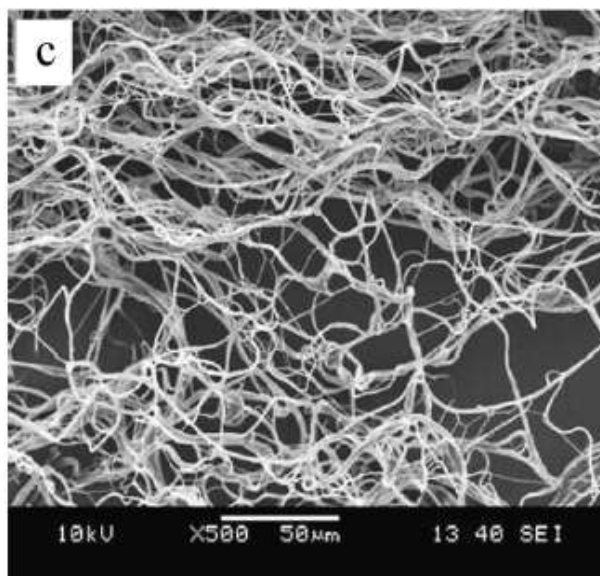


Figure 4.5 SEM images of electrospun membranes; (c) and (d); EC based nanofibers at different magnifications such as  $\times 500$  and  $\times 20\,000$ .

#### 4.4 Detection of $pK_a$ for DPAINH

The knowledge of acidity constants ( $pK_a$ ) of dyes is of fundamental importance in order to provide information on chemical reactivity range of the dyes. For this reason, the emission based pH induced response of DPAINH was investigated in PMMA nanofiber matrix. The relative signal change of emission spectra of the

DPAINH was monitored after addition of certain concentrations of buffered solutions at different pH ranges. Buffer solutions were prepared with 0.01M CH<sub>3</sub>COOH, 0.01 NaOH, and 0.01M NaH<sub>2</sub>PO<sub>4</sub> at desired pH. The preparation procedures for the buffer solutions were given in Chapter 3. pH induced fluorescence spectra of DPAINH (pH versus (I-I<sub>0</sub>)/I<sub>0</sub>) in the pH range of 3.00-7.00 and 7.00-11.00 were shown in Figure 4.6 and 4.7, respectively.

The pK<sub>a</sub> values of the fluoroionophore dye were calculated by using non linear fitting algorithm of Gauss-Newton-Marquardt method (Mills, Chang, & McMurray, 1992) in PMMA matrix both in acidic and basic forms (See Equation 4.2) When the above-mentioned Gauss-Newton-Marquardt algorithm was employed to the emission based spectral data in acidic and basic forms, the pK<sub>a</sub> values were found to be 4.99 and 9.01, respectively. The Gauss-Newton-Marquardt equation is as follows;

$$pK_a = pH + \log [(I_x - I_b)/(I_a - I_x)] \quad (4.2)$$

where I<sub>a</sub> and I<sub>b</sub> are the intensities of acidic and basic forms and I<sub>x</sub> is the intensity at a pH near to the pK<sub>a</sub>.

$$pK_a = 5.00 + \log [(270-450)/(117-270)]$$

$$pK_a = 5.00 + \log [1.18]$$

$$pK_a = 4.99 \text{ ( for acidic form)}$$

$$pK_a = 9.00 + \log [(330-188)/(470-330)]$$

$$pK_a = 9.00 + \log [1.01]$$

$$pK_a = 9.01 \text{ ( for basic form)}$$

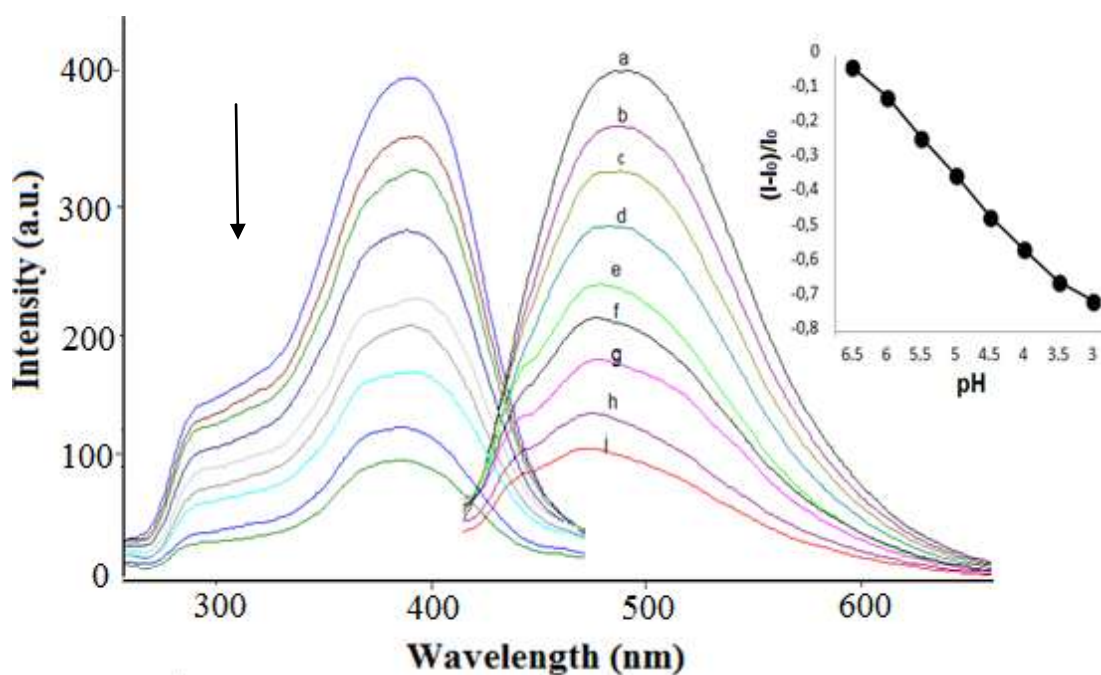


Figure 4.6 pH induced emission characteristics and sigmoidal calibration curve of DPAINH doped EC membrane in the pH range of 7.0–3.0. (a) pH=7.0, (b) pH=6.5, (c) pH= 6.0, (d) pH= 5.5, (e) pH= 5.0, (f) pH= 4.5, (g) pH= 4.0, (h) pH= 3.5, (j) pH= 3.0, (pKa=4.77).

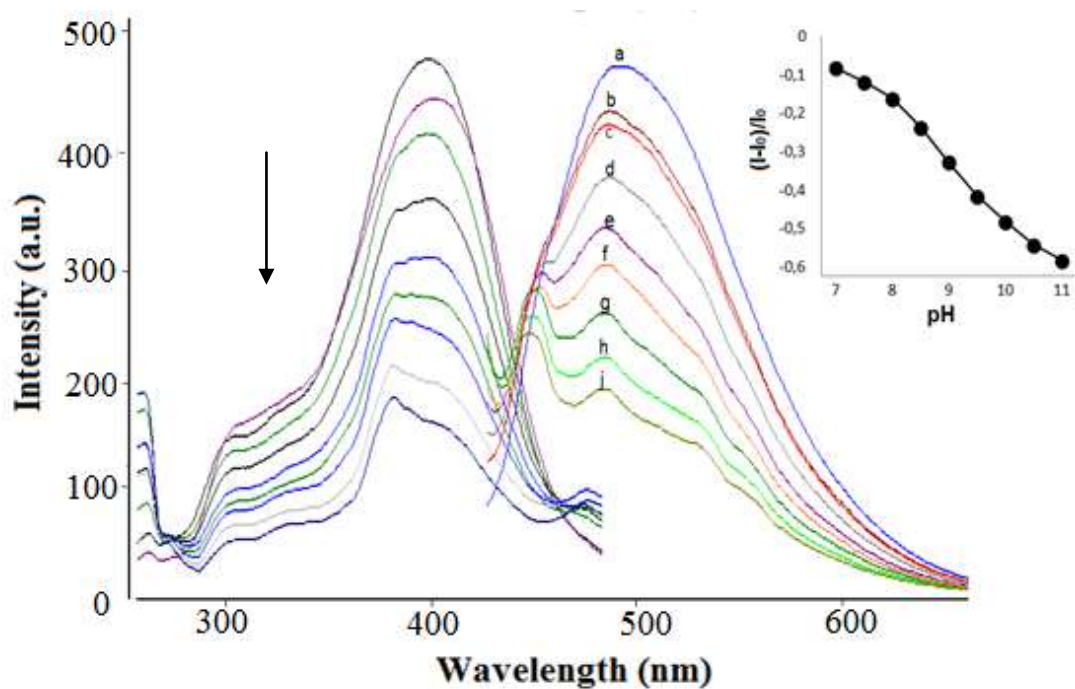


Figure 4.7 pH induced emission characteristics and sigmoidal calibration curve DPAINH doped PMMA membrane after exposure to buffer solutions in the pH range of 7.0–11.0 (a) pH=7.0, (b) pH= 7.5, (c) pH= 8.0, (d) pH= 8.5, (e) pH= 9.0, (f) pH= 9.5, (g) pH= 10.0, (h) pH= 10.5, (j) pH= 11.0, (pKa=8.60).

#### 4.5 Copper Ion Sensing Studies: Cu (II) Uptake into the Membrane and Fluorescence Based Response

The exploited Cu (II) sensitive fluoroionophore exhibited a cross sensitivity to proton ions between pH 3.0 and 11.0 in solution phase. When embedded in RTIL containing matrices the DPAINH dye became more resistive for protonation. We also tested the Cu (II) sensing ability of the chemosensor at different pH values, between pH 5.0 and 9.0 in acetic acid/acetate and phosphate buffer solutions. We obtained the highest sensitivity in acetic acid/acetate buffer and for further studies; we have chosen this buffer as optimum working condition. During calibration studies, we exploited  $5 \times 10^{-3} \text{M}$  of acetic acid/acetate buffer solutions to avoid pH induced signal fluctuations. Distribution of the Cu (II) related chemical species in the working conditions was checked with chemical equilibrium software program visual MINTEQ at pH 4.0 in presence of acetate ions. The equilibrium related species in the buffer environment were found to be as follows: acetate (aq) 15.2%; H-acetate (aq) 84.8%;  $\text{Cu}^{2+}$  (aq) 89.8%;  $\text{Cu-acetate}^+$  (aq) 10.1%. This distribution reveals that approximately 90% of the copper is in form of  $\text{Cu}^{2+}$  (aq) under these circumstances. Due to the solubility considerations acetic acid/acetate buffered solutions of pH 4.0 was used for further studies.

The optical sensors are mainly composed of a polymer compatible ion-selective indicator dye (chromoionophore), and a lipophilic anionic additive dissolved in polymer matrix material. When doped into polymeric matrices together with the anionic additive; potassium tetrakis-(4-chlorophenyl) borate; the DPAINH dye becomes a Cu (II) sensitive molecular probe. In this system, Cu (II) ions are extracted into the electrospun fibers by the enforcement of the anionic additive meanwhile two potassium ions diffuse from the polymer into the aqueous phase via the mechanism of ion exchange. Therefore, the charge balance was maintained within the polymer. Following Equation 4.3 reveals the ion exchange mechanism.

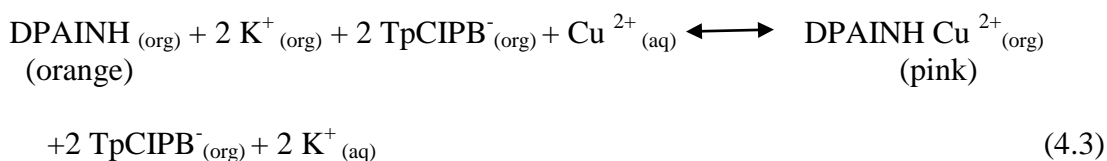


Figure 4.8 (I-II) and Figure 4.9 (I-II) show the variations in fluorescence spectra of the thin film and electrospun materials upon exposure to Cu (II) ions for PMMA and EC matrices, respectively. The emission maxima approximately 20 nm and 10 nm red shifted in form of nanofiber with respect to continuous thin films for PMMA and EC respectively (see Figure 4.8 and 4.9). In all cases, response to Cu (II) ions was in direction of decrease in signal intensity. In form of nanomaterials, the relative signal changes were approximately three times and two times better compared to the continuous thin films. In PMMA, the relative signal drops were reported as 20% and 62.5% for thin film and nanofiber forms, respectively. Similarly 40% and 83% relative signal drops were calculated for EC based matrices for thin film and nanomaterials. The insets of Figure 4.8 and 4.9 reveal intensity based linear response ranges of the ionophore to Cu (II) ions in different forms in terms of molar concentration.

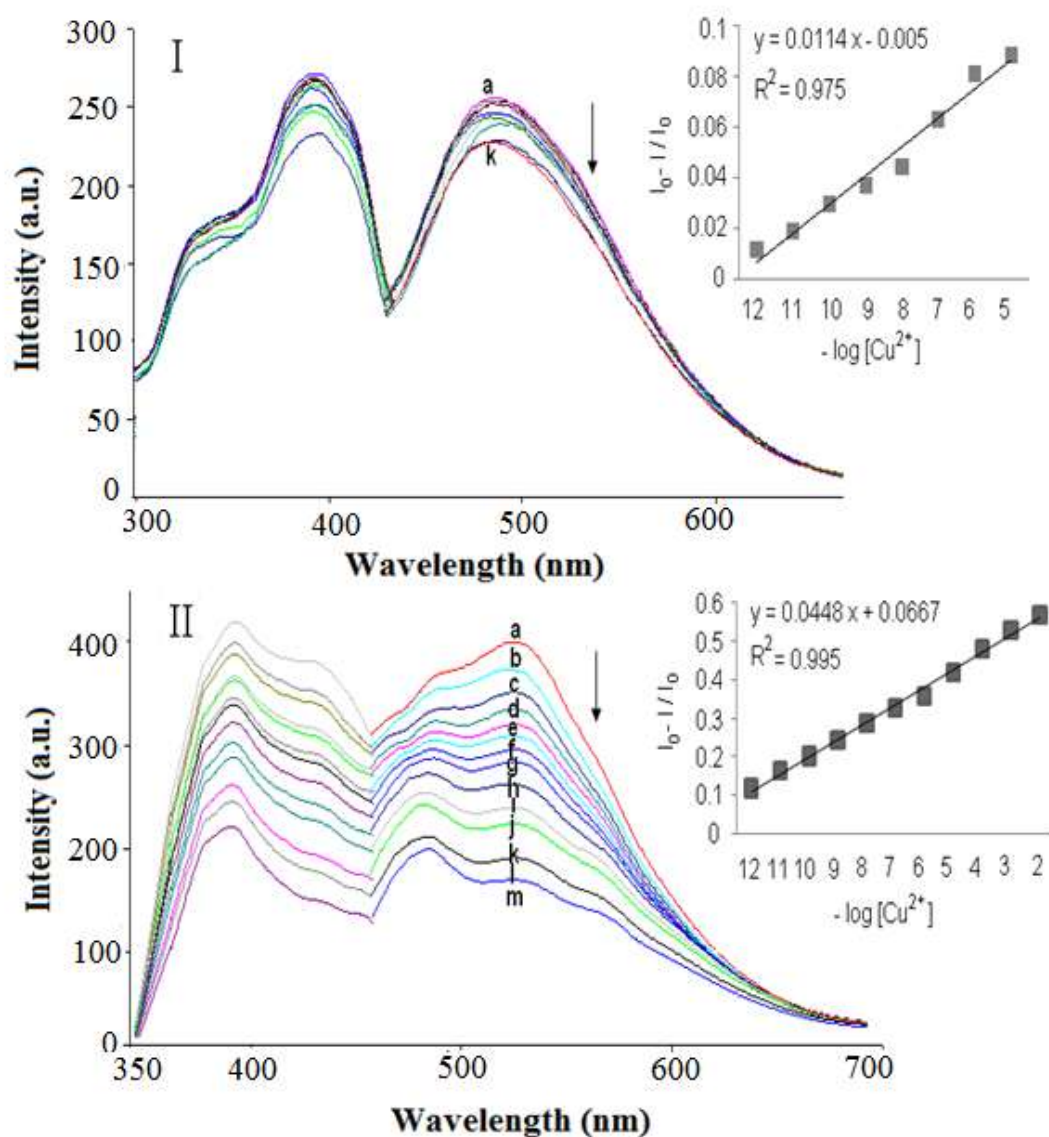


Figure 4.8 I: Fluorescence response of the dye doped PMMA thin film to Cu (II) ions at pH 4.0. (a) Cu-free buffer, (b)  $10^{-12}$  M, (c)  $10^{-11}$ , (d)  $10^{-10}$ , (e)  $10^{-9}$ , (f)  $10^{-8}$ , (g)  $10^{-7}$ , (h)  $10^{-6}$ , (i)  $10^{-5}$ , (j)  $10^{-4}$ , (k)  $10^{-3}$  M Cu(II). Inset: Linearized calibration plot for the concentration range of  $10^{-12}$ - $10^{-5}$  M Cu(II). II: Response of the PMMA based nanofiber to Cu (II) ions at pH 4.0. (a) Cu-free buffer, (b)  $10^{-12}$  M, (c)  $10^{-11}$ , (d)  $10^{-10}$ , (e)  $10^{-9}$ , (f)  $10^{-8}$ , (g)  $10^{-7}$ , (h)  $10^{-6}$ , (i)  $10^{-5}$ , (j)  $10^{-4}$ , (k)  $10^{-3}$ , (l)  $10^{-2}$ , (m)  $10^{-1}$  M Cu(II). Inset: Linearized calibration plot for the concentration range of  $10^{-12}$ - $10^{-2}$  M Cu (II).

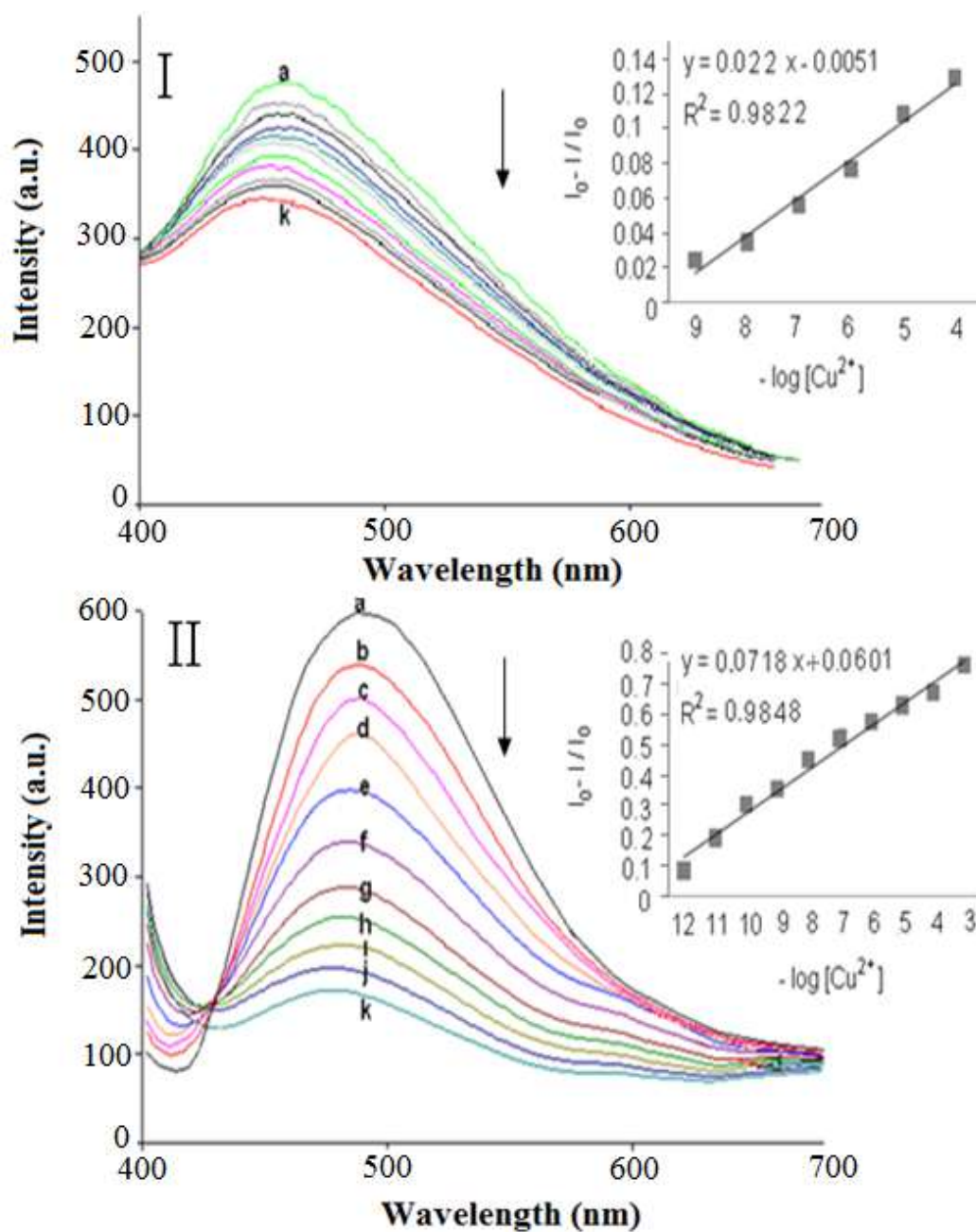


Figure 4.9 I: Fluorescence response of the dye doped EC thin film to Cu(II) ions at pH 4.0. (a) Cu-free buffer, (b)  $10^{-12}$  M, (c)  $10^{-11}$ , (d)  $10^{-10}$ , (e)  $10^{-9}$ , (f)  $10^{-8}$ , (g)  $10^{-7}$ , (h)  $10^{-6}$  (i)  $10^{-5}$ , (j)  $10^{-4}$ , (k)  $10^{-3}$  M Cu (II), Inset: Linearized Calibration plot for the concentration range of  $10^{-9}$ - $10^{-4}$  M Cu (II). II: Response of the EC based nanofiber to Cu (II) ions at pH 4.0. (a) Cu-free buffer, (b)  $10^{-12}$  M, (c)  $10^{-11}$ , (d)  $10^{-10}$ , (e)  $10^{-9}$ , (f)  $10^{-8}$ , (g)  $10^{-7}$ , (h)  $10^{-6}$ , (i)  $10^{-5}$ , (j)  $10^{-4}$ , (k)  $10^{-3}$  M Cu (II). Inset: Linearized calibration plot for the concentration range of  $10^{-12}$ - $10^{-3}$  M Cu (II).



The intensity drops are known to be due to the quenching of the DPAINH dye by Cu (II) ions.

Quenching can occur by different mechanisms. In collisional quenching, excited state fluorophore is deactivated upon contact with the ion in solution, which is called the quencher. However, sometimes the fluorophore can be quenched both by collisions and by complex formation. The intensity related data ( $I_0/I$ ) exhibiting an upward-concave curvature toward the y-axis is the evidence of the combined quenching both by collisions (dynamic quenching) and by complex formation (static quenching) by the same quencher (Lakowicz, 2006).

In case of dynamic quenching because of the collisions between the quencher and the fluorophore affect only the excited state of the molecule, no changes in absorption or excitation spectrum are expected. Contrarily, the formation of ground state complex in static quenching will influence the absorption spectra of the fluorophore. Therefore, by a careful evaluation of the absorption spectrum, mechanism of the quenching can easily be distinguished (Wang, Wang, Moses, & Heeger, 2001).

Figure 4.10 shows the absorption spectra of the fluorophore in the absence and presence of the quencher. From the absorption spectral data, it can be concluded that the quencher affects only the excited state of the fluorophore, which indicates dynamic quenching. When the linear shape of the fluorescence intensity based response and absorption spectroscopy, related data were considered together, the quenching mechanism between DPAINH and Cu (II) could be concluded as dynamic quenching.

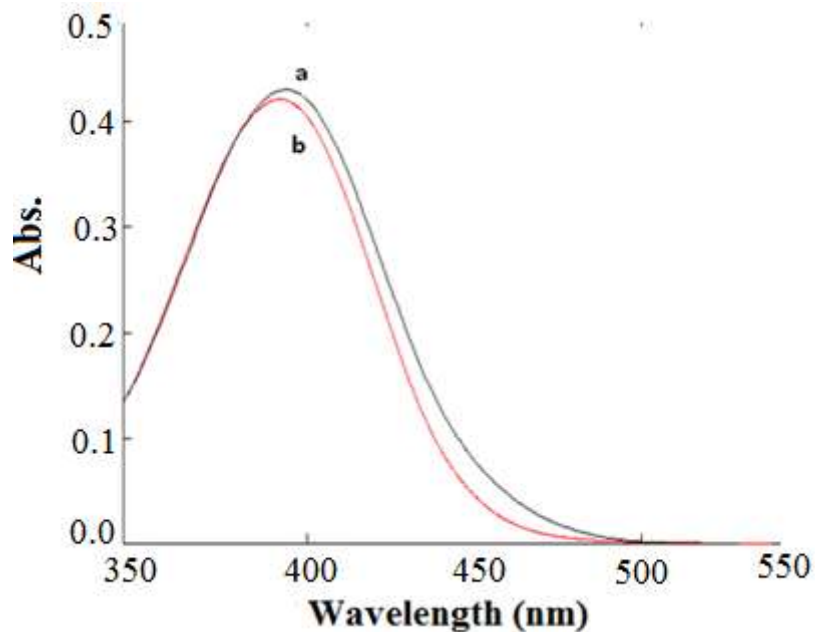


Figure 4.10 Absorption spectra of the fluoroionophore in the absence (a), and presence (b) of the quencher; Cu (II).

Sensitivity of the quenching process and consequently sensor dynamics can be manipulated by controlling the quencher diffusion rate to fluorophores encapsulated in the polymer phase via the micro structural properties of the sensing agent. The offered nano-structure was quite beneficial for both the sensitivity and dynamic characteristics of the sensor due to its large specific area, which has high number of active sites for diffusion of Cu (II) ions towards the solid phase with respect to the thin films made up of same material. In these structures, the possibility of interaction of the analyte ions with the Cu (II) selective chromoionophore molecules is higher than that of in conventional thin films.

#### 4.6 Stern–Volmer Analysis

The employed fluoroionophore is sensitive to quenching by Cu (II) ions. In a homogeneous medium, such as in solution, the quantitative measure of fluorescence quenching is described by the Stern–Volmer constant,  $K_{sv}$ .

Stern- Volmer constants ( $K_{sv}$ ) of the electrospun films, calculated from slopes of the plots were found to be 0.23 ( $M^{-1}$ ) and 0.07 ( $M^{-1}$ ) for EC and PMMA nanofibers respectively. These values are 23 and 6 fold greater than that obtained from the continuous thin film sensor slides of EC and PMMA, respectively (See Table 4.2). The higher  $K_{sv}$  values reveal important practical consequences. The sensitivity of the quenching process is enhanced by controlling the quencher diffusion rate to fluorophores employing electrospinning technique. The Stern-Volmer plots for quenching by Cu (II) in both cases, exhibited excellent linearity indicating that most of the total emission may be accessible to quenching. Additionally the recorded response time for the electrospun nanofibers is less than one minute. This value is at least five times better than that of the response times measured for continuous thin films (See Table 4.2, Figure 4.11(I) and (II)).

The data obtained by gathering Stern–Volmer analysis for each electrospun and continuous thin film are shown in Figure 4.11 (I) and (II). For quencher concentrations in the range of  $10^{-12}$ – $10^{-5}$  M, linear plots between concentration of quencher and  $I_0/I$  are obtained showing an excellent Stern–Volmer relationship.

Table 4.2 The Stern-Volmer plots related data of PMMA and EC based electrospun nanofibers and thin films.

Indicator dye	Matrix /form	Linear Stern Volmer Equation	$K_{sv}$ constant( $M^{-1}$ )
DPAINH	EC/ nanofiber	$y = 0.2323x + 0.7330$	0.23
	PMMA/nanofiber	$y = 0.0695x + 0.9900$	0.07
	EC / thin film	$y = 0.0124x + 0.9806$	0.01
	PMMA/ thin film	$y = 0.0133x + 0.9920$	0.01

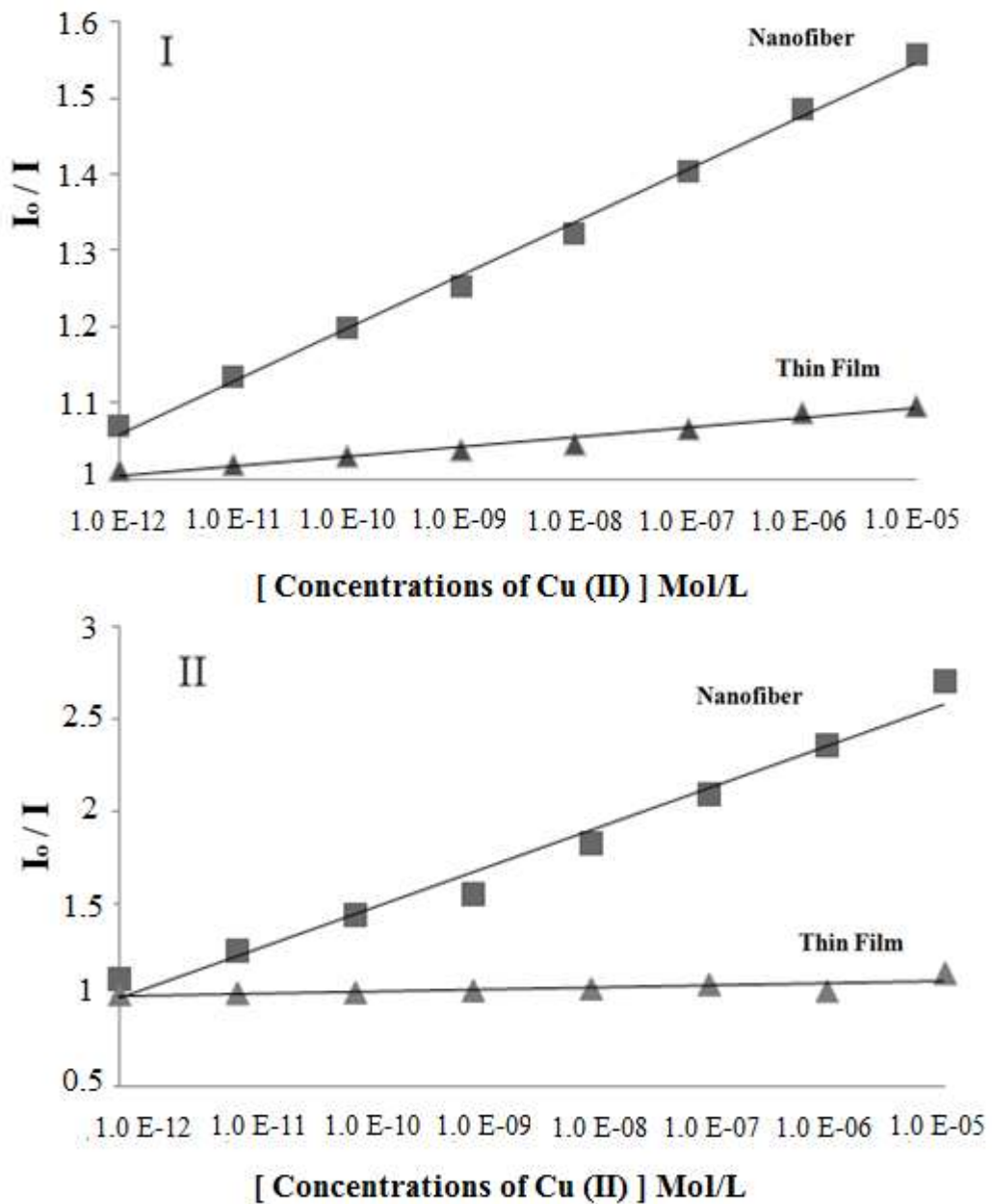


Figure 4.11 Gathered Stern Volmer plots of the electrospun nano-fibers and continuous thin films in PMMA (I) and in EC (II).

The calculated  $K_{sv}$  values reveal important practical consequences. The sensitivity of the quenching process is enhanced by controlling the quencher diffusion rate to fluorophores via the nano-structural properties of the electrospun sensing films. Additionally this type of nano-structure provides higher surface area-to-volume ratio than that of continuous thin films (Deitzel, Kleinmeyer, & Tan, 2001).

#### 4.7 Sensor Dynamics and Analytical Figures of Merit

In PMMA based matrices the working range was shifted from  $10^{-12}$ – $10^{-5}$  M to  $10^{-12}$ – $10^{-2}$  M. Similarly, in EC based sensing agents the enhancement in working range was more distinct and enlarged from  $10^{-9}$ – $10^{-4}$  M to  $10^{-12}$ – $10^{-3}$  M. The detection limits (LOD) were calculated exploiting concentration of the metal ion giving a signal equal to average of the blank signal ( $n = 20$ ) plus three standard deviation and were found to be  $3.8 \times 10^{-15}$  M for EC and  $1.4 \times 10^{-15}$  M for PMMA respectively. The attained LOD values exploiting nano-materials for the offered design is an evident of the enhanced sensitivity.

It should be remembered that, linear response offers many advantages over quadratic calibration curves such as interpolation and extrapolation. In this work, due to the compatibility of the acquired data, the ordinary least squares (OLS) regression model was employed for the fit of the calibration curves. The regression results yielded an absolute linear response with coefficients of regression ( $R^2$ ) of 0.9848 and 0.9950 for ethyl cellulose and poly (methyl methacrylate) is evidences of the attained linearity. The measured equilibrium response times of less than one minute and high analytical signal values upon exposure to Cu (II) ions with electrospun nanofibers are very promising (See Table 4.3).

Table 4.3 Calibration related characteristics of PMMA and EC based electrospun nanofibers and thin films

Indicator Dye	Matrix /Form	Linear Range (Cu(II) Mol/L)	Regression Coefficient ( $R^2$ )	LOD (Molar)
DPAINH	EC/nanofiber	$1.0 \times 10^{-12}$ to $1.0 \times 10^{-3}$	0.9848	$3.80 \times 10^{-15}$
	PMMA/nanofiber	$1.0 \times 10^{-12}$ to $1.0 \times 10^{-2}$	0.9950	$1.40 \times 10^{-15}$
	EC / thin film	$1.0 \times 10^{-9}$ to $1.0 \times 10^{-4}$	0.9822	$6.50 \times 10^{-12}$
	PMMA/ thin film	$1.0 \times 10^{-12}$ to $1.0 \times 10^{-6}$	0.9750	$6.60 \times 10^{-13}$

#### 4.8 Recovery and Selectivity Studies, Tests with Real Samples

The content of Cu(II) in the diluted certified reference material of Merck (SRM from NIST Cu(NO<sub>3</sub>)<sub>2</sub> in HNO<sub>3</sub> 0.5 mol L<sup>-1</sup> 1000 mg L<sup>-1</sup> Cu CertiPUR®) were determined by the prepared electrospun nanofibers. The tap water samples were freshly collected from the laboratory in polyethylene vials, after allowing the water to flow for 5 min. All water samples were filtered through a 0.45 μm membrane filter and analyzed as soon as possible after sampling. The recovery experiments were carried out adding certified reference material into the tap water. The resulting concentration of the Cu (II) was 10<sup>-9</sup> M. The average recovery performance was found to be 103 ± 3.7% for five measurements. The recovery test results reveal the capability of the offered sensing design for the determination of copper ions in real samples without considerable error.

In order to examine the cross sensitivities of the DPAINH dye to potential interferents of the groundwater samples, the sensing agents were treated with 10<sup>-5</sup> M concentrations of Ag<sup>+</sup>, Al<sup>3+</sup>, Ca<sup>2+</sup>, Co<sup>2+</sup>, Cu<sup>2+</sup>, Fe<sup>3+</sup>, Hg<sup>2+</sup>, Mn<sup>2+</sup>, Mg<sup>2+</sup>, Ni<sup>2+</sup>, Pb<sup>2+</sup>, Sn<sup>2+</sup> and Zn<sup>2+</sup> cations in acetic acid/acetate buffer solutions at pH 4.0. Figure 4.12 (I) and (II) reveals that the sensing agent is capable of determining Cu (II) ions with a high selectivity over other ions. The fluorescence was distinctly quenched in the presence of Cu (II) at 535 nm and 490 nm for PMMA and EC based sensing slides respectively. The interference effects of the conventional anions of NO<sub>3</sub><sup>-</sup>, ClO<sub>4</sub><sup>-</sup>, SO<sub>4</sub><sup>2-</sup>, Cl<sup>-</sup>, HCO<sub>3</sub><sup>-</sup> and HPO<sub>4</sub><sup>3-</sup> were also tested. Relative signal changes of less than 5 % were obtained for most of the tested potential interferents. Only Fe<sup>3+</sup> and HCO<sub>3</sub><sup>-</sup> ions exhibited remarkable response in terms of signal intensity. However, these problems can be overcome tuning the pH of the working conditions

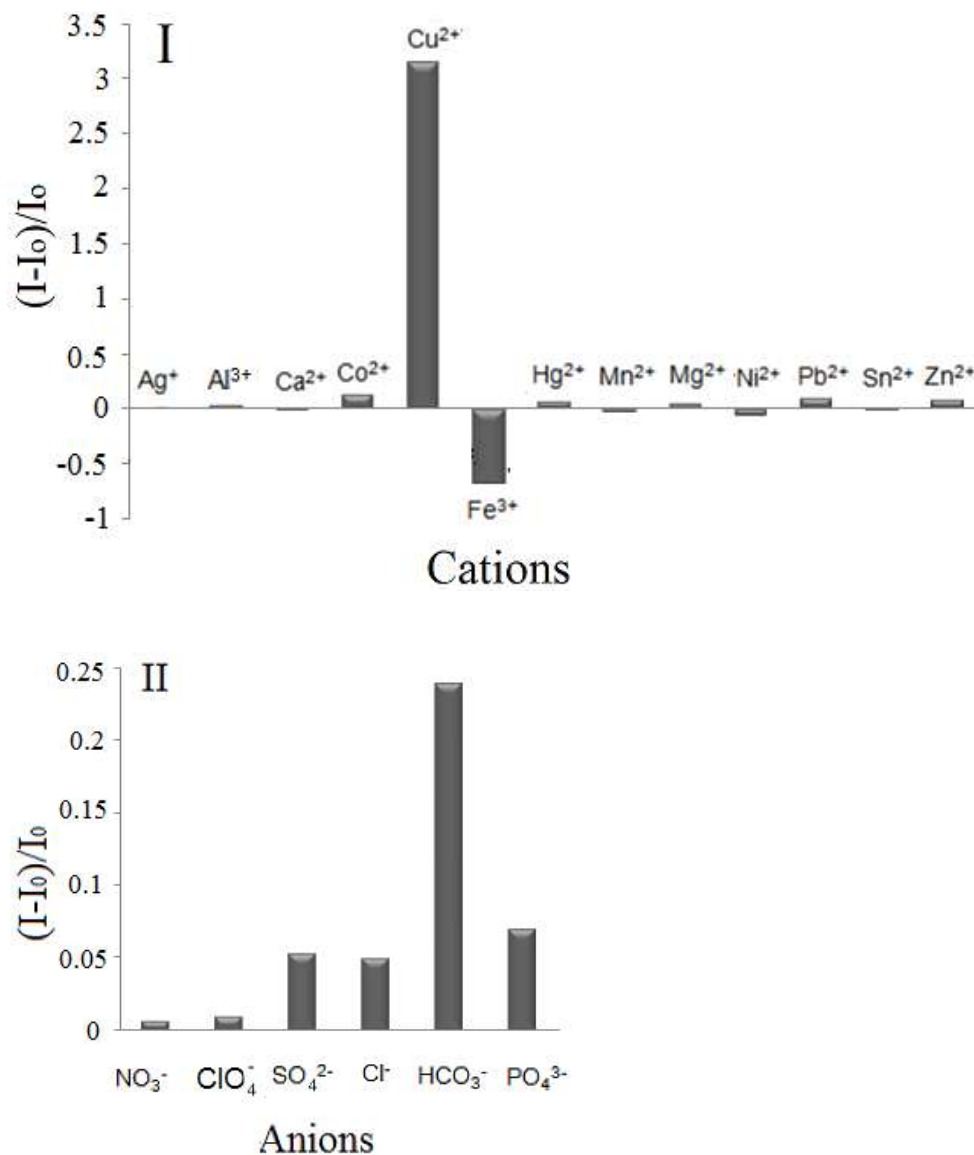


Figure 4.12 I: Response of DPAINH to  $10^{-5}$  M of different metal cations in acetic acid/acetate buffer solutions at pH 4.0. II: Response of the dye to  $10^{-5}$  M of the major anions in near neutral waters.

#### 4.9 Conclusion

Electrospinning looks like a promising, simple, and an effective method for fabricating nanomaterials. On the other hand, such kind of materials should be coupled with optical chemical sensor devices. With respect to continuous thin films, electrospun films can offer enhanced sensitivity and reactivity in sensing. In this work, we performed coupling of electrospun nanomaterials with fluorescence based measurement techniques without scattering and other side effects. We performed to

measure the Cu (II) concentrations as low as  $10^{-12}$  M exploiting nanofibrous materials. Further efforts will focus on exploring new sensing materials and polymer compositions, controlling the nanoscale size of the electrospun membranes, and optimizing the sensitivities for the detection of a variety of analytes.

The major requirements of an ideal sensor are high sensitivity, good LOD values, wide linear working range, selectivity and fast response time. The working ranges of the sensing agents calculated from emission profiles were broad enough and extends from  $10^{-12}$  to  $10^{-3}$  M and from  $10^{-12}$  to  $10^{-2}$  M for EC and PMMA respectively. The quadratic fit is more convenient for such kind of large working ranges. However, we obtained excellent linearity with nanomaterials for both of the matrices within the whole working range. Instead of groundwater samples, we used tap water as real sample in recovery tests due to the difficulties to reach the origin of Sarikiz location. However, we simulated the real groundwater samples in terms of content and ionic strength.



## CHAPTER FIVE

### DETERMINATION OF Hg (II) EXPLOITING DIFFERENT IONOPHORES

#### 5.1 A Short View to Sensing of Ionic Mercury

Among toxic trace metals, mercury (Hg) is one of most hazardous environmental contaminants. Up to now, different approaches for the determination of trace levels of different mercury species have been used. Mercuric ions can form soluble complexes with different organic and inorganic ligands in aquatic systems (Leermakers, Baeyens, Quevauviller, & Horvat, 2005).

Thus, it is still necessary to develop methods for sensitive detection of mercury even at concentrations lower than nanomolar levels. Fluorescent-based techniques have a great importance in determination of ionic mercury. Most of them exploit a fluoroionophore exhibiting a response to mercury ions in an appropriate solution. The solution phase studies provided valuable information for researchers (Vasimalai, & Abraham, 2013; Banerjee, Karak, Sahana, Guha, Lohar, & Das, 2011; Vedrinaro, Dragojević, Dragojević, & Čadež, 1997; San Vicente de la Riva, Costa-Fernández, Jun Jin, Pereiro, & Sanz-Medel, 2002).

However, in further studies the sensing agents were immobilized in polymer matrices due to the stability and sensitivity considerations. In the optical chemical sensing of mercury, the thin film approach has been used many times. Such sensors with thickness in the range of 1–30  $\mu\text{m}$  provided enhanced robustness, reversibility, stability and sensitivity with respect to the sensing studies realized in the solution phase (Aksuner, Basaran, Henden, Yilmaz, & Cukurovali, 2011; Nuriman, Kuswandi, & Verboom, 2011). On the other hand, preparation and usage of nanomaterials is a current research topic of interest in different scientific and technological areas including sensor technologies due to its promising properties. The usage of nano scale sensing materials are expected to offer good results in

comparison to sensing films prepared with the same composition (Kacmaz, Ertekin, Suslu, Ergun, Celik, & Cocen, 2012; Liang, Wang, Chen, Qian, Ling, & Fu, 2010; Xia, & Zhu, 2008; Chen, Gao, Xu, Wu, Chen, & Zhu, 2006; Fu, Wang, Chen, Bo, Zhou, & Chen, 2010).

Although there have been limited number of works regarding sensor applications of nanomaterials, they offer promising sensor performances such as enhanced LOD values, shorter response times and better long term stabilities. Electrospun membrane of fluorescent gold nanoclusters (Cai, Yan, Liu, Yuan, & Xiao, 2013) and sol-gel based electrospun fiber membranes were exploited for detection or adsorption of ionic mercury (Teng, Wang, Li, & Zhang, 2011). In this respect, nano scale materials received great research interest for chemical and biological sensor applications due to their unique high surface area and promising detection limits.

Up to now, the reported works regarding optical chemical sensor applications of electrospun nanofibers is very rare. To our knowledge, this is the first attempt using the fluoroionophore-doped EC based electrospun nano-fibrous materials for mercury sensing at sub-nanomolar level (Kacmaz et al., 2012).

In this chapter, the mercury sensitive fluoroionophore dyes were used to produce electrospun nanofibers. For detection of ionic mercury at sub-nanomolar levels, the nano-scale electrospun fiber materials were combined with optical sensing technology successfully. The nano-fibrous materials were fabricated by electrospinning technique.

## 5.2 Determination of Mercury (II) Ions Using Luminescent Carbazole Derivative at Femtomolar Levels

The luminescent carbazole derivative, 2-(9-Methyl-9H-carbazol-3-yl)-5-(pyridin-4-yl)-1,3,4-oxadiazole (ODC-3) was used for sensitive sensing of Hg (II) ions at femtomolar levels. The dye exhibited strong absorbance, high quantum yield, large Stoke's shift and excellent photo stability. Polymeric matrix material of ethyl cellulose (EC) was exploited together with ionic liquid; 1-ethyl-3-methylimidazolium tetrafluoroborate. Optical nano-fibrous chemical sensors were fabricated by electrospinning technique. The electrospun nano-fibers were characterized using scanning electron microscopy (SEM) and their average diameters were evaluated. The schematic structure of the employed molecule ODC-3 was shown in Figure 5.1.

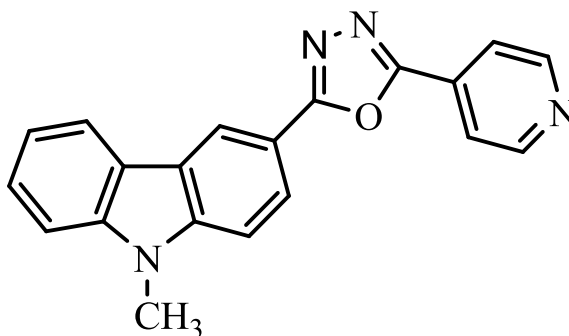


Figure 5.1 Schematic structures of the mercury sensitive fluoroionophore;2-(9-methyl-9H-carbazol-3yl) -5-(pyridin-4-yl)-1,3,4oxadiazole dye (ODC-3).

### 5.2.1 Photocharacterization of Fluoroionophore and Quantum Yield Calculations

For spectral characterization of the ODC-3, absorption excitation and corrected emission spectra were recorded in the solvents of EtOH, DCM, THF and toluene/ethanol (To:EtOH; 80:20) mixture and Toluene (See Figure 5.2 and 5.3).

The UV-Vis spectroscopy related data (absorption maxima;  $\lambda_{\text{Abs}}$ , and molar extinction coefficient; $\epsilon$ ), were shown in Table 5.1. ODC-3 exhibited very efficient absorbance and high molar extinction coefficients around 340 nm in solution phase.

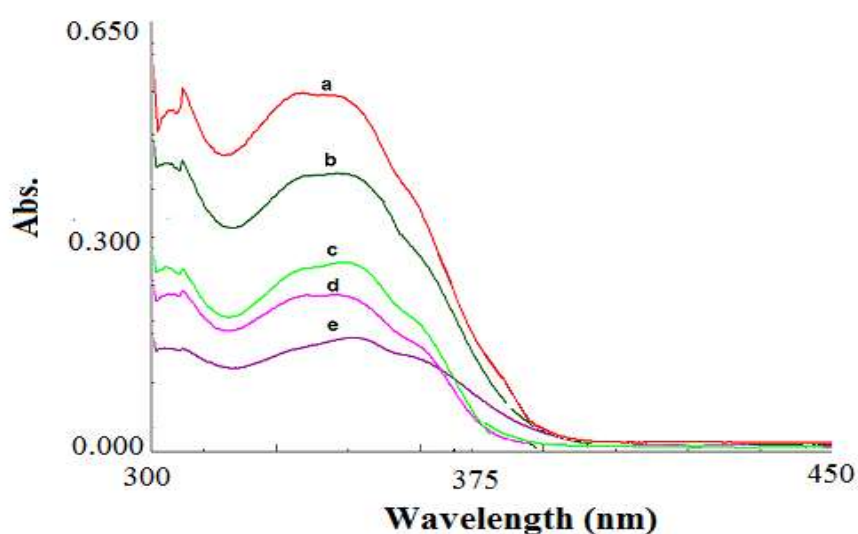


Figure 5.2 Absorption spectra of the ODC -3 dye ( $10^{-5}$  M dye or 2 mM dye/kg polymer). (a) THF, (b) DMF, (c) Toluene: EtOH, (d) DCM, (e) Toluene.

Table 5.1 UV-Vis spectra related data of ODC -3 in the solvents of EtOH, DCM, THF, Toluene, Toluene/ Ethanol mixture (80:20) and DMF.

Compound	Solvent/Matrix	$\lambda^1_{\text{abs}}$	$\lambda^2_{\text{abs}}$	$\epsilon_{\text{max}}(\lambda^1_{\text{abs}})$	$\epsilon_{\text{max}}(\lambda^2_{\text{abs}})$
ODC-3	EtOH	--	--	--	--
	DCM	--	340	--	26400
	THF	--	335	--	51100
	To: EtOH	244	360	36600	28900
	DMF	--	338	--	36500
	Toluene	--	338	--	21700

Molar extinction coefficient ( $\epsilon_{\max}$ ) of ODC-3 was increased in EC with respect to ( $\epsilon_{\max}$ ) of ODC-3 in solution phase (See Table 5.2). These data can be taken as proofs that ODC-3 molecules absorb better in plasticized EC matrices. The excitation-emission spectra and the related data of the ODC-3 are shown in Figure 5.3 and Table 5.2.

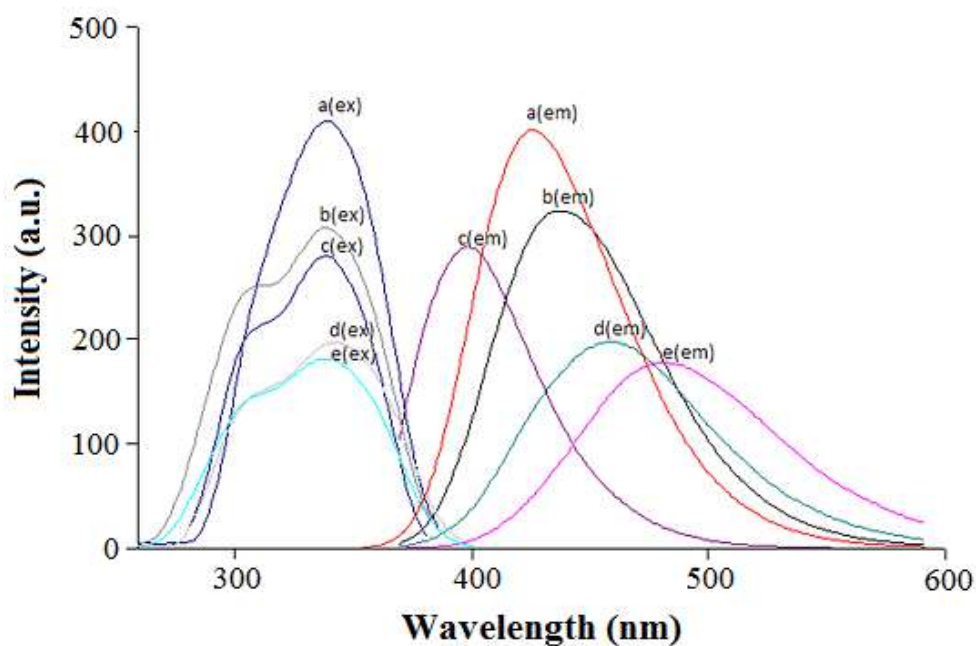


Figure 5.3 Excitation and corrected emission spectra of the ODC -3 dye ( $10^{-5}$ M dye or 2 mM dye/kg polymer). (a)THF, (b) DCM, (c) Toluene, (d) To: EtOH, (e) DMF.

Figure 5.3 reveals excitation and corrected emission spectra of the ODC -3 dye in different solvents with varying polarity. As expected, from non-polar toluene to polar DMF, the emission maxima of the dye exhibited a significant red shift from 397 to 483 nm. In all of the exploited moieties, the dye exhibited high Stoke's shift values extending from 60 to 146 nm. When doped in solid matrix EC, the observed Stoke's shift was 85 nm.

Quantum yield values were calculated according to procedure mentioned in the prior chapter and were found to be 0.39 and 1.12 for THF and EC moieties. It should be remembered that the quantum yield values were calculated with respect to quinine sulphate, which has a quantum yield of 0.47. The calculated quantum yield of 1.12 in

EC indicates bright fluorescence efficiency of the dye in the employed matrix (See Figure 5.4).

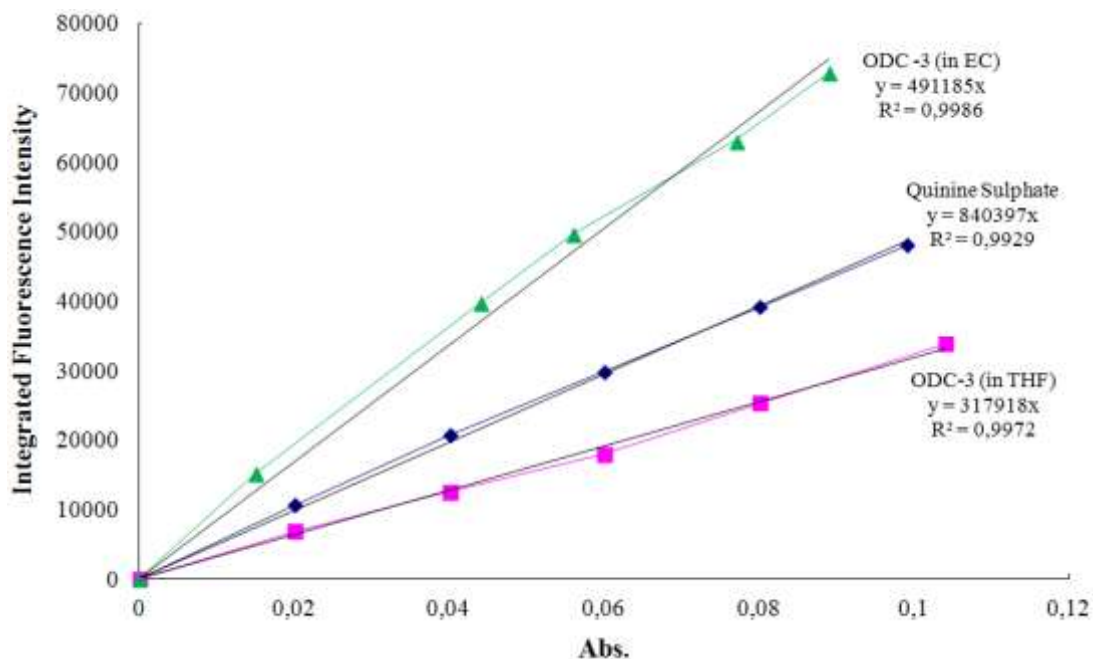


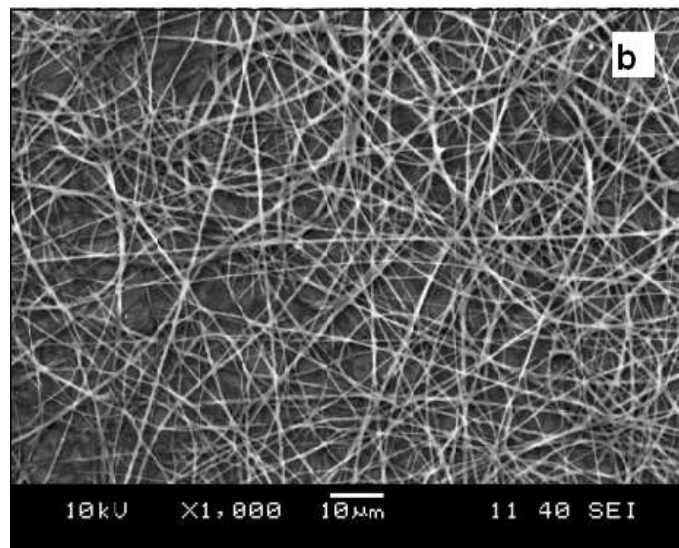
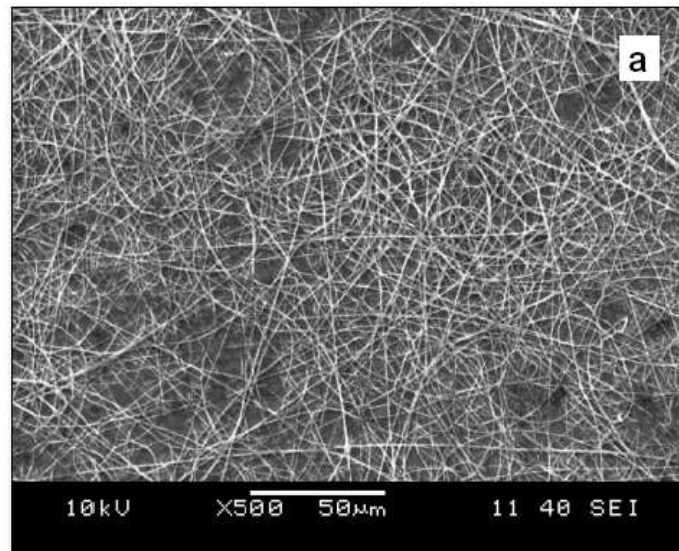
Figure 5.4 The integrated fluorescence intensities vs absorbance values of Quinine Sulphate in  $H_2SO_4$ , ODC-3 dye in EC and ODC-3 dye in THF.

Table 5.2 Emission and excitation spectra related data of ODC-3 in the solvents of EtOH, DCM, THF, Toluene, Toluene/Ethanol mixture (80:20), DMF and in solid matrix of EC.

Compound	Matrix	$\lambda_{max}^{em}$	$\lambda_{max}^{ex}$	$\Delta\lambda_{ST}$ (Stoke's shift)	$\phi_F$ (Quantum yield)
ODC -3	EtOH	--	--	--	0.39
	DCM	437	337	100	
	THF	425	338	87	
	To:EtOH	460	342	118	
	DMF	483	337	146	
	Toluene	397	337	60	
	EC	415	330	85	

### 5.2.2 SEM Images of Electrospun Membranes

The scanning electron microscope (SEM) images of an electrospun membrane are shown in Figure 5.5. The fiber shapes were as expected and bead-free, distribution was random and diameters were approximately in the range of 234 -361 nm.



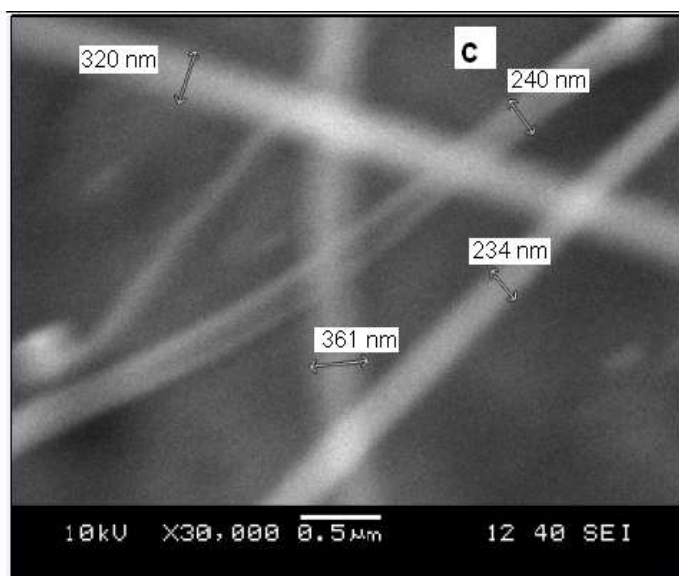


Figure 5.5 SEM images of EC based electrospun nanofibers (a), (b) and (c); EC based nanofibers at different magnifications such as  $\times 500$ ,  $\times 1000$  and  $\times 30\,000$ .

### 5.2.3 Effect of pH

The effect of pH on sensing ability of EC thin films was investigated between pH 4.0 and 10.0 exploiting acetic acid/acetate and phosphate buffer solutions (See Figure 5.6). We obtained the highest sensitivity to mercuric ions in acetic acid/acetate buffer and for further studies; this buffer was chosen as optimum working condition. During calibration studies, we used  $5 \times 10^{-3}$  M of acetic acid/acetate buffer solutions to avoid pH induced signal fluctuations. Distribution of the Hg (II) related chemical species in the working condition was also checked with chemical equilibrium software program (Visual MINTEQ) at pH 5.0 [ $\text{CH}_3\text{COO}^-$  (aq): 1%,  $\text{CH}_3\text{COOH}$  (aq): 99%,  $\text{Hg}(\text{OH})_2$  (aq): 31.3%,  $\text{Hg}^{2+}$  (aq): 50.1% and  $\text{Hg}(\text{OH})^+$  (aq): 18.6%]. Looking at the  $I_0/I$  parameters (2.89 and 2.37), the fluorophore dye was found to be responsive to both, Hg(I) and Hg (II) in buffered solutions at pH 5.0. Therefore, the mercuric ions should be in the highest oxidation state (Hg (II)) during analysis. Due to the solubility considerations, an acetic acid/acetate buffered solution of pH 5.0 was used for further studies.



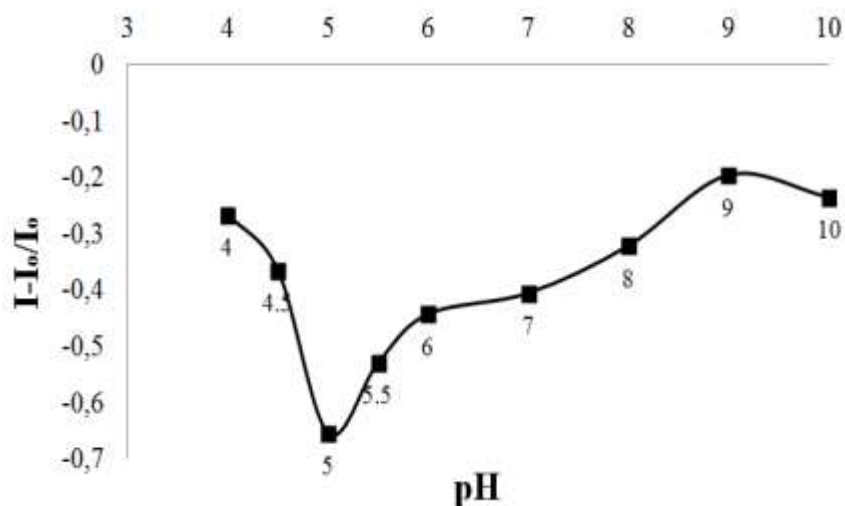


Figure 5.6 The pH dependency of ODC-3 dye in presence of Hg (II) ions between pH 4.0-10.0 using the EC based thin films.

#### 5.2.4 Response to Hg (II) Ions

When doped into modified EC matrices along with the anionic additive; potassium tetrakis-(4-chlorophenyl) borate; the ODC-3 dye becomes a Hg (II) selective probe. Because of the ion-exchange mechanism, in this system, Hg (II) ions are selectively extracted into the electrospun fibers or optode membrane by the anionic additive meanwhile potassium ions diffuse from the membrane into solution. The following ion-exchange pathway shown in Equation 5.1 can explain physical aspect of the response mechanism of ODC-3 dye.

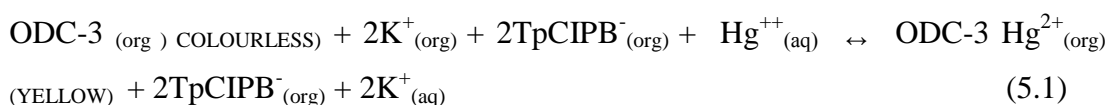


Figure 5.7 and Figure 5.8 shows the change in fluorescence spectra of thin film and electrospun materials as a function of different concentrations of Hg-(II) ions. Thin film and electrospun materials exhibited similar spectral response to Hg (II). On addition of Hg-(II) ions, the intensity of the signal of the emission spectra at 418 nm decreased whereas that at 505 nm increased both in thin film and nanofiber structures. The emission spectra had an isobestic point at 485 nm allowing ratiometric measurements (See Figure 5.7 and 5.8). Insets of Figure 5.7 and 5.8 show

linearized calibration plots of the optodes. The calibration curves were plotted exploiting the algorithm  $[(I_0-I)/I_0]$  for y-axis where  $I_0$  and  $I$  are the intensities of fluorescence in the absence and in the presence of the quencher, respectively.

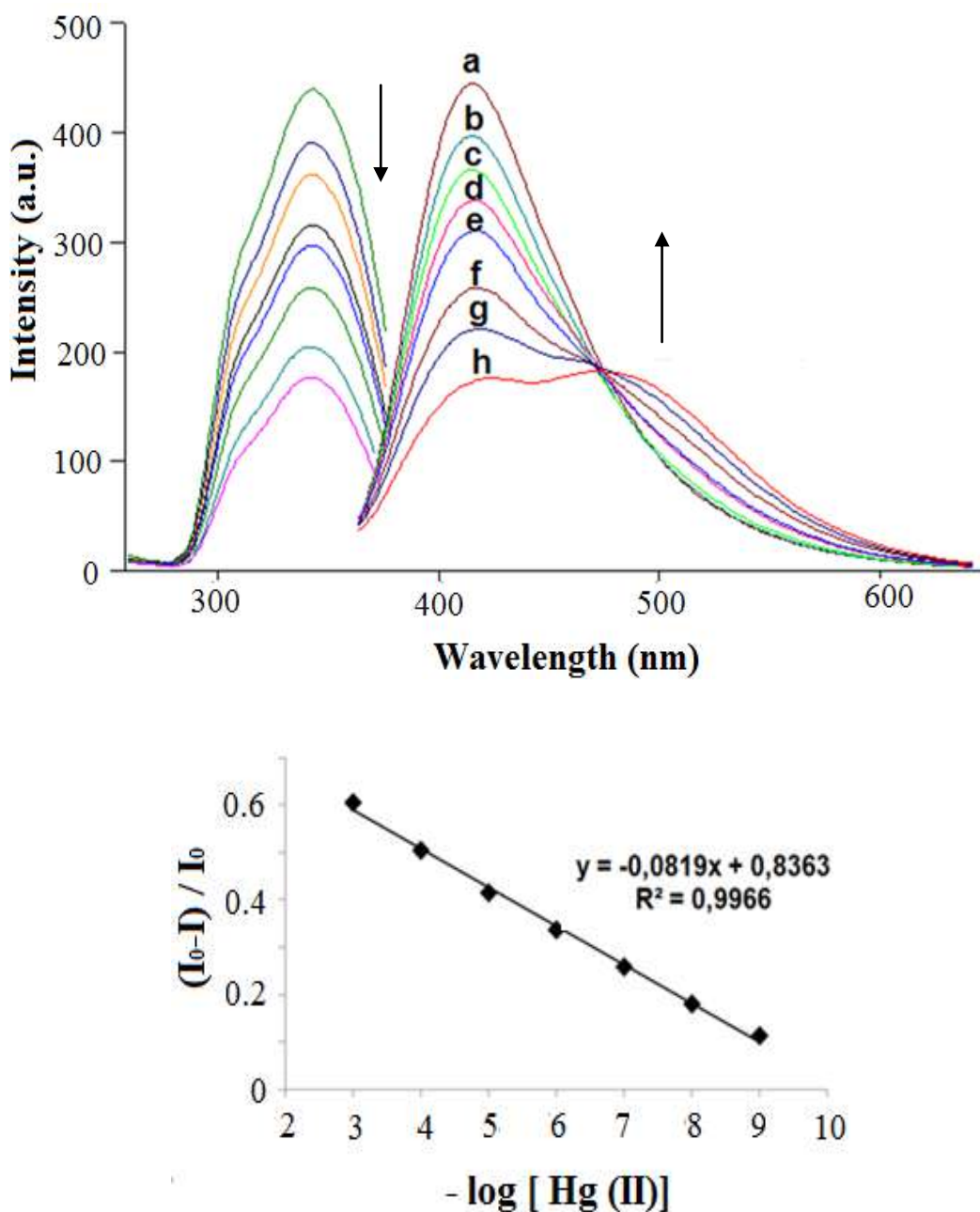


Figure 5.7 Fluorescence response of the EC based thin film to Hg (II) ions at pH 5.0. (a) Hg-free buffer, (b)  $10^{-9}$  M Hg (II), (c)  $10^{-8}$ , (d)  $10^{-7}$ , (e)  $10^{-6}$ , (f)  $10^{-5}$ , (g)  $10^{-4}$ , (h)  $10^{-3}$  M Hg (II), and linearized calibration plot for the concentration range of  $10^{-9}$ - $10^{-3}$  M Hg (II).

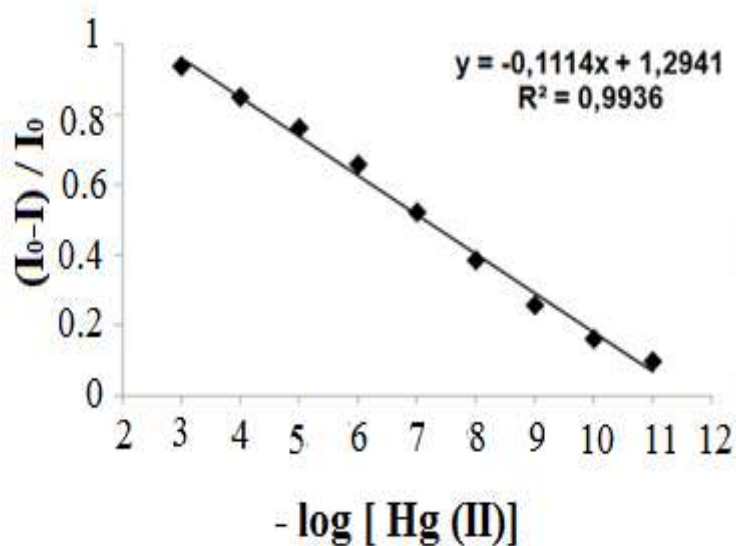
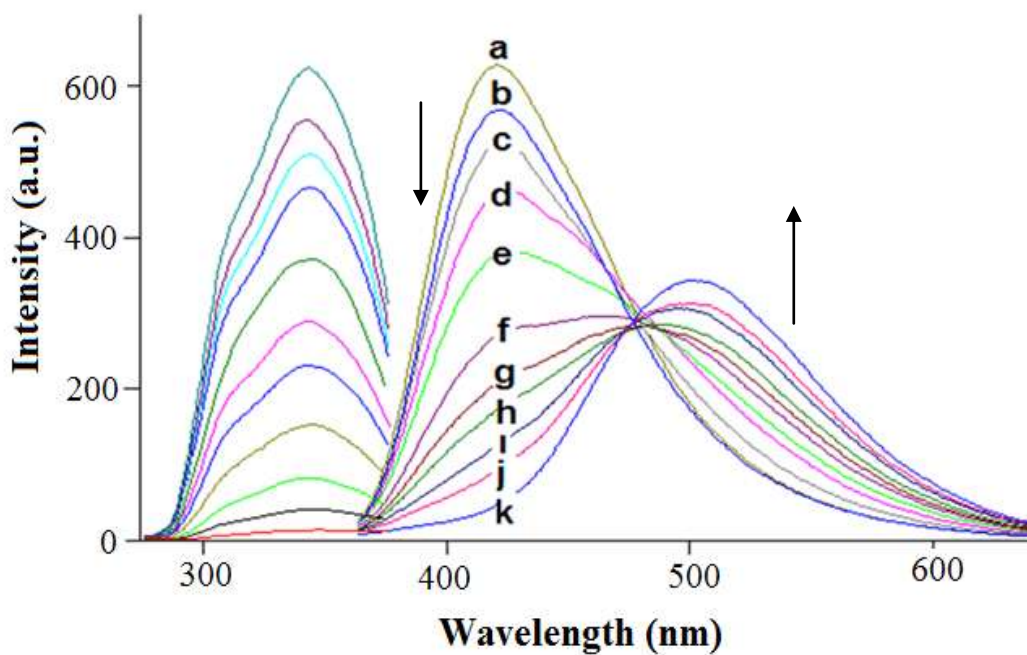


Figure 5.8 Fluorescence response of the EC based nanofibers to Hg (II) ions at pH 5.0. (a) Hg-free buffer, (b)  $10^{-11}$  M Hg (II), (c)  $10^{-10}$ , (d)  $10^{-9}$ , (e)  $10^{-8}$ , (f)  $10^{-7}$ , (g)  $10^{-6}$ , (h)  $10^{-5}$ , (i)  $10^{-4}$ , (j)  $10^{-3}$ , (k)  $10^{-2}$  M Hg (II), and linearized calibration plot for the concentration range of  $10^{-11}$ - $10^{-3}$  M Hg (II).

Due to the applied algorithm, good straight lines over the dynamic working range were obtained. The linearized calibration plots described by the equations,  $y = -0.0819x + 0.8363$  ( $R^2 = 0.9966$ ) and  $y = -0.1114x + 1.2941$  ( $R^2 = 0.9936$ ) for thin film and nanofiber forms, yielded quite good  $R^2$  values. The nanofibers exhibited

distinctly better relative signal change, working range and LOD values with respect to the thin films. The detection limits (LOD) were calculated exploiting concentration of the metal ion giving a signal equal to average of the blank signal ( $n = 20$ ) plus three standard deviation and were found to be  $1.70 \times 10^{-15}$  M and  $1.90 \times 10^{-13}$  M for electrospun nanofiber and continuous thin films, respectively. The attained LOD values exploiting nano-materials for the offered design is an evident of the enhanced sensitivity (See Table 5.3).

Table 5.3 gives a comparison of performance characteristics of thin film and nanofibers made up of same material in terms of working range, LOD, relative signal change and linearity.

Table 5.3 Calibration related characteristics of ODC-3 doped EC based electrospun nanofibers and thin films for Hg (II) ions.

Indicator Dye	Matrix /Form	Linear Range (Hg(II) Mol/L)	Regression Coefficient ( $R^2$ )	LOD (Molar)	% Relative Signal Changes
ODC-3	EC/ nanofiber	$1.0 \times 10^{-11}$ to $1.0 \times 10^{-3}$	0.9936	$1.70 \times 10^{-15}$	98.5
	EC / thin film	$1.0 \times 10^{-9}$ to $1.0 \times 10^{-3}$	0.9966	$1.90 \times 10^{-13}$	60

### 5.2.5 Stern-Volmer Analysis

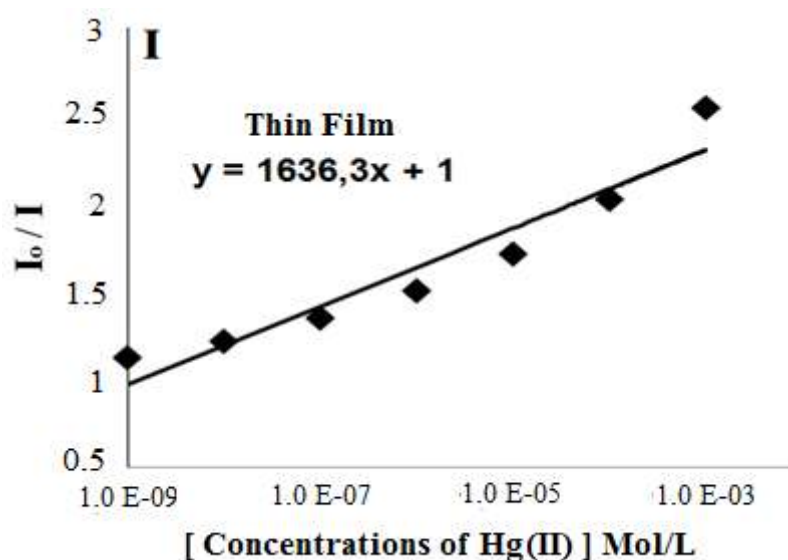
In a homogeneous medium, such as in solution or gas phase, the quantitative measure of fluorescence quenching is described by the Stern-Volmer constant,  $K_{sv}$ ,

$$(I_0/I) = 1 + K_{sv} [Q] \quad (5.2)$$

The Equation 5.2 reveals that  $I_0/I$  increases directly proportional to the concentration of the quencher. The higher the  $K_{sv}$  values mean enhanced sensitivity. In a heterogeneous medium, such as in polymer films or nano-structures a negative

deviation from the linear Stern-Volmer equation may occur at high quencher concentrations (Bacon, & Demas, 1987; Carraway, Demas, DeGraff, & Bacon, 1991; Wang, Drew, Lee, Senecal, Kumar, & Samuelson, 2002).

The data regarding results of the Stern-Volmer analysis for electrospun and continuous thin films were shown in Table 5.4. The electrospun nanofibers yielded an excellent Stern-Volmer relationship for quencher concentrations between  $1 \times 10^{-11}$ - $1 \times 10^{-6}$  M.  $K_{sv}$  value of the electrospun film, calculated from slope of the plot was found to be  $2.00 \times 10^6$  ( $M^{-1}$ ). This value is 1000 orders of magnitude greater than that obtained from the continuous thin film slides (See Table 5.4 and Figure 5.9).  $K_{sv}$  values reveal important practical consequences. The sensitivity of the quenching process can be enhanced by controlling the quencher diffusion rate to fluorophores via the nano-structural properties of the sensing materials.



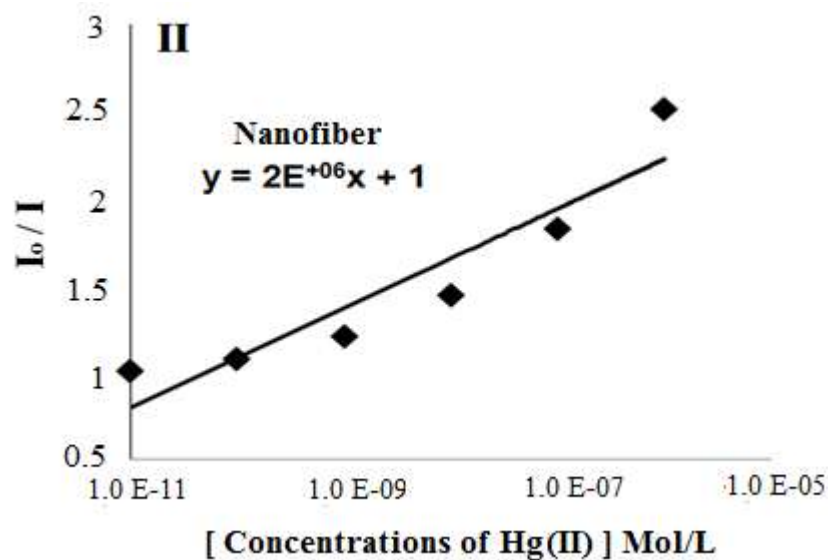


Figure 5.9 I: The Stern Volmer plots of EC based thin films, II: electrospun nanofibers in presence of the quencher.

Table 5.4  $K_{sv}$  Constant of EC based electrospun nanofibers and thin films for Hg(II) ions.

Indicator Dye	Matrix /Form	Linear Regression Equation (Hg(II) Mol/L)	$K_{sv}$ Constant
ODC-3	EC/ electrospun nanofiber	$y = 2E^{+06}x + 1$	$2.00 \times 10^6$
	EC / thin film	$y = 1636.3x + 1$	$1.60 \times 10^3$

### 5.2.6 Lifetime Analysis

Fluorescence lifetimes were recorded using a Time Correlated Single Photon Counting (TCSPC) system that was from Edinburgh Instruments (UK). The instrument was equipped with a 367 nm pulsed laser (pulse width: 79 picoseconds) as the excitation source. During measurements, the Instrument Response Function (IRF) was obtained from a non-fluorescing suspension of a colloidal silica (LUDOX 30 %, Sigma Aldrich) in water, held in 10 mm path length quartz cell and was considered to be wavelength independent. All lifetimes were fit to a  $\chi^2$  value of less than 1.1 and with residuals trace symmetrically distributed around the zero axes. In this work, the exploited dye excited at 367 nm with a picoseconds pulsed laser and intensity decay data accusation was performed at 415 nm. Excited state lifetimes of

the fluorophore were recorded in THF and in embedded form, in the absence and presence of the ionic mercury. The intensity decrease is known to be due to the quenching of the dye by Hg (II) ions. In many instances, the fluorophore can be quenched both by collisions and by complex formation. The intensity based data (Stern-Volmer plot), lifetime measurements and changes in the absorption integral upon exposure to mercuric ions, when evaluated all together, can be informative in the explanation of the mechanism of quenching. In case of dynamic quenching, because of the collisions between the quencher and the fluorophore, the excited state lifetime would be affected in direction of decrease. On the other hand, pure static quenching will not reduce the excited state lifetime of the fluorophore. Table 5.5 reveals the excited state lifetimes of the fluorophore recorded in THF and in embedded form, in the absence and presence of the quencher. The ODC-3 dye yielded mono exponential, bi exponential and three exponential lifetimes in solution, thin film and nanofiber forms respectively. In solution phase measurements, there is no dramatic change in excited state lifetimes neither in the absence nor in presence of the Hg (II) ions. In THF, the decay times were changed from 2.90 to 2.77 ns, in absence and presence of the quencher. However, in solid-state measurements, upon exposure to Hg (II) ions the excited state lifetimes exhibited slight differences, which can be attributed to the dynamic component of the quenching.

Table 5.5 Florescence lifetimes of the carbazole derivative in THF, EC based thin films and electrospun nanofibers in the presence and absence of the quencher.

ODC - 3		Solvent		Thin Film		Nanofiber	
		Value (ns)	% Relative	Value (ns)	% Relative	Value (ns)	% Relative
Metal Free	$\tau_1$	2.90	100	1.05	58.36	0.07	22.41
	$\tau_2$	--	--	3.30	41.64	1.22	55.41
	$\tau_3$	--	--	--	--	4.65	22.18
		Value (ns)	% Relative	Value (ns)	% Relative	Value (ns)	% Relative
Hg(II)	$\tau_1$	0.20	7.08	0.57	66.55	0.60	33.55
	$\tau_2$	2.77	92.92	2.86	33.45	1.88	49.96
	$\tau_3$	--	--	--	--	6.88	16.49



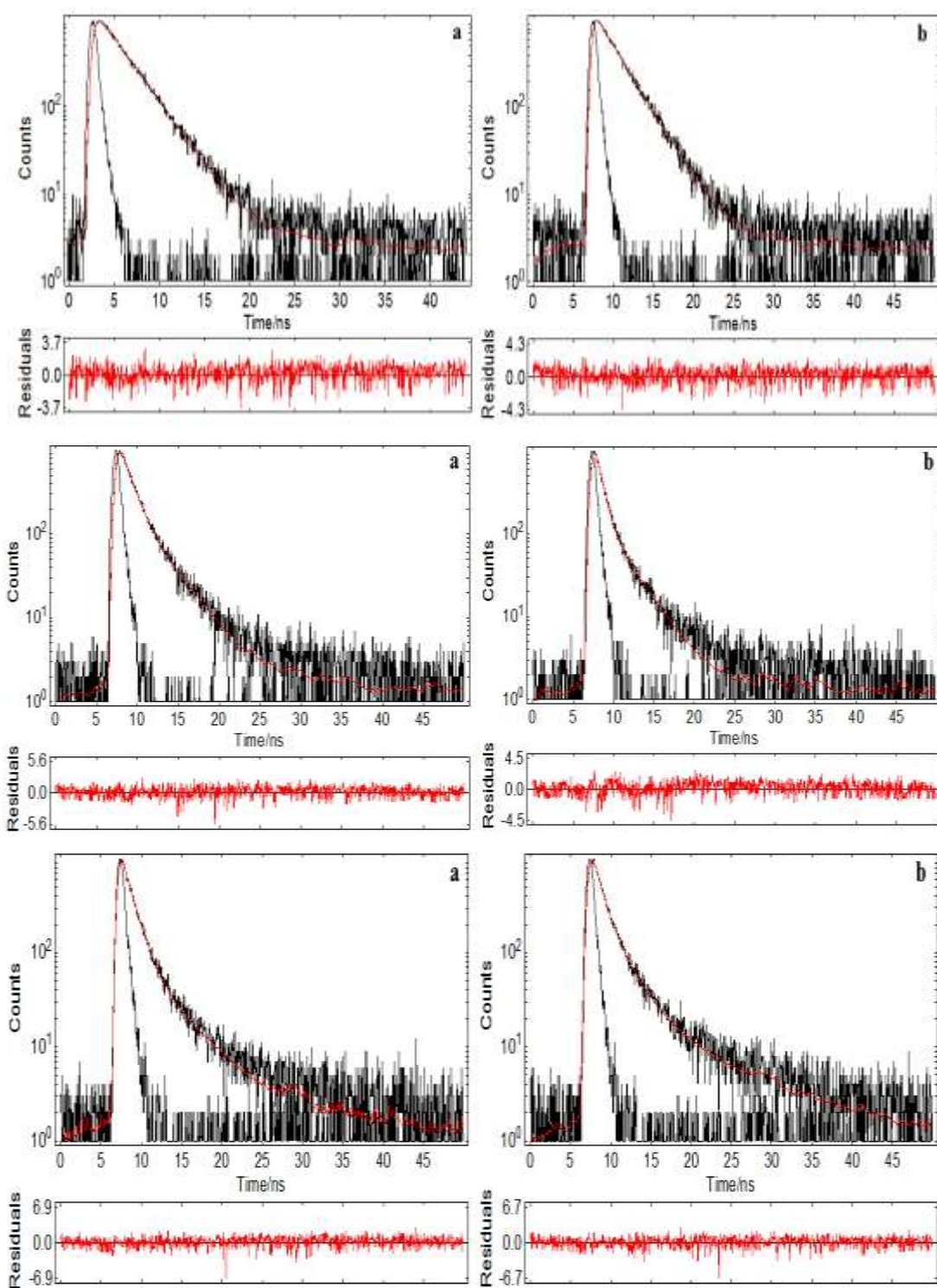


Figure 5.10 Decay curves of the exploited dye in THF, in thin film form and in form of nanofiber, respectively. In all cases a and b shows quencher free and quencher containing decay profiles. The dye excited at 367 nm with a picoseconds pulsed laser and intensity decay data acquisition was performed at 415 nm.



In case of dynamic quenching because the collisions between the quencher and the fluorophore, only the excited state of the fluorophore is disturbed, no changes in the absorption or excitation spectrum are expected. On the contrary, the formation of ground-state complex in static quenching will perturb the absorption spectra of the fluorophore. Thus, by careful examination of the absorption or excitation spectrum, one can attempt to distinguish static and dynamic quenching (Wang, Wang, Moses, & Heeger, 2001).

Figure 5.11 shows the absorption spectra of the ODC-3 dye in absence and presence of the quencher. The discernible change in the absorption integral may be an evidence of formation of ground a state complex. However, probably the complex between ODC-3 and mercuric ions is not strong enough and the association constant is around  $1.0 \times 10^7 \text{ M}^{-1}$ . As a result, in our case combined quenching, by collisions and by complex formation with the Hg (II) ions is observed.

Variation of emission spectra and accompanying discernible color change of the dye from colorless to yellow may be an evidence of complex formation with Hg (II) ions.

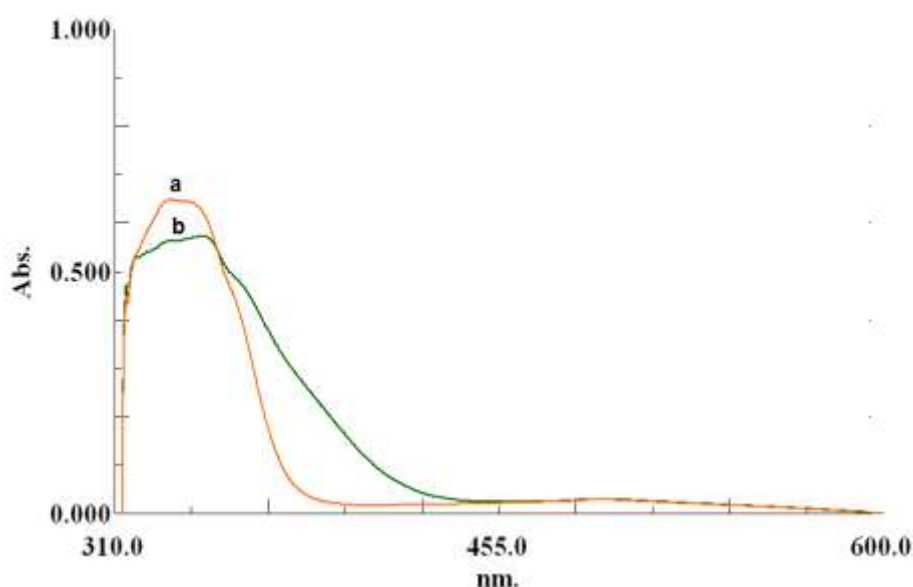


Figure 5.11 Absorption spectra of the fluoroionophore (a) in the absence, and (b) in presence of the quencher; Hg (II).

The intensity based data ( $I_0/I$ ) exhibiting an upward-concave curvature toward the y-axis is the evidence of combined quenching both by collisions (dynamic quenching) and by complex formation (static quenching) with the same quencher (Lakowicz, 2006). The non-linearized data observed in Figure 5.9 exhibits a slightly upward-concave curvature characteristic that can be concluded as an evidence of combined quenching.

### ***5.2.7 Selectivity Studies***

In order to test the response of the dye to possible interfering cations, the ODC-3 dye was treated with  $10^{-3}$  M concentrations of  $\text{Hg}^{2+}$  and  $\text{Hg}^+$ ,  $\text{Al}^{3+}$ ,  $\text{Ag}^+$ ,  $\text{Ca}^{2+}$ ,  $\text{Co}^{2+}$ ,  $\text{Cr}^{3+}$ ,  $\text{Cu}^{2+}$ ,  $\text{Fe}^{3+}$ ,  $\text{Fe}^{2+}$ ,  $\text{Li}^+$ ,  $\text{K}^+$ ,  $\text{Mn}^{2+}$ ,  $\text{Mg}^{2+}$ ,  $\text{Na}^+$ ,  $\text{NH}_4^+$ ,  $\text{Ni}^{2+}$ ,  $\text{Pb}^{2+}$  and  $\text{Zn}^{2+}$  ions in acetic acid/acetate buffer solutions at pH 5.0. The ODC-3 dye did not response to the major cations of both water and groundwater samples ( $\text{Ca}^{2+}$ ,  $\text{Mg}^{2+}$ ,  $\text{Na}^+$  and  $\text{K}^+$ ) and physiologically relevant fluids. However, when exposed to considerably high concentrations of Fe (III), the dye exhibited an emission based response to these ions at a single wavelength; 418 nm. As mentioned earlier, differently from this response, on addition of Hg (II) ions, the intensity of the signal at 418 nm decreased whereas that at 505 nm increased both in thin film and nanofiber structures. We also tested interference effects of the conventional anions of  $\text{F}^-$ ,  $\text{Cl}^-$ ,  $\text{Br}^-$ ,  $\text{NO}_3^-$ ,  $\text{SO}_4^{2-}$  and  $\text{PO}_4^{3-}$ . Relative signal changes of approximately 5 % were observed for EC doped films. The relative signal intensity changes caused by the tested potential interferent cations were shown in Figure 5.12 (I) and (II).

The fluorescence was dramatically decreased in the presence of mercuric ions exhibiting a relative signal change ratio of 98.5 %. From following figures it can be concluded that, the sensing design is capable of determining Hg (II) ions with a high selectivity over other ion except that of Fe (III). In a recent work of Lu and co-workers (2009), 1mM of sodium citrate was used to form a stable complex with Fe (III) and the Fe (III) ions successfully masked. The presence of citrate at this concentration did not affect the detection of Hg (II). A similar approach has been adapted to this work for masking of Fe (III).

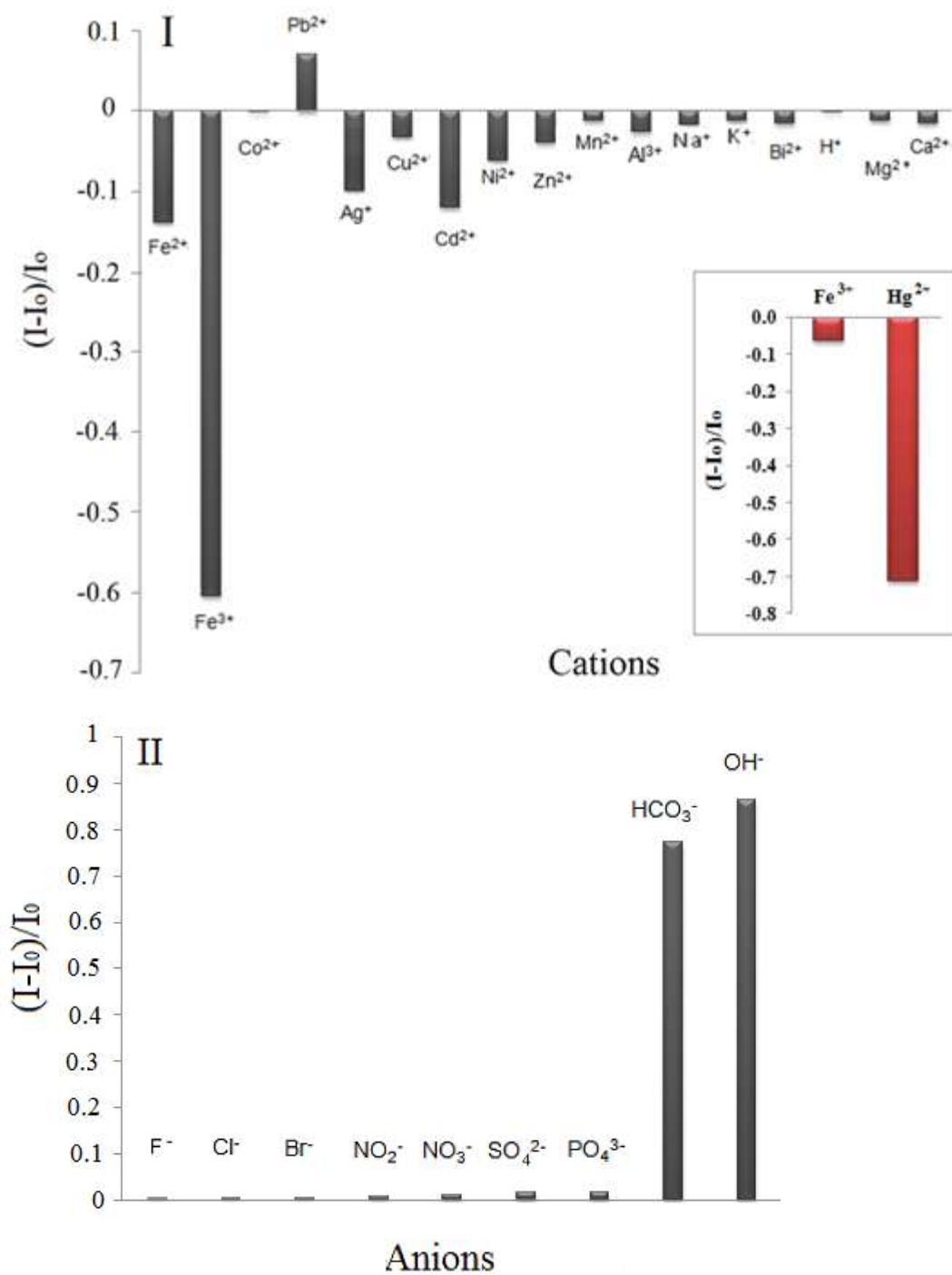


Figure 5.12 I: Metal-ion response of mercury sensitive ODC-3 at pH 5.0. Inset: Response to Hg (II) ions when Fe (III) suppressed with masking agent; citrate. II: Response to the anions of the same composition at near neutral pH. Results were plotted as relative fluorescence changes;  $(I-I_0)/I_0$ .

### ***5.2.8 Recovery and Regeneration Studies with Real Groundwater Samples***

The applicability of the sensing system for real samples was tested for the mineral water of Sarikiz (Sarikiz, Manisa; Turkey; Latitude: 38° 44' 83 N, Longitude: 28° 04' 84 E). The temperature of water from well was remarkably constant and 16.9 °C. The content of Hg (II) in the diluted certified reference material of Merck (SRM from NIST Hg (NO<sub>3</sub>)<sub>2</sub> in HNO<sub>3</sub> 0.5 mol L<sup>-1</sup> 1000 mg L<sup>-1</sup> Hg CertiPUR®) was determined by exploiting the electrospun nanofibers. All mineral water samples were collected in polyethylene vials, degassed using ultrasonic bath and analyzed as soon as possible after sampling. The recovery experiments were carried out adding 1×10<sup>-8</sup>M of certified reference material into the mineral water. The average concentration of the Hg (II) was found to be 3.01×10<sup>-8</sup> M for 10 replicate measurements. The recovery performance was found to be 103 ± 3.1%. These results reveal the capability of the offered sensing design for the determination of mercury ions in real samples without considerable error. Only Fe (III), HCO<sub>3</sub><sup>-</sup> and OH<sup>-</sup> look like potential interferents for real groundwater samples. The OH<sup>-</sup> and HCO<sub>3</sub><sup>-</sup> can be neutralized adjusting the pH. Fe (III) can be suppressed using citrate as explained earlier.

### ***5.2.9 Conclusion***

Electrospinning looks like a promising, simple, and an effective method for fabricating nanomaterials. On the other hand such kind of materials should be coupled with optical chemical sensor devices. With respect to continuous thin films, electrospun fibers can offer enhanced sensitivity and reactivity in sensing applications. In this work, we performed coupling of electrospun nanomaterials with fluorescence based measurement techniques without scattering and other side effects. We performed to measure the Hg (II) concentrations as low as 10<sup>-11</sup> M exploiting nanofibrous materials. Our sensing approach resulted with large linear working ranges extending to 10<sup>-11</sup>–10<sup>-3</sup> mol L<sup>-1</sup> Hg (II). To our knowledge, these are the largest reported working ranges and best LOD values among similar emission based sensing methods. Further efforts will focus on exploring new sensing materials and polymer compositions, controlling the nanoscale size of the electrospun membranes, and optimizing the sensitivities for the detection of a variety of analytes.

### 5.3 Sensing of Hg (II) Ions with Embedded Carbazole Derivative

In this part of the thesis, the emission based performance of the carbazole derivative, 2-(9-hexyl-9H-carbazol-3-yl)-5-(pyridin-4-yl)-1,3,4-oxadiazole (ODC-5) was tested for measurement of different cations and anions and then combined with fiber optic systems that allow determination of sub-nanomolar levels of Hg (II) ions. The exploited dye is very similar to the ODC-3 dye in terms of solubility, spectral efficiency and selectivity to metal cations.

The ODC-5 dye looks like more lipophilic than that of the ODC-3 due to the hexyl moiety on pyrrol ring. Spectral characteristics were also similar to each other with spectral shifts of 5- 10 nm in absorption and emission maxima. Ethyl cellulose was used as polymeric support materials to produce nanofibrous and continuous thin films. We fabricated the novel optical chemical nanosensors using electrospinning technique. Emission based spectral data, fluorescence lifetime and photo stability of the sensing agents was determined in thin film, nanofibrous materials and/or in THF, respectively. The dye exhibited strong absorbance, high quantum yield, large Stoke's shift and excellent photo stability. The electrospun nano-fibers have been characterized using scanning electron microscopy (SEM) and their average diameters were assessed. The schematic structure of the employed molecule ODC-5 was shown in Figure 5.13.

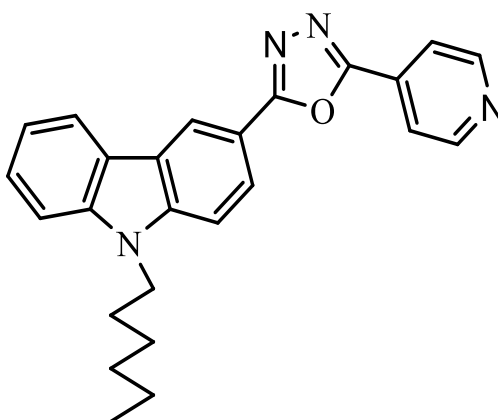


Figure 5.13 Schematic structures of the mercury sensitive fluoroionophore;2-(9-hexyl-9Hcarbazol -3-yl)-5-(pyridin-4-yl)-1,3,4-oxadiazole (ODC-5)

### 5.3.1 The Photophysical Properties and Quantum Yield Calculations of the Indicator Dye

The absorption excitation and corrected emission spectra were recorded in the solvents of EtOH, DCM, THF and toluene/ethanol (To: EtOH; 80:20) mixture and Toluene (See Figure 5.14 and 5.15). The UV-Vis spectroscopy related data (absorption maxima;  $\lambda_{Abs}$ , and molar extinction coefficient; ( $\epsilon$ ), were shown in Table 5.6 and 5.7. ODC-5 exhibited very efficient absorbance and high molar extinction coefficients around 340 nm in solution phase. The quantum yield, molar extinction coefficients and Stock's shift values were also calculated.

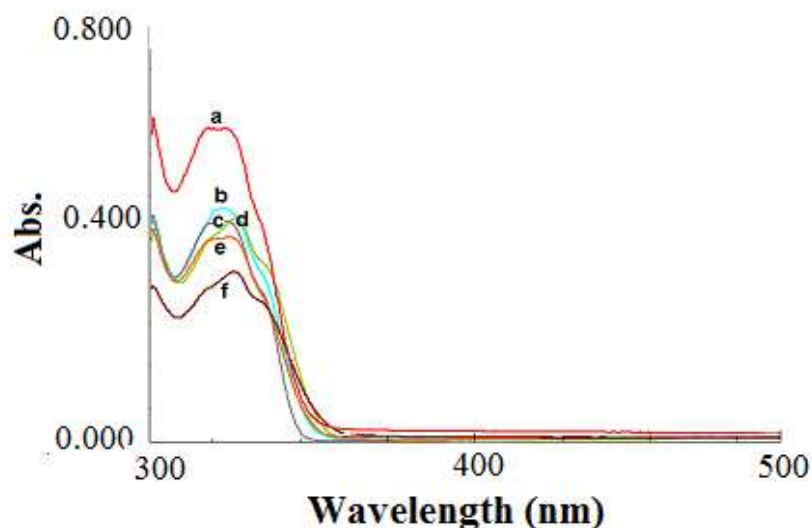


Figure 5.14 Absorption spectra of the ODC -5 dye ( $10^{-5}$  M dye or 2 mM dye/kg polymer). (a) THF, (b) DCM, (c) Toluene: EtOH, (d) Toluene, (e) DMF, (f) EtOH.

Table 5.6 UV-Vis spectra related data of ODC -5 in the solvents of EtOH, DCM, THF, Toluene/Ethanol mixture (80:20), DMF and Toluene.

Compound	Solvent/Matrix	$\lambda_{abs}^1$	$\epsilon_{max}(\lambda_{abs}^1)$
ODC-5	EtOH	345	32600
	DCM	344	44400
	THF	338	60000
	To: EtOH	345	43000
	DMF	338	40000
	Toluene	340	42200

The ODC-5 dye exhibited absorption maxima around 345 nm in most of the solvents. The molar extinction coefficient of 60000 was reported in THF. This can be attributed to the effective absorption behavior of the dye when dissolved in THF.

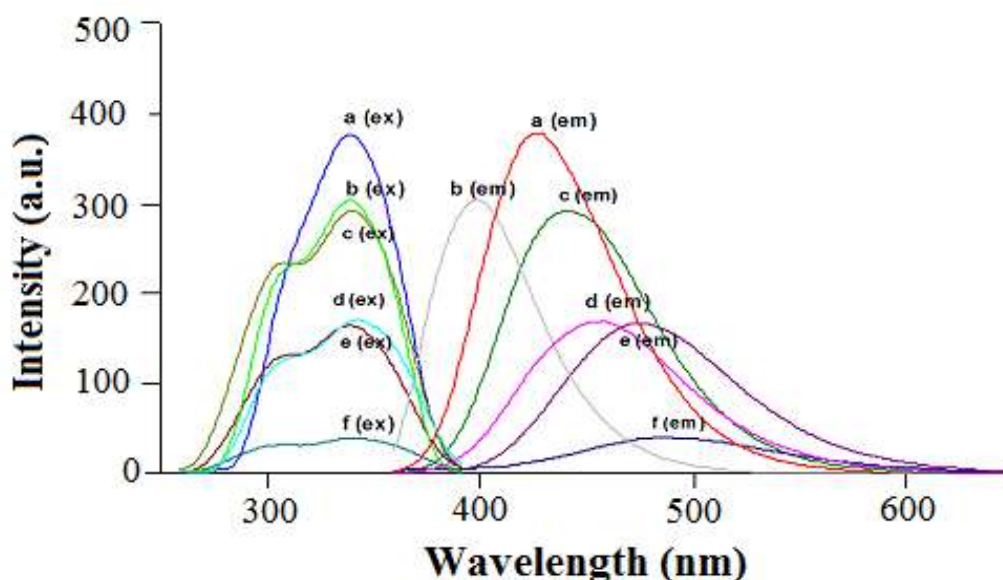


Figure 5.15 Excitation and corrected emission spectra of the ODC-5 dye ( $10^{-5}$  M dye or 2 mM dye/kg polymer). (a)THF, (b) Toluene, (c) DCM, (d) To: EtOH, (e) DMF, (f) EtOH.

Figure 5.15 shows excitation and corrected emission spectra of the ODC-5 dye in different solvents. The dye exhibited a distinct red shift from Toluene to EtOH in the emission maxima, which can be attributed to the differences of solvent polarity. The highest Stoke's shift was observed in the polar solvent, EtOH. Contrary the lowest value observed in Toluene. When immobilized in EC, the dye exhibited similar spectral behavior as observed in THF. This result can be concluded as an evidence of compatibility of EC matrix for further spectral studies.

Quantum yield values were calculated according to procedure mentioned in the prior chapter and were found to be 0.72 and 1.01 for THF and EC moieties (See Figure 5.16). It should be remembered that the quantum yield values were calculated with respect to quinine sulphate, which has a quantum yield of 0.47. The calculated quantum yield of 1.01 in EC indicates bright fluorescence efficiency of the dye in the employed matrix. The calculated quantum yield values are better than the  $\Phi_F$  values

calculated for ODC-5. This enhancement in the quantum yield can be attributed to the presence of electron releasing hexyl tail.

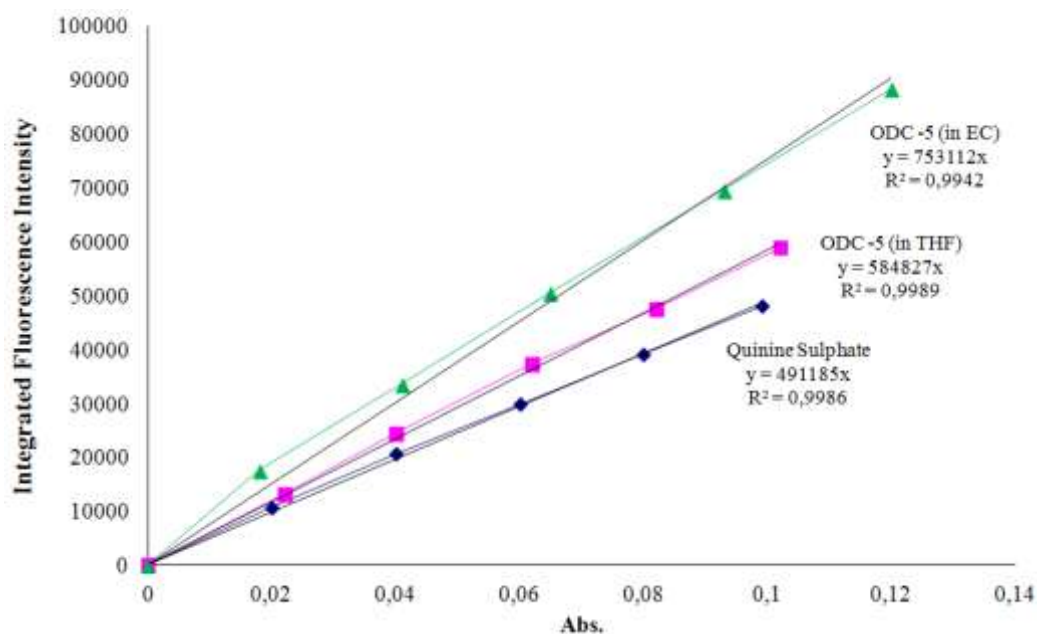


Figure 5.16 The integrated fluorescence intensities vs absorbance values of Quinine Sulphate in H<sub>2</sub>SO<sub>4</sub>, ODC-5 dye in EC and ODC-5 dye in THF.

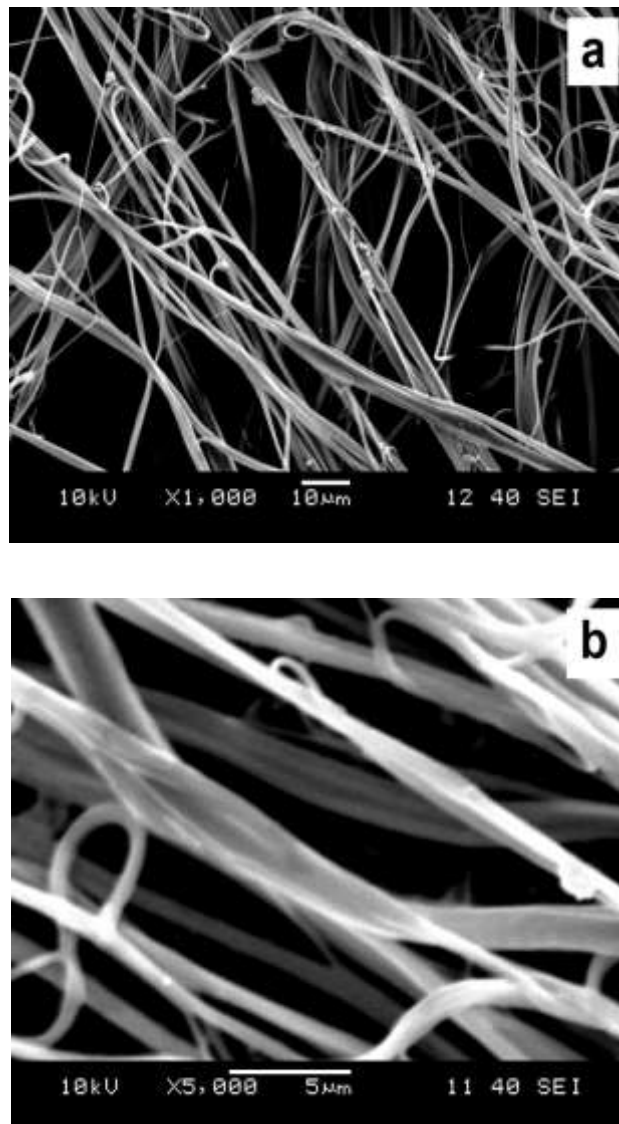
Table 5.7 Emission and excitation spectra related data of ODC-5 in the solvents of EtOH, DCM, THF, Toluene, Toluene/ Ethanol mixture (80:20), DMF and in solid matrices of EC.

Compound	Matrix	$\lambda_{\max}^{em}$	$\lambda_{\max}^{ex}$	$\Delta\lambda_{ST}$ (Stoke's shift)	$\phi_F$ (Quantum yield)
ODC -5	EtOH	490	340	150	0.72
	DCM	440	340	100	
	THF	425	340	85	
	To:EtOH	455	340	115	1.01
	DMF	470	340	130	
	Toluene	400	340	60	
	EC	420	340	80	



### 5.3.2 SEM Images of Electrospun Membranes

The SEM images of EC based electrospun membranes at various magnifications are denoted in Figure 5.17. The membrane has a 3-D structure with a random fiber orientation that is evenly distributed on the substrate. It can be seen from Figure 5.17 that the diameters of the fibers were between 588 and 799 nm.



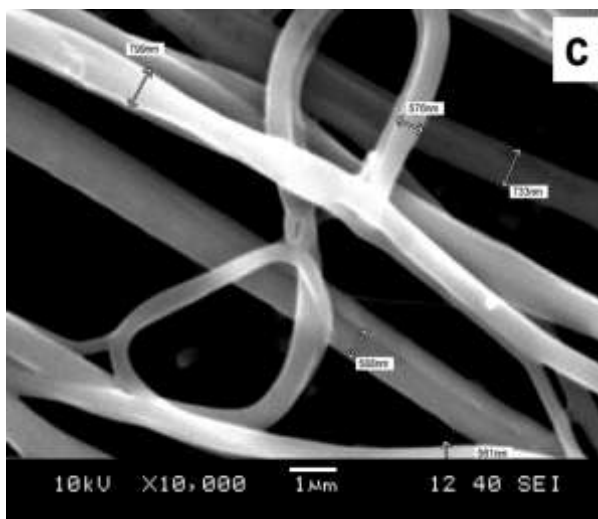


Figure 5.17 SEM images of EC based electrospun nanofibers (a), (b) and (c); EC based nanofibers at different magnifications such as  $\times 1000$ ,  $\times 5000$  and  $\times 10\,000$ .

### 5.3.3 Dynamic Working Range and Hg (II) Response

When doped into plasticized EC together with the anionic additive; potassium tetrakis-(4-chlorophenyl) borate; the ODC-5 dye acts as a Hg (II) sensitive molecular probe. The dye also exhibits a similar spectral response for Fe (III) ions. Therefore, the Fe (III) ions should be considered as potential interferents and appropriate measures like masking should be taken for selective sensing of Hg (II). When Fe (III) ions removed, the Hg (II) ions can selectively be extracted into the optode membrane by the anionic additive meanwhile two potassium ions diffuse from the membrane. The ion-exchange equation (See Equation 5.3) can be shown by the following equation.

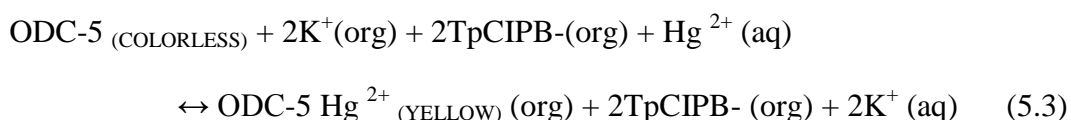


Figure 5.18 shows the absorption spectrum of the ODC-5 dye in the absence and presence of Hg (II) ions in THF. Although there is no a dramatic change in the absorption band, it is observed that the spectrum broadened to higher wavelength in the presence of mercury ions.

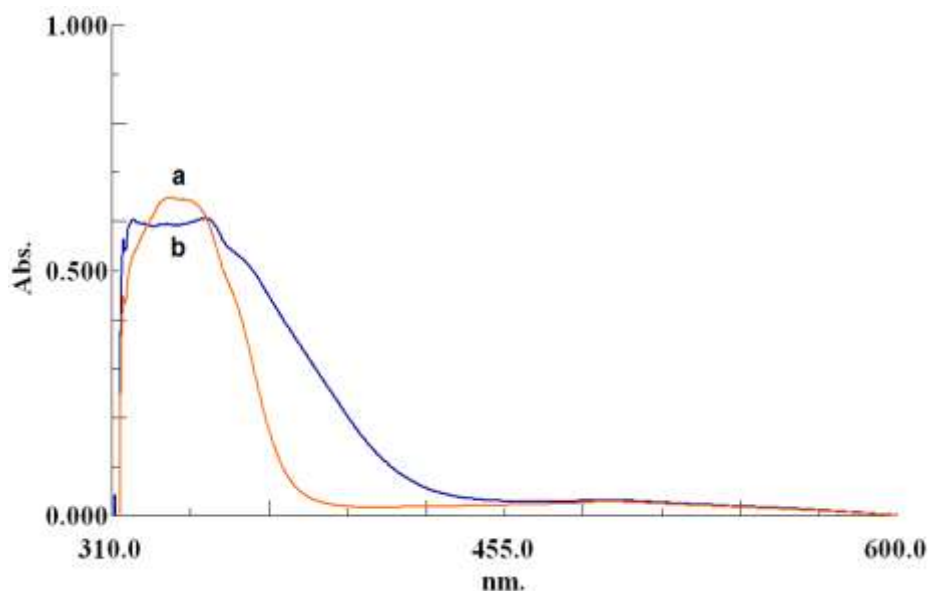


Figure 5.18 Absorption spectrum of the ODC-5 dye in THF (a) Hg (II) free, (b) in presence of  $5 \times 10^{-5}$  M Hg (II).

The effect of pH on sensing ability of EC thin films was investigated between pH 4.0 and 10.0 exploiting acetic acid/acetate and phosphate buffer solutions (See Figure 5.19). We obtained the highest sensitivity to mercuric ions in acetic acid/acetate buffer and for further studies; this buffer was chosen as optimum working condition. During calibration studies, we used  $5 \times 10^{-3}$  M of acetic acid/acetate buffer solutions to avoid pH induced signal fluctuations.

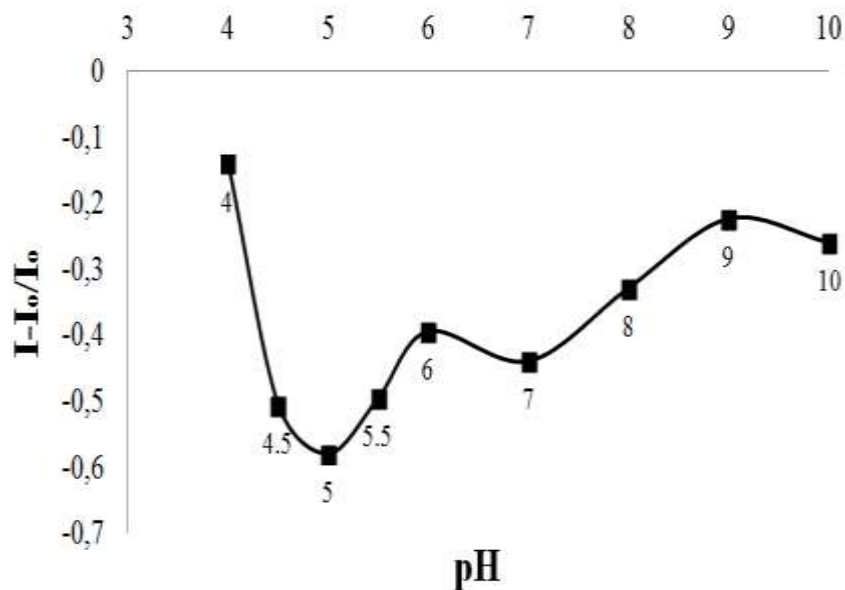


Figure 5.19 The pH dependency of ODC-5 dye in presence of Hg (II) ions between pH 4.0-10.0 using the EC based thin films.

Figure 5.20 and 5.21 shows the change in fluorescence spectra of thin film and electrospun materials as a function of different concentrations of Hg (II) ions. The ODC-5 doped thin films demonstrated a linear response over range of  $1 \times 10^{-9}$ - $1 \times 10^{-2}$  M for Hg (II) ions. Testing sensor compositions are demonstrated 47% relative signal change, excellent linearity, and good sensitivity to Hg (II) ions. The regression results yielded an absolute linear response with coefficients of regression ( $R^2$ ) of 0.9979 for EC thin films (See Table 5.8). The limit of detection (LOD) for Hg (II) was defined as the concentration at which the signal is equal to the blank signal ( $n = 20$ ) plus  $3\sigma$  and found to be  $1.90 \times 10^{-13}$  M for continuous thin films.

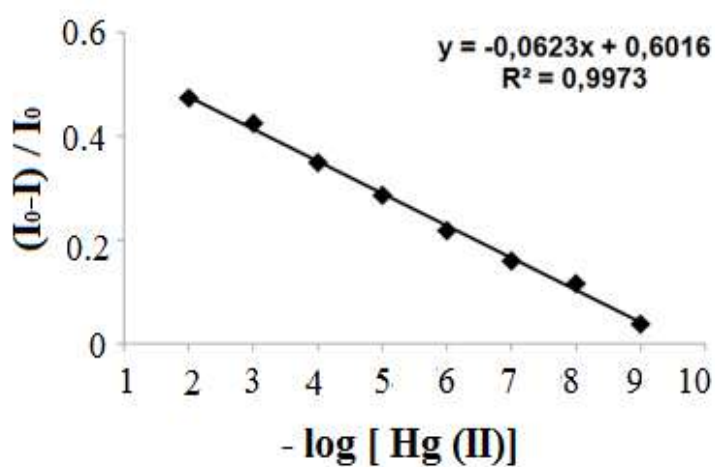
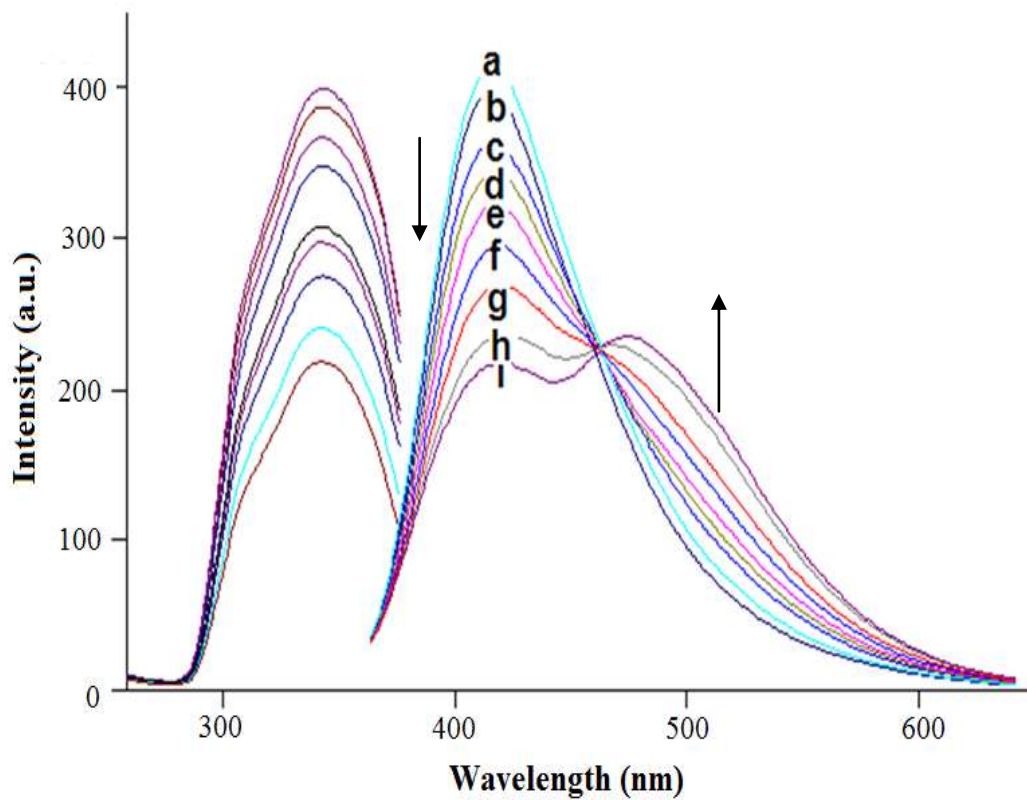


Figure 5.20 Fluorescence response of the ODC-5-doped EC based thin film to Hg (II) ions at pH 5.0. (a) Hg-free buffer (b)  $10^{-9}$  M, (c)  $10^{-8}$ , (d)  $10^{-7}$ , (e)  $10^{-6}$ , (f)  $10^{-5}$ , (g)  $10^{-4}$ , (h)  $10^{-3}$ , (i)  $10^{-2}$  mol/L Hg (II), and linearized calibration plot for the concentration range of  $10^{-9}$ - $10^{-2}$ M Hg (II).

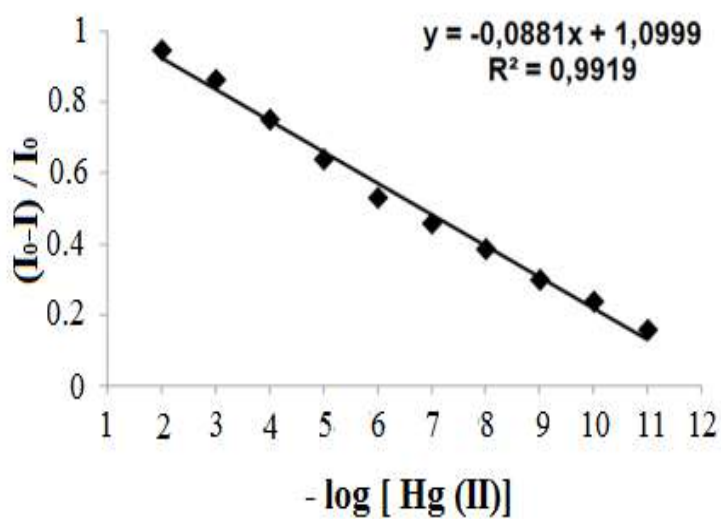
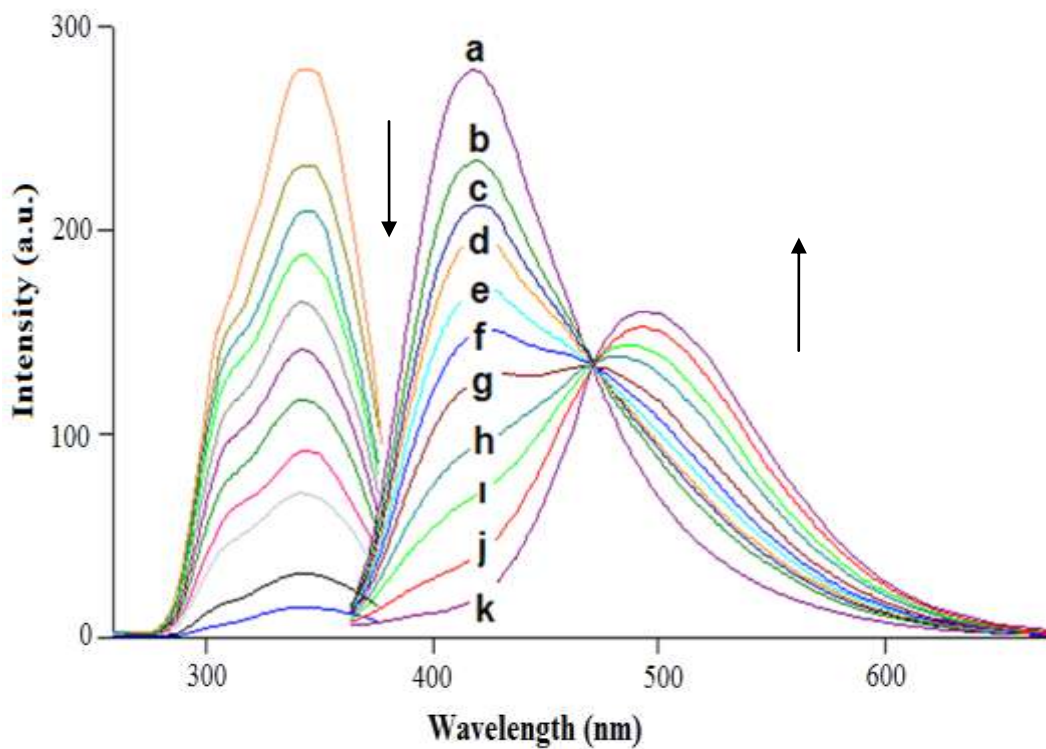


Figure 5.21 Fluorescence response of the ODC-5-doped EC based nanofiber to Hg (II) ions at pH 5.0. (a) Hg-free buffer (b)  $10^{-11}$  M, (c)  $10^{-10}$ , (d)  $10^{-9}$ , (e)  $10^{-8}$ , (f)  $10^{-7}$ , (g)  $10^{-6}$ , (h)  $10^{-5}$ , (i)  $10^{-4}$ , (j)  $10^{-3}$ , (k)  $10^{-2}$  mol/L Hg(II), and linearized calibration plot for the concentration range of  $10^{-11}$ - $10^{-2}$  M Hg (II).

The ODC-5 doped eletrospun nanofibers demonstrated a linearizable response over range of  $5 \times 10^{-11}$ - $5 \times 10^{-2}$  M for Hg (II) ions. However, the response is not exactly linear. The calibration plot exhibits slightly upward concave characteristic. Testing sensor compositions are demonstrated large relative signal change and very good sensitivity to Hg (II) ions. The regression results yielded a linear response with coefficients of regression ( $R^2$ ) of 0.9919 for EC electrospun nanofibers (See Table 5.8). The limit of detection (LOD) for Hg (II) was defined as the concentration at which the signal is equal to the blank signal ( $n = 20$ ) plus  $3\sigma$  and found to be  $9.40 \times 10^{-14}$  M for electrospun nanofibers.

Table 5.8 gives a comparison of performance characteristics of thin film and nanofibers made up of same material in terms of working range, LOD, relative signal change and linearity.

Table 5.8 Calibration characteristics of EC based electrospun nanofibers and thin films.

Indicator Dye	Matrix /Form	Linear Range (Hg(II) Mol/L)	Regression Coefficient ( $R^2$ )	LOD (Molar)	% Relative Signal Changes
ODC-5	EC/nanofiber	$1.0 \times 10^{-11}$ to $1.0 \times 10^{-2}$	0.9919	$9.40 \times 10^{-14}$	94.5
	EC / thin film	$1.0 \times 10^{-9}$ to $1.0 \times 10^{-2}$	0.9979	$1.90 \times 10^{-13}$	47.5

#### 5.3.4 Stern-Volmer Analysis

The quenching process of the offered sensor can be described by the well-known Stern-Volmer equation, which was explained in former chapters.

Figure 5.22 and Table 5.9 show the Stern-Volmer analysis results of electrospun nanomaterials and continuous thin films of ODC-5 dye. The  $K_{sv}$  value of the electrospun fibers and continuous thin film, calculated from slopes of the plots were found to be  $3.2 \times 10^4$  ( $M^{-1}$ ) and  $9.7 \times 10^1$  ( $M^{-1}$ ), respectively. The  $K_{sv}$  value calculated

for nanofiber is approximately 330 fold greater than that obtained from the continuous thin films. As it is seen, the diffusion rate of the quencher to fluorophores doped in the polymer is related to the micro-structural properties of the sensing agent. Therefore, the significant enhancement is observed in the sensitivity of the nano sensor compared with the continuous thin films. The large specific area of the nano-structure sensor enables the diffusion of high number of mercury ions towards to the solid phase. In these structures, the possibility of interaction of the analyte ions with the Hg (II) sensitive chromoionophore is higher than that of observed in conventional thin films.

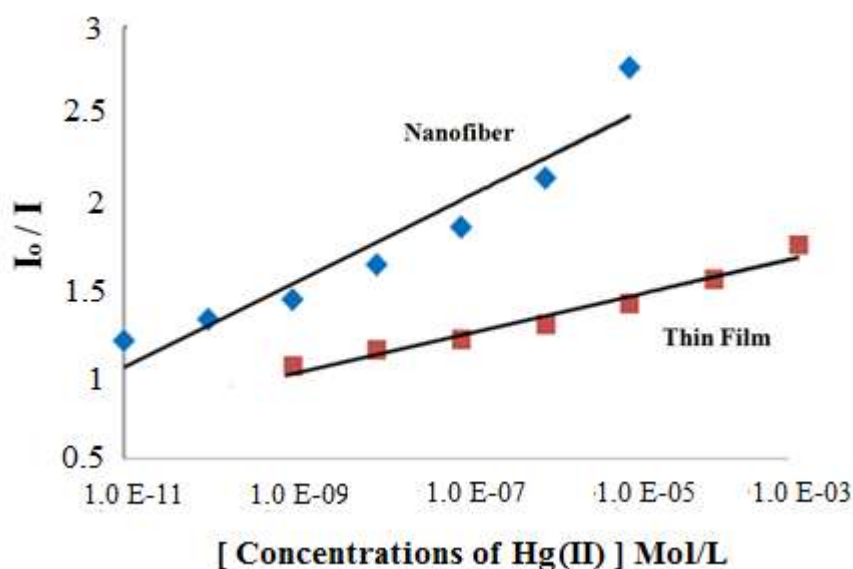


Figure 5.22 The Stern Volmer plot of EC based I: thin films and II: electrospun nanofibers.

Table 5.9 The Stern Volmer plot and  $K_{sv}$  Constant of EC based electrospun nanofibers and thin films.

Indicator Dye	Matrix /form	Linear Regression Equation	$K_{sv}$ Constant
ODC-5	EC/ nanofiber	$y = 3172x + 1$	$3.17 \times 10^4$
	EC / thin film	$y = 97.30x + 1$	$9.73 \times 10^1$



### 5.3.5 Lifetime Analysis

The excited state lifetimes of the ODC-5 in THF and in solid matrix of EC, in the absence and presence of the quencher were shown in Table 5.10. The measured lifetimes exhibited a distribution with two components in solution and thin film forms. In case of nanofibers, numbers of the components were three. In solution phase measurements a slight decrease was observed in fluorescence lifetime when exposed to metal ions. A parallel behavior was also observed in thin film forms. The nanofiber forms exhibited slight changes when exposed to Hg (II) ions in three lifetime components. These slight changes can be attributed to the dynamic component of the quenching. In excited state lifetimes in the presence of the Hg (II) ions.

Table 5.10 Florescence lifetimes of the carbazole derivative in THF, EC based thin films and electrospun nanofibers in the presence and absence of the quencher.

ODC - 5		Solvent		Thin Film		Nanofiber	
		Value (ns)	% Relative	Value (ns)	% Relative	Value (ns)	% Relative
Metal Free	$\tau_1$	2.28	28.54	1.00	46.43	0.82	22.79
	$\tau_2$	3.15	71.46	2.86	53.57	2.09	55.99
	$\tau_3$	--	--	--	--	3.84	21.22
		Value (ns)	% Relative	Value (ns)	% Relative	Value (ns)	% Relative
Hg(II)	$\tau_1$	0.28	4.78	0.69	49.74	0.24	31.98
	$\tau_2$	2.95	95.22	2.49	50.26	1.25	46.29
	$\tau_3$	--	--	--	--	3.33	21.73

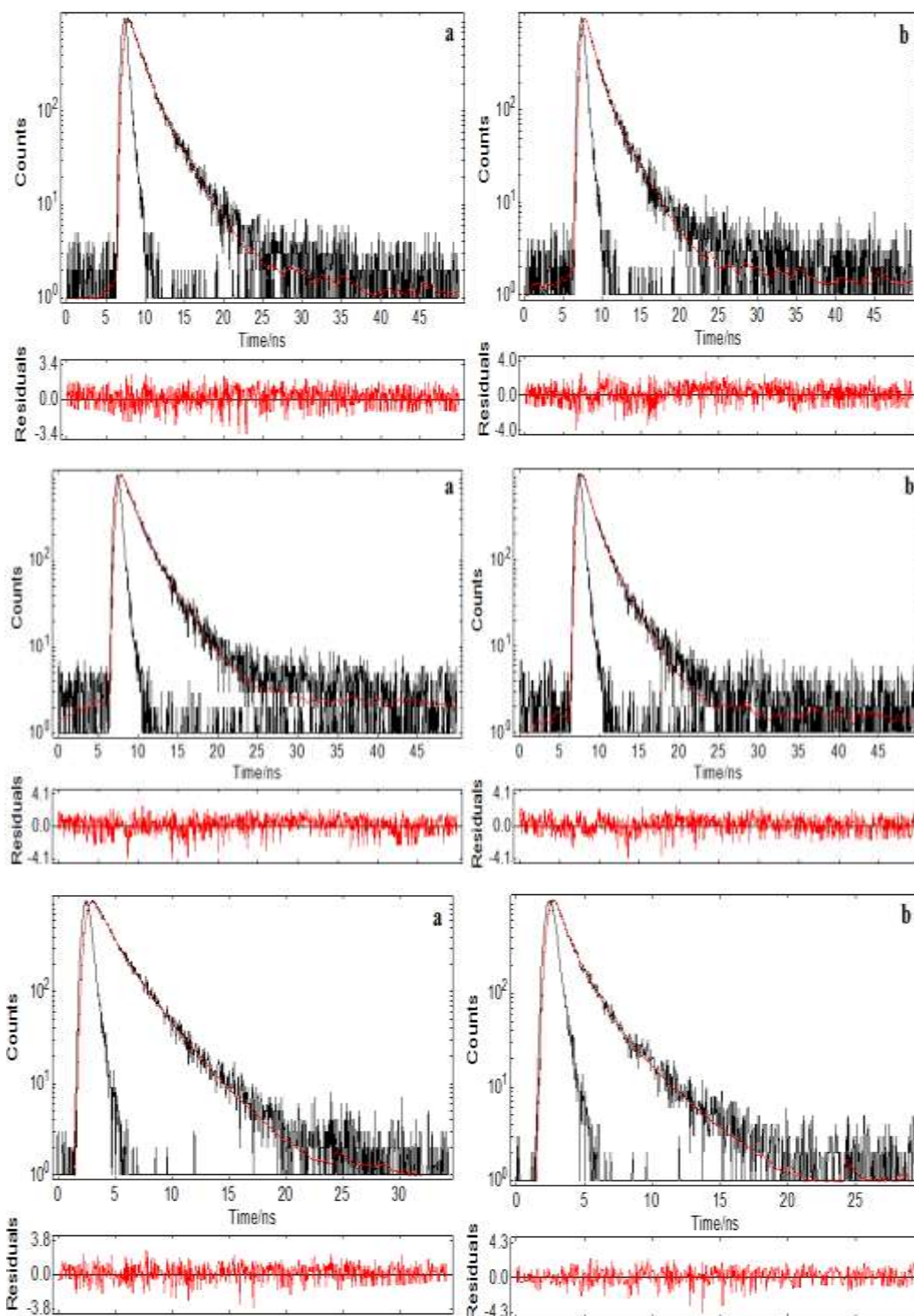


Figure 5.23 Decay curves of the exploited dye in THF, in thin film form and in form of nanofiber, respectively. In all cases a and b shows quencher free and quencher containing decay profiles. The dye excited at 367 nm with a picoseconds pulsed laser and intensity decay data acquisition was performed at 412 nm.

Quenching requires molecular contact between the fluorophore and quencher. This contact can be due to diffusive encounters, which is dynamic quenching, or due to complex formation, which is static quenching (Lakowicz, 2006).

Static quenching arises when the quencher (Q) forms a stable complex with the fluorophore in the ground state. Mainly, this complex is non-fluorescent. In such cases, dramatic changes occur in the absorption spectrum of the fluorophore in the presence of the quencher. Non-linear Stern-Volmer plots are also indicators of static quenching.

Dynamic quenching occurs after a collision between the fluorophore and the quencher when the fluorophore is in the excited state. This collision is due to the diffusional movements between the two molecules. A reduction in fluorescence quantum yield, or a decrease in lifetime are evidences of the effect of the excited state dynamic quenching (Biocrice, 2012).

If a plot of  $I_0/I$  versus concentration of the quencher has an upward curvature, it is the evidence of combined quenching both by collisions (dynamic quenching) and by complex formation (static quenching) with the same quencher (Lakowicz, 2006). The non-linearized data observed in Figure 5.22 exhibits both static and dynamic quenching is occurring in the sample.

Variation of emission spectra and accompanying discernible color change of the dye from colorless to yellow can be an evidence of complex formation with Hg (II) ions, which is an indicator of static quenching. When fluorescence intensity based response, absorption spectroscopy and lifetime measurements related data were evaluated together, the mechanism between indicator dye and sensing agent can be concluded as combined quenching of the ODC-5 dye by Hg (II) ions.

### 5.3.6 Selectivity Studies

In order to examine the response of the dye to possible interfering cations, the ODC-5 dye was treated with  $10^{-3}$  M concentrations of  $\text{Hg}^{2+}$  and  $\text{Hg}^+$ ,  $\text{Al}^{3+}$ ,  $\text{Ag}^+$ ,  $\text{Ca}^{2+}$ ,  $\text{Co}^{2+}$ ,  $\text{Cr}^{3+}$ ,  $\text{Cu}^{2+}$ ,  $\text{Fe}^{3+}$ ,  $\text{Fe}^{2+}$ ,  $\text{Li}^+$ ,  $\text{K}^+$ ,  $\text{Mn}^{2+}$ ,  $\text{Mg}^{2+}$ ,  $\text{Na}^+$ ,  $\text{NH}_4^+$ ,  $\text{Ni}^{2+}$ ,  $\text{Pb}^{2+}$  and  $\text{Zn}^{2+}$  ions in acetic acid/acetate buffer solutions at pH 5.0. The ODC-5 dye did not respond to the major cations of groundwater samples ( $\text{Ca}^{2+}$ ,  $\text{Mg}^{2+}$ ,  $\text{Na}^+$  and  $\text{K}^+$ ) and physiologically relevant fluids. However when exposed to considerably high concentrations of Fe (III), the dye exhibited an emission based response. We also tested interference effects of the conventional anions of  $\text{F}^-$ ,  $\text{Cl}^-$ ,  $\text{Br}^-$ ,  $\text{NO}_3^-$ ,  $\text{SO}_4^{2-}$  and  $\text{PO}_4^{3-}$ . Relative signal changes of approximately 5 % were observed for EC doped films. The relative signal intensity changes caused by the tested potential interferent cations were shown in Figure 5.24 (I) and (II).

From following figures it can be concluded that, the sensing design is capable of determining Hg (II) ions with a high selectivity over other ions except that of Fe (III). In a recent work of Lu and co-workers (2009), 1mM of sodium citrate was used to form a stable complex with Fe (III) and the Fe (III) ions successfully masked. The presence of citrate at this concentration did not affect the detection of Hg (II). A similar approach has been adapted to this work for masking of Fe (III). The fluorescence was dramatically decreased in the presence of mercuric ions exhibiting a relative signal change ratio of 98.5 %.

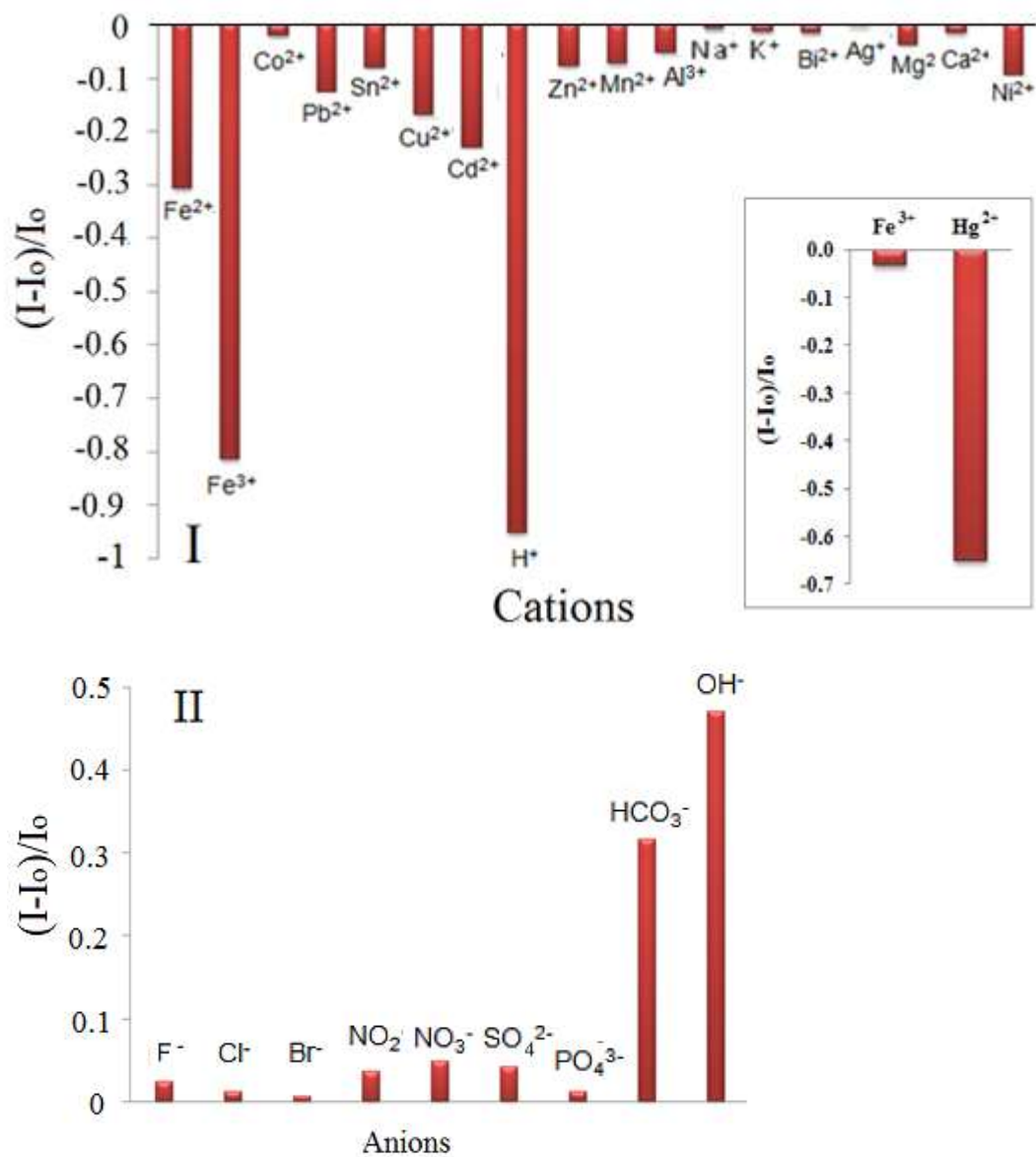


Figure 5.24 I: Metal-ion response of mercury sensitive ODC-5 at pH 5.0. Inset: Response to ionic mercury in presence of Fe (III). Fe (III) ions have been suppressed with citrate buffer. II: Response to the anions of the same composition at near neutral pH. Results were plotted as relative fluorescence changes;  $(I-I_0)/I_0$ .

### ***5.3.7 Recovery and Regeneration Studies With Real Groundwater Samples***

The applicability of the sensing system for real samples was tested for the mineral water of Sarikiz (Sarikiz, Manisa; Turkey; Latitude: 38° 44' 83 N, Longitude: 28° 04' 84 E). The temperature of water from well was remarkably constant and 16.9 °C. The content of Hg (II) in the diluted certified reference material of Merck (SRM from NIST Hg (NO<sub>3</sub>)<sub>2</sub> in HNO<sub>3</sub> 0.5 mol L<sup>-1</sup> 1000 mg L<sup>-1</sup> Hg CertiPUR®) was determined by exploiting the electrospun nanofibers. All mineral water samples were collected in polyethylene vials, degassed using ultrasonic bath and analyzed as soon as possible after sampling. The recovery experiments were carried out adding 1x10<sup>-8</sup> M of certified reference material into the mineral water. The average concentration of the Hg (II) was found to be 3.52×10<sup>-8</sup> M for 10 replicate measurements. The recovery performance was found to be 104 ± 5.3%. These results reveal the capability of the offered sensing design for the determination of mercury ions in real samples without considerable error. Potential interferents of HCO<sub>3</sub><sup>-</sup>, OH<sup>-</sup> and Fe (III) have been overcome adjusting the pH and using citrate buffer as masking agent.

### ***5.3.8 Conclusion***

A fiber optic sensor system has been fabricated for sensitive detection of Hg (II) at picomolar level. The sensitive determination of Hg (II) was accomplished by use of the newly synthesized ODC-5 dye in electrospun EC nanofibers. In this research, the polymer based nanofiber produced by electrospinning. With respect to continuous thin films, electrospun nanofibers offered enhanced sensitivity, lower LOD values and reactivity in optical chemical sensing of Hg (II). The ODC-5 doped EC nanofiber exhibited a 94.5 % relative signal change in direction of decrease in fluorescence intensity when exposed to Hg (II) in the concentration range of 1.0×10<sup>-11</sup>-1.0×10<sup>-2</sup> at pH 5.0. This is approximately two fold of the response of thin film, which was calculated as 47.5%. A quite good LOD (9.40×10<sup>-14</sup>) was reached and the sensor characteristics were investigated such as response time, reversibility, linear working range, effect of pH and interference effect.

## 5.4 A Fluorescent Probe; Chlorophenyl Imino Molecule in Form of Nanofibers for Sensing of Hg (II) Ions

Here, we used chlorophenyl imino molecule for the determination of nanomolar levels of mercuric ions. Ethyl Cellulose (EC) based electrospun nanofibers were fabricated together with appropriate additives. 2-{(E)-[(4-chlorophenyl) imino] methyl} phenol (DMK-1A) dye was used as selective chromoionophore. The chemical structure of the mercury sensitive molecule was shown in Figure 5.25.

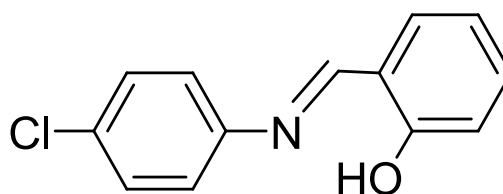


Figure 5.25 Structure of mercury sensitive molecule, 2-{(E)-[(4-chlorophenyl)imino] methyl} phenol (DMK-1A)

### 5.4.1 The Spectral Assessment and Quantum Yield Calculations of Newly Synthesized DMK-1A Dye

The absorption, excitation and corrected emission spectra of the DMK-1A dye were enrolled in the solvents of DCM, EtOH, DMF, and toluene/ethanol (To: EtOH; 80:20) mixture and in solid matrices of EC and PMMA. The spectral assessment of the synthesized dye was performed exploiting obtained data Figure 5.26 and 5.27 show the obtained absorption, excitation and emission spectra of the DMK-1A dye in different moieties. The maximum absorption wavelengths ( $\lambda_{Abs}$ ) and the molar extinction coefficients ( $\epsilon$ ) of the DMK-1A dye in the solvents of EtOH, DCM, Toluene/ Ethanol mixture (80:20) and DMF were given in Table 5.11. The dye exhibited broad and efficient absorbance extending from 230 to 400 nm, and high molar extinction coefficients in solution phase. Table 5.12 reveal emission based spectral characteristics of DMK-1A dye in the employed solvents and in solid matrices of EC and PMMA. The quantum yield and Stock's shift values were also calculated.

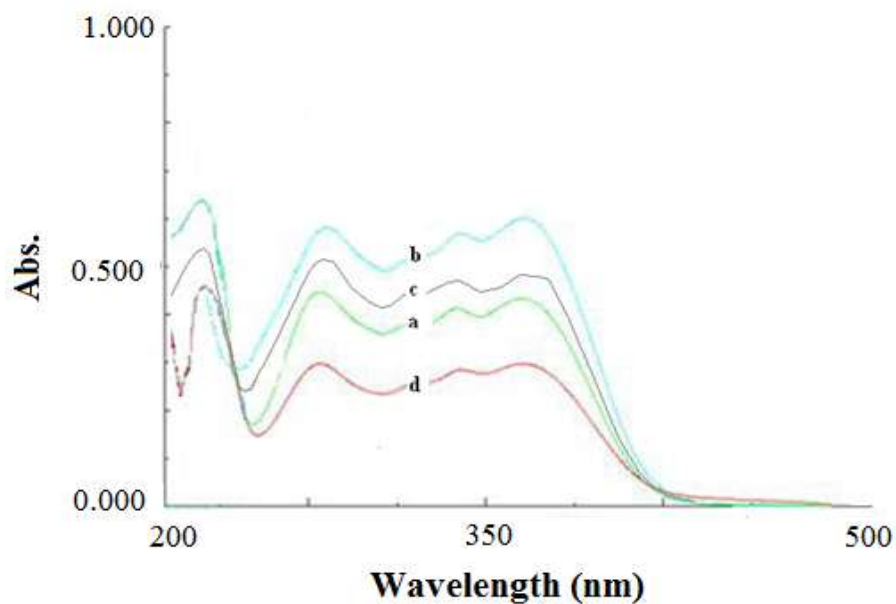


Figure 5.26 Absorption spectra of the DMK-1A dye ( $10^{-5}$  M dye or 2 mM dye/kg polymer). (a) DCM, (b) EtOH, (c) DMF, (d) Toluene: EtOH.

Table 5.11 UV-Vis spectra related data of DMK-1A in the solvents of EtOH, DCM, Toluene/ Ethanol mixture (80:20) and DMF.

Compound	Solvent/Matrix	$\lambda^1_{\text{abs}}$	$\lambda^2_{\text{abs}}$	$\lambda^3_{\text{abs}}$	$\epsilon_{\text{max}}(\lambda^1_{\text{abs}})$	$\epsilon_{\text{max}}(\lambda^2_{\text{abs}})$	$\epsilon_{\text{max}}(\lambda^3_{\text{abs}})$
DMK-1A	DCM	355	271	231	44500	44200	68800
	EtOH	352	272	230	65000	67000	95300
	DMF	348	272	228	90400	87100	71800
	To: EtOH	355	272	229	58000	56000	71800



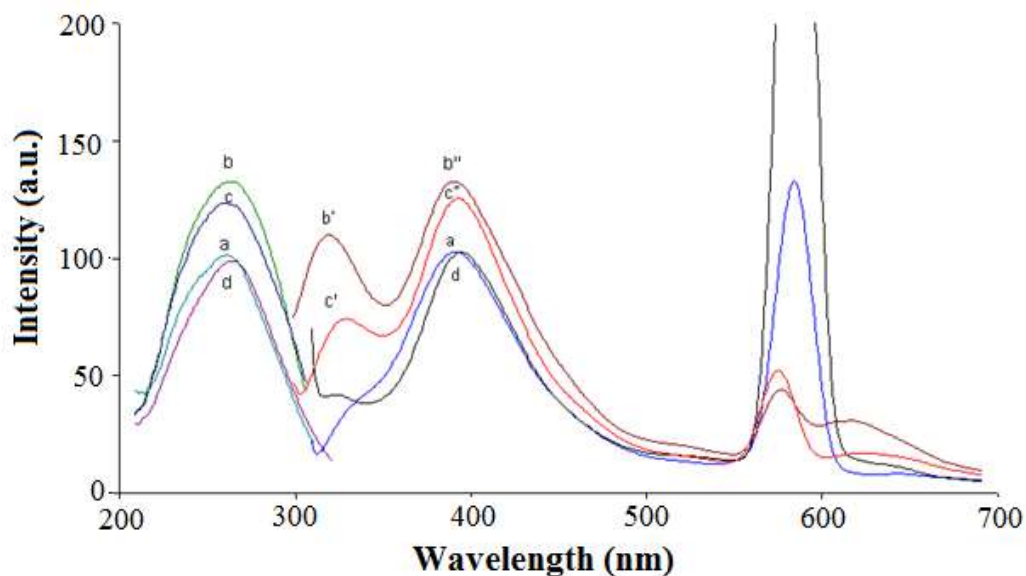


Figure 5.27 Excitation and corrected emission spectra of the DMK-1A dye ( $10^{-5}$  M dye or 2 mM dye/kg polymer). (a) DCM, (b) EtOH, (c) DMF), (d) To: EtOH.

Quantum yield values were calculated according to procedure mentioned in earlier chapters and were found to be 0.11 and 0.32 for THF and EC moieties. Quantum yield values of the exploited dye are lower than that of the quinine sulphate (See Figure 5.28). However,  $\phi F$  in EC is approximately three times higher than the  $\phi F$  in THF, which can be attributed to the hindered rotation movements of the molecule around single bonds in immobilized case.

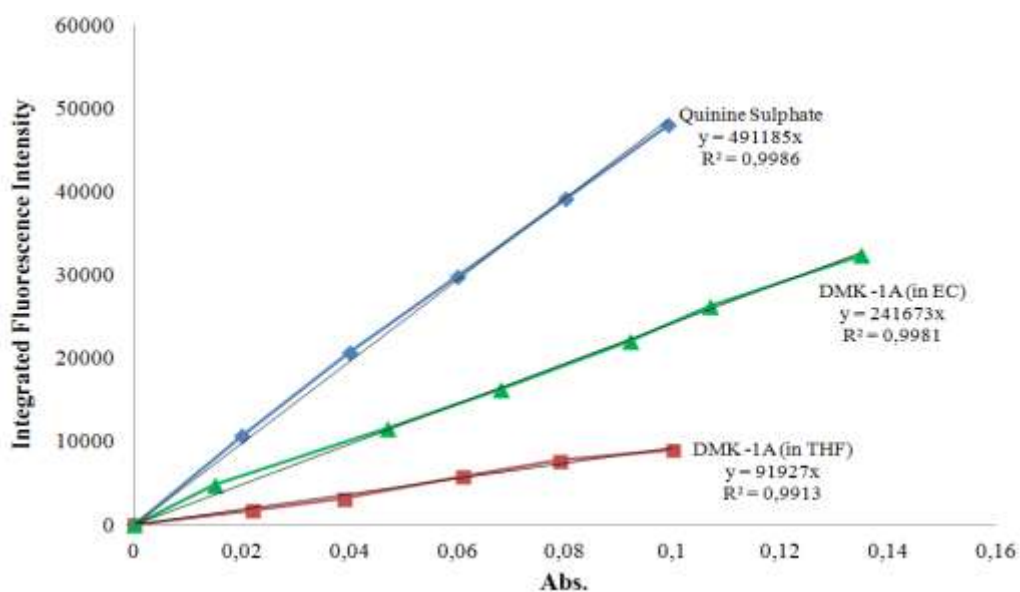


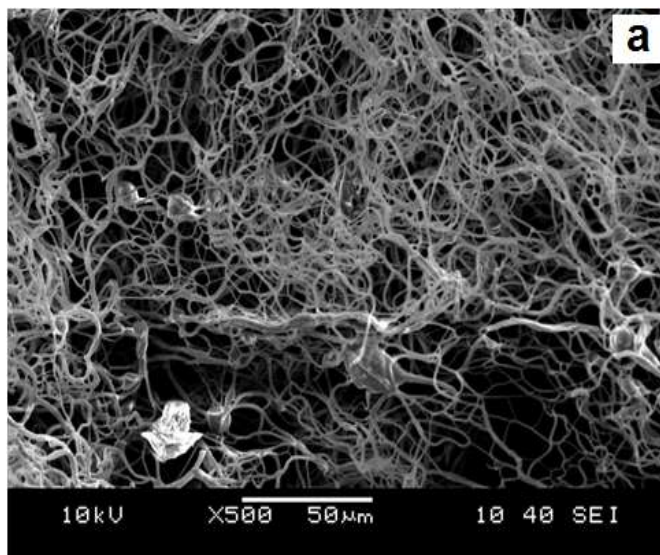
Figure 5.28 The integrated fluorescence intensities vs absorbance values of Quinine Sulfate in  $H_2SO_4$ , DMK-1A dye in EC and DMK-1A dye in THF.

Table 5.12 Emission and excitation spectra related data of DMK-1A in the solvents of EtOH, DCM, Toluene/ Ethanol mixture (80:20), DMF and in solid matrices of EC and PMMA.

Compound	Matrix	$\lambda_{\max}^{em}$	$\lambda_{\max}^{ex}$	$\Delta\lambda_{ST}$ (Stoke's shift)	$\phi_F$ (Quantum yield)
DMK-1A	DCM	390	260	130	0.11
	EtOH	390	262	128	
	DMF	345	270	75	
	To:EtOH	395	260	135	
	EC	380	270	110	0.32
	PMMA	385	290	95	

#### 5.4.2 SEM Images

The electro-spinning conditions were optimized to obtain continuous, regular scale and bead-free EC based nanofibers. Figure 5.29 shows scanning electron microscope (SEM) images of an electrospun EC nanofiber. It can be seen from Figure 5.29 that the diameters of the fibers were between 544 and 847 nm.



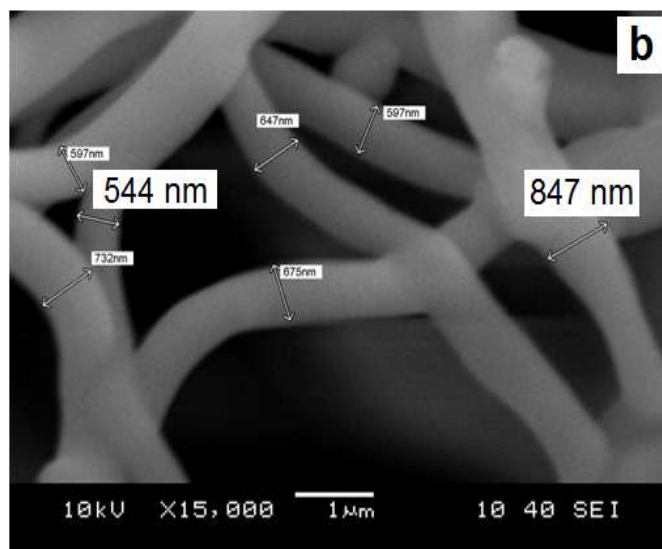


Figure 5.29 SEM images of EC based electrospun nanofibers (a) and (b); EC based nanofibers at different magnifications such as  $\times 500$  and  $\times 15\,000$ .

### 5.4.3 Effect of pH

The absorption, fluorescence emission and sensing efficiency of the indicator dye have affected by the pH of the environment. We researched the pH dependence of the dye upon complexation with ionic mercury at constant concentrations of Hg (I) and Hg (II) to find out optimum pH conditions, separately. The  $(I-I_0/I_0)$  was measured for DMK-1A doped EC and PMMA membranes in presence of Hg(I) and Hg(II) ions, as the analytical signal in the pH range of 3.5–6.5 (See Figure 5.30 and 5.31). The signal produced by the dye-doped EC membranes was approximately 3.5-fold of the signal produced by the PMMA membranes in the presence of Hg(I) at pH 5.5 (See Figure 5.30). Similarly, at pH 6.0, in the presence of Hg (II) ions the signal produced by the EC membrane was observed approximately 10-fold of the signal produced by the PMMA membrane (See Figure 5.31). Therefore, pH 5.5 and 6.0 were chosen as working condition for further studies for Hg (I) and Hg (II), respectively.

Distribution of the Hg (I) and Hg (II) ions related chemical species in the working conditions were theoretically checked with chemical equilibrium software

programme (Visual MINTEQ) at pH 5.5 and pH 6.0 in presence of acetate ions, respectively. The Hg (I) ion distribution was as following: [(CH<sub>3</sub>COO<sup>-</sup>(aq): 85.61%, CH<sub>3</sub>COOH (aq): 14.39%, Hg<sub>2</sub><sup>2+</sup> (aq); 100%]. Similar tests were also performed for Hg (II) ions [(CH<sub>3</sub>COO<sup>-</sup>(aq): 94.87 %, CH<sub>3</sub>COOH (aq): 5.13 % and Hg (OH)<sub>2</sub>(aq); 99.78%, Hg (CH<sub>3</sub>COO<sup>-</sup>)<sub>2</sub>; 0.13%; and Hg (OH)<sup>+</sup> (aq); 0.062%]. Due to the solubility considerations, [Acetate<sup>1-</sup>, Hg (I), Hg (II) and H<sup>1+</sup>; dissolved 100%] acetic acid/acetate buffered solutions of pH 5.5 and 6.0 were chosen further studies in the presence of Hg(I) and Hg(II) ions, respectively.

We also tested whether it has been possible to determine the two-oxidation states of mercury: Hg (I) and Hg (II). Calibration sets for speciation of mercury species; Hg (I) and Hg (II) were prepared separately at pH 6.0 and pH 5.5, respectively. The relative signal changes observed for Hg (I) and Hg (II) ions for same concentration, 5.0x10<sup>-5</sup> M, were 3.9% and 93% respectively at pH 6.0. The Hg (I) species did not induce significantly the fluorescence signal either in thin film form or in nanomaterial at pH 6.0. This result confirms that Hg (I) and Hg (II) can be distinguished with an error of 4.2 % quantitatively in the region assessed.

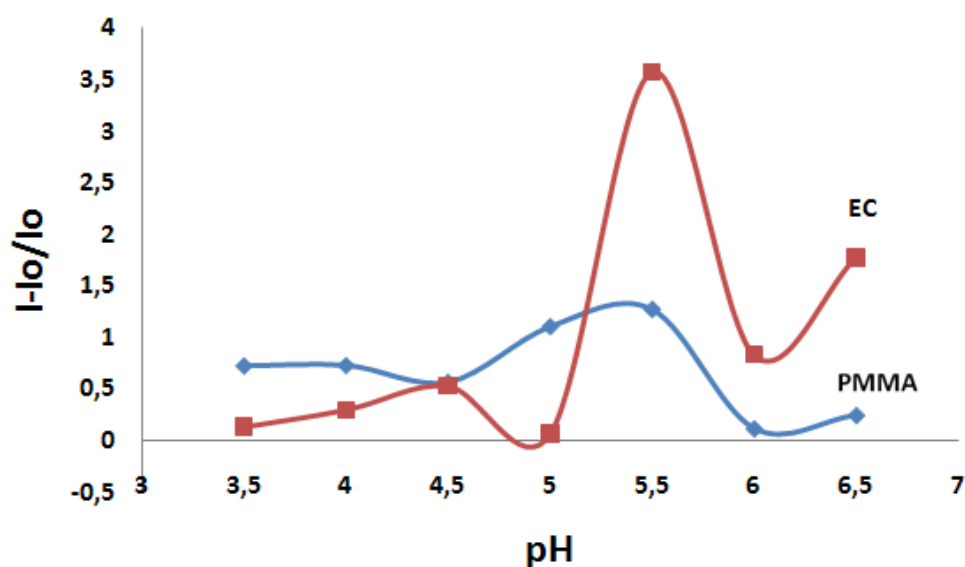


Figure 5.30 The pH dependency of DMK-1A dye in presence of Hg (I) ions between pH 3.5-6.5 using the EC and PMMA based nanofibers, respectively.

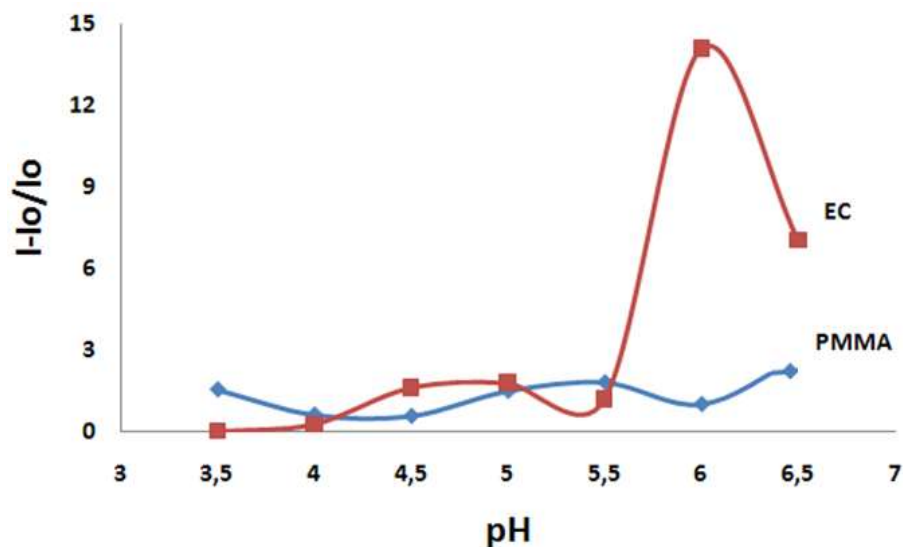


Figure 5.31 The pH dependency of DMK-1A dye in presence of Hg (II) ions between pH 3.5-6.5 using the EC and PMMA based nanofibers, respectively.

#### 5.4.4 Dynamic Working Range and Response of Mercuric Ions

In presence of potassium tetrakis-(4-chlorophenyl) borate, DMK-1A doped polymer (EC) matrix acts as a selective probe to Hg (I) ions at pH 5.5 and to Hg (II) ions at pH 6.0, respectively. In this system, potassium ions diffuse from the membrane into the aqueous phase, meanwhile, Hg (I) and Hg (II) ions are selectively extracted into the polymer phase in by the help of the anionic additive. Physical aspect of the ion-exchange pathway can be explained by the following scheme (See Figure 5.32).

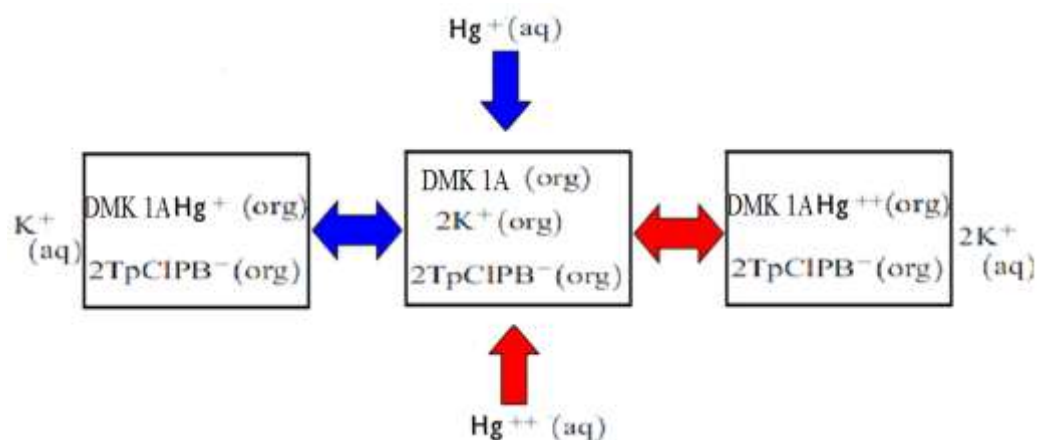


Figure 5.32 Physical aspect of the ion-exchange pathway scheme

Figure 5.33 and 5.34 show the changes in absorption spectra of the dye in THF upon exposure to  $5 \times 10^{-3} \text{M}$  concentration of Hg (I) and Hg (II) ions, respectively. The dye exhibited absorption based response in direction of decrease in signal intensity for both Hg (I) and Hg (II) species. However, the response for Hg (II) was approximately three fold of the response recorded for Hg (I).

The absorption integral and wavelength in the presence of Hg (II) ions exhibited a slight change. This enhancement in the absorption integral cannot be concluded as a distinct evidence for complex formation and consequently static quenching.

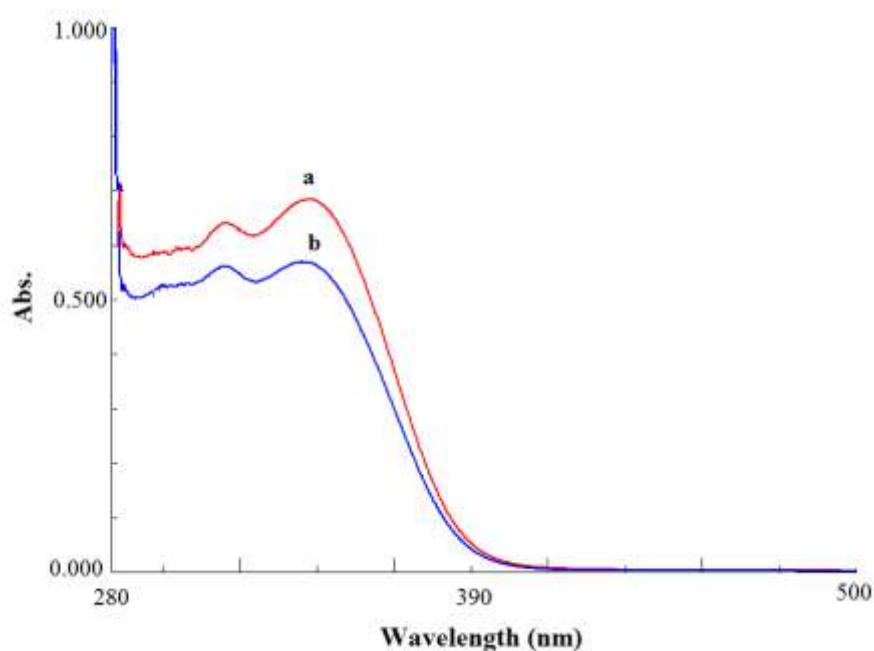


Figure 5.33 Absorption spectrum of the DMK-1A dye in THF (a) Hg (I) free, (b) in presence of  $5 \times 10^{-5} \text{M}$  Hg (I).

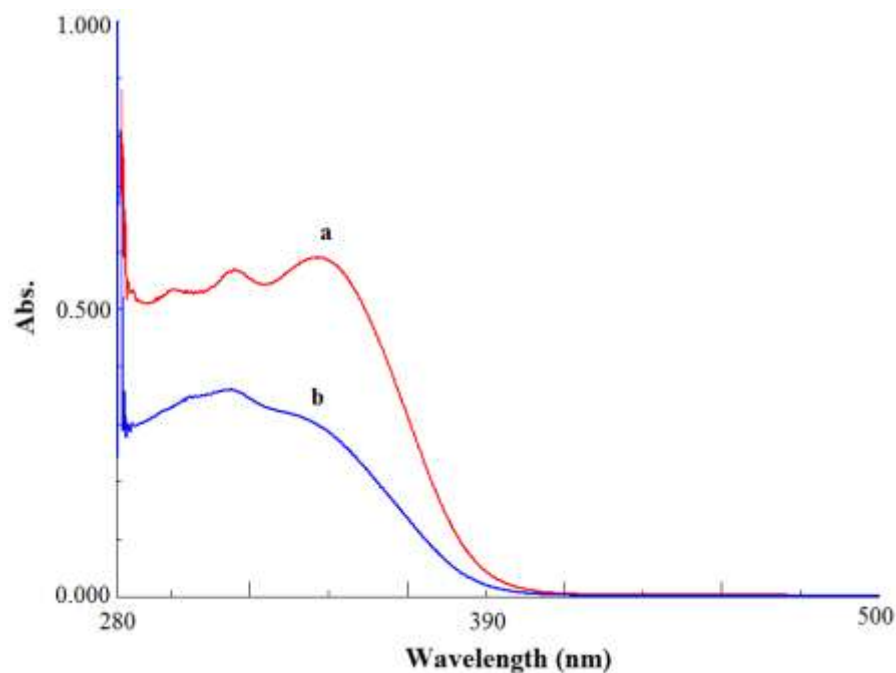


Figure 5.34 Absorption spectrum of the DMK-1A dye in THF (a) Hg (II) free, (b) in presence of  $5 \times 10^{-5}$  M Hg (II).

Figure 5.35 and 5.36 show the change in fluorescence response of EC based thin film and nanofibers as a function of concentration of Hg (II) ions at pH 6.0. A parallel study was also performed for a different concentration range of Hg (I) ions at pH 5.5. Figure 5.37 and 5.38 show the spectral changes of EC based thin film and nanofibers upon exposure to Hg (I) ions.

In order to determine the affinity of the fluoroionophore to ionic mercury the dissociation constant were calculated for thin film and fiber forms according to the following equation and were found to be  $1.0 \times 10^{-8}$  and  $5.0 \times 10^{-7}$  M for nanofiber and thin film, respectively (See Equation 5.4).

$$K_D = [A] \times (F_{\max} - F) / (F - F_{\min}) \quad (5.4)$$

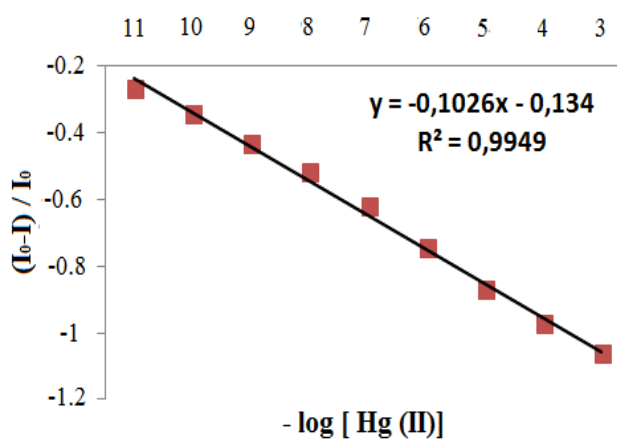
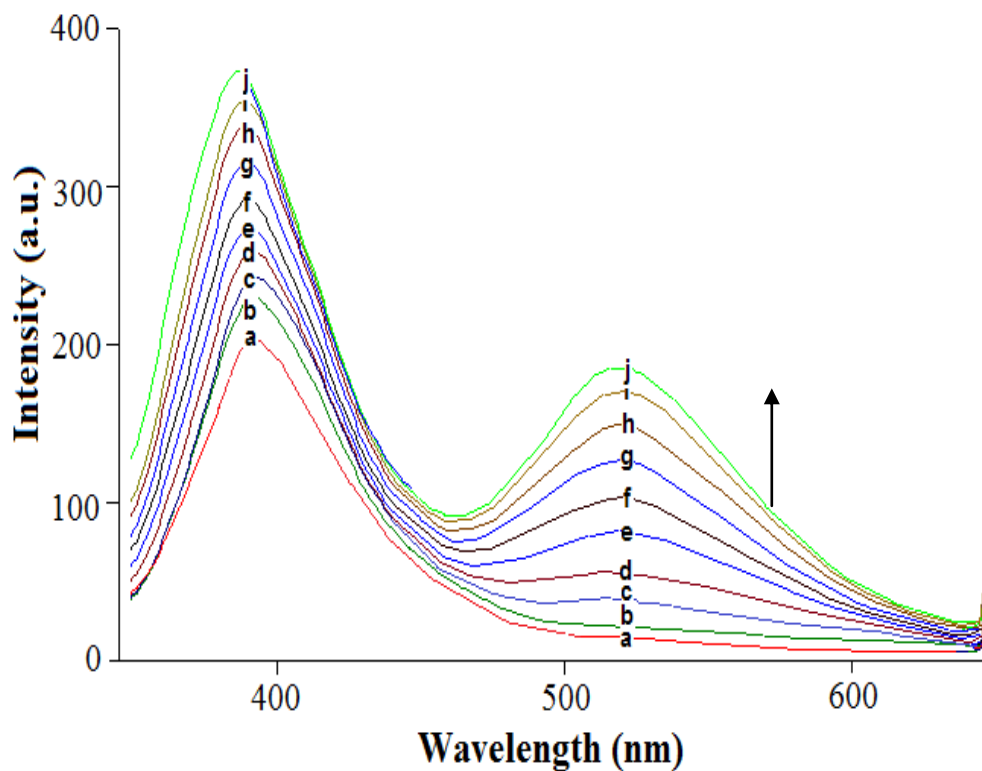


Figure 5.35 Fluorescence response of the EC based thin film to Hg (II) ions at pH 6.0. (a) Hg-free buffer, (b)  $10^{-11}$  M Hg (II), (c)  $10^{-10}$ , (d)  $10^{-9}$ , (e)  $10^{-8}$ , (f)  $10^{-7}$ , (g)  $10^{-6}$ , (h)  $10^{-5}$ , (i)  $10^{-4}$ , (j)  $10^{-3}$  M Hg(II), and linearized calibration plot for the concentration range of  $10^{-11}$ - $10^{-3}$  M Hg (II).



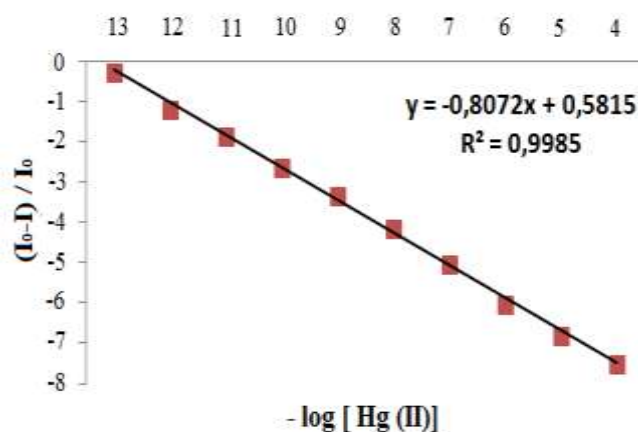
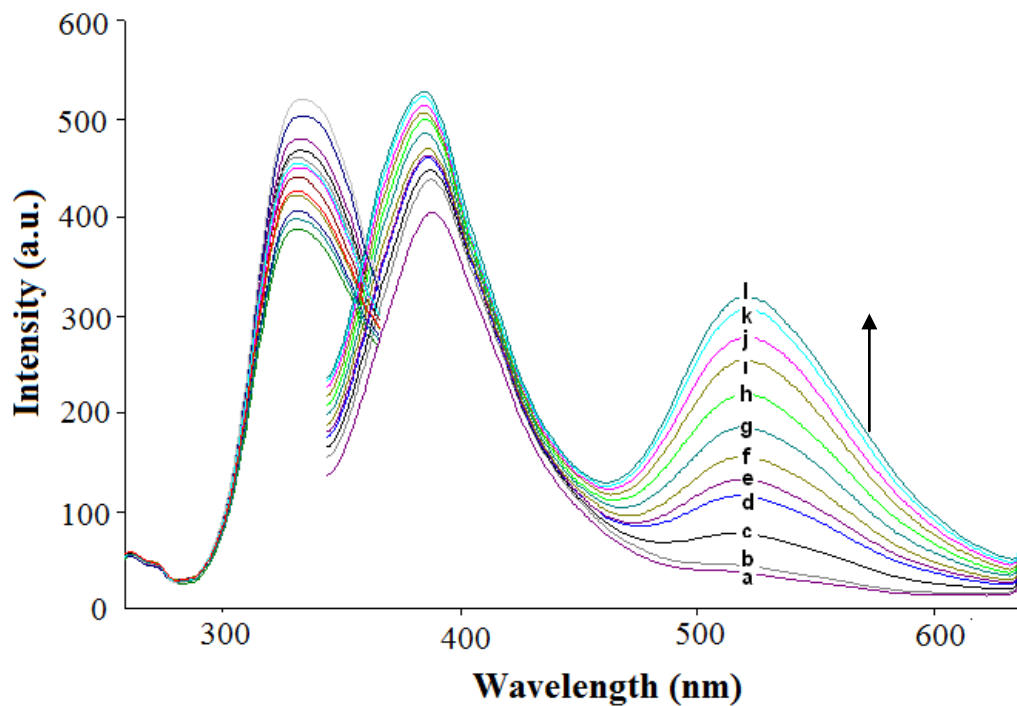


Figure 5.36 Fluorescence response of the EC based nanofiber to Hg (II) ions at pH 6.0. (a) Hg-free buffer, (b)  $10^{-13}$  M Hg (II), (c)  $10^{-12}$ , (d)  $10^{-11}$ , (e)  $10^{-10}$ , (f)  $10^{-9}$ , (g)  $10^{-8}$ , (h)  $10^{-7}$ , (i)  $10^{-6}$ , (j)  $10^{-5}$ , (k)  $10^{-4}$ , (l)  $10^{-3}$  M Hg(II), Inset: Calibration plot for the concentration range of  $10^{-9}$ - $10^{-3}$  M Hg (II) and linearized calibration plot for the concentration range of  $10^{-13}$ - $10^{-4}$  M Hg (II).

Thin film and electrospun materials exhibited similar spectral response to Hg (I) and Hg (II) ions. On addition of mercuric ions, the intensity of the signal of the emission spectra at 380 nm decreased whereas that at 520 nm increased both in thin film and nanofiber structures. Insets of figures show linearized calibration plots of the optodes. The calibration curves were plotted exploiting the algorithm  $[(I_0 - I)/I_0]$  for y-axis where  $I_0$  and  $I$  are the intensities of fluorescence in absence and in

presence of the quencher, respectively. Due to the applied algorithm, good straight lines over the dynamic working range were obtained. In all cases, the relative signal changes measured for Hg (II) was higher than that of the ones obtained for Hg (I). In EC based nanofibers these values were calculated as 80 and 60%, respectively. The relative signal changes for Hg (II) and Hg (I) were found to be 55 and 40% for thin film forms.

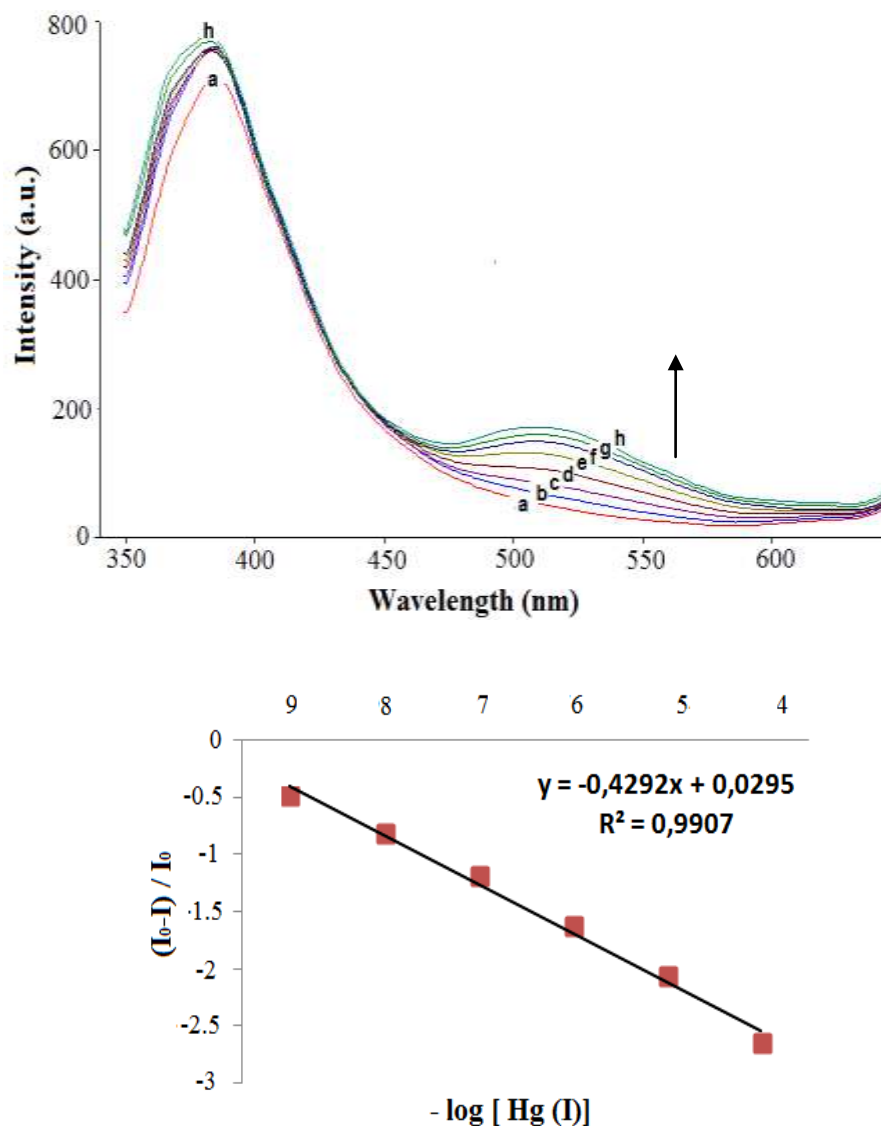


Figure 5.37 Fluorescence response of the EC based thin film to Hg (I) ions at pH 5.5. (a) Hg-free buffer, (b)  $10^{-9}$  M Hg (I), (c)  $10^{-8}$ , (d)  $10^{-7}$ , (e)  $10^{-6}$ , (f)  $10^{-5}$ , (g)  $10^{-4}$ , (h)  $10^{-3}$  M Hg (I), and linearized calibration plot for the concentration range of  $10^{-9}$ - $10^{-4}$  M Hg (I).

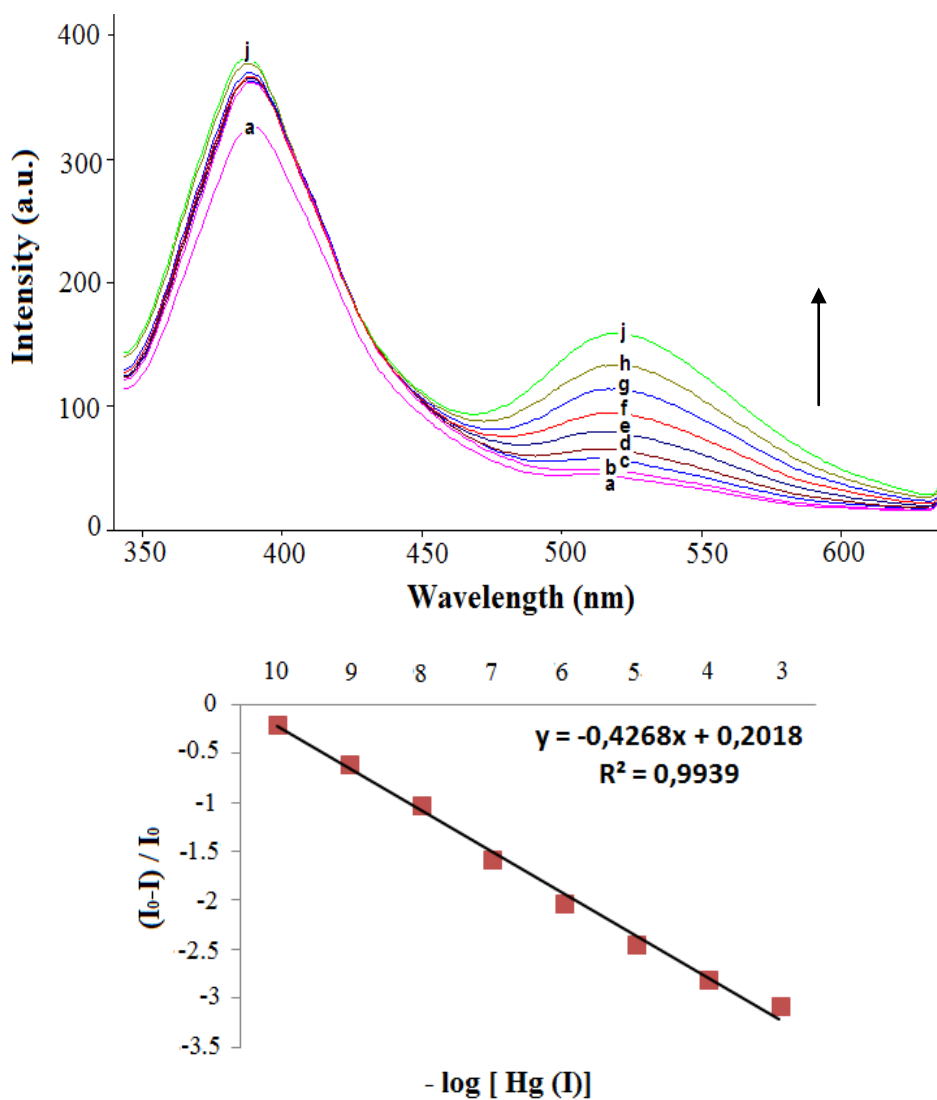


Figure 5.38 Fluorescence response of the EC based nanofiber to Hg (I) ions at pH 5.5. (a) Hg-free buffer, (b)  $10^{-10}$  M Hg (I), (c)  $10^{-9}$ , (d)  $10^{-8}$ , (e)  $10^{-7}$ , (f)  $10^{-6}$ , (g)  $10^{-5}$ , (h)  $10^{-4}$ , (j)  $10^{-3}$  M Hg (I), and linearized calibration plot for the concentration range of  $10^{-10}$ - $10^{-3}$  M Hg (I).

Variation of emission spectra and accompanying discernible color change of the dye from light yellow to dark yellow can be an evidence of complex formation with Hg (II) ions. Similar color changes were also observed for Hg (I) ions.

DMK-1A doped electrospun nanofibers showed a linear response in the concentration range of  $10^{-10}$ - $10^{-4}$  M for the Hg (I) ions at pH 5.5. The regression results yielded an absolute linear response with coefficient of regression ( $R^2$ ) of 0.9939 for EC electrospun nanofibers (See Table 5.13).

However, due to the low relative signal changes observed for Hg (I) species, we focused on Hg (II) ions for further studies.

The linearized calibration plots for Hg (II) ions described by the equations,  $y = -0.8072x + 0.5815$  ( $R^2 = 0.9985$ ) and  $y = -0.1026x - 0.134$  ( $R^2 = 0.9949$ ) for EC based nanofiber and thin film forms. They exhibited quite good  $R^2$  values. The tested nano-components exhibited large relative signal change, excellent linearity and good sensitivity compared to thin film forms. The nanofibers increase in sensitivity compared to thin films and provided lower levels of LOD. The detection limits (LOD) were calculated exploiting concentration of the Hg (II) ions at which the signal is equal to the blank signal plus  $3\sigma$  and were found to be  $1.8 \times 10^{-15}$  M and  $2.9 \times 10^{-13}$  M for electrospun nanofiber and continuous thin films, respectively. Table 5.13 gives a comparison of performance characteristics of thin film and nanofibers made up of same material in terms of working range, LOD, relative signal change and linearity.

Table 5.13 Calibration characteristics of EC based electrospun nanofibers and thin films.

Indicator Dye	Sensing Agent	Matrix /Form	Linear Range	Regression Coefficient ( $R^2$ )	LOD (Molar)	% Relative Signal Changes
DMK-1A	Hg(I)	EC/ nanofiber	$1.0 \times 10^{-10}$ to $1.0 \times 10^{-3}$	0.9939	$4.2 \times 10^{-12}$	60
		EC / thin film	$1.0 \times 10^{-9}$ to $1.0 \times 10^{-4}$	0.9907	$3.5 \times 10^{-11}$	40
	Hg(II)	EC/ nanofiber	$1.0 \times 10^{-13}$ to $1.0 \times 10^{-4}$	0.9985	$1.8 \times 10^{-15}$	80
		EC / thin film	$1.0 \times 10^{-11}$ to $1.0 \times 10^{-3}$	0.9949	$2.9 \times 10^{-13}$	55

### 5.4.5 Lifetime Analysis

The excited state lifetimes of the DMK-1A in THF and in solid matrices, in the absence and presence of the quencher were shown in Table 5.14. Either in solution phase or in solid-state measurements, we did not observe a significant change in fluorescence lifetimes. Upon exposure to Hg (II), the decay time of the dye changed from 0.47 to 0.37 ns in THF. Similarly, in EC matrix, the lifetime changed from 0.32 to 0.33 ns. These excited state lifetime related data can be attributed to the dynamic component of the quenching.

Table 5.14 Fluorescence lifetimes of the carbazole derivative in THF, PMMA based thin films and electrospun nanofibers in the presence and absence of the quencher

DMK 1A		Solvent			Thin Film		
		Value (ns)	Std. Dev. (ns)	% Relative	Value (ns)	Std. Dev. (ns)	% Relative
Metal Free	t <sub>1</sub>	0.47	0.0138	100	0.32	0.0015	82.19
	t <sub>2</sub>	--	--	--	0.80	0.0098	17.81
	t <sub>3</sub>	--	--	--	--	--	--
		Value (ns)	Std. Dev. (ns)	% Relative	Value (ns)	Std. Dev. (ns)	% Relative
Hg (II)	t <sub>1</sub>	0.37	0.0039	87.19	0.33	0.0014	77.70
	t <sub>2</sub>	0.91	0.0383	12.81	0.80	0.0071	22.30
	t <sub>3</sub>	--	--	--	--	--	--

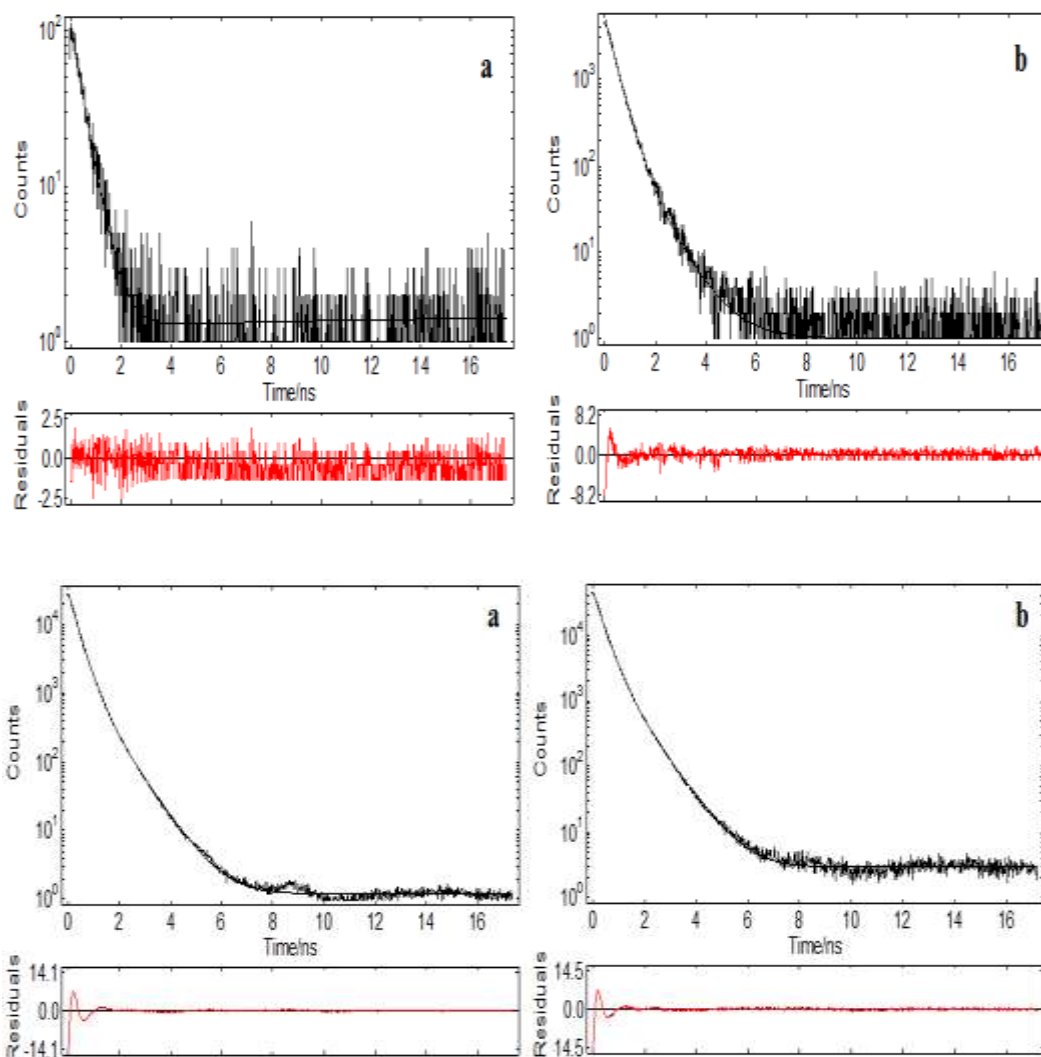
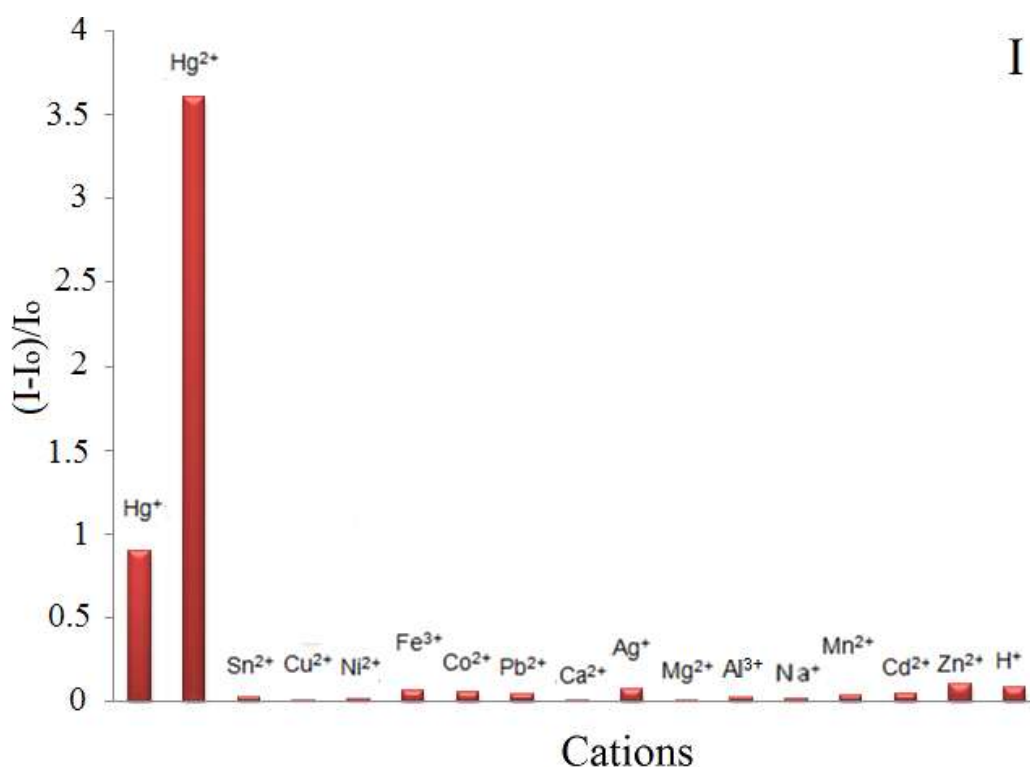


Figure 5.39 Decay curves of the exploited dye in THF and in thin film form, respectively. In all cases a and b shows quencher free and quencher containing decay profiles. The dye excited at 367 nm with a picoseconds pulsed laser.

When the absorption based and lifetime based data were evaluated together, the mechanism of quenching can be concluded as combined quenching. We did not observe a significant change in absorption integral upon addition to quencher. This can be concluded as the evidence of dynamic quenching. We also did not observe a distinguishable change in decay times in the presence of the quencher. This is evidence of static quenching. Therefore, the overall mechanism of quenching is ‘combined quenching’.

#### 5.4.6 Selectivity Characteristics and Interference Effect

Nearly all elements in the periodic table may still occur at low concentrations in groundwater (typically  $<0.01$  mg / L). Among these, the importance of some ions (e.g.,  $\text{Cd}^{2+}$ ,  $\text{Hg}^{2+}$ ), in quantification are toxic to humans, outweigh in practical terms (Prasanna, 2010). However, in the determination of mercury, some ions found in the groundwater samples may act as potential interferents. In chemosensing-based approaches, affinity of the chromoionophore for metal ions is still a problem. To determine the selectivity of the proposed method, the effect of a number of cations were investigated. Tests were performed for  $\text{Ag}^+$ ,  $\text{Al}^{3+}$ ,  $\text{Ba}^{2+}$ ,  $\text{Ca}^{2+}$ ,  $\text{Co}^{2+}$ ,  $\text{Cr}^{3+}$ ,  $\text{Cu}^{2+}$ ,  $\text{Fe}^{3+}$ ,  $\text{Hg}^+$ ,  $\text{Hg}^{2+}$ ,  $\text{Li}^+$ ,  $\text{K}^+$ ,  $\text{Mn}^{2+}$ ,  $\text{Mg}^{2+}$ ,  $\text{Na}^+$ ,  $\text{Ni}^{2+}$ ,  $\text{Pb}^{2+}$ ,  $\text{Sn}^{2+}$  and  $\text{Zn}^{2+}$  ions in acetic acid/acetate buffer solutions at pH 6.0. These tests reveal that, the sensing membrane could be used for the determination of mercuric ions with a high selectivity (See Figure 5.40-I). The fluorescence was dramatically quenched and exhibited a relative signal change ratio; 93% when inserted the quencher agent. The interference effects of the major anions;  $\text{OH}^-$ ,  $\text{F}^-$ ,  $\text{Cl}^-$ ,  $\text{Br}^-$ ,  $\text{NO}_3^-$ ,  $\text{NO}_2^-$ ,  $\text{SO}_4^{2-}$  and  $\text{PO}_4^{3-}$  were also tested. Relative signal changes of less than 2% were observed for EC doped films at pH 5.5 (See Figure 5.40-II).



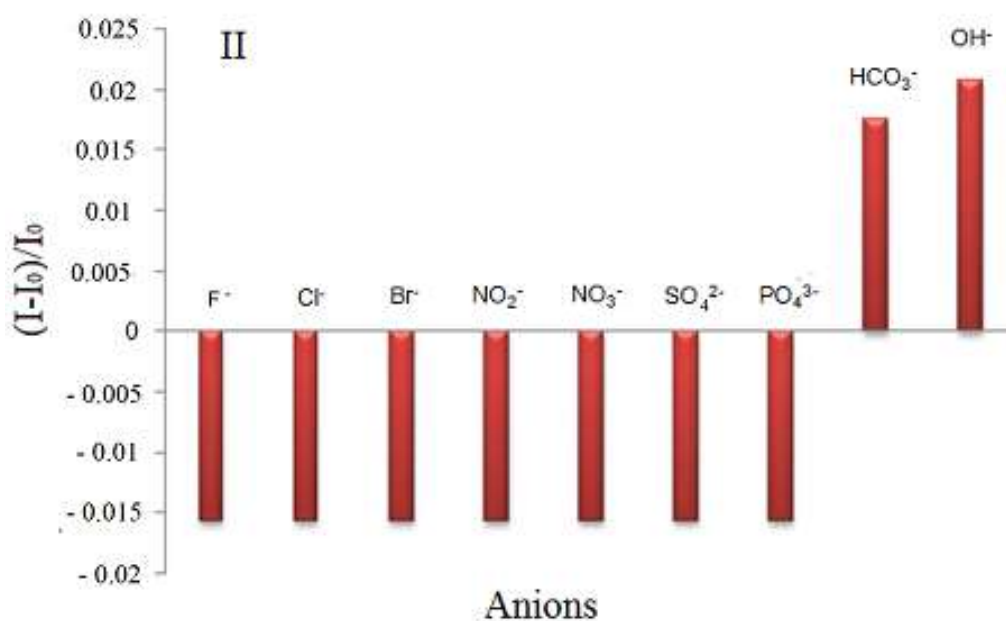


Figure 5.40 I: Metal ion response of EC based nanofibers at pH 6.0. II: Response to the anions of the same composition at near neutral pH. Results were plotted as relative fluorescence changes;  $(I-I_0)/I_0$ .

#### 5.4.7 Recovery and Regeneration Studies with Real Groundwater Samples

The applicability of the sensing system for real samples was tested for the mineral water of Sarikiz (Sarikiz, Manisa; Turkey; Latitude: 38° 44' 83 N, Longitude: 28° 04' 84 E). The temperature of water from well was reports as 16.9 °C. The content of Hg (II) in the diluted certified reference material of Merck (SRM from NIST Hg (NO<sub>3</sub>)<sub>2</sub> in HNO<sub>3</sub> 0.5 mol L<sup>-1</sup> 1000 mg L<sup>-1</sup> Hg CertiPUR®) was determined by exploiting the electrospun nanofibers. All mineral water samples were collected in polyethylene vials degassed using ultrasonic bath and analyzed as soon as possible. The recovery experiments were carried out adding 1×10<sup>-8</sup> M of certified reference material into the mineral water. The average concentration of the Hg (II) was found to be 2.19×10<sup>-8</sup> M for 10 replicate measurements. The recovery performance was found to be 102 ± 0.7 %. These results reveal the capability of the offered sensing design for the determination of mercury ions in real samples without considerable error.



#### **5.4.8 Conclusion**

DMK-1A dye was used as a novel fluorescent probe for sensing of ionic mercury. The dye is not able to differentiate the Hg (I) and Hg (II) species from each other. However, emission based response of the dye for an Hg (II) ions, is quite strong. Exploiting the DMK-1A and EC, polymeric matrix nano-scale fibers were produced by electrospinning technique. Due to their high surface area; nanofiber based sensors are more sensitive for ions with respect to the thin film forms of sensors. Due to these consequences, lower LOD values and faster response times were measured in optical chemical sensing of mercuric ions.

In this study, we introduced highly responsive fluorescent electrospun nanosensors based on fluorescence quenching of a mercury selective fluoroionophore. The DMK-1A dye was used for the first time as a chemosensor in the optical sensing of Hg (II). The detectable concentration range was measured as  $10^{-13}$ - $10^{-4}$  M for quantitative determination of Hg (II) at pH 6.0. A quite good LOD was reached. In addition, the sensor has a response time of <70 s.

## CHAPTER SIX

### FLUORESCENT Fe (III) SENSING AT NANO/SUB-NANO MOLAR LEVEL WITH OPTICAL CHEMICAL SENSORS

#### 6.1 Introduction

Selective determination of trace amounts of Fe (III) ions in the samples is of vital importance as chemical, physiological and environmental considerations. Today, a variety of advanced instrumental techniques used for the determination of trace amounts of iron. So far, many methods have been employed to determinate Fe (III) including flame atomic absorption (Quaresma, Cassella, Guardia, & Santelli, 2004; Reis, Knochen, Pignalosa, Cabrera, & Giglio, 2004; Yaman, & Kaya, 2005), inductively coupled plasma mass (ICP-MS) (Aydin, & Soylak, 2009; Niemelä, Perämäki, Kola, & Piispanen, 2003; Kozonoa, & Haraguchi, 2003), colorimetry (Narayanaswamy, & Govindaraju, 2012), electrochemical methods (Bolea, Arroyo, Laborda, & Castell, 2006; Meng, Chen, Liu, Jin, Sun, & Liu, 2010), flow injection (Settheeworrit, Hartwell, Lapanatnoppakhun, Jakmune, Christian, & Grudpan, 2005; Lae's, Vuillemin, Leilde, Sarthou, Bournot-Marec, & Blain, 2005; Chen, Gao, & Song, 2006) and fluorescence (Sharma, Saxena, & Gohil, 2009; Cabon, Giamarchi, & Bihan, 2009).

Different dyes have been used for the spectral detection of iron either in immobilized or in free form. Alternatively, many promising chemosensing systems have been designed utilizing the molecular framework of rhodamine (Mao, He, & Liu, 2010; Liu, & Wu, 2012) and rhodamine amide (Du, Chen, Zhang, Luo, He, Li, & Chen, 2012),  $\beta$ -aminobisulfonate (Singh, Kaur, Dunn, MacKay, & Callan, 2009), triphenyl butene derivatives (Han, Li, & Wang, 2012), benzimidazole (Jung, Singh, & Jang, 2009), terbium imidazole-4,5-dicarboxylic acid complex (Tan, Wang, & Zheng, 2010), 5-hydroxytryptophan (James, Byrne, & Mason, 2009), calix[4]arene (Patra, Lo, Chakraborty, Gunupuru, Maity, Ganguly, & Paul, 2013), and 4,7-diphenyl-1,10-phenanthroline (Salem, 2006).

These researches have provided valuable information for chemosensing of iron ions. Sometimes, the indicators proposed for the determination of Fe (III) exhibited weak or strong response to the other cations (Ma, & Hider, 2009). In recent years, to fabricate more stable sensors, researchers have begun to use chemosensing agents in embedded form in solid matrix materials (Oter, Ertekin, Kirilmis, Koca, & Ahmedzade, 2007; Oter, Ertekin, Kılınçarslan, Ulusoy, & Cetinkaya, 2007). In this way, in the limits of detection, selectivity, specificity, shelf life and response time's improvements were observed. In these designs, the sensor agent (a chromoionophore, an ionophore or a chromophore) immobilized on a polymeric support material, a resin, glassy matrix material, mainly in form of polymeric thin film for optical chemical sensing of Fe (III) ions.

However, the development of more selective and sensitive detection techniques Fe (III) ions is required to provide the requirements of the developing technology. In this regard, nanoscale sensors have been attracting considerable attention in recent years due to the promising properties.

Poiata et al. (2012), was reported the magnetite nanoparticles with chemically modified surface on *Pseudomonas aeruginosa* germ as fluorescence quenching-based optical sensors for iron ions. In this approach the coated magnetic nanoparticles could function as probes, the possibility of designing a chemical device was considered based on the sensing of iron reduction from Fe (III) into the more soluble Fe (II), for detecting various levels of contamination of biological specimens and environmental samples.

In another work, Manciualea and co-workers (2009) investigated the fluorescence quenching behavior of manufactured iron oxide nanoparticles on the standard Suwannee River fulvic acid (SRFA). The aggregated form of iron was found to be the strongest quencher, assuming no chemical reactions occurred. Aggregates of iron oxide present at pH 7–8 appeared to have a much larger effect on quenching compared with dispersed nanoparticles or dissolved phase iron.

However, the number of published works exploiting nano materials in the field of optical chemical sensing of the Fe (III) ions is very limited. In this respect, the usage of such nanomaterials is expected to offer good results in terms of sensitivity and other sensor dynamics like response time and reversibility in comparison to the previously published optical chemical sensors having the similar composition.

## 6.2 Sensing of Fe (III) Ions with Embedded Carbazole Derivative

In this part of thesis, the usage of electrospun nanofibrous materials as highly responsive fluorescence quenching-based Fe (III) sensitive chemosensor is reported. Fe (III) sensors based on the change in the fluorescence signal intensity of fluoroionophore 9-hexyl-9H-carbazole-3-carbonitrile (ODC 1) (See Figure 6.1). Structural characteristics of the exploited dye have been explained into detail in Chapter 3.

The electrospinning technique was used as a novel way to fabricate highly responsive optical chemical sensors for Fe (III) ions. Matrix material of ethyl cellulose (EC) was used to produce nanofibrous mats and continuous thin films. ODC 1 dye was chosen as the indicator due to the selective response, high quantum yield, large Stoke's shift and excellent photo stability. The electrospun nanofibers were characterized using scanning electron microscopy (SEM) and their average diameters were evaluated.

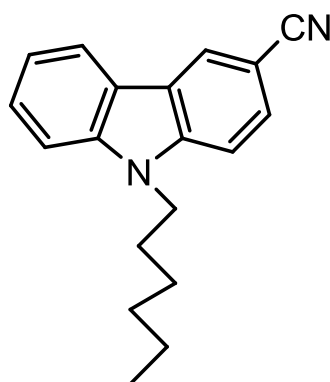


Figure 6.1 Structures of the iron sensitive fluoroionophore-,9-hexyl-9H-carbazole-3-carbonitrile (ODC 1).

### 6.2.1 The Photophysical Properties of the Indicator Dye in Different Solvents and Quantum Yield Calculations

The absorption excitation and corrected emission spectra were recorded in the solvents of EtOH, DCM, THF and toluene/ethanol (To: EtOH; 80:20) mixture and Toluene (See Figure 6.2 and 6.3). The UV-Vis spectroscopy related data (absorption maxima;  $\lambda_{\text{Abs}}$ , and molar extinction coefficient; ( $\epsilon$ ), were shown in Table 6.1 and 6.2. ODC-1 exhibited very efficient absorbance and high molar extinction coefficients around 330 and 347 nm in solution phase. The quantum yield, molar extinction coefficients and Stock's shift values were also calculated.

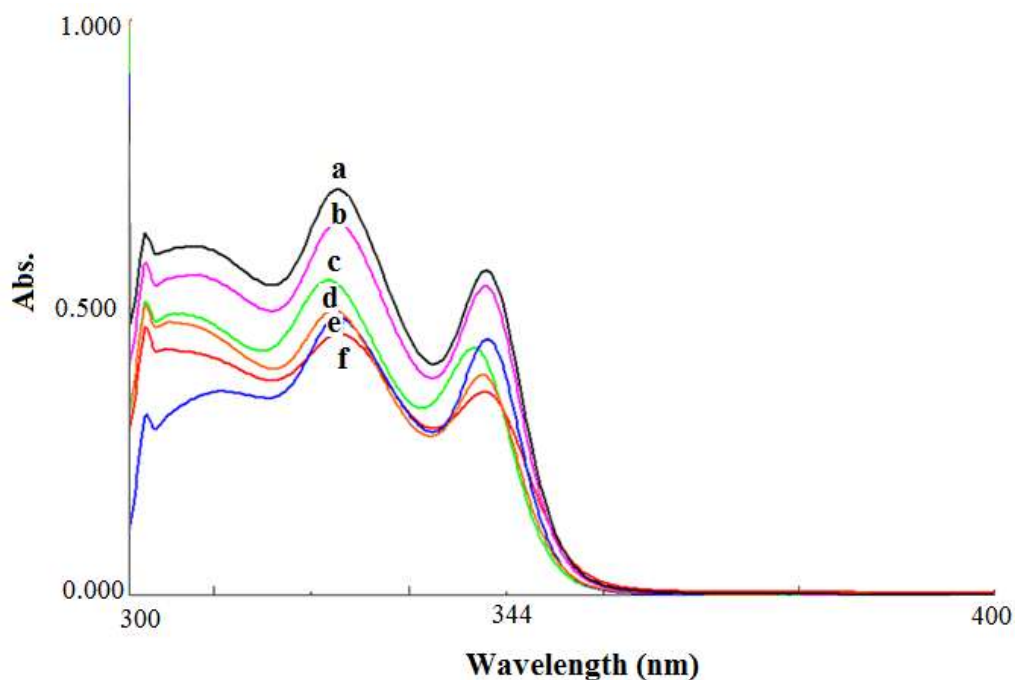


Figure 6.2 Absorption spectra of the ODC -1 dye ( $10^{-5}$  M dye or 2 mM dye/kg polymer). (a)EtOH, (b) To: EtOH (80:20), (c) DCM, (d) THF, (e) Toluene, (f) DMF.

Table 6.1 UV-Vis spectra related data of ODC -1 in the solvents of EtOH, DCM, THF, Toluene, Toluene/ Ethanol mixture (80:20) and DMF.

Compound	Solvent/Matrix	$\lambda_{\text{abs}}^1$	$\lambda_{\text{abs}}^2$	$\epsilon_{\text{max}} (\lambda_{\text{abs}}^1)$	$\epsilon_{\text{max}} (\lambda_{\text{abs}}^2)$
ODC-1	EtOH	331	347	82200	64500
	DCM	333	347	106300	85000
	THF	332	347	74200	57300
	To: EtOH	333	347	97100	80000
	DMF	333	347	68400	52600
	Toluene	333	347	72800	66400

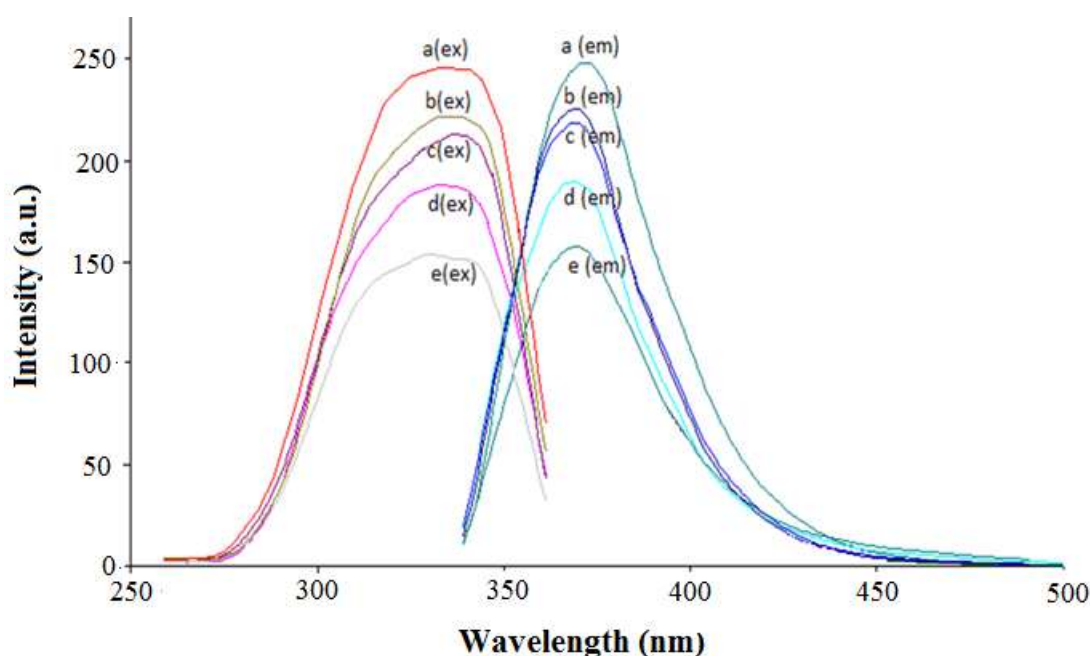


Figure 6.3 3 Excitation and corrected emission spectra of the ODC -1 dye ( $10^{-5}$  M dye or 2 mM dye/kg polymer) (a)THF, (b) DCM, (c) Toluene, (d) To: EtOH, (e) DMF.

Quantum yield values were calculated according to procedure mentioned in earlier chapters and were found to be 0.17 and 0.23 for THF and EC moieties. Quantum yield values of the exploited dye are lower than that of the quinine sulphate (See Figure 6.4). However,  $\phi_F$  in EC is higher than the  $\phi_F$  in THF, which can be attributed to the hindered vibrations of the molecule in immobilized case.

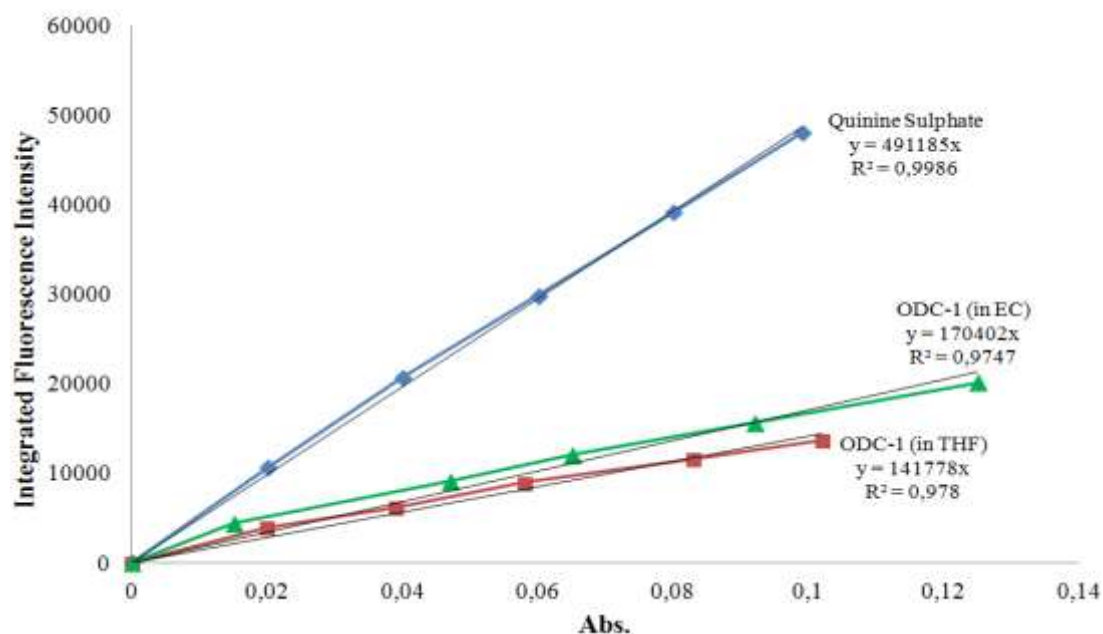


Figure 6.4 The integrated fluorescence intensities vs absorbance values of Quinine Sulphate in H<sub>2</sub>SO<sub>4</sub>, ODC-1 dye in EC and ODC-1 dye in THF.

Table 6.2 Emission and excitation spectra related data of ODC-1 in the solvents of EtOH, DCM, THF, Toluene, Toluene/ Ethanol mixture (80:20), DMF and in solid matrices of EC and PMMA.

Compound	Matrix	$\lambda_{\max}^{em}$	$\lambda_{\max}^{ex}$	$\Delta\lambda_{ST}$ (Stoke's shift)	$\phi_F$ (Quantum yield)
ODC -1	EtOH	368	341	27	0.17
	DCM	370	330	40	
	THF	369	330	39	
	To:EtOH	368	340	28	
	DMF	368	333	35	
	Toluene	368	338	30	
	EC	370	330	40	0.23
PMMA	370	330	40		

### 6.2.2 SEM Images of Electrospun Membranes

The SEM images of EC based electrospun membranes at various magnifications are denoted in Figure 6.5. The membrane has a 3-D structure with a random fiber orientation that is evenly distributed on the substrate. It can be seen from Figure 6.5 that the diameters of the fibers were ranged from 644 nm and 1.12  $\mu\text{m}$ .

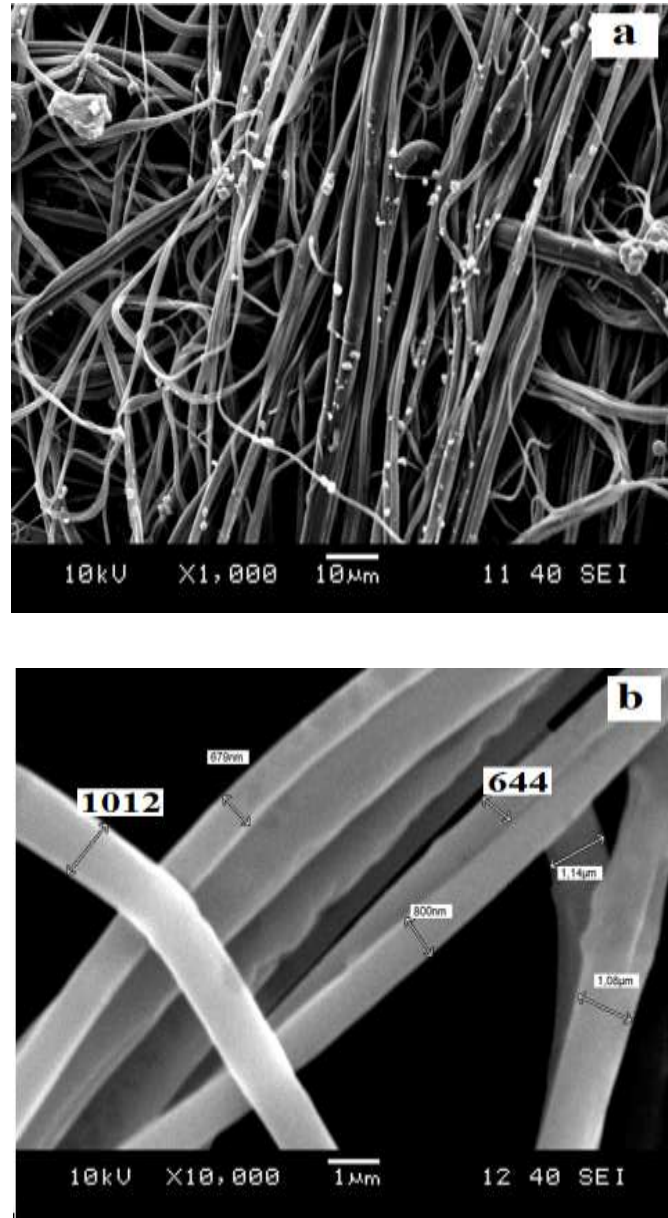


Figure 6.5 SEM images of EC based electrospun nanofibers (a), and (b); EC based nanofibers at different magnifications such as  $\times 1000$  and  $\times 10\,000$ .



### 6.2.3 Effect of pH

For specification, pH effect was investigated at different pH values for constant concentrations of Fe (III) ions. Figure 6.6 shows pH dependent response of ODC-1 dye to Fe (III) between pH 4.0-10.0. The absorption and emission characteristics of the ODC-1 dye are slightly affected from the pH of the environment. Notwithstanding the slight pH dependency, we investigated the optimum conditions of pH separately at constant concentrations of Fe (III) ions. Distribution of the Fe(III) related chemical species in the working conditions was theoretically checked with chemical equilibrium software program (Visual MINTEQ) at pH 5.5 in presence of acetate ions. The ion distribution was as following:  $[(\text{CH}_3\text{COO}^-: 85.01\%, \text{CH}_3\text{COOH}(\text{aq}): 14.99\%, \text{Fe}(\text{OH})^{2+}: 98.17\%, \text{Fe}(\text{OH})_3(\text{aq}): 0.017\%, \text{Fe}(\text{CH}_3\text{COO})^{2+}: 0.017\%$  and  $\text{FeOH}^+_{2}: 1.793\%]$ . The  $\text{Fe}^{3+}$  ions were in coordinated form  $(\text{Fe}(\text{OH}))^{+2}(\text{aq})$  and/or  $\text{Fe}(\text{OH})_2^+$  rather than naked  $\text{Fe}^{3+}(\text{aq})$ .

Due to the solubility considerations, acetic acid/acetate buffered solutions of pH 5.5 were chosen further studies.

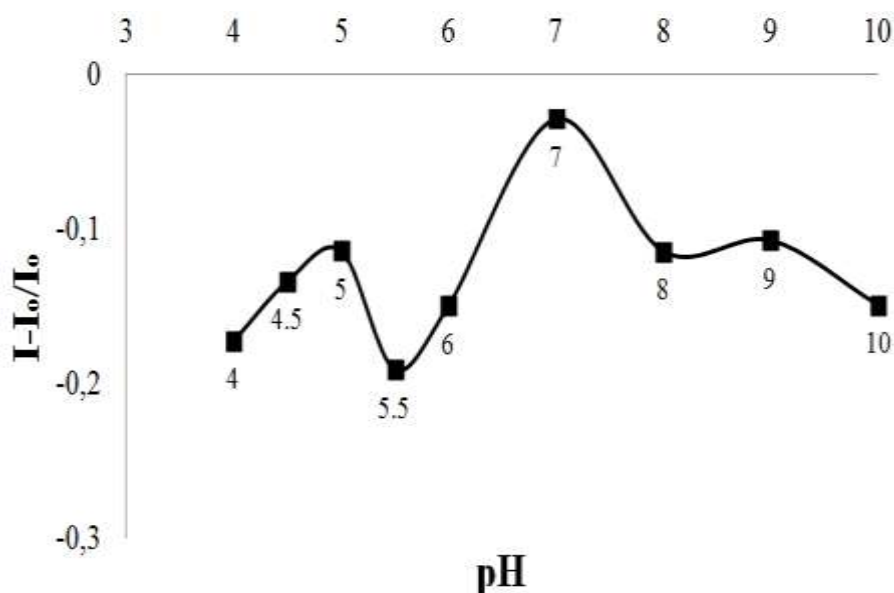


Figure 6.6 The pH dependency of ODC-1 dye in presence of Fe (III) ions between pH 4.0-10.0 using the EC based thin films.

#### 6.2.4 Dynamic Working Range and Response for Fe (III)

When doped into plasticized EC along with the anionic additive; potassium tetrakis-(4-chlorophenyl) borate; the ODC-1 dye becomes a Fe (III) selective probe. In this system, Fe (III) ions are selectively extracted into the optode membrane by the anionic additive meanwhile potassium ions diffuse from the membrane into the aqueous phase due to the mechanism of ion exchange. Physical aspect of the ion-exchange pathway can be explained by the following equation 6.1.

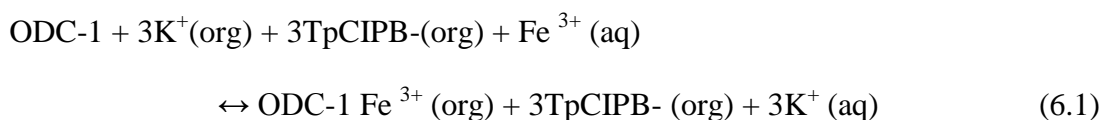


Figure 6.7 shows the absorption spectrum of the ODC-1 dye in the absence and presence of Fe (III) ions in THF. The absorption integral and wavelength in the presence of iron ions exhibited a slight change. This enhancement in the absorption integral cannot be concluded as a distinct evidence for complex formation and consequently static quenching.

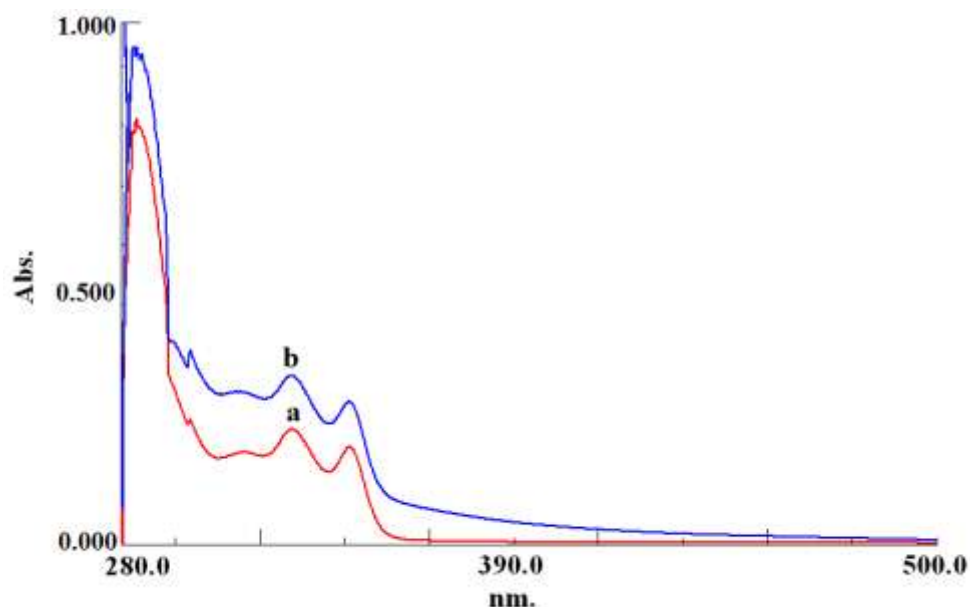


Figure 6.7 Absorption spectrum of the ODC-1 dye in THF (a) Fe (III) free, (b) in presence of  $5 \times 10^{-5}$  M Fe (III).

Figure 6.8 and 6.9 shows the change in fluorescence spectra of thin film and electrospun materials as a function of different concentrations of Fe (III) ions.

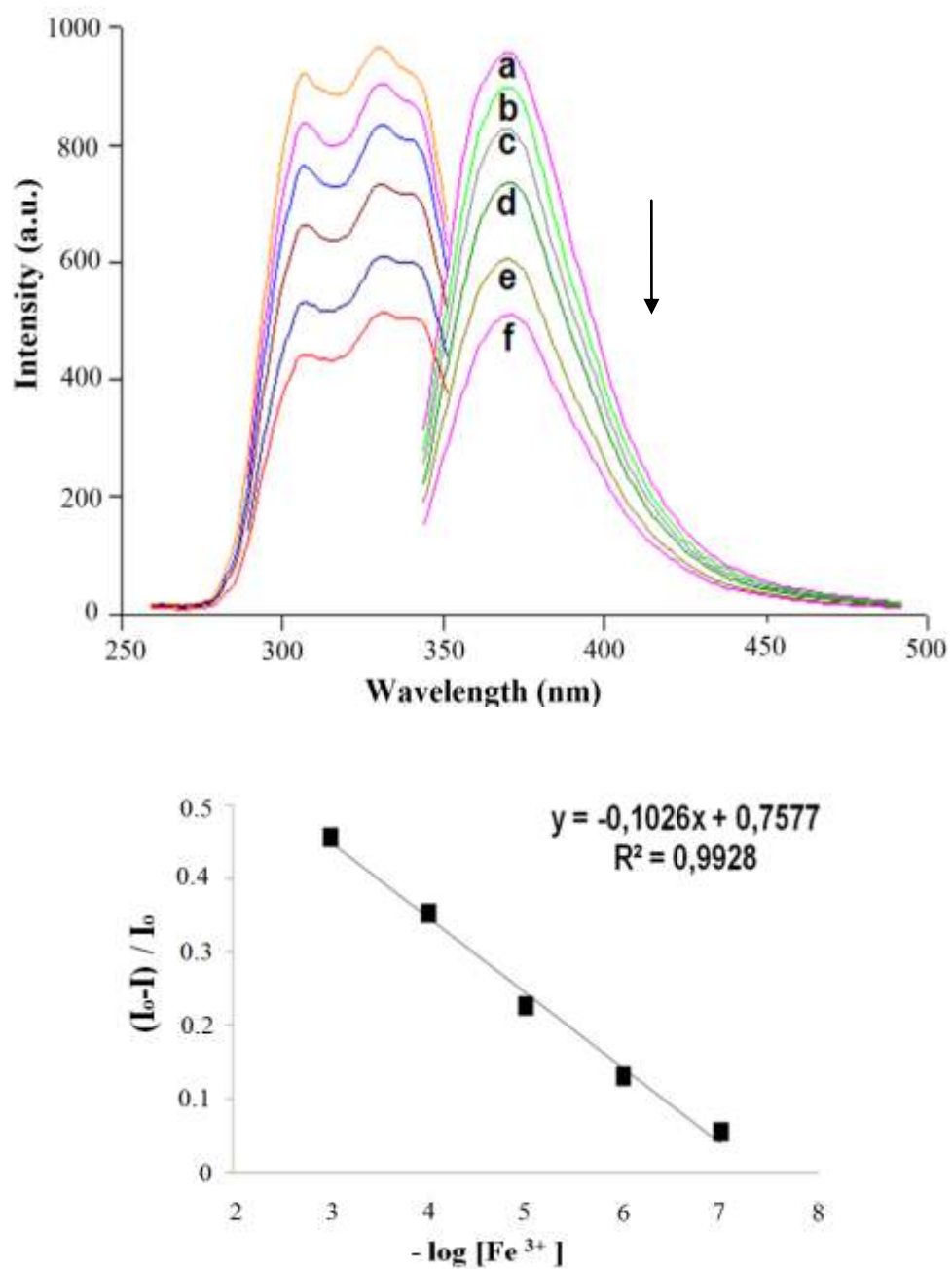


Figure 6.8 Fluorescence response of the ODC-1-doped EC based thin film to Fe (III) ions at pH 5.5. (a) Fe-free buffer (b)  $10^{-7}$ , (c)  $10^{-6}$ , (d)  $10^{-5}$ , (e)  $10^{-4}$ , (f)  $10^{-3}$  M Fe (III), and linearized calibration plot for the concentration range of  $10^{-7}$ - $10^{-3}$  M Fe (III).

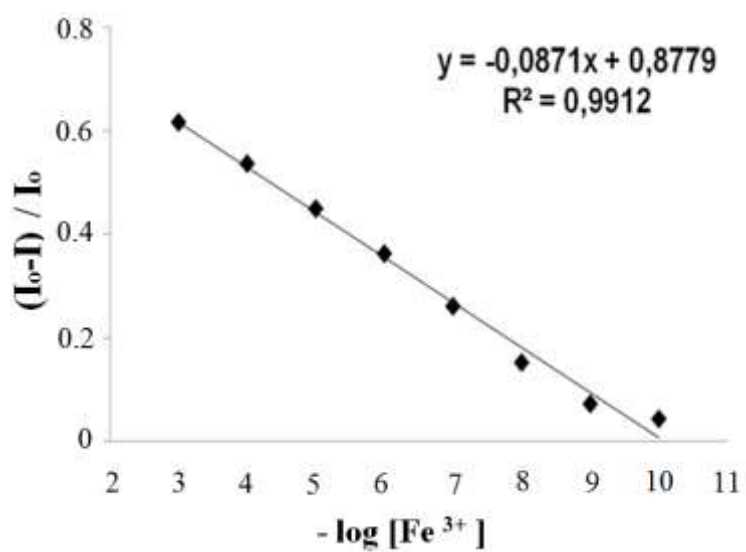
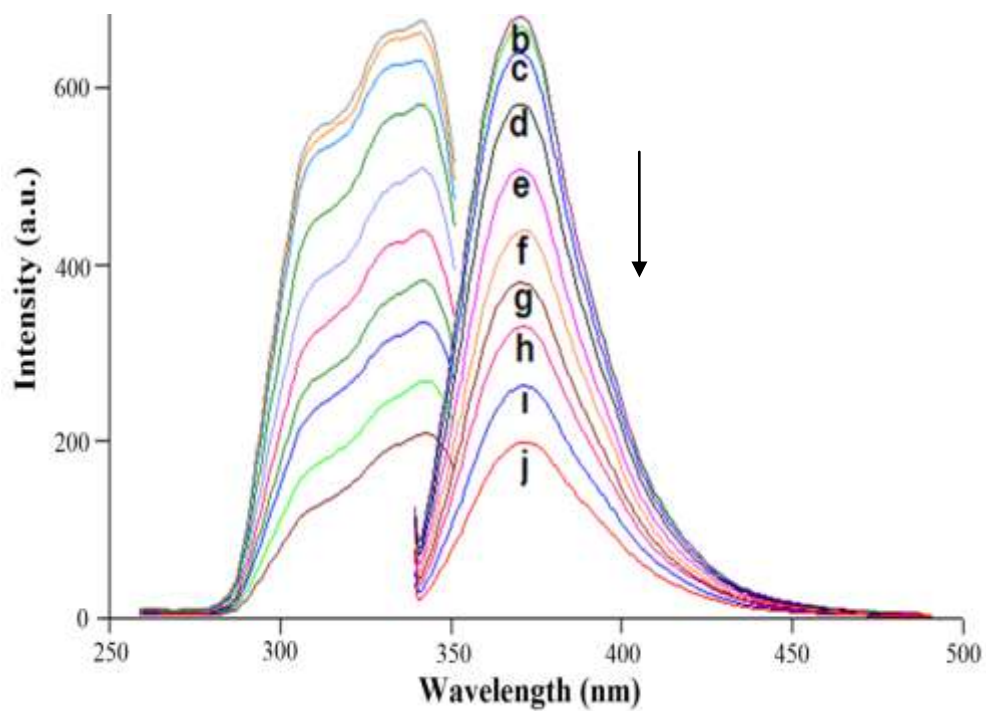


Figure 6.9 Fluorescence response of the ODC-1-doped EC based nanofiber to Fe (III) ions at pH 5.5.(a) Fe-free buffer (b)  $10^{-10}$ , (c)  $10^{-9}$ , (d)  $10^{-8}$ , (e)  $10^{-7}$ , (f)  $10^{-6}$ , (g)  $10^{-5}$ , (h)  $10^{-4}$ , (i)  $10^{-3}$ , (j)  $10^{-2}$  M Fe (III), and linearized calibration plot for the concentration range of  $10^{-10}$ - $10^{-3}$  M Fe (III).

The ODC-1 doped eletrospun nanofibers demonstrated a linear response over range of  $1 \times 10^{-10}$ - $1 \times 10^{-2}$  M for Fe (III) ions. Testing sensor compositions demonstrated large relative signal change, excellent linearity, and very good sensitivity to Fe (III) ions. The regression results yielded an absolute linear response with coefficients of regression ( $R^2$ ) of 0.9937 for EC electrospun nanofibers (See Table 6.3). The limit of detection (LOD) for Fe (III) was defined as the concentration at which the signal is equal to the blank signal ( $n = 20$ ) plus  $3\sigma$  and found to be  $2.40 \times 10^{-14}$  and  $2.70 \times 10^{-11}$  M for electrospun nanofiber and continuous thin films, respectively.

Table 6.3 gives a comparison of performance characteristics of thin film and nanofibers made up of same material in terms of working range, LOD, relative signal change and linearity.

Table 6.3 Calibration characteristics of EC based electrospun nanofibers and thin films.

Indicator Dye	Matrix /Form	Linear Range (Hg(II) Mol/L)	Regression Coefficient ( $R^2$ )	LOD (Molar)	% Relative Signal Changes
ODC-1	EC/nanofiber	$1.0 \times 10^{-10}$ to $1.0 \times 10^{-2}$	0.9937	$2.40 \times 10^{-14}$	72
	EC / thin film	$1.0 \times 10^{-7}$ to $1.0 \times 10^{-3}$	0.9928	$2.70 \times 10^{-11}$	45

### 6.2.5 Stern-Volmer Analysis

The data regarding results of the Stern-Volmer analysis for electrospun and continuous thin films were shown in Table 6.4. The electrospun nanofibers yielded an excellent Stern-Volmer relationship for quencher concentrations between  $1 \times 10^{-10}$ - $1 \times 10^{-5}$  M.  $K_{sv}$  value of the electrospun film, calculated from slope of the plot was found to be  $1.23 \times 10^4$  ( $M^{-1}$ ). This value is 14 fold greater than that obtained from the continuous thin films made up of the same material (See Table 6.4 and Figure 6.10).  $K_{sv}$  values reveal important consequences. The sensitivity of the quenching process

can be enhanced by controlling the quencher diffusion rate to fluorophores via the structural properties of the sensing materials.

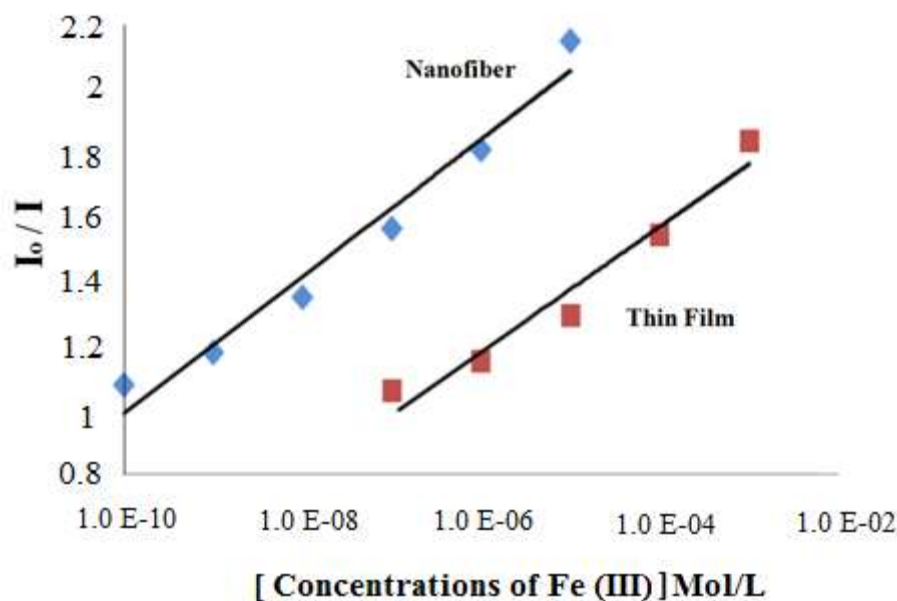


Figure 6.10 I: The Stern Volmer plots of EC based thin films, II: electrospun nanofibers in presence of the quencher.

Table 6.4  $K_{sv}$  Constant of EC based electrospun nanofibers and thin films for Fe (III) ions.

Indicator Dye	Matrix /Form	Linear Regression Equation (Fe (III) Mol/L)	$K_{sv}$ Constant
ODC-1	EC/ electrospun nanofiber	$y = 1231x + 1$	$1.23 \times 10^4$
	EC / thin film	$y = 889.53x + 1$	$8.89 \times 10^2$

### 6.2.6 Lifetime Analysis

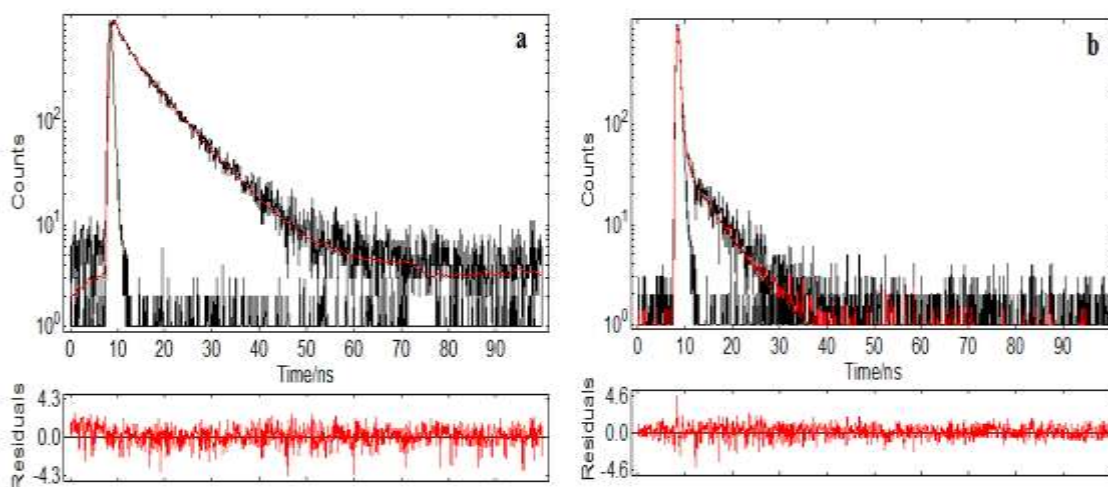
The excited state lifetimes of the ODC-1 in THF and in solid matrices, in the absence and presence of the quencher were shown in Table 6.5. The decay time data were obtained after excitation with a 367 nm pulsed laser and data acquisition at 380 nm. Both in solution phase and solid-state measurements, a dramatic decrease was observed in the decay times of the dye. In THF, the lifetime changed from 7950 to 46 ps. The lifetimes changed from 66 to 36 ps and from 30 to 11 ps in thin film and

nanofiber forms, respectively. These lifetime dependent data can be attributed to the dynamic component of the quenching.

Table 6.5 Fluorescence lifetimes of the carbazole derivative in THF, EC based thin films and electrospun nanofibers in the presence and absence of the quencher.

ODC - 1		Solvent		Thin Film		Nanofiber	
		Value (ns)	% Relative	Value (ps)	% Relative	Value (ps)	% Relative
Metal Free	$\tau_1$	1.91	14.78	66.78	100	30.02	100
	$\tau_2$	7.95	85.22	--	--	--	--
	$\tau_3$	--	--	--	--	--	--
		Value (ns)	% Relative	Value (ps)	% Relative	Value (ps)	% Relative
Fe (III)	$\tau_1$	0.05	70.89	36.65	100	11.66	100
	$\tau_2$	1.24	2.29	--	--	--	--
	$\tau_3$	6.15	26.82	--	--	--	--

When fluorescence intensity based response, absorption spectroscopy and lifetime related data were considered together, the mechanism between indicator dye and quencher can be concluded as ‘dynamic quenching’ of the ODC-1 dye by Fe (III) ions.



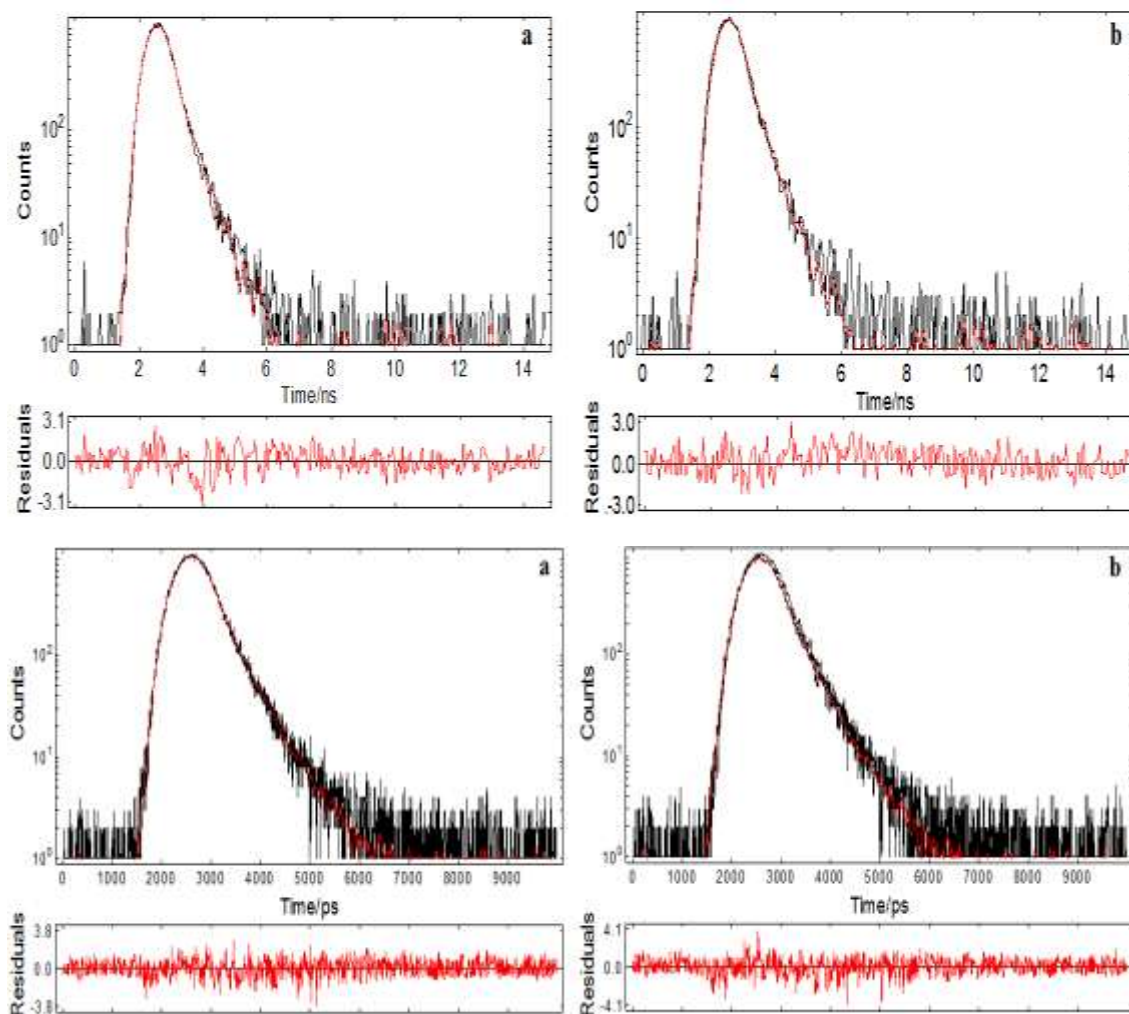


Figure 6.11 Decay curves of the exploited dye in THF, in thin film form and in form of nanofiber, respectively. In all cases, a and b show quencher free and quencher containing decay profiles. The dye excited at 367 nm with a picoseconds pulsed laser and intensity decay data accusation was performed at 370 nm.

### 6.2.7 Selectivity Studies

In order to examine the response of the dye to possible interfering cations, the sensing agents were treated with  $10^{-3}$  M concentrations of  $\text{Hg}^{2+}$  and  $\text{Hg}^+$ ,  $\text{Al}^{3+}$ ,  $\text{Ag}^+$ ,  $\text{Ca}^{2+}$ ,  $\text{Co}^{2+}$ ,  $\text{Cr}^{3+}$ ,  $\text{Cu}^{2+}$ ,  $\text{Fe}^{3+}$ ,  $\text{Fe}^{2+}$ ,  $\text{Li}^+$ ,  $\text{K}^+$ ,  $\text{Mn}^{2+}$ ,  $\text{Mg}^{2+}$ ,  $\text{Na}^+$ ,  $\text{NH}_4^+$ ,  $\text{Ni}^{2+}$ ,  $\text{Pb}^{2+}$  and  $\text{Zn}^{2+}$  ions in acetic acid/acetate buffer solutions at pH 5.5. The ODC-1 dye did not response to the major cations of water samples ( $\text{Ca}^{2+}$ ,  $\text{Mg}^{2+}$ ,  $\text{Na}^+$  and  $\text{K}^+$ ) and physiologically relevant fluids. We also tested interference effects of the conventional anions of  $\text{F}^-$ ,  $\text{Cl}^-$ ,  $\text{Br}^-$ ,  $\text{NO}_3^-$ ,  $\text{SO}_4^{2-}$  and  $\text{PO}_4^{3-}$ . Relative signal changes



of approximately 3 % were observed for EC doped films. The relative signal intensity changes caused by the tested potential interferents cations and anions were shown in Figure 6.12 (I) and (II). From following figures, it can be concluded that, the sensing design is capable of determining Fe (III) ions with a high selectivity over other ions. The fluorescence was dramatically decreased in the presence of iron ions exhibiting a relative signal change ratio of 98.5 %.

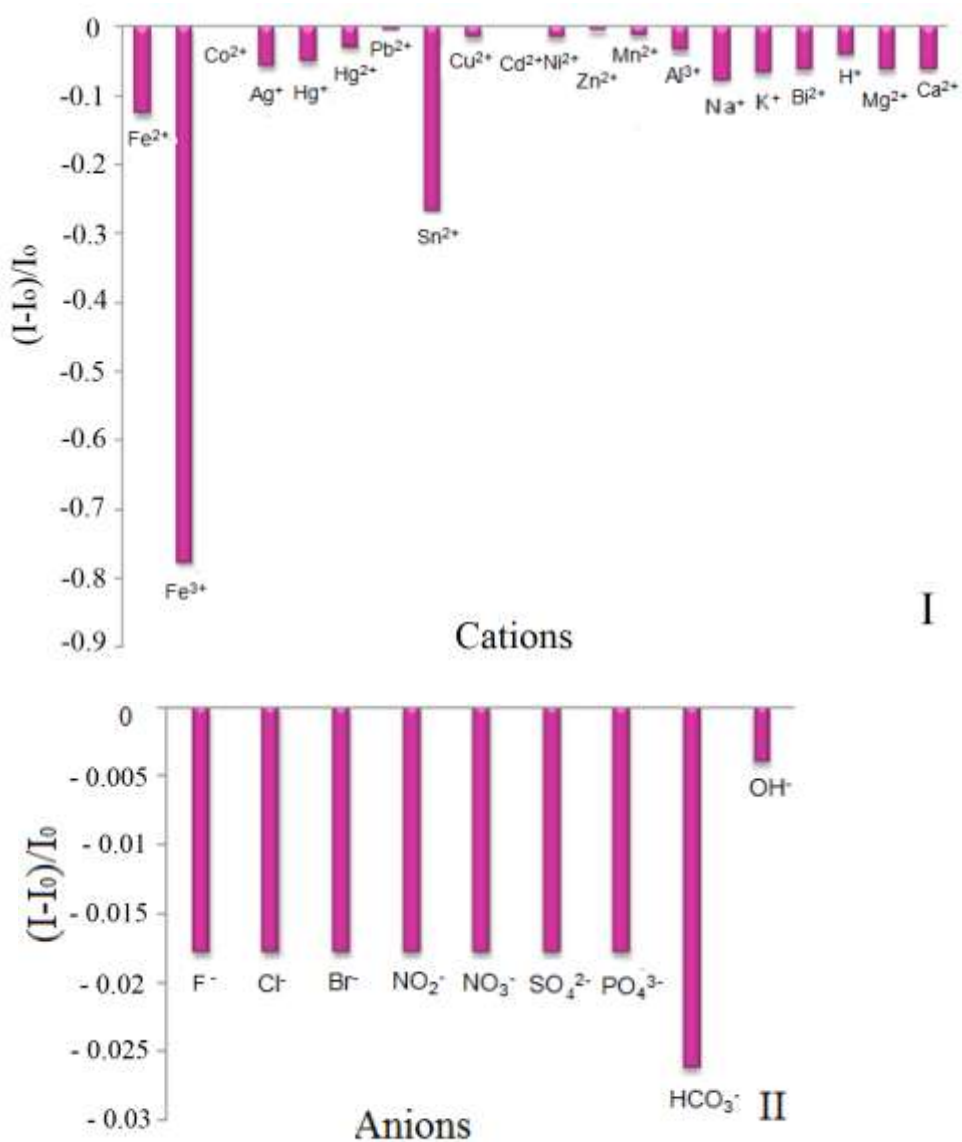


Figure 6.12 I: Metal-ion response of ODC-1 at pH 5.50. II: Response to the anions of the same composition at near neutral pH. Results were plotted as relative fluorescence changes;  $(I-I_0)/I_0$ .

### ***6.2.8 Recovery and Regeneration Studies in Real Groundwater Samples***

The performance of the sensing system for real samples was tested for the mineral water of Sarikiz (Sarikiz, Manisa; Turkey; Latitude: 38° 44' 83 N, Longitude: 28° 04' 84 E). The temperature of water from well was recorded as 17 °C. The content of Fe (III) in the diluted certified reference material of Merck (SRM from NIST FeCl<sub>3</sub> in HNO<sub>3</sub> 0.5 mol L<sup>-1</sup> 1000 mg L<sup>-1</sup> Fe CertiPUR®) was determined by exploiting the sensing electrospun nanofibers. All mineral water samples were collected in polyethylene vials degassed using ultrasonic bath and analyzed as soon as possible. The recovery experiments were carried out adding 1×10<sup>-7</sup> M of certified reference material into the mineral water. The average concentration of the Fe (III) was found to be 3.8×10<sup>-7</sup> M for 10 replicate measurements. The recovery performance was found to be 104 ± 0.6%. These results reveal the capability of the offered sensing design for the determination of mercury ions in real samples without considerable error.

### ***6.2.9 Conclusion***

The fluorophore ODC-1 is shown to be a highly selective reagent for the determination of Fe (III) ion at sub-nanomolar (picomolar) level. The fluorescence of ODC-1 is dynamically quenched by Fe (III) ions. A dynamic working range of iron (III) determination from 1.0×10<sup>-10</sup> to 1.0×10<sup>-2</sup> M was obtained. Electrospinning resembles a promising, simple, and an effective method for fabricating polymer based chemosensors. With respect to continuous thin films, electrospun nanomaterials provided enhanced sensitivity and reactivity in emission based iron sensing.

### 6.3 Response of ODC-3 to Fe (III) Ions

#### 6.3.1 Dynamic Working Range and Response for Fe (III)

Spectral characterization and Hg (II) response of this dye was discussed earlier in Chapter 3. The mercury sensitive dye also exhibits a considerable response for Fe(III) ions. In earlier chapter, we concluded the Fe (III) ions as potential interferents and offered to mask exploiting citrate buffer. In this part of chapter, we researched response of the ODC-3 dye to the Fe (III) ions into detail. However, it should be mentioned that, the dye could only work as an iron probe in the absence of ionic mercury. Otherwise, the Hg (II) will act as a potential interferent. In this case, thiocyanate has been used for masking of ionic mercury around pH 5-6. The complex between thiocyanate and ionic mercury is so strong that, the added thiocyanate can decompose the mercury-EDTA complex and liberate the EDTA (Raoot, K.N., Raoot, S., & Kumari, 1983). Figure 6.13 shows the absorption characteristics of the ODC-5 in THF in the absence and presence of the quencher. When Fe (III) ions were added into the THF, the absorption integral significantly enhances. This can be evidence of a complex formation between the analyte and the dye.

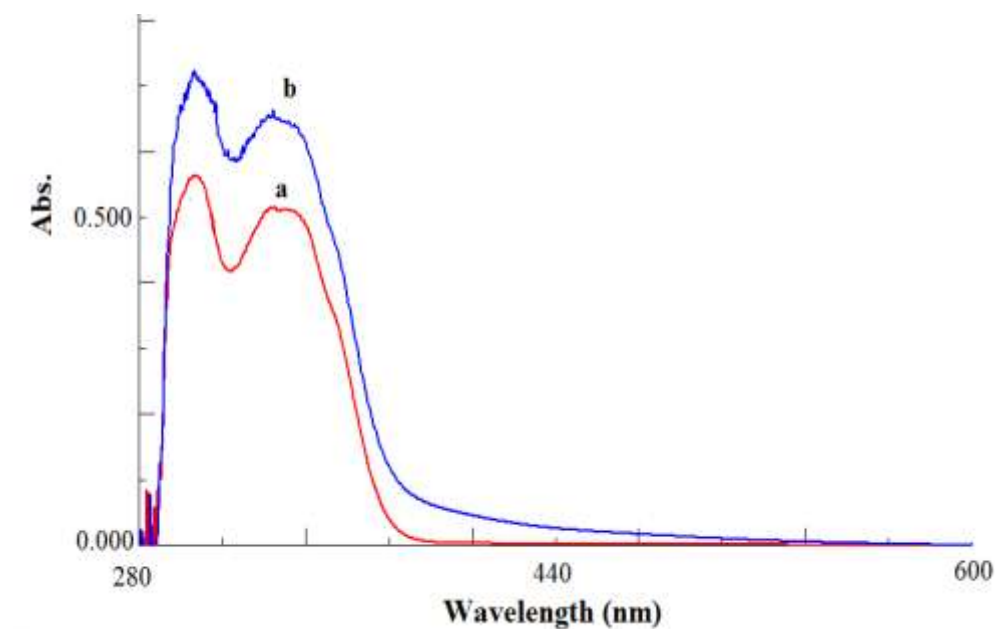


Figure 6.13 Absorption spectrum of the ODC-3 dye in THF (a) Fe (III) free, (b) in presence of  $5 \times 10^{-5}$  M Fe (III).

Figure 6.14 shows pH dependency of the ODC-3 dye when exposed to constant amount of  $10^{-5}$  M Fe (III) ions in the pH range of 4.0 – 6.0. The intensity-based results were acquired with EC based thin films. Further studies were performed at pH 5.0.

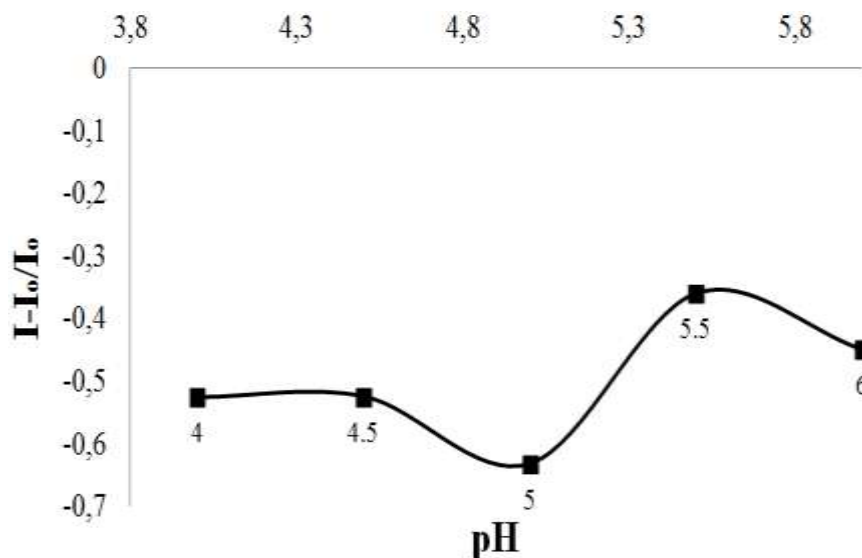


Figure 6.14 The pH dependency of ODC-3 dye in presence of Fe (III) ions between pH 4.0-6.0 using the EC based thin films.

When doped into plasticized EC along with the anionic additive; potassium tetrakis-(4-chlorophenyl) borate; the ODC-3 dye acts as a Fe (III) selective probe. In this system, Fe (III) ions selectively extracted into the optode membrane by the anionic additive, meanwhile three potassium ions diffuse from the membrane into the aqueous phase due to the mechanism of ion exchange.

Figure 6.15 and 6.16 reveal emission based response of ODC-3 dye in embedded form in EC matrix.

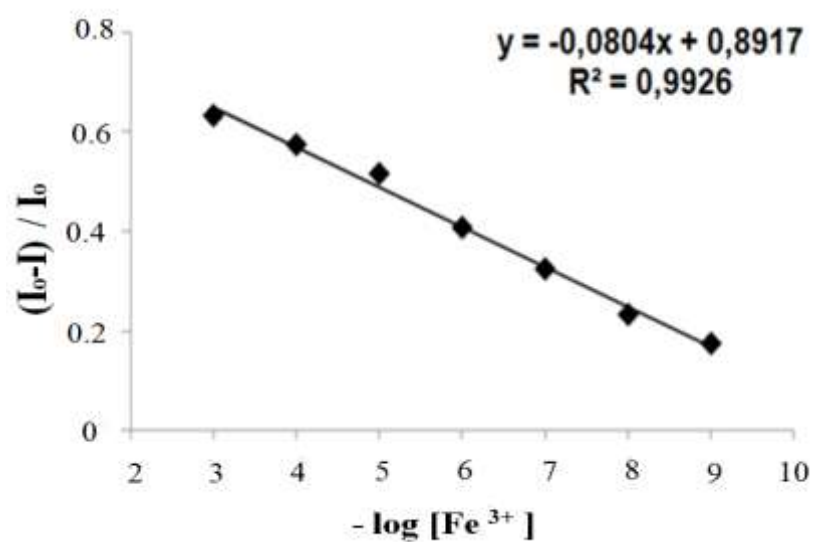
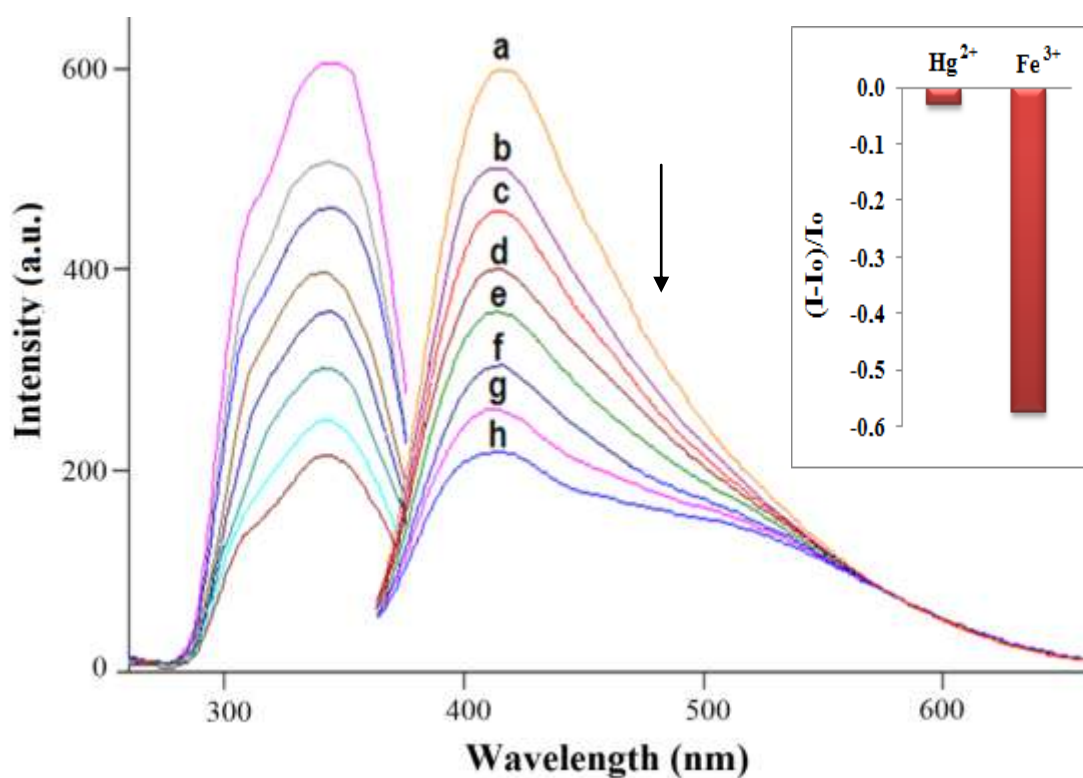


Figure 6.15 Excitation - emission spectra of thin film. Emission based response of the ODC-3 doped EC based thin film to different concentrations of Fe (III) and linearized calibration curve at pH=5.0. (a) Buffer, (b) 10<sup>-9</sup>, (c) 10<sup>-8</sup>, (d) 10<sup>-7</sup>, (e) 10<sup>-6</sup>, (f) 10<sup>-5</sup>, (g) 10<sup>-4</sup>, (h) 10<sup>-3</sup> mol/L. Inset: Response to Fe (III) when the potential interferent ionic mercury has been suppressed with thiocyanate.

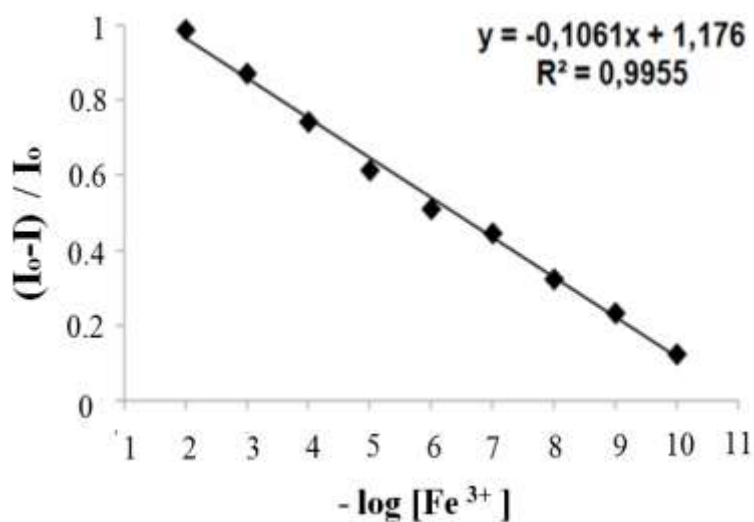
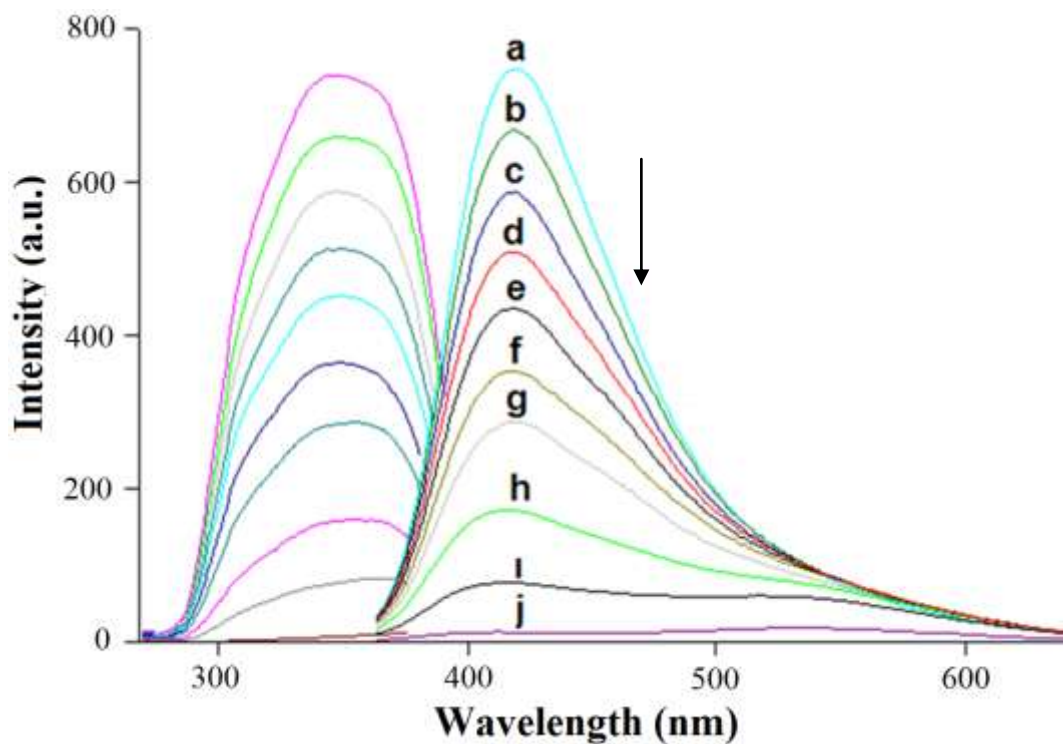


Figure 6.16 Excitation- emission spectra of electrospun fibers. Emission based response of the ODC-3 doped EC based nanofiber to different concentrations of Fe (III) and linearized calibration curve at pH=5.0. (a) Buffer, (b)  $10^{-10}$ , (c)  $10^{-9}$ , (d)  $10^{-8}$ , (e)  $10^{-7}$ , (f)  $10^{-6}$ , (g)  $10^{-5}$ , (h)  $10^{-4}$ , (i)  $10^{-3}$ , (j)  $10^{-2}$  mol/L.

The ODC-3 doped eletrospun nanofibers demonstrated a linear response over range of  $1 \times 10^{-10}$ - $1 \times 10^{-2}$  M for Fe (III) ions. Testing sensor compositions demonstrated large relative signal change, excellent linearity, and very good sensitivity to Fe (III) ions with an LOD value of  $2.20 \times 10^{-14}$  M. The regression results yielded an absolute linear response with coefficients of regression ( $R^2$ ) of 0.9955 for EC electrospun nanofibers (See Table 6.6). The limit of detection (LOD) for Fe (III) was defined as the concentration at which the signal is equal to the blank signal ( $n = 20$ ) plus  $3\sigma$  and found to be  $2.20 \times 10^{-14}$  and  $2.20 \times 10^{-13}$  M for electrospun nanofiber and continuous thin films, respectively.

Table 6.6 gives a comparison of performance characteristics of thin film and nanofibers made up of same material in terms of working range, LOD, relative signal change and linearity.

Table 6.6 Calibration characteristics of EC based electrospun nanofibers and thin films.

Indicator Dye	Matrix /Form	Linear Range (Hg(II) Mol/L)	Regression Coefficient ( $R^2$ )	LOD (Molar)	% Relative Signal Changes
ODC-3	EC/nanofiber	$1.0 \times 10^{-10}$ to $1.0 \times 10^{-2}$	0.9955	$2.20 \times 10^{-14}$	98.5
	EC / thin film	$1.0 \times 10^{-9}$ to $1.0 \times 10^{-3}$	0.9926	$2.20 \times 10^{-13}$	63.5

### 6.3.2 Stern-Volmer Analysis

The data regarding results of the Stern-Volmer analysis for electrospun and continuous thin films were shown in Table 6.7. The electrospun nanofibers yielded quite good Stern-Volmer relationships for quencher concentrations between  $1 \times 10^{-10}$ - $1 \times 10^{-5}$  M.  $K_{sv}$  value of the electrospun film, calculated from slope of the plot was found to be  $1.23 \times 10^4$  ( $M^{-1}$ ). This value is 91 fold greater than that obtained from the continuous thin film slides (See Table 6.7 and Figure 6.17).  $K_{sv}$  values reveal important practical results. As evidence with experiments, the sensitivity of the

quenching process can be enhanced by controlling the quencher diffusion rate to fluorophores via the structural properties of the sensing materials.

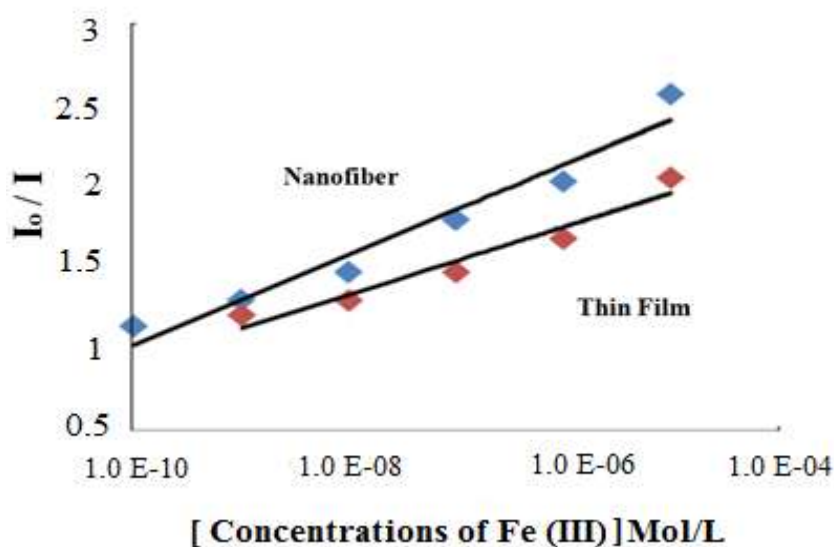


Figure 6.17 I: The Stern Volmer plots of EC based thin films, II: electrospun nanofibers in presence of the quencher.

Table 6.7  $K_{sv}$  Constant of EC based electrospun nanofibers and thin films for Fe (III) ions.

Indicator Dye	Matrix /Form	Linear Regression Equation (Fe (III) Mo/L)	$K_{sv}$ Constant
ODC-3	EC/ electrospun nanofiber	$y = 168602x + 1$	$1.68 \times 10^5$
	EC / thin film	$y = 1855.3x + 1$	$1.85 \times 10^3$

When fluorescence intensity based response, absorption spectroscopy and lifetime measurements related data were evaluated together, the mechanism between indicator dye and sensing agent can be concluded as quenching of the ODC-3 dye by Fe (III) ions.

If a plot of  $I_0/I$  versus concentration of the quencher has an upward curvature, it is the evidence of combined quenching both by collisions (dynamic quenching) and by complex formation (static quenching) with the same quencher (Lakowicz, 2006). The non-linearized data observed in Figure 6.17 exhibits both static and dynamic quenching is occurring in the sample.



### 6.3.3 Lifetime Analysis

The excited state lifetimes of the ODC-3 in THF and in solid matrices, in the absence and presence of the quencher were shown in Table 6.8. In solution phase and solid-state measurements there is a very slight change in the lifetimes. In THF, the decay times were changed from 2.90 to 3.21 ns, in absence and presence of the quencher. In nanofiber forms, presence of quencher did not significantly disturb the lifetimes. These experimental results can be attributed to the static component of the quenching. The slight enhancement in the absorption integral in presence of Fe (III) ions also supports static quenching. However, slightly upward characteristic of the non-linearized Stern-Volmer plot can be concluded as evidence of both, dynamic quenching component and matrix in homogeneity. As a result, the mechanism of quenching can be predominantly concluded as ‘static’.

Table 6.8 Florescence lifetimes of the carbazole derivative in THF, EC based thin films and electrospun nanofibers in the presence and absence of the quencher.

ODC - 3		Solvent		Thin Film		Nanofiber	
		Value (ns)	% Relative	Value (ns)	% Relative	Value (ns)	% Relative
Metal Free	$\tau_1$	2.90	100	0.36	16.38	0.34	2.56
	$\tau_2$	--	--	1.31	55.71	1.80	53.41
	$\tau_3$	--	--	3.69	27.91	3.20	44.02
		Value (ns)	% Relative	Value (ns)	% Relative	Value (ns)	% Relative
Fe (III)	$\tau_1$	0.39	7.28	0.30	28.79	0.28	2.71
	$\tau_2$	3.21	92.72	1.23	57.22	1.50	41.29
	$\tau_3$	--	--	4.59	13.98	3.00	56.00

### ***6.3.4 Recovery and Regeneration Studies in Real Groundwater Samples***

The performance of the sensing system for real samples was tested for the mineral water of Sarikiz. The temperature of water from well was recorded as 17 °C. The content of Fe (III) in the diluted certified reference material of Merck (SRM from NIST FeCl<sub>3</sub> in HNO<sub>3</sub> 0.5 mol L<sup>-1</sup> 1000 mg L<sup>-1</sup> Fe CertiPUR®) was determined by exploiting the sensing electrospun nanofibers. The recovery experiments were carried out adding 1×10<sup>-7</sup> M of certified reference material into the mineral water.

The average concentration of the Fe (III) was found to be 3.9×10<sup>-7</sup> M for 10 replicate measurements. The recovery performance was found to be 104 ± 0.5%. These results reveal the capability of the offered sensing design for the determination of mercury ions in real samples without considerable error.

### ***6.3.5 Conclusion***

The fluorophore ODC-3 is shown to be a highly selective reagent for the determination of Fe (III) ion at sub-nanomolar (picomolar) level. The fluorescence of ODC-3 is dynamically quenched by Fe (III) ions. A dynamic working range of iron (III) determination from 1.0×10<sup>-10</sup> to 1.0×10<sup>-2</sup> M was obtained. Electrospinning resembles a promising, simple, and an effective method for fabricating polymer based chemosensors. With respect to continuous thin films, electrospun nanomaterials provided enhanced sensitivity and reactivity in emission based iron sensing.

## 6.4 Response of ODC-5 to Fe (III) Ions

### 6.4.1 *Dynamic Working Range and Response for Fe (III)*

As you may remember, structural properties of ODC-3 and ODC-5 were similar except that of a substituted group on the carbazole moiety. These two dyes exhibited similar spectral characteristics and sensing properties for the analytes of Hg (II) and Fe (III). However, exploiting the analytical techniques, such as masking or adjusting the pH, sub-nanomolar sensing of both Hg (II) and Fe (III) have been performed in separate solutions.

Spectral characterization and Hg (II) response of this dye was discussed earlier in Chapter 3. The ODC-5 dye also exhibits a distinct response for Fe (III) ions. In the earlier chapter, we concluded the Fe (III) ions as potential interferent and masked exploiting citrate buffer. In this part of chapter, we investigated response of the dye to the Fe (III) ions into detail. It should be mentioned that, the dye could only work as an iron probe in the absence of ionic mercury. Otherwise, the Hg (II) will act as a potential interferent. Figure 6.18 shows the absorption characteristics of the ODC-5 in THF in the absence and presence of the quencher. When Fe (III) ions were added into the THF, the absorption integral significantly enhances. This can be evidence of a complex formation between the analyte and the dye.

In order to prevent the interference of Hg (II) in iron sensing, thiocyanate has been used as a masking agent for ionic mercury around pH 5-6. As mentioned earlier, the complex between thiocyanate and ionic mercury is so strong that, the added thiocyanate can decompose the mercury-EDTA complex and liberate the EDTA (Raoot, K.N., Raoot, S., & Kumari, 1983).

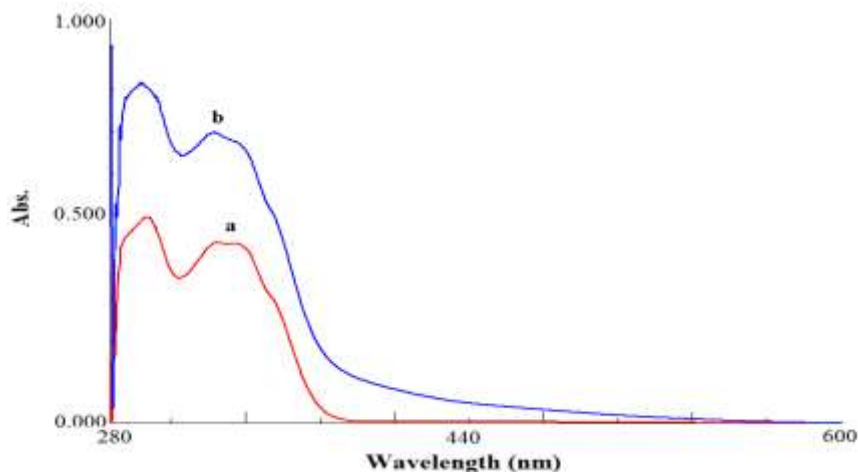


Figure 6.18 Absorption spectrum of the ODC-5 dye in THF (a) Fe (III) free, (b) in presence of  $5 \times 10^{-5}$  M Fe (III).

Figure 6.19 shows pH dependency of the ODC-5 dye when exposed to constant amount of  $10^{-5}$  M Fe(III) ions in the pH range of 4.0– 6.0. The intensity-based results were acquired with EC based thin films. Further studies were performed at pH 5.0.

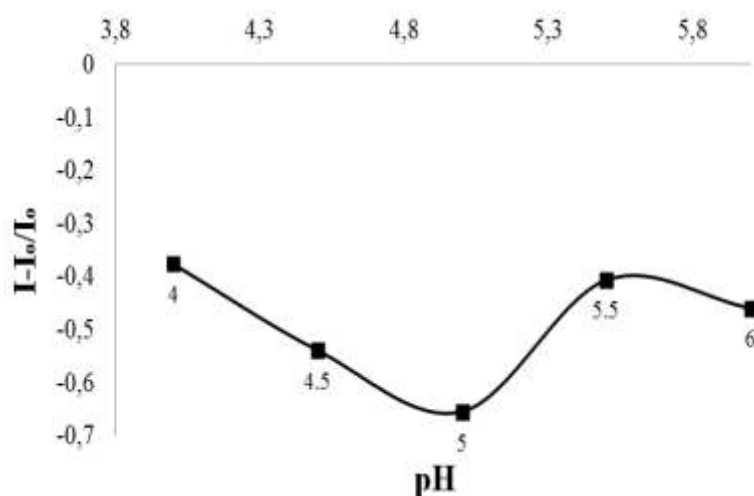


Figure 6.19 The pH dependency of ODC-5 dye in presence of Fe (III) ions between pH 4.0-6.0 using the EC based thin films.

Figure 6.20 and 6.21 reveal emission based response of ODC-5 dye in embedded form in EC matrix. The dye exhibited an excellent response to Fe (III) ions with relative signal changes of 80 and 95% for thin film and nanofiber forms, respectively. The concentration ranges were calculated as  $1.0 \times 10^{-9}$  to  $1.0 \times 10^{-3}$  and  $1.0 \times 10^{-11}$  to  $1.0 \times 10^{-3}$  for thin film and nanofiber-based sensors.

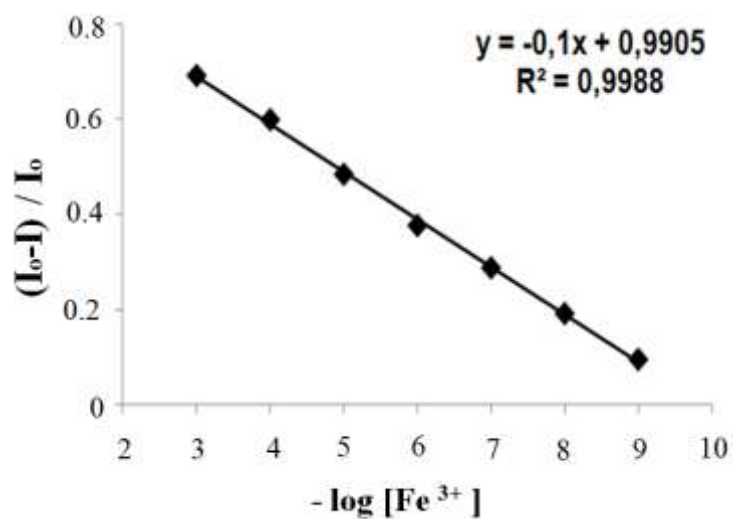
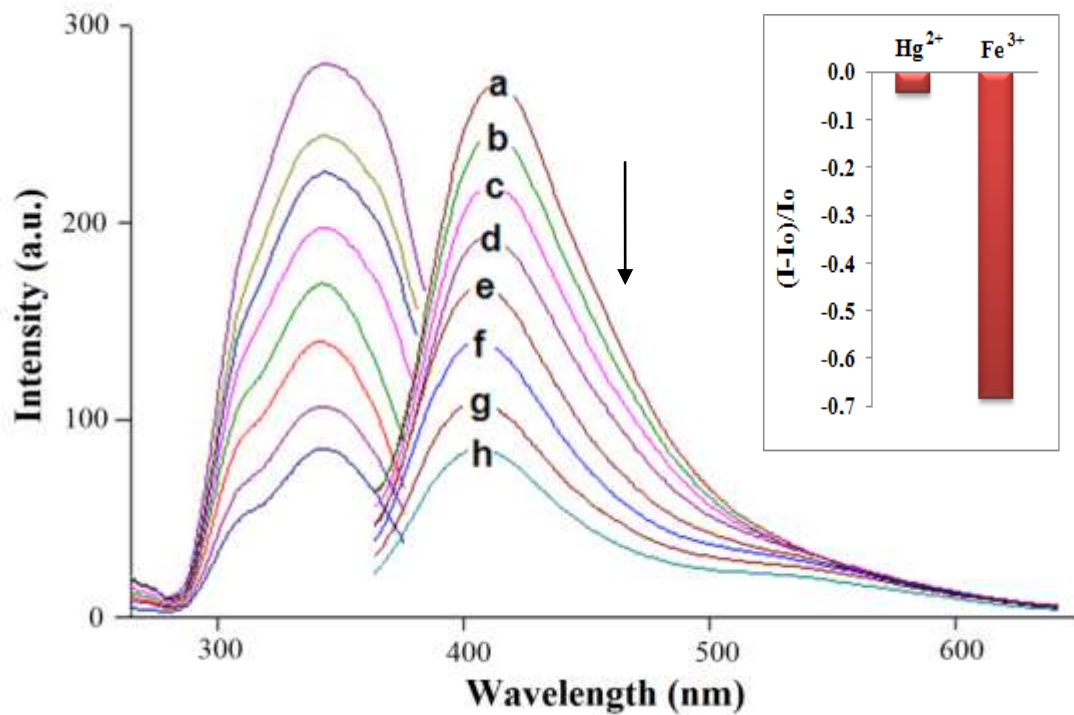


Figure 6.20 Fluorescence response of the ODC-5-doped EC based thin film to Fe (III) ions at pH 5.0. (a) Fe-free buffer, (b) 10<sup>-9</sup>, (c) 10<sup>-8</sup>, (d) 10<sup>-7</sup>, (e) 10<sup>-6</sup>, (f) 10<sup>-5</sup>, (g) 10<sup>-4</sup>, (h) 10<sup>-3</sup> mol/L Fe (III) and linearized calibration plot for the concentration range of 10<sup>-9</sup>-10<sup>-3</sup> M Fe (III). Inset: Response to Fe (III) when the potential interferent ionic mercury has been suppressed with thiocyanate.

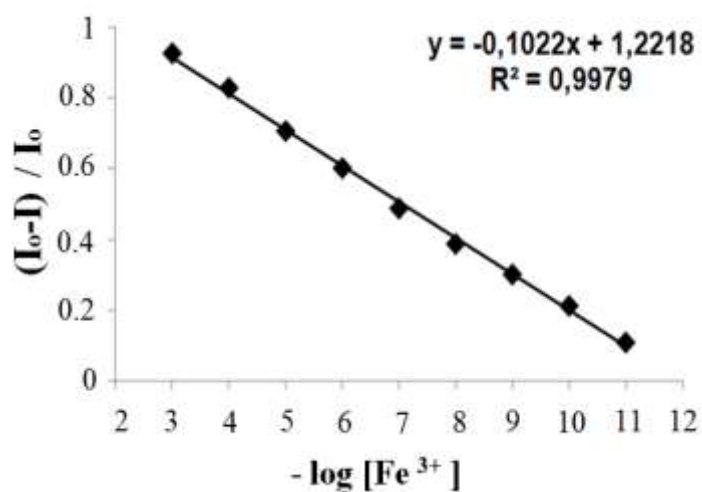
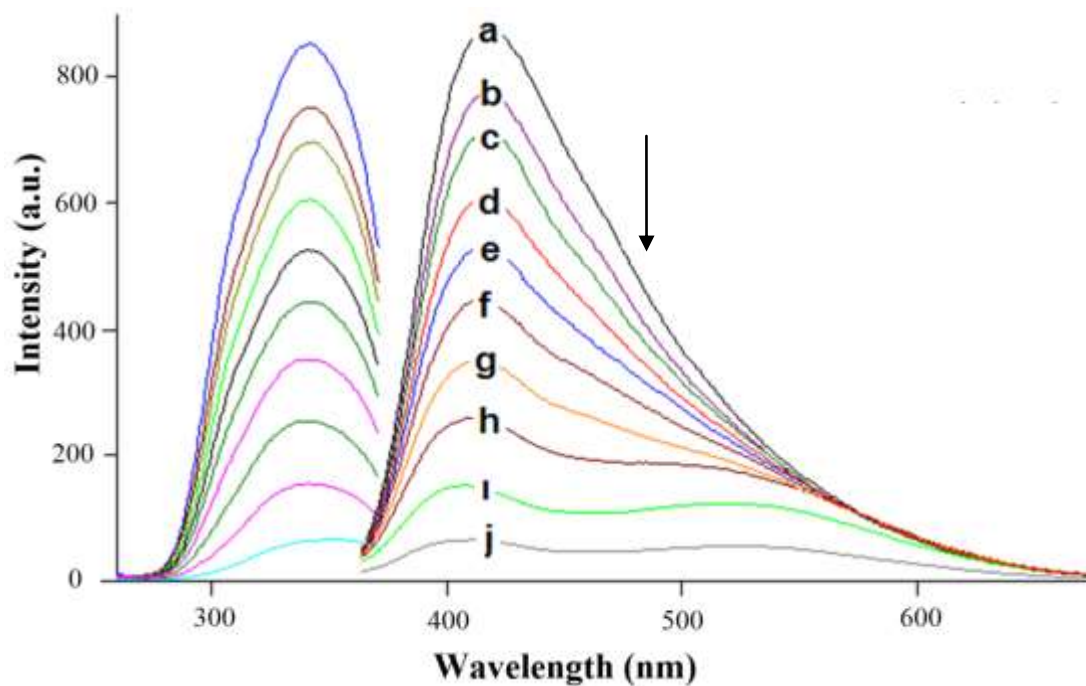


Figure 6.21 Fluorescence response of the ODC-5-doped EC based nanofiber to Fe (III) ions at pH 5.0. (a) Fe-free buffer, (b)  $10^{-11}$ , (c)  $10^{-10}$ , (d)  $10^{-9}$ , (e)  $10^{-8}$ , (f)  $10^{-7}$ , (g)  $10^{-6}$ , (h)  $10^{-5}$ , (i)  $10^{-4}$ , (j)  $10^{-3}$  mol/L Fe (III) and linearized calibration plot for the concentration range of  $10^{-11}$ - $10^{-3}$  M Fe (III).

The ODC-5 doped eletrospun nanofibers demonstrated a linear response over range of  $1 \times 10^{-11}$ - $1 \times 10^{-3}$  M for Fe (III) ions. Testing sensor compositions are demonstrated large relative change signal, excellent linearity, and very good sensitivity to Fe (III) ions. The regression results yielded an absolute linear response with coefficients of regression ( $R^2$ ) of 0.9979 for EC electrospun nanofibers (See Table 6.9). The limit of detection (LOD) for Fe (III) was defined as the concentration at which the signal is equal to the blank signal ( $n = 20$ ) plus  $3\sigma$  and found to be  $2.50 \times 10^{-15}$  and  $8.10 \times 10^{-12}$ M for electrospun nanofiber and continuous thin films, respectively.

Table 6.9 gives a comparison of performance characteristics of thin film and nanofibers made up of same material in terms of working range, LOD, relative signal change and linearity.

Table 6.9 Calibration characteristics of EC based electrospun nanofibers and thin films.

Indicator Dye	Matrix /Form	Linear Range (Hg(II) Mol/L)	Regression Coefficient ( $R^2$ )	LOD (Molar)	% Relative Signal Changes
ODC-5	EC/nanofiber	$1.0 \times 10^{-11}$ to $1.0 \times 10^{-3}$	0.9979	$2.50 \times 10^{-15}$	92.5
	EC / thin film	$1.0 \times 10^{-9}$ to $1.0 \times 10^{-3}$	0.9988	$8.10 \times 10^{-12}$	69.5

#### 6.4.2 Stern-Volmer Analysis

The data extracted from the Stern-Volmer plots for electrospun and continuous thin films were shown in Table 6.10. The electrospun nanofibers yielded a linearizable Stern-Volmer relationship for quencher concentrations between  $1 \times 10^{-11}$ - $1 \times 10^{-6}$  M.  $K_{sv}$  value of the electrospun film, calculated from slope of the plot was found to be  $2.53 \times 10^5$  ( $M^{-1}$ ). This value is 106 fold of the  $K_{SV}$  obtained from the continuous thin film slides (See Table 6.10 and Figure 6.22). Shape of Stern-Volmer plots reveals important results.

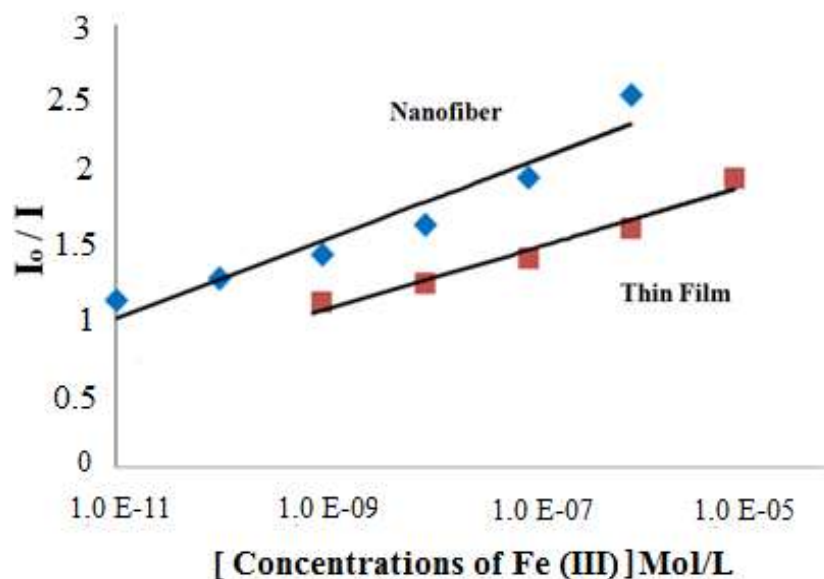


Figure 6.22 I: The Stern Volmer plots of EC based thin films, II: electrospun nanofibers in presence of the quencher.

Table 6.10 K<sub>sv</sub> Constant of EC based electrospun nanofibers and thin films for Fe (III) ions.

Indicator Dye	Matrix /Form	Linear Regression	K <sub>sv</sub> Constant
		Equation (Fe (III) Mol/L)	
ODC-5	EC/ electrospun nanofiber	$y = 253375x + 1$	$2.53 \times 10^5$
	EC / thin film	$y = 2389x + 1$	$2.38 \times 10^3$

When fluorescence intensity based response, absorption spectroscopy and lifetime measurements related data were evaluated together, the mechanism between indicator dye and sensing agent can be concluded as quenching of the ODC-5 dye by Fe (III) ions.

If a plot of I<sub>0</sub>/I versus concentration of the quencher has an upward curvature, it is the evidence of combined quenching both by collisions (dynamic quenching) and by complex formation (static quenching) with the same quencher (Lakowicz, 2006). The non-linearized data observed in Figure 6.22 exhibits both static and dynamic quenching is occurring in the sample.



### 6.4.3 Lifetime Analysis

The excited state lifetimes of the ODC-5 in THF and in solid matrices, in the absence and presence of the quencher were shown in Table 6.11. The dye exhibited biexponential and three exponential lifetimes in THF, thin film and nanofiber forms, respectively. The decay times did not exhibit a significant change in THF upon exposure to quencher (from 3.1 to 3.2 ns). A similar behavior was also observed in nanofibers (See Table 6.11). Results obtained from solution phase and solid-state measurements can be attributed to the static quenching in excited state in the presence of the Fe (III) ions. The slightly upward concave characteristics of the Stern-Volmer plot can be interfered to the matrix in homogeneity. As a result, the mechanism of quenching can be predominantly concluded as ‘static’.

Table 6.11 Florescence lifetimes of the carbazole derivative in THF, EC based thin films and electrospun nanofibers in the presence and absence of the quencher.

ODC - 5		Solvent		Thin Film		Nanofiber	
		Value (ns)	% Relative	Value (ns)	% Relative	Value (ns)	% Relative
Metal Free	$\tau_1$	2.28	28.54	1.00	46.43	0.40	11.45
	$\tau_2$	3.15	71.46	2.86	53.57	1.55	53.82
	$\tau_3$	--	--	-	--	3.25	34.72
		Value (ns)	% Relative	Value (ns)	% Relative	Value (ns)	% Relative
Fe (III)	$\tau_1$	0.34	4.55	0.69	49.74	0.55	7.57
	$\tau_2$	3.22	95.45	2.49	50.26	1.73	65.11
	$\tau_3$	--	--	--	--	3.44	27.33

### 6.4.4 Recovery and Regeneration Studies in Real Groundwater Samples

The performance of the sensing system for real samples was tested for the mineral water of Sarikiz. The temperature of water from well was recorded as 17 °C. The content of Fe (III) in the diluted certified reference material of Merck (SRM from NIST FeCl<sub>3</sub> in HNO<sub>3</sub> 0.5 mol L<sup>-1</sup> 1000 mg L<sup>-1</sup> Fe CertiPUR®) was determined by

exploiting the sensing electrospun nanofibers. The recovery experiments were carried out adding  $1 \times 10^{-7}$  M of certified reference material into the mineral water. The average concentration of the Fe (III) was found to be  $1.8 \times 10^{-7}$  M for 10 replicate measurements. The recovery performance was found to be  $102 \pm 0.8\%$ . These results reveal the capability of the offered sensing design for the determination of mercury ions in real samples without considerable error.

#### **6.4.5 Conclusion**

The fluorophore ODC-5 is shown to be a highly selective reagent for the determination of Fe (III) ion at sub-nanomolar (picomolar) level. The fluorescence of ODC-5 is dynamically quenched by Fe (III) ions. A dynamic working range of iron (III) determination from  $1.0 \times 10^{-10}$  to  $1.0 \times 10^{-2}$  M was obtained. Electrospinning resembles a promising, simple, and an effective method for fabricating polymer based chemosensors. With respect to continuous thin films, electrospun nanomaterials provided enhanced sensitivity and reactivity in emission based iron sensing.

### **6.5 Design of a Fluorescent Optical Sensor Using Nanofibers for Fe (III)**

In this part of thesis, we reported the usage of Fe (III) sensitive dye 2- $\{(E)-[(4\text{-bromo-2,6-dimethylphenyl)imino]methyl}\}$ phenol (MS-4) in form of electrospun polymer fibers as highly responsive fluorescent optical sensors. Chemical structure of the exploited dye was shown in Figure 6.23.

The sensing agents were doped into poly-methyl-methacrylate (PMMA) together with ionic liquid and other additives as usual. Composite fibers were fabricated by electrospinning and characterized by SEM. PMMA based nanofibers, allow a calibration response for Fe (III) ions over a wide concentration range of  $1.0 \times 10^{-12}$  to  $1.0 \times 10^{-7}$  M. It has a response time of  $\approx 90$ s.

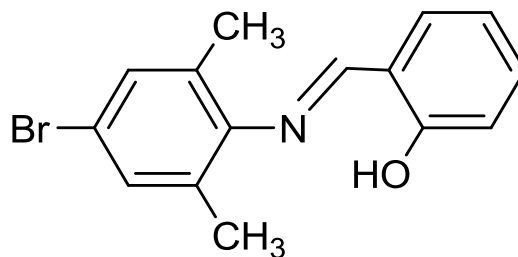


Figure 6.23 Structure of iron sensitive molecule, 2-{[(4-bromo-2,6dimethylphenyl) imino] methyl} phenol (MS-4).

### 6.5.1 Spectral Evaluation of the Newly Synthesized Dye

In order to perform spectral evaluation of the MS-4 dye; absorption, excitation and corrected emission spectra were recorded in the solvents of THF, EtOH, DMF, and toluene/ethanol (To: EtOH; 80:20) mixture and in PMMA matrix. The gathered absorption, excitation and emission spectra of the MS-4 dye were shown in Figures 6.24 and 6.25, respectively. Absorption spectra related molar extinction coefficients ( $\epsilon$ ) and maximum absorption wavelengths ( $\lambda_{Abs}$ ) of the dye in employed solvents and PMMA were given in Table 6.12.

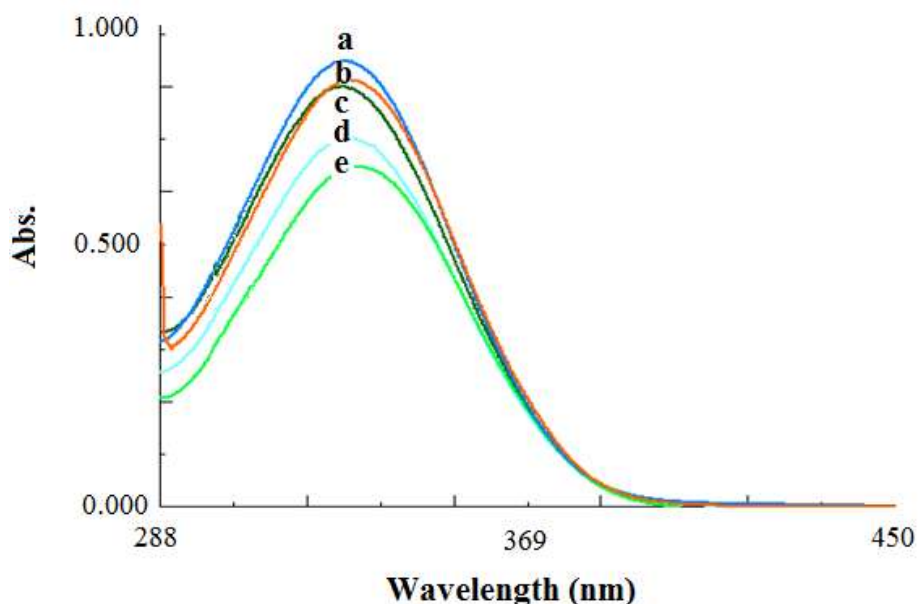


Figure 6.24 Absorption spectra of the MS-4 dye ( $10^{-5}$  M dye or 2 mM dye/kg polymer). (a) EtOH, (b) THF, (c) DMF, (d) DCM, (e) To: EtOH(80:20).

Table 6.12 UV-Vis spectra related data of MS-4 in the solvents of THF, EtOH, To: EtOH (toluene/ethanol mixture (80:20)), DCM and DMF.

Compound	Solvent/Matrix	$\lambda_{\text{abs}}^1$	$\epsilon_{\text{max}} (\lambda_{\text{abs}}^1)$
MS-4	THF	330	81100
	EtOH	330	58100
	To: EtOH	330	65100
	DCM	329	70500
	DMF	328	80000

The excitation-emission spectra and the related data of the MS-4 in different solvents are shown in Figure 6.25. Molar extinction coefficient ( $\epsilon_{\text{max}}$ ) of MS-4 dye in EC phase and in solutions is shown in Table 6.13.

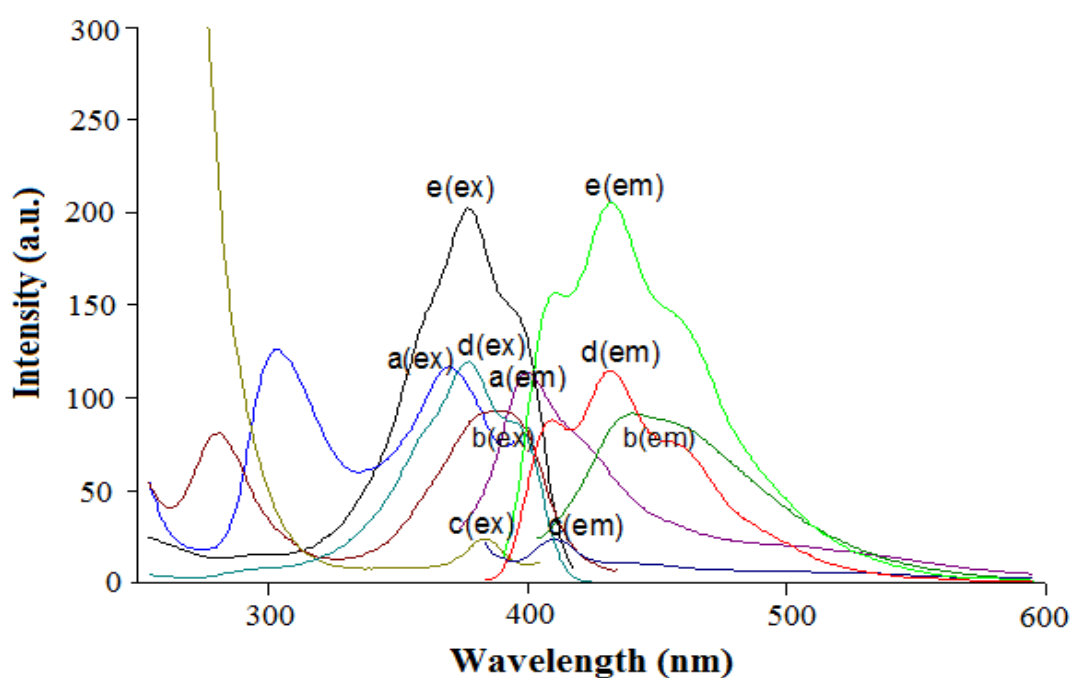


Figure 6.25 Excitation and corrected emission spectra of the MS-4 dye ( $10^{-5}$  M dye or 2 mM dye/kg polymer). (a)THF, (b) EtOH, (c) To: EtOH(80:20), (d) DCM, (e) DMF.

The dye exhibited time dependent signal instability after long waiting periods. However, the signal was stable for one hour in solution and a few hours in solid matrices. Therefore, we performed our measurements within 45 minutes after preparation of the sensing material. We could not calculate the quantum yield efficiencies due to the observed signal instabilities after long waiting periods.

Table 6.13 Emission and excitation spectra related data of MS-4 in the solvents of EtOH, DCM, THF, Toluene, Toluene/ Ethanol mixture (80:20), DMF and in solid matrices of EC and PMMA.

Compound	Matrix	$\lambda_{\max}^{em}$	$\lambda_{\max}^{ex}$	$\Delta\lambda_{ST}$ (Stoke's shift)
MS-4	EtOH	410	360	50
	DCM	440	370	70
	THF	410	360	50
	To:EtOH	430	370	60
	DMF	433	377	56
	EC	380	330	50
	PMMA	400	330	70

### 6.5.2 SEM Images of Electrospun Membranes

The SEM images of PMMA based electrospun membranes at various magnifications are denoted in Figure 6.26. It can be seen from Figure 6.26 that the diameters of the fibers were between 502 nm and 937nm.

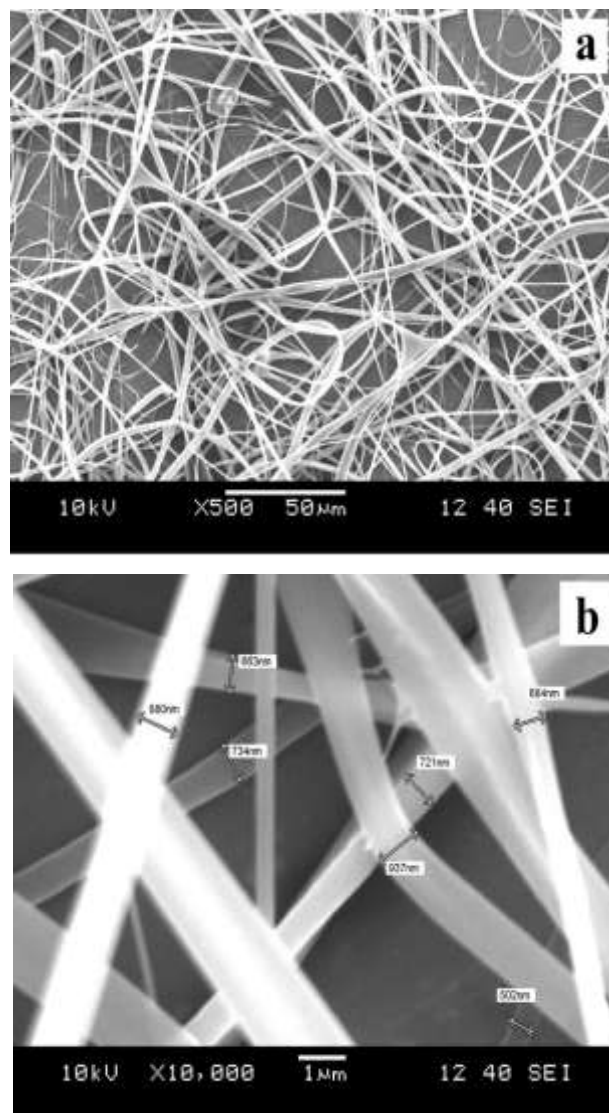


Figure 6.26 SEM images of PMMA based electrospun nanofibers (a) and (b); PMMA based nanofibers at different magnifications such as  $\times 500$  and  $\times 10000$ .

### 6.5.3 Effect of pH

The absorption, fluorescence emission, and sensing efficiency of the MS 4 dye is slightly affected from the pH of the environment. We researched the optimum pH conditions at constant concentrations of Fe (III) ions in separate solutions. The  $(I-I_0)/I_0$  was measured with PMMA membranes in presence of Fe (III) ions, following the analytical signal in the pH range of 4.0–10.0 (See Figure 6.27).

Distribution of the Fe (III) ions related chemical species in the working conditions was theoretically checked with chemical equilibrium software program (Visual MINTEQ) at pH 5.5 in presence of acetate ions. The ion distribution was as following:  $[(\text{CH}_3\text{COO}^-(\text{aq}): 85.61\%, \text{CH}_3\text{COOH}(\text{aq}): 14.39\%, \text{Fe}(\text{OH})^{+2}(\text{aq}): 2\%, \text{Fe}(\text{OH})^{+2}(\text{aq}): 95.63\%, \text{Fe}(\text{CH}_3\text{COO}^-)^{+2}: 1.27\%, \text{Fe}(\text{CH}_3\text{COO}^-)_3: 0.98\%, \text{Fe}(\text{OH})_3(\text{aq}): 0.016\%]$ . Due to the solubility considerations, pH 5.5-buffered solution was chosen as working condition for further studies for Fe (III) ions.

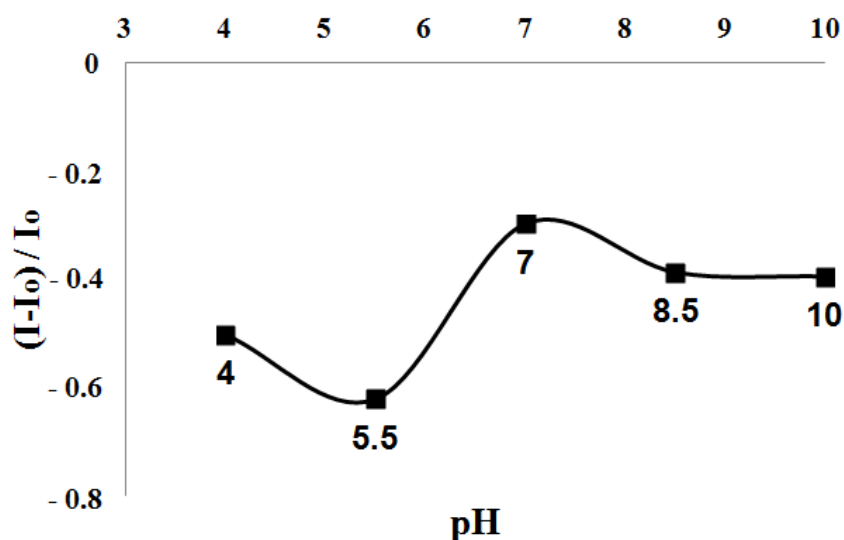


Figure 6.27 pH dependent response of MS-4 dye doped PMMA membrane to Fe (III) ions at pH 4.0-10.0.

#### 6.5.4 Dynamic Working Range and Response for Fe (III) Ions

When doped into modified PMMA matrices, in presence of the potassium tetrakis-(4-chlorophenyl) borate; the Fe (III) ions can selectively be extracted into the optode membrane. The following ion-exchange pathway shown in equation 6.2 can explain the response mechanism of MS-4 dye.

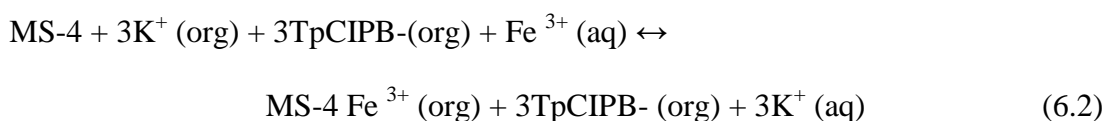


Figure 6.28 shows the absorption spectrum of the MS-4 dye in the absence and presence of Fe (III) ions in THF. Although there is no spectral shift, the absorption band around 330 nm exhibited a signal enhancement around 20% in the absence and in the presence of  $5 \times 10^{-5}$  M of ferric ions.

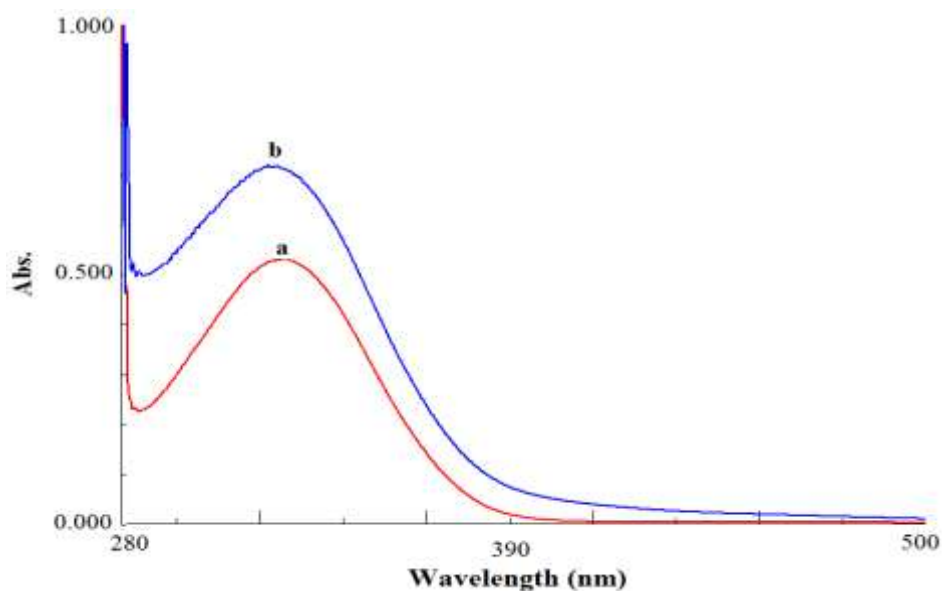


Figure 6.28 Absorption spectrum of the MS-4 dye in THF (a) Fe (III) free, (b) in presence of  $5 \times 10^{-5}$  M Fe (III).

Figure 6.29 and 6.30 show the change in fluorescence spectrum of thin film and nanofibers as a function of different concentrations of Fe (III) ions.



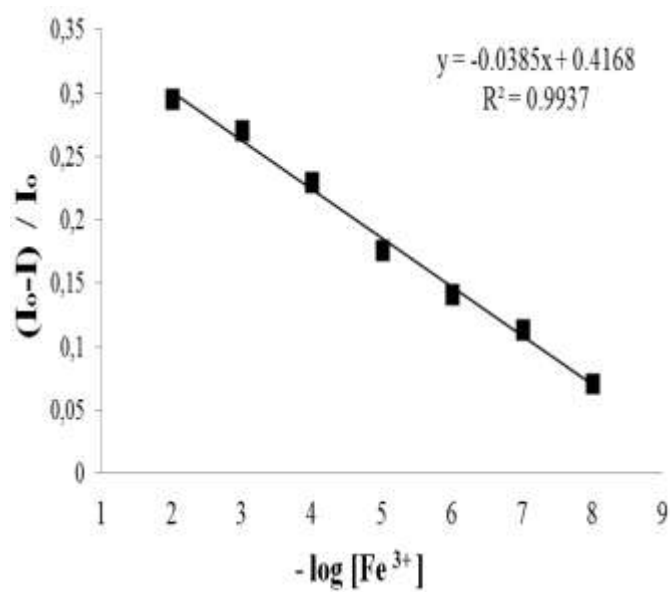
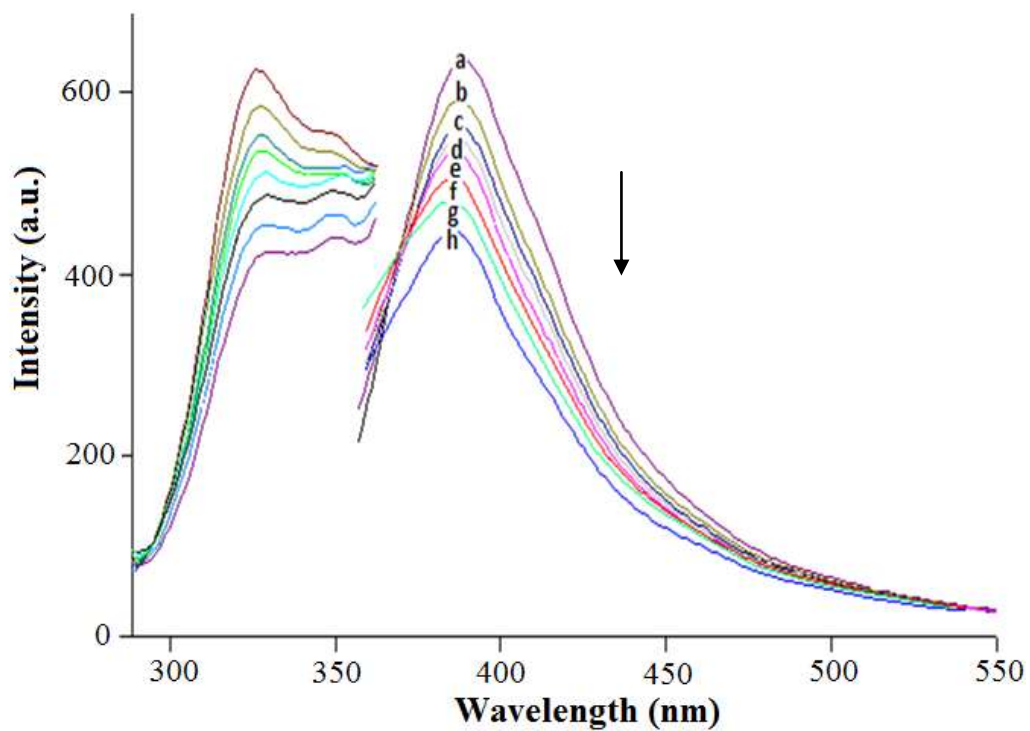


Figure 6.29 Response of the MS 4 doped PMMA based thin film to Fe (III) ions at pH 5.5. (a) Fe (III)-free, (b)  $10^{-8}$ , (c)  $10^{-7}$ , (d)  $10^{-6}$ , (e)  $10^{-5}$ , (f)  $10^{-4}$ , (g)  $10^{-3}$ , (h)  $10^{-2}$  Mol/L, and linearized calibration plot for the concentration range of  $10^{-8}$ - $10^{-2}$  M Fe (III).

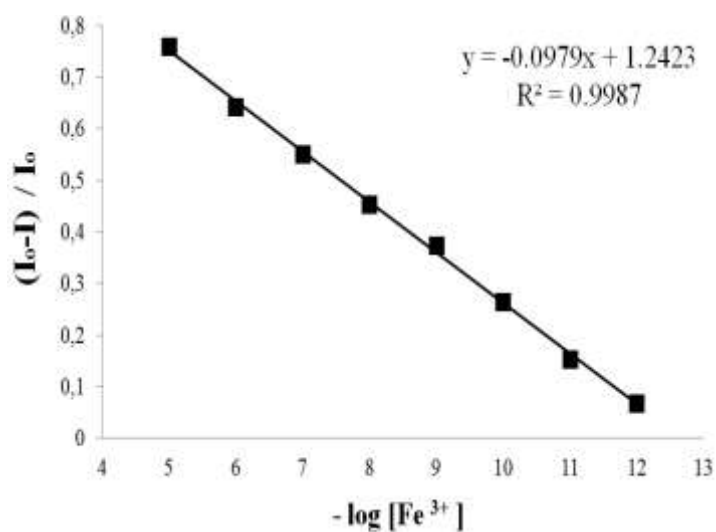
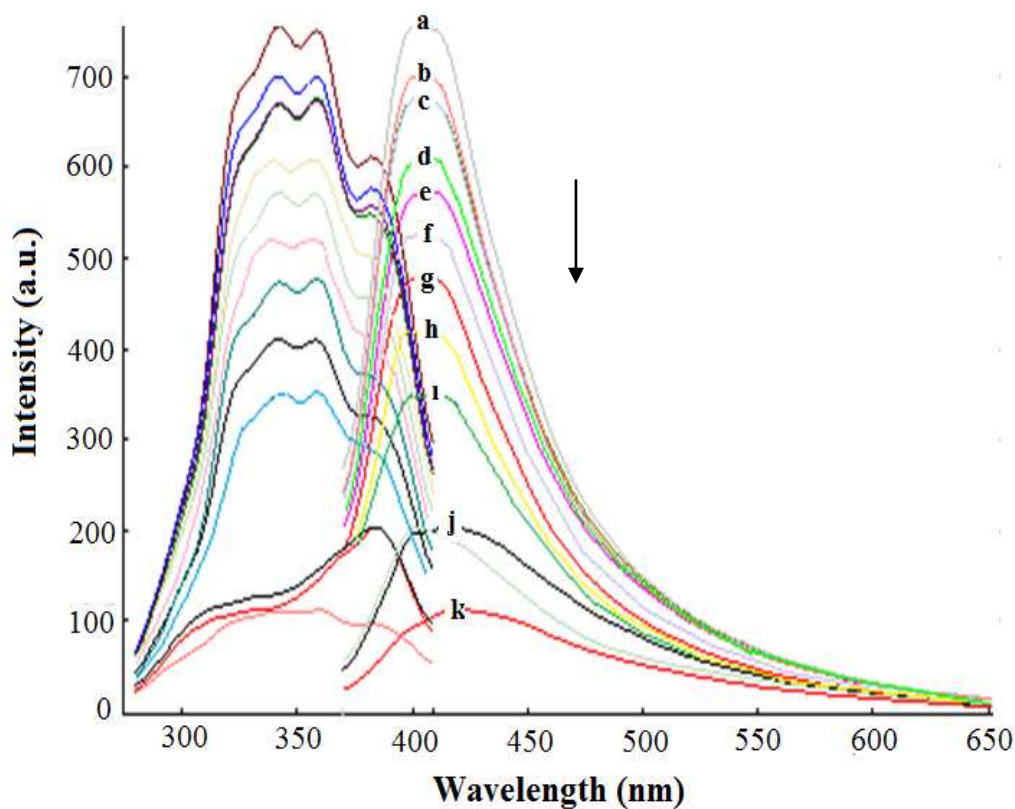


Figure 6.30 Response of the MS 4 doped PMMA based nanofiber to Fe (III) ions at pH 5.5. (a) Fe (III)-free, b)  $10^{-12}$ , (c)  $10^{-11}$ , (d)  $10^{-10}$ , (e)  $10^{-9}$ , (f)  $10^{-8}$ , (g)  $10^{-7}$ , (h)  $10^{-6}$ , (i)  $10^{-5}$ , (j)  $10^{-4}$ , (k)  $10^{-3}$  Mol/L, and linearized calibration plot for the concentration range of  $10^{-12}$ - $10^{-5}$  M Fe (III).

The MS 4-doped electrospun nanofibers demonstrated a linear response over range of  $10^{-12}$  -  $10^{-4}$  M for Fe (III) ions. Response of the nano-scale sensing materials was approximately three fold of the response of the thin film based sensing agents. The tested nanoscale sensor compositions exhibited large relative signal change, excellent linearity and very good sensitivity to Fe (III) ions. The regression results yielded an absolute linear response with coefficients of regression ( $R^2$ ) of 0.9987 for PMMA electrospun nanofibers (See Table 6.14).

The limit of detection (LOD) for was defined as the concentration at which the signal is equal to the blank signal plus  $3\sigma$  and was found to be  $2.45 \times 10^{-14}$  M for PMMA based electrospun nanofiber. The LOD of  $5.00 \times 10^{-12}$  M was calculated for the continuous thin film made up of the same composition (See Table 6.14).

Table 6.14 Calibration related characteristics of PMMA based electrospun nanofibers and thin films.

Indicator Dye	Matrix /Form	Linear Range (Fe (III) Mol/L)	Regression Coefficient ( $R^2$ )	LOD (Molar)	% Relative Signal Changes
MS 4	PMMA nanofiber	$1.0 \times 10^{-12}$ to $1.0 \times 10^{-5}$	0.9987	$2.45 \times 10^{-14}$ M	88
	PMMA thin film	$1.0 \times 10^{-9}$ to $1.0 \times 10^{-3}$	0.9937	$5.00 \times 10^{-12}$ M	30

### 6.5.5 Stern-Volmer Analysis

The data regarding results of the Stern-Volmer analysis for electrospun and continuous thin films were shown in Table 6.15. The electrospun nanofibers yielded characteristic Stern-Volmer relationship for quencher concentrations between  $1 \times 10^{-12}$  -  $1 \times 10^{-6}$  M.  $K_{sv}$  value of the electrospun film, calculated from slope of the plot was found to be  $2.00 \times 10^6$  ( $M^{-1}$ ). This value is 400 fold greater than that obtained from the continuous thin film slides. (See Table 6.15 and Figure 6.31).  $K_{sv}$  values reveal important practical consequences. The sensitivity of the quenching process can be enhanced by controlling the quencher diffusion rate to fluorophores via the nano-structural properties of the sensing materials.

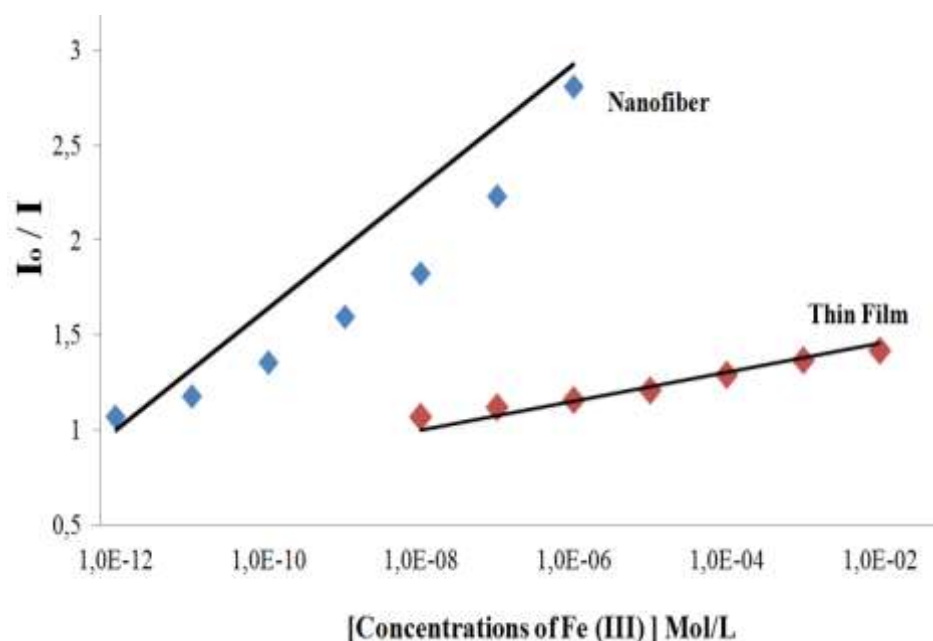


Figure 6.31 I: The Stern Volmer plots of PMMA based thin films, II: electrospun nanofibers in presence of the quencher.

Table 6.15  $K_{sv}$  Constant of PMMA based electrospun nanofibers and thin films for Fe (III) ions.

Indicator Dye	Matrix /Form	Linear Regression Equation (Fe (III) Mol/L)	$K_{sv}$ Constant
MS-4	PMMA/ electrospun nanofiber	$y = 2E^{+06}x + 1$	$2.00 \times 10^6$
	PMMA / thin film	$y = 4563.4x + 1$	$4.56 \times 10^3$

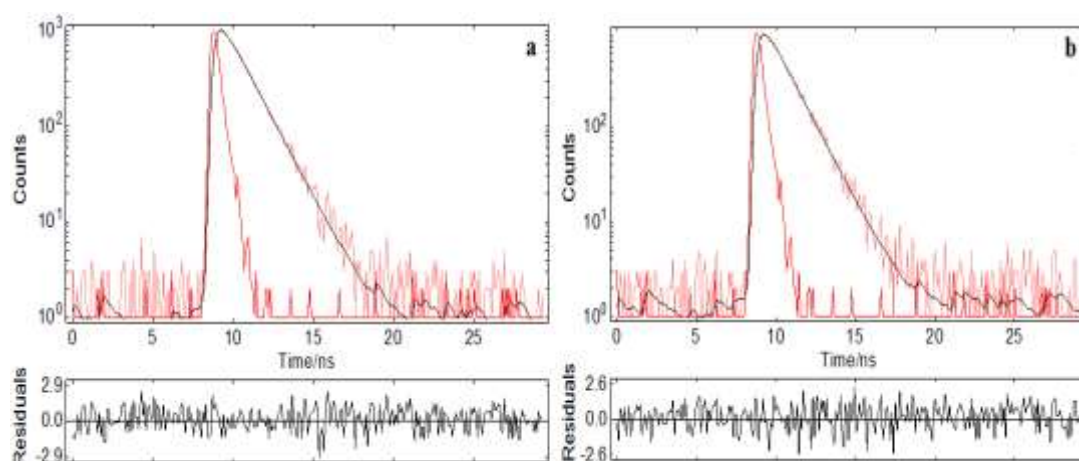
### 6.5.6 Lifetime Analysis

Decay curves of the exploited dye in THF, in thin film form and in form of nanofiber were measured and shown in the Figure 6.31. The excited state lifetimes of the MS-4 in THF and in solid matrices, in the absence and presence of the quencher were shown in Table 6.16. In solution phase and solid-state measurements there is a slight enhancement in the fluorescence decay times that can be attributed to the dynamic component of the quenching. In excited state lifetimes in the presence of the Fe (III) ions.

Table 6.16 Fluorescence lifetimes of the carbazole derivative in THF, PMMA based thin films and electrospun nanofibers in the presence and absence of the quencher.

MS-4	Solvent		Thin Film		Nanofiber		
		Value (ns)	% Relative	Value (ns)	% Relative	Value (ns)	% Relative
Metal Free	$\tau_1$	1.31	100	0.04	78.54	0.49	16.29
	$\tau_2$	--	--	1.51	21.46	1.99	43.16
	$\tau_3$	--	--	--	--	5.03	40.55
		Value (ns)	% Relative	Value (ns)	% Relative	Value (ns)	% Relative
Fe (III)	$\tau_1$	1.30	100	0.05	89.30	0.51	19.16
	$\tau_2$	--	--	2.11	10.70	2.54	55.48
	$\tau_3$	--	--	--	--	6.16	25.35

When fluorescence intensity based response, absorption spectroscopy and lifetime measurements related data were evaluated together, the mechanism between indicator dye and sensing agent can be concluded as ‘combined quenching’ of the MS-4 dye by Fe (III) ions.



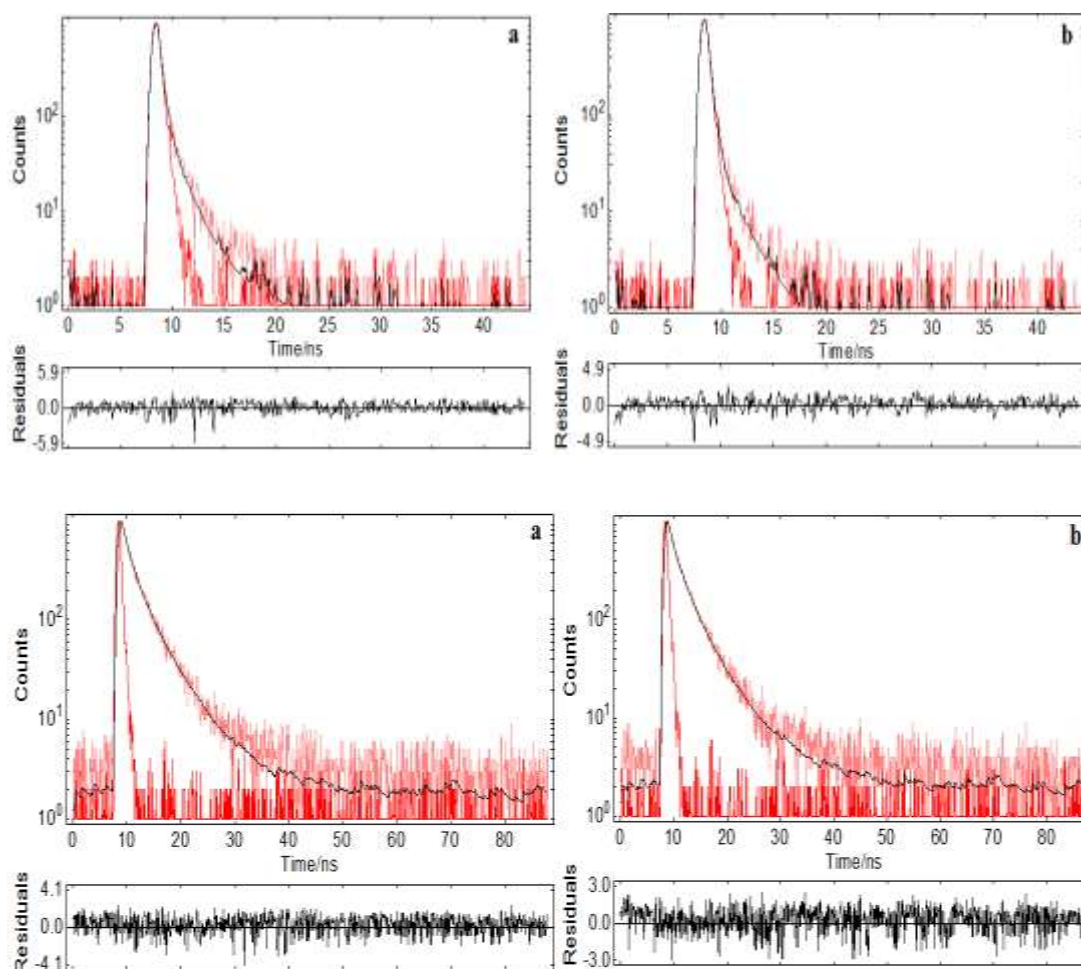


Figure 6.32 Decay curves of the exploited dye in THF, in thin film form and in form of nanofiber, respectively. In all cases a and b show quencher free and quencher containing decay profiles. The dye excited at 367 nm with a picoseconds pulsed laser.

### 6.5.7 Interference Effects

In order to test the selectivity of the proposed method for iron ions, the influences of a number of cations were investigated. Interference tests were performed for  $\text{Ag}^+$ ,  $\text{Al}^{3+}$ ,  $\text{Bi}^{2+}$ ,  $\text{Ca}^{2+}$ ,  $\text{Co}^{2+}$ ,  $\text{Cd}^{2+}$ ,  $\text{Cu}^{2+}$ ,  $\text{Fe}^{3+}$ ,  $\text{Fe}^{2+}$ ,  $\text{Hg}^{2+}$ ,  $\text{Hg}^+$ ,  $\text{Li}^+$ ,  $\text{K}^+$ ,  $\text{Mn}^{2+}$ ,  $\text{Mg}^{2+}$ ,  $\text{H}^+$ ,  $\text{Ni}^{2+}$ ,  $\text{Pb}^{2+}$ ,  $\text{Sn}^{2+}$  and  $\text{Zn}^{2+}$  ions in acetic acid/acetate buffer solutions at pH 5.5. From Figure 6.33-I, it can be concluded that, the sensing membrane is capable of determining ferric ions with a high selectivity over other cations.

The interference effects of the anions;  $F^-$ ,  $Cl^-$ ,  $Br^-$ ,  $NO_3^-$ ,  $NO_2^-$ ,  $SO_4^{2-}$  and  $PO_4^{3-}$  were also tested (See Figure 6.33 - II). Relative signal changes of less than 4% were observed for PMMA doped films at pH 5.5.

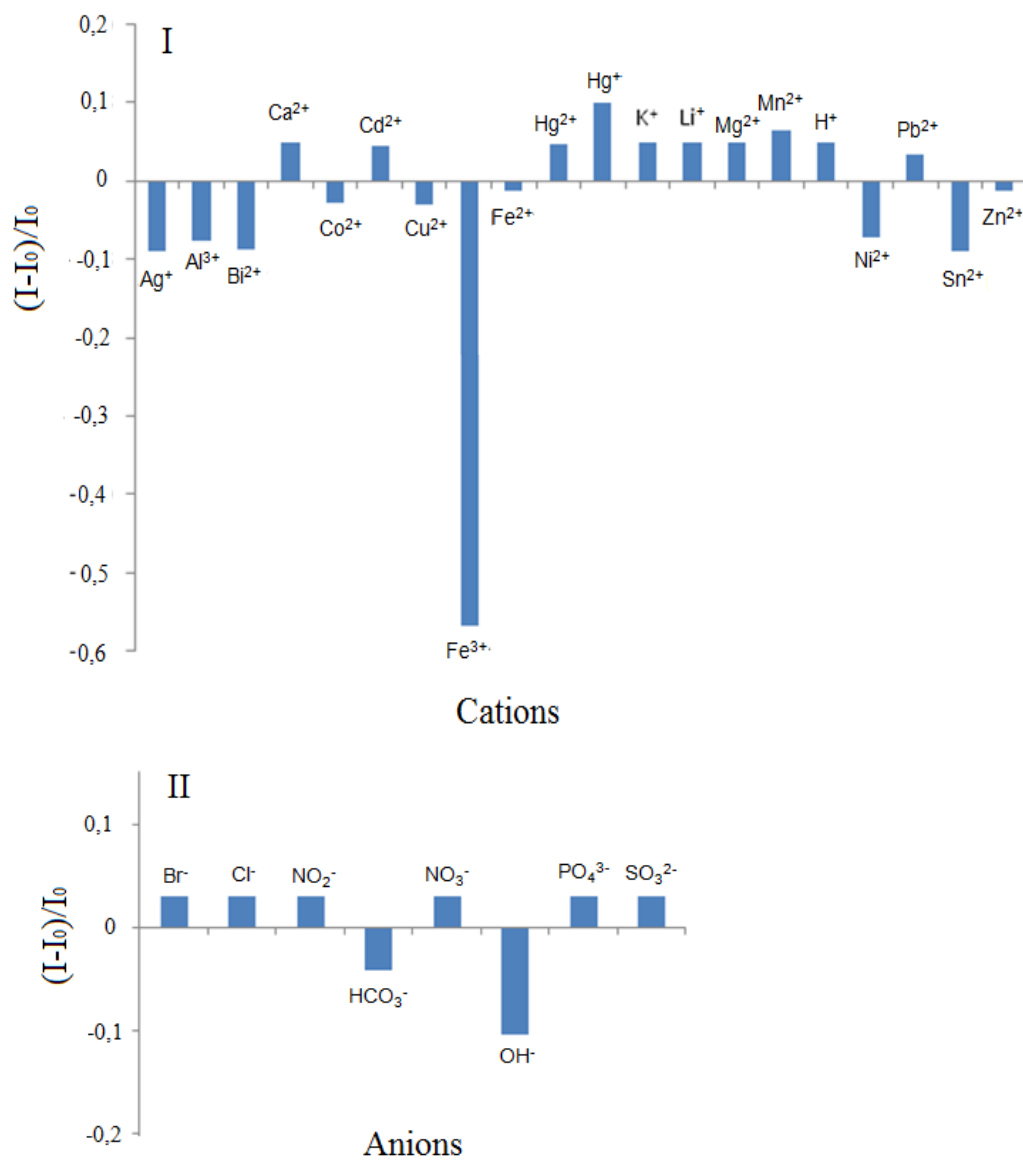


Figure 6.33 I: Metal-ion response of MS-4 at pH 5.50. II: Response to the anions of the same composition at near neutral pH. Results were plotted as relative fluorescence changes;  $(I-I_0)/I_0$ .

### **6.5.8 Recovery and Regeneration Studies**

The applicability of the sensing system for real samples was tested for the mineral water of Sarikiz. The temperature of the water from well was 17.2 °C. The content of Fe (III) in the diluted certified reference material of Merck (SRM from NIST FeCl<sub>3</sub> in HNO<sub>3</sub> 0.5 mol L<sup>-1</sup> 1000 mg L<sup>-1</sup> Fe CertiPUR®) was determined by exploiting the electrospun nanofibers. All mineral water samples were collected in polyethylene vials, degassed using ultrasonic bath and analyzed as soon as possible after sampling. The recovery experiments were carried out adding 1x10<sup>-7</sup> M of certified reference material into the mineral water. The average concentration of the Fe (III) was found to be 2.95x10<sup>-7</sup> M for 10 replicate measurements. The recovery performance was found to be 103 ± 0.8 %. These results reveal the capability of the offered sensing design for the determination of ferric ions in real samples without considerable error.

### **6.5.9 Conclusion**

A novel fluorescent optical sensor using electrospun polymeric nanofibrous membrane for the quantitative analysis of Fe (III) ion was presented. Electrospinning was used as a novel and facile method to fabricate optical chemical sensor devices. With respect to continuous thin films, electrospun nanofibers offered enhanced sensitivity, lower LOD values and reactivity in optical chemical sensing of Fe (III). The MS-4 dye was used for the first time as a fluoroionophore in the optical iron sensing. The MS-4 dye doped nanofibers in PMMA can be used at pH 4.0 for quantitative determination of Fe (III) in the concentration range of 10<sup>-12</sup> - 10<sup>-5</sup>M. A quite good LOD was reached.



## CHAPTER SEVEN

### A SENSITIVE DETERMINATION OF Sn (II) WITH FLUORESCENCE SPECTROSCOPY EXPLOITING ELECTROSPUN FIBERS

#### 7.1 Introduction

Tin is a soft, white, silvery and water-insoluble metal. It can easily combine with other chemicals to form various compounds. Metallic tin is widely used to line cans for food, beverages, and aerosols. When the tin is reacted with chlorine, sulfur, or oxygen, it is called an inorganic tin compound. Tin or its compounds can be found in soil, toothpaste, perfumes, soaps, coloring agents, food additives, and dyes. Tin also can combine with carbon to form organic tin compounds are used in making plastics, food packages, plastic pipes, pesticides, paints, wood preservatives, and rodent (rats and mice) repellents (Eoearth, 2012).

The organic tin compounds are the most hazardous forms of tin for humans (Lenntech, 2012). Therefore, the monitoring of this element in a great variety of environmental and biological samples is important due to its potential toxicity even at low concentrations. Due to the above-mentioned consequences, the development of simple and highly sensitive methods to evaluate the tin levels is required.

Many different techniques have been developed for the determination of tin in solid, water and environmental samples such as graphite furnace atomic absorption spectrometry (Özcan, & Akman, 2000; Belarra, Resano, & Castillo, 1997; Haug, & Yiping, 1995), electrothermal atomic absorption spectrometry (ETAAS) (López-García, Arnau-Jerez, Campillo, & Hernández-Córdoba, 2004; Silva, Giacomelli, Souza, & Curtius, 1998; Mahía, Lorenzo, Fernández, & Rodríguez, 2002), voltammetry (Adelaju, & Pablo, 1992; Heppeler, Sander, & Henze, 1996; Li, Long, & Zhou, 2005), inductively coupled plasma mass spectroscopy (ICP-MS) (Hosick, Ingamells, & Machemer, 2002), potentiometry (Ratana-ohpas, Kanatharana, Ratana-

ohpas, & Kongsawasdi, 1996), and fluorescence method (Manzoori, Amjadi, & Abolhasani, 2006; Jourquina, Mahederob, Paredesa, Virea, & Kauffmann, 1996; Anderson, Garnett, & Lock, 1960; Garcia-Alonso, Sanz-Medel, & Ebdon, 1993). Moreover, in order to improve the sensitivity, many procedures have also been used in combination with the above-mentioned techniques.

In addition to these techniques, nowadays, determination of tin is possible even at concentrations lower than nanomolar levels using the fluorescent-based techniques. Most of these studies exploit a fluoroionophore signaling the tin ions in appropriate solutions (Chen, Zhang, Chen, & Huang, 2001).

However, to improve the stability and sensitivity, further studies are necessary. In such kind of designs, the sensitive agents were immobilized in polymer matrices. The thin film application has been used many times in the optical chemical sensing of the metal ions. Compared to the solution phase the sensing studies of thin-film phase have been shown more robustness, reversibility, stability, and sensitivity for ions to be determined (Shamsipura, Alizadehb, Hosseinib, Caltagironec, & Lippolisc, 2006).

In this respect, nano-scale materials received great research interest for chemical and biological sensor applications due to their unique high surface area and promising detection limits. Compared with several fluorescence methods, they have wider linear range, enhanced LOD values, shorter response times, higher sensitivity and stability (Zhang, & Wang, 2009; Chen, & Zhu, 2005; Wang, Liang, Chen, Liu, Qian, & Fu, 2008). In this part of thesis, we tested sensor properties of the tin sensitive ionophore; 3-(2,4,6-trimethoxybenzyl)-3,4-dihydroquinazoline (MS-3), both in thin film and nanofiber forms.

## 7.2 Sensor Design

The Sn (II) sensitive fluorescent ionophore, 3-(2,4,6-trimethoxybenzyl)-3,4-dihydroquinazoline (MS-3), (See Figure 7.1) was provided by Prof. Dr. Engin ÇETİNKAYA, from the University of Ege, department of chemistry. The information regarding synthetic procedure was given earlier.

The sensing agents were doped into polymethylmethacrylate (PMMA) together with ionic liquid and other additives. Composite fibers were fabricated by electrospinning and characterized by Scanning Electron Microscopy (SEM). PMMA based nanofibers, allow a calibration response for Sn (II) ions over a wide concentration range of  $1.0 \times 10^{-10}$  to  $1.0 \times 10^{-3}$  M. It has a response time of  $\approx 120$ s.

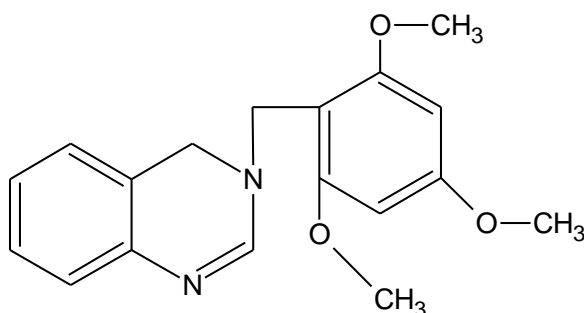


Figure 7.1 Structure of tin sensitive molecule, 3-(2,4,6-trimethoxybenzyl)-3,4-dihydroquinazoline (MS-3)

### 7.2.1 Spectral Evaluation of Newly Synthesized Dye and Quantum Yield Calculations

In order to perform spectral evaluation of the MS-3 dye; absorption, excitation and corrected emission spectra were recorded in the conventional solvents (THF, EtOH, DMF, and toluene/ethanol (To: EtOH; 80:20) mixture) and in PMMA matrix. The gathered absorption, excitation and emission spectra of the MS-3 dye were shown in Figure 7.2 and 7.3, respectively. Absorption spectra related molar

extinction coefficients ( $\epsilon$ ) and maximum absorption wavelengths ( $\lambda_{\text{Abs}}$ ) of the dye in the employed solvents and PMMA were given in Table 7.1.

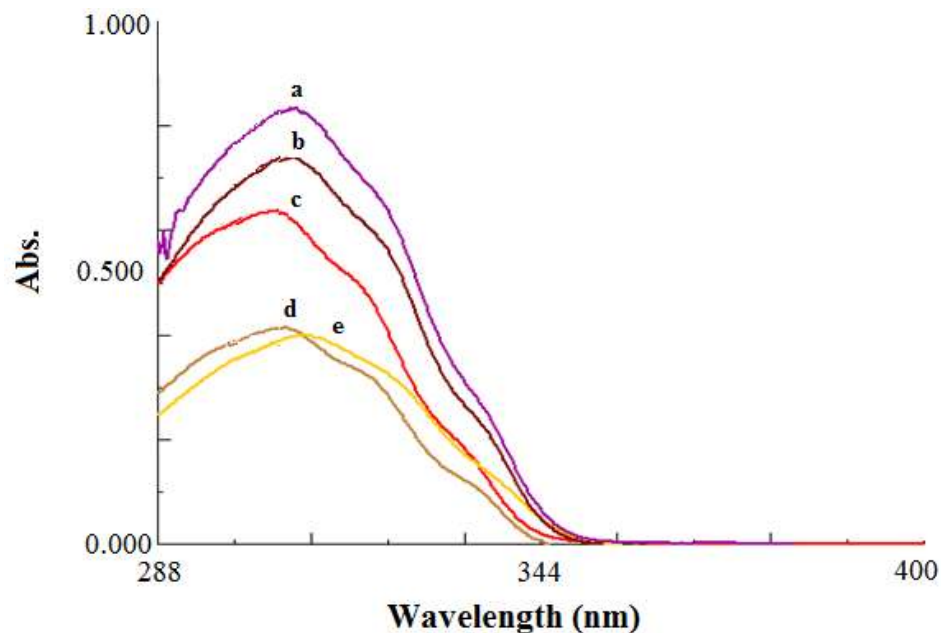


Figure 7.2 Absorption spectra of the MS-3 dye ( $10^{-5}$  M dye or 2 mM dye/kg polymer). (a)THF, (b) DCM, (c) EtOH, (d) To: EtOH(80:20), (e) DMF.

Table 7.1 UV-Vis spectra related data of MS-3 in the solvents of THF, EtOH, To: EtOH (80:20), DCM and DMF.

Compound	Solvent/Matrix	$\lambda^1_{\text{abs}}$	$\epsilon_{\text{max}}$ ( $\lambda^1_{\text{abs}}$ )
MS-3	THF	308	83300
	EtOH	300	58100
	To: EtOH	307	45100
	DCM	307	71000
	DMF	309	40100

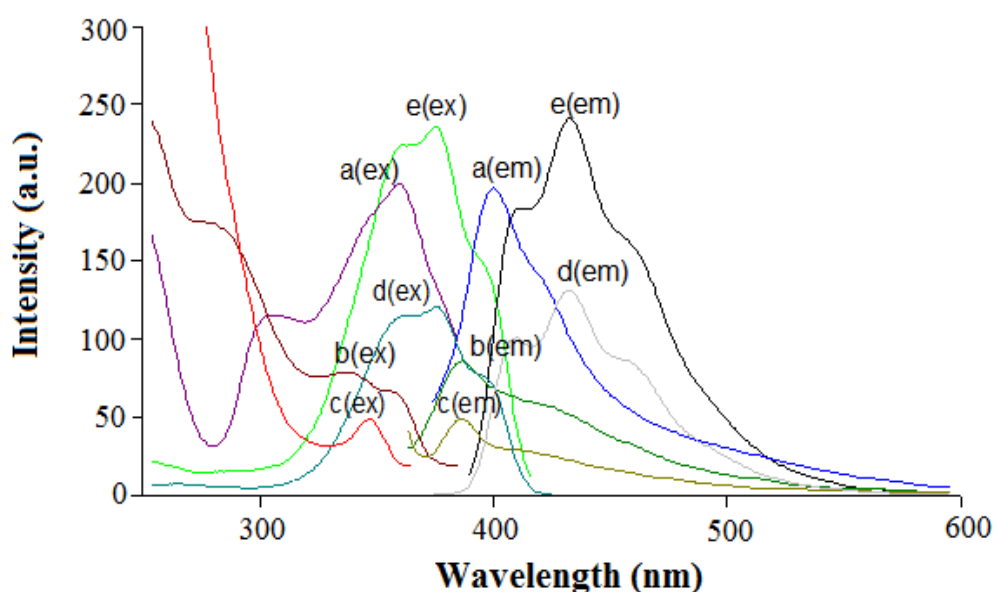


Figure 7.3. Excitation and corrected emission spectra of the MS-3 dye ( $10^{-5}$  M dye or 2 mM dye/kg polymer). (a) THF, (b) EtOH, (c) To: EtOH, (d) DCM, (e) DMF.

The dye exhibited time dependent signal instability after long waiting periods. However, the signal was stable for approximately one hour in solution and a few hours in the solid matrix. Therefore, we performed our measurements within 45 minutes after preparation of the sensing material. We could not calculate the quantum yield efficiencies due to the observed signal instabilities after long waiting periods (See Table 7.2).

Table 7.2 Emission and excitation spectra related data of MS-3 in the solvents of EtOH, DCM, THF, To: EtOH (80:20), DMF and in solid matrices of EC and PMMA.

Compound	Matrix	$\lambda_{\max}^{em}$	$\lambda_{\max}^{ex}$	$\Delta\lambda_{ST}$ (Stoke's shift)
MS-3	EtOH	400	350	50
	DCM	440	360	80
	THF	400	360	40
	To:EtOH	385	350	35
	DMF	431	376	55
	EC	420	350	70
	PMMA	445	365	80

### 7.2.2 SEM Images of Electrospun Membranes

The SEM images of PMMA based electrospun membranes at various magnifications are denoted in Figure 7.4. The membrane has a 3-D structure with a random fiber orientation that is evenly distributed on the substrate. It can be seen from Figure 7.4 that the diameters of the fibers ranged from micrometer to nanometer (between 696 nm and 1.32  $\mu\text{m}$ ).

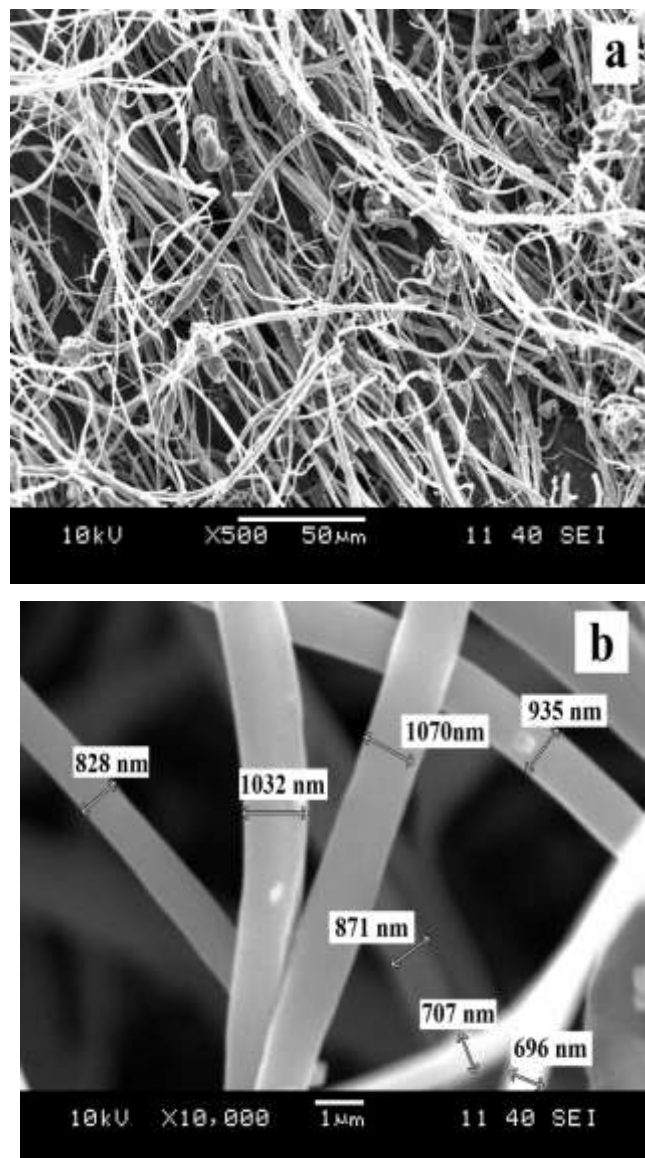


Figure 7.4 SEM images of PMMA based electrospun nanofibers (a) and (b); PMMA based nanofibers at different magnifications such as  $\times 500$  and  $\times 10000$ .

### 7.2.3 Effect of pH

The absorption, fluorescence emission, and sensing efficiency of the MS 3 dye were slightly affected from the pH of the environment. We used the constant concentrations of Sn (II) ions to find out optimum pH conditions in separate solutions. The  $(I-I_0/I_0)$  was recorded as the analytical signal for MS 3 dye doped PMMA membranes in presence of Sn (II) ions, in the pH range of 4.0–10.0 (See Figure 7.5).

Distribution of the Sn (II) ions related chemical species in the working conditions was theoretically calculated with chemical equilibrium software program (Visual MINTEQ) at pH 4.0 in presence of acetate ions. The Sn (II) ion distribution was as following:  $[\text{CH}_3\text{COO}^-(\text{aq})]$ : 15.19%,  $\text{CH}_3\text{COOH}(\text{aq})$ : 84.75%,  $\text{Sn}(\text{CH}_3\text{COO})_2(\text{aq})$ : 0.66%,  $\text{Sn}(\text{OH})_2$ : 57.28%,  $\text{Sn}(\text{OH})^+$ : 29.19%,  $\text{Sn}(\text{CH}_3\text{COO})^+$ : 4.57%,  $\text{Sn}^{+2}$ : 7.83%. Due to the solubility requirements, pH 4.0 was chosen as working condition for further studies for Sn (II) ions.

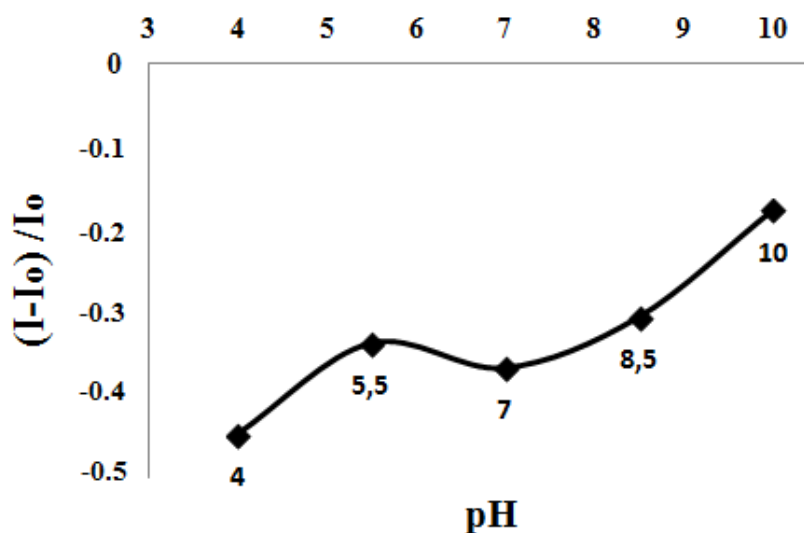


Figure 7.5 pH dependent response of MS-3 dye doped PMMA membrane to Sn (II) ions at pH 4.0-10.0.

#### 7.2.4 Dynamic Working Range and Response for Sn (II) Ions

When doped into modified PMMA matrices along with the potassium tetrakis-(4-chlorophenyl) borate; Sn (II) ions were selectively extracted into the optode membrane by the help of the anionic additive. Meanwhile the MS-3 dye acted as a Sn (II) sensitive probe following the ion exchange mechanism.

The ion-exchange pathway was shown in the following Equation 7.1;

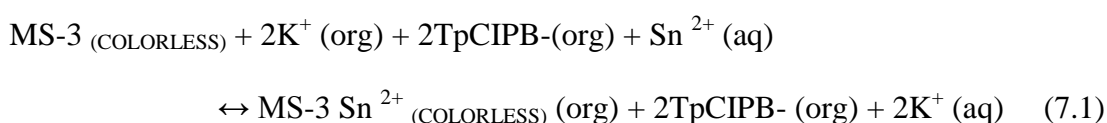


Figure 7.6 shows the absorption spectrum of the MS-3 dye in the absence and presence of Sn (II) ions in THF. Although there is no change in the absorption integral, the absorption maximum was 22 nm blue-shifted upon exposure to  $5 \times 10^{-5}$  M of Sn (II) ions.

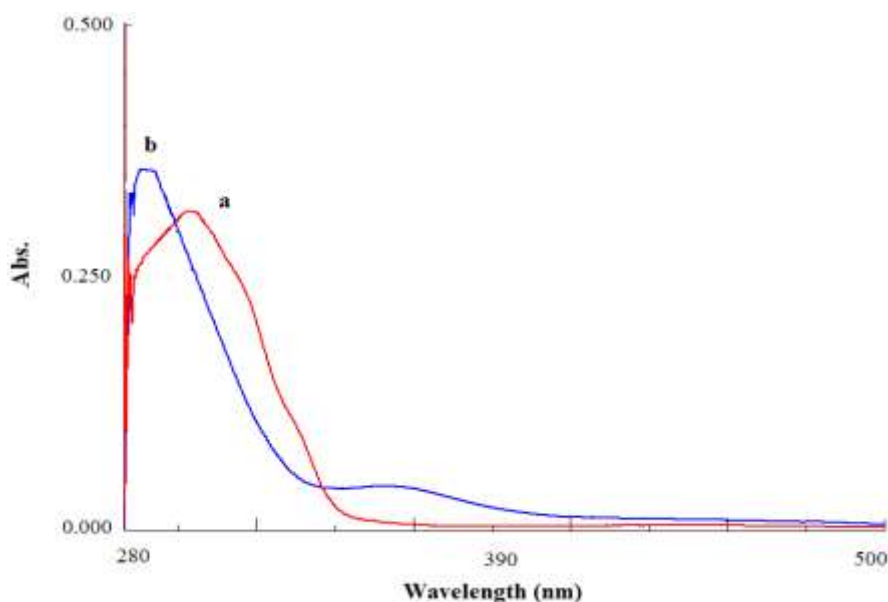


Figure 7.6 Absorption spectrum of the MS-3 dye in THF (a) Sn (II) free, (b) in presence of  $5 \times 10^{-5}$  M Sn (II).



Figure 7.7 and Figure 7.8 show the change in fluorescence spectrum of thin film and nanofibers as a function of different concentrations of Sn (II) ions. The calibration plots were drawn using the extracted intensity based data.

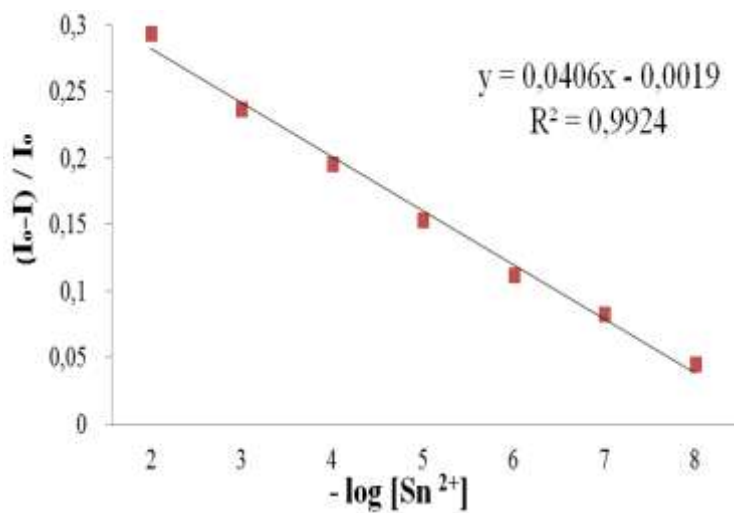
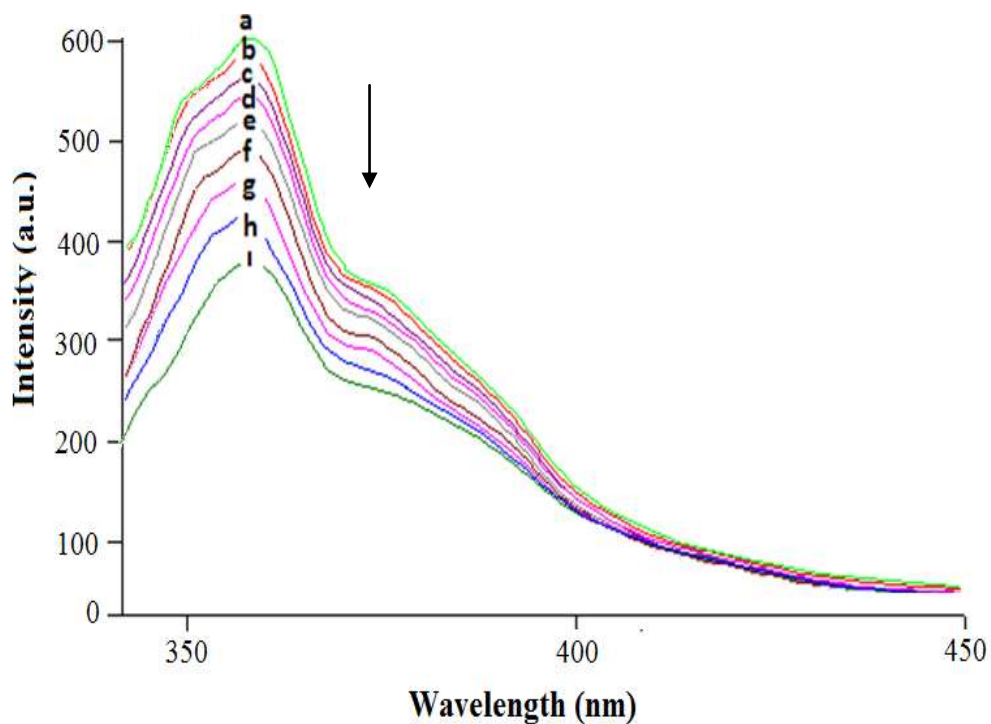


Figure 7.7 Fluorescence response of the MS-3 doped PMMA based thin film to Sn (II) ions at pH 4.0. (a) Sn (II) -free buffer, (b) 10<sup>-8</sup>, (c) 10<sup>-7</sup>, (d) 10<sup>-6</sup>, (e) 10<sup>-5</sup>, (f) 10<sup>-4</sup>, (g) 10<sup>-3</sup>, (h) 10<sup>-2</sup>, (i) 10<sup>-1</sup> Mol/L, and linearized calibration plot for the concentration range of 10<sup>-8</sup>-10<sup>-2</sup> M Sn (II).

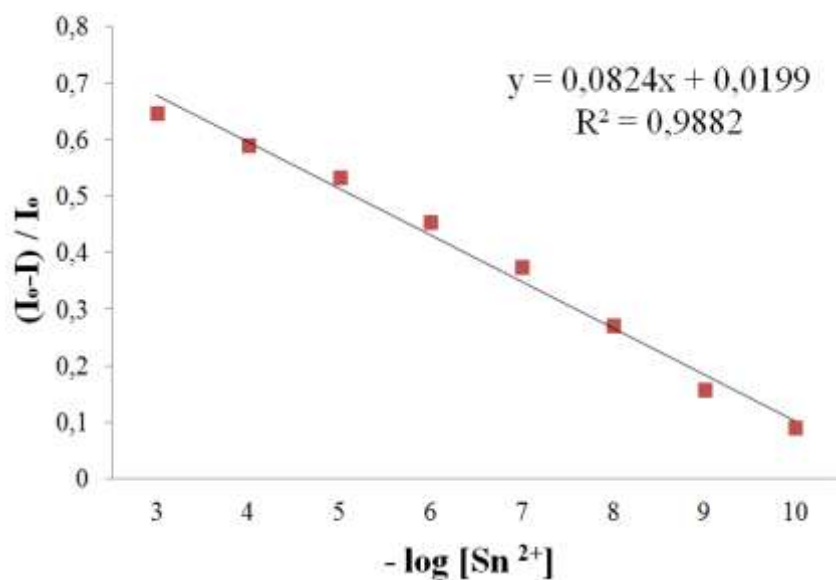
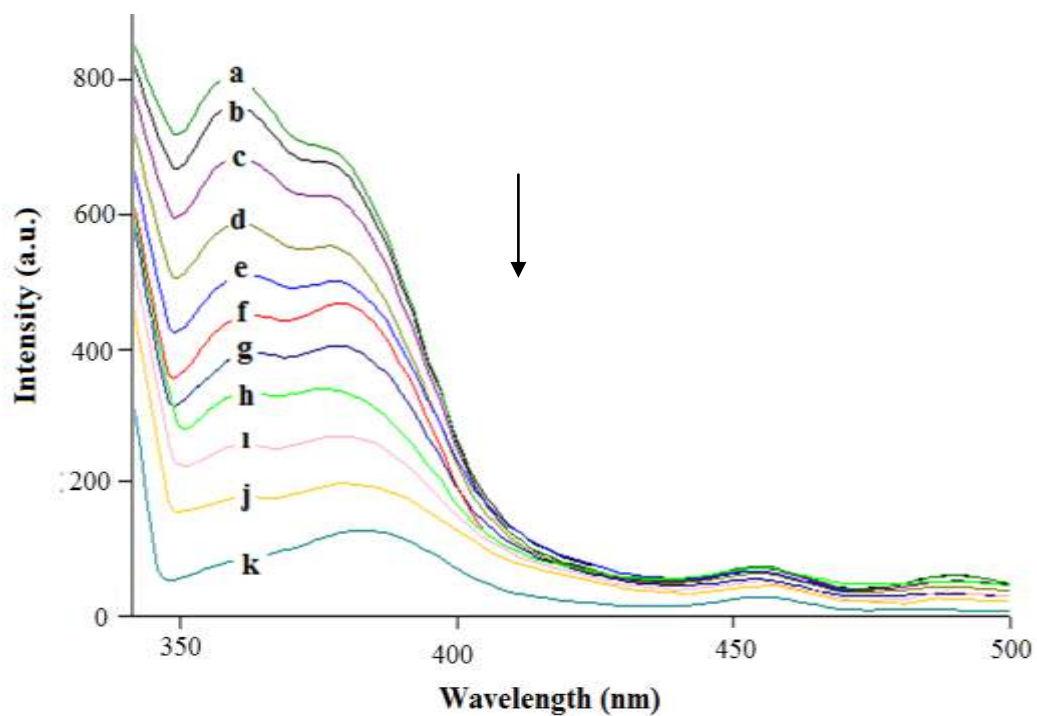


Figure 7.8 Response of the PMMA based nanofiber to Sn (II) ions at pH 4.0. (a) Sn (II) free, (b)  $10^{-10}$ , (c)  $10^{-9}$ , (d)  $10^{-8}$ , (e)  $10^{-7}$ , (f)  $10^{-6}$ , (g)  $10^{-5}$ , (h)  $10^{-4}$ , (i)  $10^{-3}$ , (j)  $10^{-2}$ , (k)  $10^{-1}$  Mol/L, and linearized calibration plot for the concentration range of  $10^{-10}$ - $10^{-3}$  M Sn (II).

The MS 3-doped electrospun nanofibers demonstrated a linear response over the concentration range of  $10^{-10}$ - $10^{-3}$  M for Sn (II) ions. The tested sensor compositions exhibited large relative signal change, excellent linearity and very good sensitivity to Sn (II) ions. The regression results yielded a linear response with coefficients of regression ( $R^2$ ) of 0.9882 for PMMA electrospun nanofibers (See Table 7.3).

The limit of detection (LOD) for the MS-3 dye was defined as the concentration at which the signal is equal to the blank signal plus  $3\sigma$  and was found to be  $1.60 \times 10^{-14}$  M for nanofibers. The detection limit of  $4.50 \times 10^{-12}$  M was calculated for continuous thin film form of the same composition (See Table 7.3).

Table 7.3 Calibration related characteristics of PMMAbased electrospun nanofibers and thin films

Indicator Dye	Matrix /Form	Linear Range (Sn (II) Mol/L)	Regression Coefficient ( $R^2$ )	LOD (Molar)	% Relative Signal Changes
MS 3	PMMA nanofiber	$1.0 \times 10^{-10}$ to $1.0 \times 10^{-3}$	0.9882	$1.60 \times 10^{-14}$ M	88
	PMMA thin film	$1.0 \times 10^{-8}$ to $1.0 \times 10^{-2}$	0.9924	$4.50 \times 10^{-12}$ M	36

### 7.2.5 Stern-Volmer Analysis

The data regarding results of the Stern-Volmer analysis for electrospun and continuous thin films were shown in Figure 5.9 and Table 7.4. The electrospun nanofibers yielded usual Stern-Volmer relationship for quencher concentrations between  $1 \times 10^{-10}$ -  $1 \times 10^{-3}$  M.  $K_{sv}$  value of the electrospun nanofiber, calculated from slope of the plot was found to be  $1.98 \times 10^3$  ( $M^{-1}$ ). This value is approximately 440 fold greater than that of the one obtained from the continuous thin film slides (See Table 7.4 and Figure 7.9).  $K_{sv}$  values reveal important practical consequences. The sensitivity of the quenching process can be enhanced by controlling the quencher diffusion rate towards fluorophores via the nano-structural properties of the sensing materials.

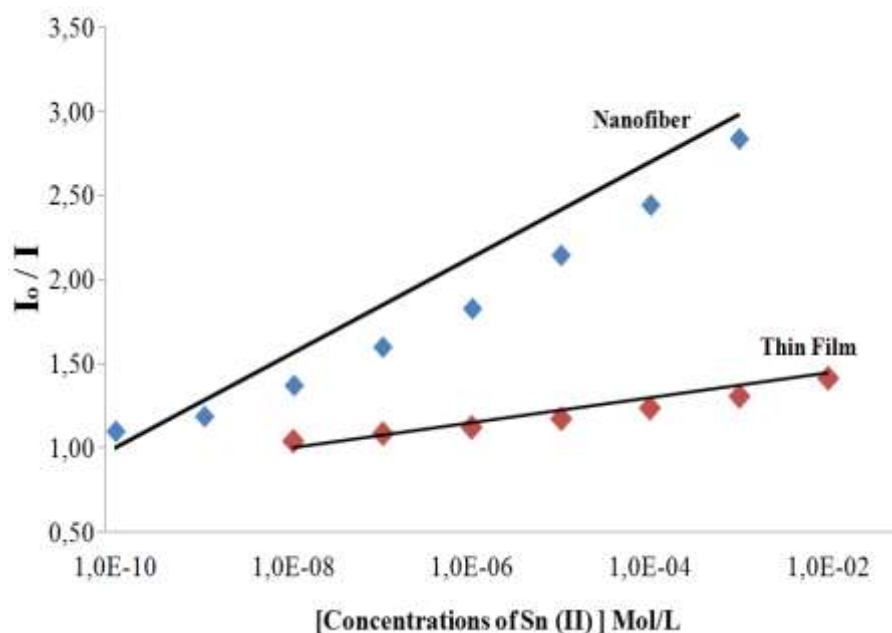


Figure 7.9. I: The Stern Volmer plots of PMMA based thin films, II: electrospun nanofibers in presence of the quencher.

Table 7.4  $K_{sv}$  Constant of PMMA based electrospun nanofibers and thin films for Sn (II) ions.

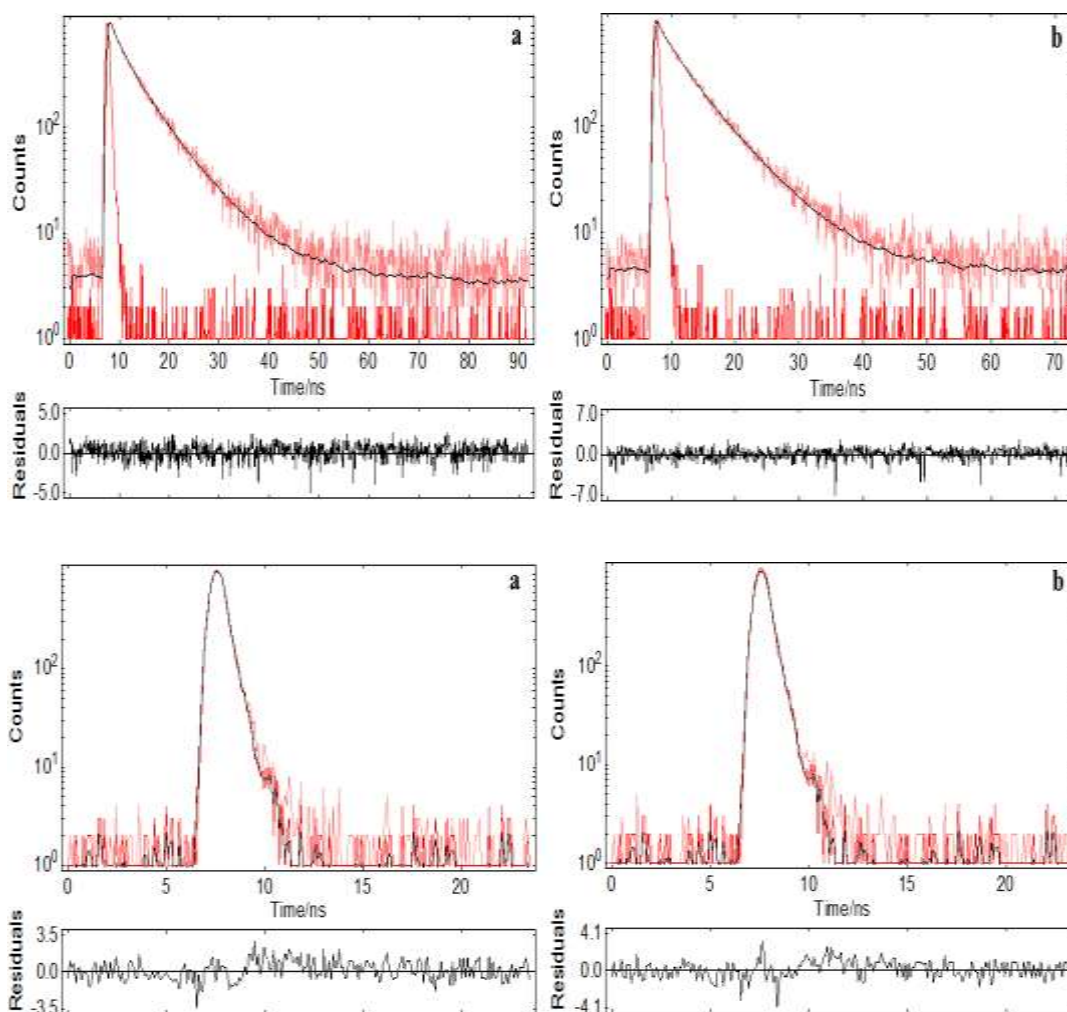
Indicator Dye	Matrix /Form	Linear Regression Equation (Sn (II) Mol/L)	$K_{sv}$ Constant
MS-3	PMMA/ electrospun nanofiber	$y = 1975.5x + 1$	$1.98 \times 10^3$
	PMMA / thin film	$y = 44.578x + 1$	$4.46 \times 10^1$

### 7.2.6 Lifetime Analysis

Decay curves of the exploited dye in THF, in thin film form and in form of nanofiber were measured and shown in the Figure 7.9 The excited state lifetimes of the MS-3 in THF and in solid matrices, in the absence and presence of the quencher were shown in Table 7.5. In solution phase and solid-state measurements, there is a slight decrease in the excited state lifetimes after addition of Sn (II) ions, which can be attributed to the dynamic component of the quenching.

Table 7.5 Florescence lifetimes of the carbazole derivative in THF, PMMA based thin films and electrospun nanofibers in the presence and absence of the quencher.

MS-3		Solvent		Thin Film		Nanofiber	
		Value (ns)	% Relative	Value (ns)	% Relative	Value (ns)	% Relative
Metal Free	$\tau_1$	0.45	5.74	0.05	100	0.16	21.80
	$\tau_2$	2.93	28.58	--	--	2.09	34.66
	$\tau_3$	7.13	65.68	--	--	6.34	43.53
		Value (ns)	% Relative	Value (ns)	% Relative	Value (ns)	% Relative
Sn (II)	$\tau_1$	0.12	7.29	0.06	100	0.10	17.91
	$\tau_2$	2.70	21.99	--	--	1.78	33.22
	$\tau_3$	6.41	70.72	--	--	6.19	48.87



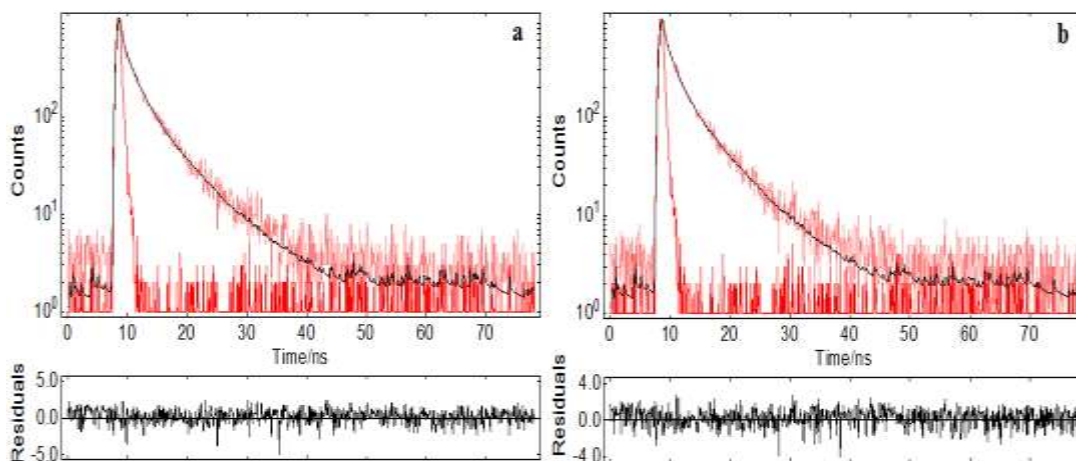


Figure 7.10 Decay curves of the exploited dye in THF, in thin film form and in form of nanofiber, respectively. In all cases a and b shows quencher free and quencher containing decay profiles. The dye excited at 367 nm with a picoseconds pulsed laser.

The spectral shifts observed in the absorption spectrum in presence of Sn (II) ions can be considered as evidence of complex formation and consequently, static quenching. However, the limited change in the decay time is the indicator of dynamic quenching. The slightly upward concave characteristic of the Stern- Volmer plot supports the combined quenching. As a result, mechanism of the quenching can be concluded as ‘combined quenching’.

### 7.2.7 Interference Effects

In order to test the selectivity of the proposed method for iron ions, the influences of a number of cations were investigated. Interference tests were performed for  $\text{Ag}^+$ ,  $\text{Al}^{3+}$ ,  $\text{Bi}^{2+}$ ,  $\text{Ca}^{2+}$ ,  $\text{Co}^{2+}$ ,  $\text{Cd}^{2+}$ ,  $\text{Cu}^{2+}$ ,  $\text{Fe}^{3+}$ ,  $\text{Fe}^{2+}$ ,  $\text{Hg}^{2+}$ ,  $\text{Hg}^+$ ,  $\text{Na}^+$ ,  $\text{K}^+$ ,  $\text{Mn}^{2+}$ ,  $\text{Mg}^{2+}$ ,  $\text{H}^+$ ,  $\text{Ni}^{2+}$ ,  $\text{Pb}^{2+}$ ,  $\text{Sn}^{2+}$  and  $\text{Zn}^{2+}$  ions in acetic acid/acetate buffer solutions at pH 5.5. From Figure 7.11-I, it can be concluded that, the sensing membrane is capable of determining tin ions with a high selectivity over other cations except that of  $\text{Ag}^+$  and  $\text{Fe}^{3+}$ . However, their interference effects can be masked with appropriate masking agents. As explained earlier, the citrate buffer and thiocyanate are proper masking agents at chosen pH (pH 4.0) for  $\text{Fe}^{3+}$  and  $\text{Ag}^+$ , respectively.

The interference effects of the conventional anions;  $F^-$ ,  $Cl^-$ ,  $Br^-$ ,  $NO_3^-$ ,  $NO_2^-$ ,  $OH^-$ ,  $HCO_3^-$ ,  $SO_4^{2-}$  and  $PO_4^{3-}$ ; were also tested (See Figure 7.11 - II). Relative signal changes of less than 1% were observed for these anions for PMMA doped films at near neutral pH.

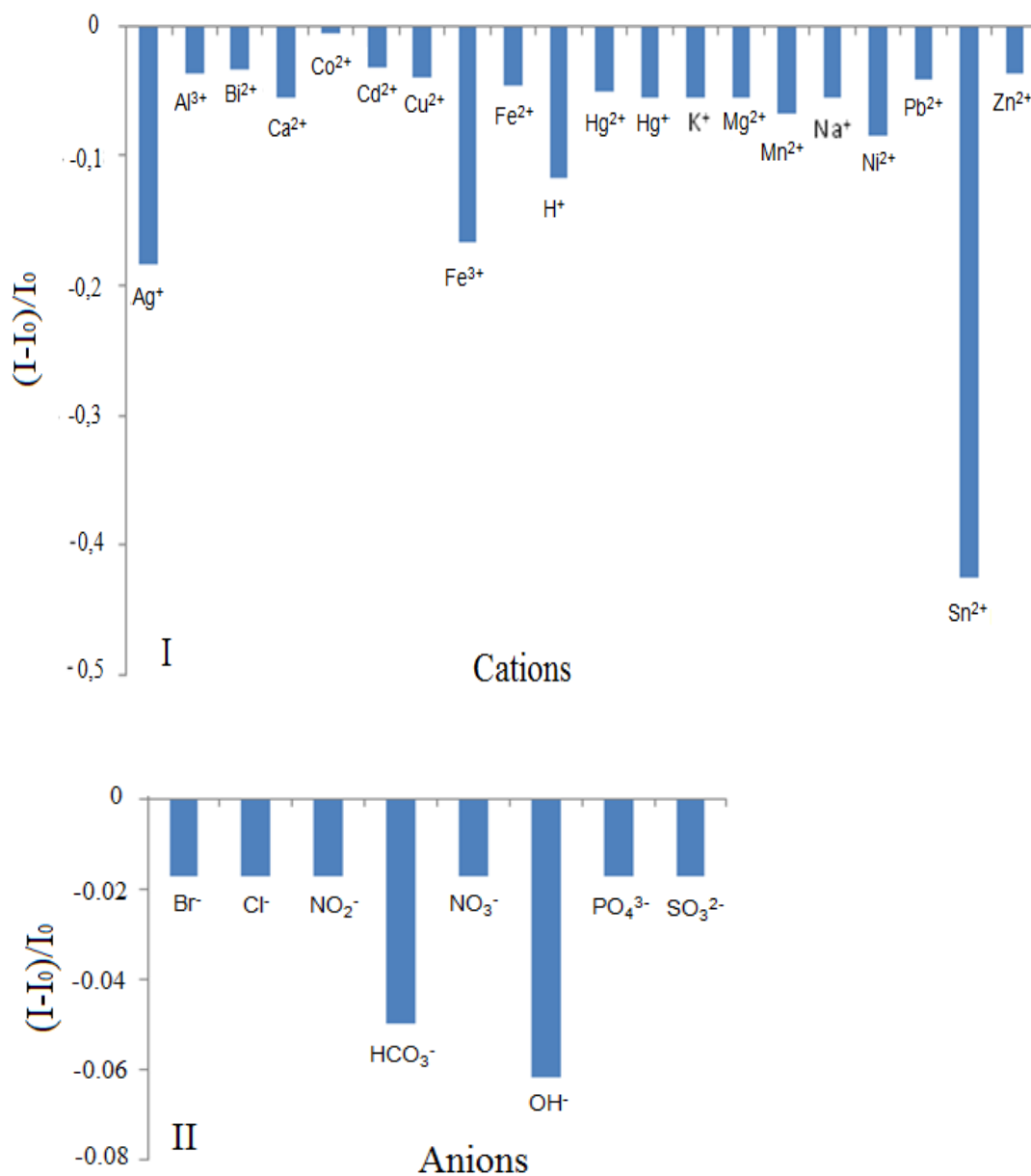


Figure 7.11 I: Metal-ion response of MS-3 at pH 5.50. II: Response to the anions of the same composition at near neutral pH. Results were plotted as relative fluorescence changes;  $(I-I_0)/I_0$ .

### ***7.2.8 Recovery and Regeneration Studies***

The applicability of the sensing system for real samples was tested for the mineral water of Sarikiz location. The temperature of water from well was remarkably constant and 18 °C. The content of Sn (II) ions in the diluted certified reference material of Merck (SRM from NIST SnCl<sub>2</sub> in HNO<sub>3</sub> 0.5 mol L<sup>-1</sup> 1000 mg L<sup>-1</sup> Sn CertiPUR®) was determined by exploiting the electrospun nanofibers. All mineral water samples were collected in polyethylene vials degassed using ultrasonic bath and analyzed as soon as possible. The recovery experiments were carried out adding 1x10<sup>-8</sup> M of certified reference material into the mineral water. The average concentration of the Sn (II) was found to be 3.19x10<sup>-8</sup> M for 10 replicate measurements. The recovery performance was found to be 103 ± 0.5%. These results reveal the capability of the offered sensing design for the determination of mercury ions in real samples without considerable error.

### ***7.2.9 Conclusion***

A novel fluorescent optical sensor using electrospun polymeric nanofibrous membrane for the quantitative analysis of Sn (II) ion was presented. Electrospinning was used as a novel and facile method to fabricate optical chemical sensor devices. With respect to continuous thin films, electrospun nanofibers offered enhanced sensitivity, lower LOD values and reactivity in optical chemical sensing of Sn (II). The MS-3 dye was used for the first time as a fluoroionophore in the optical iron sensing. The MS-3 dye doped nanofibers in PMMA can be used at pH 4.0 for quantitative determination of Sn (II) in the concentration range of 10<sup>-10</sup> - 10<sup>-3</sup> M. A quite good LOD was reached.



## CHAPTER EIGHT

### CONCLUSIONS

The thesis describes the design of the optical chemical nanosensors based on electrospun nanomaterials for the determination of some cations in aqueous samples. In this thesis, seven different fluoro-ionophores were tested and investigated into detail in order to reveal their sensor characteristics. Some of them were newly synthesized dyes. The major requirements of an ideal sensor are high sensitivity, good LOD values, wide linear working range, selectivity and fast response time. Highly sensitive nanosensors for Copper (II), Mercury (II), Iron (III) and Tin (II) were developed. In the beginning, we clarified the spectral characteristics of these ionophores in conventional solvents and solid matrices. Then, we investigated the selectivity and following the sensor performances of these ionophores into detail in terms of sensitivity, selectivity, working range, short-term stability and response time. We checked accuracies of the offered sensors exploiting recovery tests and following we performed real sample applications with groundwater samples. A grate effort has also been given for development of a sensor to detect the conventional anions throughout the studies. We observed a significant response only for  $\text{HCO}_3^-$  and  $\text{OH}^-$  ions with ODC-3 and ODC-5 dyes. The observed response was not a selective response for  $\text{HCO}_3^-$  but rather, a response to pH in the alkaline range of the pH scale.

In this thesis, we used conventional thin film technique for preparation of sensing slides. We also offered fabrication of electrospun nano-scale sensing materials as a promising approach for sensing devices. For each fluoroionophore, we compared our results and revealed the advantages of the nano-scale materials over existing thin film approach.

Here, we performed coupling of electrospun nanomaterials with fluorescence based measurement techniques without scattering and other side effects. Further efforts will focus on exploring new sensing materials and polymer compositions,

controlling the nanoscale size of the electrospun membranes, and optimizing the sensitivities for the detection of a variety of analytes.

In chapter 4, we offered a fluoroionophore and a sensing scheme for detection of ionic copper. The working ranges of the sensing agents were calculated from emission profiles and was broad enough; extends from  $10^{-12}$  to  $10^{-2}$  M. The quadratic fit is more convenient for such kind of large working ranges. However, we obtained excellent linearity with nanomaterials for both of the matrices within the whole working range (Ongun et. al., 2012)

In chapter 5, we offered three different fluorescent dyes for sensing of ionic mercury. The dyes were encoded as ODC-3 ODC-5 DMK-1A. The sensor characteristics of response time, reversibility, linear working range, pH and interference effects were investigated in different moieties. All of them exhibited highly sensitive and selective linear response to Hg (II). The detection limits (LOD) were extended to sub-nanomolar levels (Ongun et. al., 2013).

In chapter 6, we offered four different fluorescent dyes for sensing of ferric ions. The dyes were encoded as ODC-3 ODC-5, ODC-1 and MS-4, respectively. The sensor characteristics of response time, reversibility, linear working range, pH and interference effects were investigated in different moieties. All of them exhibited highly sensitive and selective linear response to Fe (III). The detection limits (LOD) were extended to sub-nanomolar levels.

In chapter 7, we offered tin sensitive molecule, 3-(2,4,6-trimethoxybenzyl)-3,4-dihydroquinazoline (MS-3) as sensing agent for sub-pico molar levels ( $10^{-14}$  M) of ionized tin. Similarly, the sensor characteristics of response time, reversibility, linear working range, pH and interference effects were investigated in different moieties. The dye exhibited highly sensitive and selective linear response to ionic tin. The detection limit (LOD) was extended to sub-picomolar levels.

## REFERENCES

- Abbott, D.W. (2007). *Wells and words*. Retrieved October 21, 2012, from <http://www.grac.org/wellsandwords.pdf>
- Adelaju, S. B. O., & Pablo, F. (1992). Determination of ultra-trace concentrations of tin by adsorptive cathodic stripping voltammetry on a glassy carbon mercury film electrode. *Analytica Chimica Acta*, 270, 143–152. Retrieved December 26, 2012, from Web of Science database.
- Aksuner, N., Henden, E., Yilmaz, I., & Cukurovali, A. (2008). Selective optical sensing of copper(II) ions based on a novel cyclobutane-substituted schiff base ligand embedded in polymer films. *Sensors and Actuators B*, 134, 510-515. Retrieved October 27, 2012, from Web of Science database.
- Aksuner, N., Basaran, B., Henden, E., Yilmaz, I., & Cukurovali, A. (2011). A sensitive and selective fluorescent sensor for the determination of mercury (II) based on a novel triazine-thione derivative. *Dyes and Pigments*, 88,143-148. Retrieved October 24, 2012, from Web of Science database.
- Allen, W. M. (2010). *Measurement of fluorescence quantum yields*. Retrieved October 27, 2012, from <http://www.thermofisher.com.au/Uploads/file/ENewsAU/Technical-Note-Measurement-of-Fluorescence-Quantum-Yields.PDF>
- Anderson, J.R.A., Garnett, J.L., & Lock, L.C. (1960). The use of naphthalene derivatives in inorganic analysis: The effect of substituents in the naphthalene nucleus on the fluorimetric detection of tin. *Analytica Chimica Acta*, 22, 1–7. Retrieved October 27, 2012, from Web of Science database.

- Annamdas, V. G. M. (2011). Review on developments in fiber optical sensors and applications. *International Journal of Materials Engineering, 1*, 1-16. Retrieved October 27, 2012, from Web of Science database.
- Anthony, J.L., Maginn, E.J., & Brennecke, J.F. (2002). Solubilities and thermodynamic properties of gases in the ionic liquid 1-N-butyl-3-methylimidazolium hexafluorophosphate. *The Journal of Physical Chemistry B, 106*, 7315–7320. Retrieved November 01, 2012, from Web of Science database.
- Aydin, F. A., & Soylak, M. (2010). Separation, preconcentration and inductively coupled plasma-mass spectrometric (ICP-MS) determination of thorium(IV), titanium(IV), iron(III), lead(II) and chromium(III) on 2-nitroso-1-naphthol impregnated MCI GEL CHP20P resin. *Journal of Hazardous Materials, 173*, 669–674. Retrieved November 26, 2012, from Web of Science database.
- Bacon, J.R., & Demas, J. N. (1987). Determination of oxygen concentrations by luminescence quenching of a polymer-immobilized transition-metal complex, *Analytical Chemistry, 59*, 2780–2785. Retrieved October 25, 2012, from Web of Science database.
- Banerjee, A., Karak, D., Sahana, A., Guha, S., Lohar, S., & Das D. (2011). Methionine–pyrene hybrid based fluorescent probe for trace level detection and estimation of Hg(II) in aqueous environmental samples: Experimental and computational studies. *Journal of Hazardous Materials, 186*, 738-744. Retrieved November 01, 2012, from Web of Science database.
- Barry, F. (n.d.). *Nanotechnology: A short introduction*. Retrieved November 05, 2012, from <http://www.nanocap.eu/Flex/Site/Download7d29.pdf>
- Bates, E.D., Mayton, R.D., Ntai, I., & Davis, J.H. (2002). CO<sub>2</sub> capture by a task specific ionic liquid. *Journal of the American Chemical Society, 124*, 926–927. Retrieved November 01, 2012, from Web of Science database.

- Bednar, A.J., Kirgan, R.A., & Jones, W.T. (2009). Comparison of standard and reaction cell inductively coupled plasma mass spectrometry in the determination of chromium and selenium species by HPLC–ICP–MS. *Analytica Chimica Acta*, 632, 27-34. Retrieved November 11, 2012, from Web of Science database.
- Belarra, M. A., Resano, M., & Castillo, J. R. (1997). Expanding the working concentration range in graphite furnace atomic absorption spectrometry; effect of non-stop flow on the determination of tin. *Spectrochimica Acta Part B: Atomic Spectroscopy*, 52, 1223–1227. Retrieved December 27, 2012, from Web of Science database.
- Biala, N. (2001). *An introduction to fiber-optic sensors*. Retrieved October 12, 2012, from <http://www.sensorsmag.com/sensors/machine-vision/an-introduction-fiber-optic-sensors-1075>
- Blanchard, L.A., Gu, Z., & Brennecke, J.F. (2001). High-pressure phase behavior of ionic liquid/CO<sub>2</sub> systems. *The Journal of Physical Chemistry B*, 105, 2437–2444. Retrieved November 04, 2012, from Web of Science database.
- Bolea, E., Arroyo, D., Laborda, F., & Castillo, J.R. (2006). Determination of antimony by electrochemical hydride generation atomic absorption spectrometry in samples with high iron content using chelating resins as on-line removal system. *Analytica Chimica Acta*, 569, 227–233. Retrieved November 28, 2012, from Web of Science database.
- Bonhote, P., Dias, A.P., Armand, M., Papageorgiou, N., & Gratzel, M. (1996). Hydrophobic, highly conductive ambient-temperature molten salts. *Inorganic Chemistry*, 35, 1168–1178. Retrieved November 25, 2012, from Web of Science database.

- Bottari, B., Maccari, R., Monferto, F., Ottana, R., Rotondo, E., & Vigorita, M.G. (2000). Isoniazid-related copper(II) and nickel(II) complexes with antimycobacterial in vitro activity. *Bioorganic & Medicinal Chemistry Letters*, *10*, 657-660. Retrieved October 27, 2012, from Web of Science database.
- Bright, F. V., & Munson, C. A. (2003). Time-resolved fluorescence spectroscopy for illuminating complex systems. *Analytica Chimica Acta*, *500*, 71-104. Retrieved October 14, 2012, from Web of Science database.
- Cabon, J.Y., Giamarchi, P., & Le Bihan, A. (2010). Determination of iron in seawater by electrothermal atomic absorption spectrometry and atomic fluorescence spectrometry: A comparative study. *Analytica Chimica Acta*, *664*, 114-120. Retrieved November 20, 2012, from Web of Science database.
- Cadena, C., Anthony, J.L., Shah, J.K., Morrow, T.I., Brennecke, J.F., & Maginn, E.J. (2004). Why is CO<sub>2</sub> so soluble in imidazolium based ionic liquids? *American Chemical Society*, *126*, 5300-5308. Retrieved October 28, 2012, from Web of Science database.
- Cai, Y., Yan, L., Liu, G., Yuan, H., & Xiao, D. (2013). In-situ synthesis of fluorescent gold nanoclusters with electrospun fibrous membrane and application on Hg (II) sensing. *Biosensors and Bioelectronics*, *41*, 875-879. Retrieved October 19, 2012, from Web of Science database.
- Camper, D., Scovazzo, P., Koval, C., & Noble, R. (2004). Gas solubilities in room temperature ionic liquids. *Industrial & Engineering Chemistry Research*, *43*, 3049-3054. Retrieved October 21, 2012, from Web of Science database.
- Carraway, E.R., Demas, J.N., DeGraff, B.A., & Bacon, J.R. (1991). Luminescence quenching mechanism for microheterogeneous systems. *Analytical Chemistry*, *63*, 337-342. Retrieved October 14, 2012, from Web of Science database.

- Cattrall, R. W. (1997). *Chemical sensors*, (1st ed.). Oxford; New York: Oxford University Press.
- Chen, H.Q., Liang, A.N., Wang, L., Liu, Y., & Qian, B.B. (2009). Ultrasensitive determination of  $\text{Cu}^{2+}$  by synchronous fluorescence spectroscopy with functional nanoparticles. *Microchim. Acta*, *164*, 453–458. Retrieved October 11, 2012, from Web of Science database.
- Chen, J., Gao, Y.C., Xu, Z.B., Wu, G.H., Chen, Y.C., & Zhu, C.Q. (2006). A novel fluorescent array for mercury (II) ion in aqueous solution with functionalized cadmium selenide nanoclusters. *Analytica Chimica Acta*, *577*, 77–84. Retrieved November 24, 2012, from Web of Science database.
- Chen, J.Q., Gao, W., & Song, J.F. (2006). Flow-injection determination of iron(III) in soil by biamperometry using two independent redox couples. *Sensors and Actuators B*, *113*, 194–200. Retrieved November 18, 2012, from Web of Science database.
- Chen, Y., Zhang, B., Chen, J.G., & Huang, D.Y. (2001). Solvent effects on the absorption and fluorescence characteristics of tin (IV) mesoporphyrin. *Spectrochimica Acta Part A: Molecular and Biomolecular Spectroscopy*, *57*, 2451–2456. Retrieved December 24, 2012, from Web of Science database.
- Cody, J., & Fahni, C.J. (2004). Fluorescence sensing based on cation-induced conformational switching: Copper-selective modulation of the photoinduced intramolecular charge transfer of a donor-acceptor biphenyl fluorophore. *Tetrahedron*, *60*, 11099-11107. Retrieved October 17, 2012, from Web of Science database.
- Cohen, S.D., Digby, S.A., & Miller, J. A. (1997). *Understanding fiber optic cables and connectors*. Retrieved October 15, 2012, from <http://archives.sensorsmag.com/articles/0898/un0898/>.

D'Archivio, A. A., Ruggieri, F., Mazzeo, P., & Tettamanti, E. (2007). Modelling of retention of pesticides in reversed-phase high-performance liquid chromatography: Quantitative structure-retention relationships based on solute quantum-chemical descriptors and experimental (solvatochromic and spin-probe) mobile phase descriptors. *Analytica Chimica Acta*, 593(2), 140-151. Retrieved October 11, 2012, from Web of Science database.

De Clercq, B., & Ugent, F. V. (2002). A new class of ruthenium complexes containing Schiff base ligands as promising catalysts for atom transfer radical polymerization and ring opening metathesis polymerization. *Journal of Molecular Catalysis A-Chemical*, 180, 67-76. Retrieved October 28, 2012, from Web of Science database.

Deitzel, J., Kleinmeyer, J., & Tan, N.B. (2001). The effect of processing variables on the morphology of electrospun nanofibers and textiles. *Polymer*, 42, 261-272. Retrieved October 14, 2012, from Web of Science database.

Del Sesto, R. E., Corley, C., Robertson, A., & Wilkes, J. S. (2005). Tetraalkylphosphonium-based ionic liquids. *Journal of Organometallic Chemistry*. 690, 2536-2542. Retrieved November 01, 2012, from Web of Science database.

Ding, B., Wang, M., Yu, J., & Sun, G. (2009). Gas sensors based on electrospun nanofibers. *Sensors*, 9, 1609-1624. Retrieved November 03, 2012, from Web of Science database.

*Dionex Reference Library*. (2007). Recorded by Dionex Corporation, On [CD].

Drew, C., Wang, X., Senecal, K., Gibson, S.H., He, J., Tripathy, S., & Samuelson, L. (2000). Electrospun nanofibers of electronic and photonic polymer systems. *Proceeding of the Society of Plastics Engineers ANTEC*, 1477-1481. Retrieved October 10, 2012, from Web of Science database.



Ertekin, K., Yenigül, B., Akkaya, E.U. (2002). Potassium sensing by using a newly synthesized squaraine dye in sol-gel matrix. *Journal of Fluorescence*, 12, 2, 263-268. Retrieved November 21, 2012, from Web of Science database.

*Fiber optic sensor*. (n.d.). Retrieved January 20, 2013, from [http://en.wikipedia.org/wiki/Fiber\\_optic\\_sensor](http://en.wikipedia.org/wiki/Fiber_optic_sensor)

Fidanboyulu, K., & Efendioglu, H. S. (2009). *Fiber optic sensors and their applications*. Retrieved October 05, 2012, from [http://iats09.karabuk.edu.tr/press/pro/02\\_KeynoteAddress.pdf](http://iats09.karabuk.edu.tr/press/pro/02_KeynoteAddress.pdf)

*FLS920 Series*, (n.d.). Retrieved January 05, 2012, from <http://www.edinburghphotonics.com/files/file/brochures/FLS920-Brochure.pdf>

*Fluorescence*. (n.d.). Retrieved October 09, 2012, from [http://www-bioc.rice.edu/~graham/BIOS481/chapters/Chapter\\_4.pdf](http://www-bioc.rice.edu/~graham/BIOS481/chapters/Chapter_4.pdf)

Frohne, H. (2004). *Doping of hole conducting polymers utilized to enhance polymer electronics*. Retrieved October 27, 2012, from <http://kups.ub.uni-koeln.de/1096/>.

Fuller, J., Carlin, R.T., Delong, H.C., & Haworth, D. (1994). The properties of ionic liquids. *Chemical Communications*, 3, 299–300. Retrieved November 02, 2012, from Web of Science database.

Fu, J., Wang, L., Chen, H., Bo, L., Zhou, C., & Chen, J. (2010). A selective fluorescence probe for mercury ion based on the fluorescence quenching of terbium (III)-doped cadmium sulfide composite nanoparticles. *Spectrochimica Acta Part A: Molecular and Biomolecular Spectroscopy*, 77, 625–629. Retrieved November 12, 2012, from Web of Science database.

- Garcia-Alonso, J.I., Sanz-Medel, A., & Ebdon, L. (1993). Determination of butyl in ion species by ion-exchange chromatography with inductively coupled plasma mass spectrometric and spectrofluorimetric detection. *Analytica Chimica Acta*, 283, 261–271. Retrieved January 17, 2012, from Web of Science database.
- Gholivand, M.B., Niroomandi, P., Yari, A., & Joshagani, M. (2005). Characterization of an optical copper sensor based on N,N'-bis(salicylidene)-1,2-phenylenediamine. *Analytica Chimica Acta*, 538, 225–231. Retrieved October 09, 2012, from Web of Science database.
- Gibon, P., Schreuder-Gibson, H., & Rivin, D. (2001). Transport properties of porous membranes based on electrospun nanofibers, *Colloids and Surfaces A*, 187/188, 469-481. Retrieved October 19, 2012, from Web of Science database.
- González, A.P.S., Firmino, M.A., Nomura, C.S., Rocha, F.R.P., Oliveira, P.V. & Gaubeur, I. (2009). Peat as a natural solid-phase for copper preconcentration and determination in a multicommuted flow system coupled to flame atomic absorption spectrometry. *Analytica Chimica Acta*, 636, 198–204. Retrieved October 01, 2012, from Web of Science database.
- Haghi, A. K., & Zaikov, G. E. (2011). *Advances in nanofibre research*. Shrewsbury: Smithers Rapra Technology.
- Han, J., Li, G., & Wang, T. (2012). Synthesis, spectroscopic characterization, and molecular structure of triphenyl butene derivatives containing a cyclopentadienyl iron unit. *Inorganica Chimica Acta*, 392, 374–379. Retrieved November 25, 2012, from Web of Science database.
- Haug, H.O., & Yiping, L. (1995). Automated determination of tin by hydride generation using in situ trapping on stable coatings in graphite furnace atomic absorption spectrometry. *Spectrochimica Acta Part B: Atomic Spectroscopy*, 50, 1311–1324. Retrieved December 12, 2012, from Web of Science database.

- He, J., Liu, Y., Mo, L., Wan, Y., & Xu, L. (2008). Electrospun nanofibres and their applications. *Shawbury United Kingdom: iSmithers*, 163-165. Retrieved October 26, 2012, from Web of Science database.
- Heppeler, F., Sander, S., & Henze, G. (1996). Determination of tin traces in water samples by adsorptive stripping voltammetry. *Analytica Chimica Acta*, 319, 19–24. Retrieved December 21, 2012, from Web of Science database.
- Holbrey, J.D., & Seddon, K.R. (1999). Ionic liquids. *Clean Products and Processes*, 1, 223–236. Retrieved October 29, 2012, from Web of Science database.
- Hosick, T. J., Ingamells, R. L., & Macheimer, S. D. (2002). Determination of tin in soil by continuous hydride generation and inductively coupled plasma mass spectrometry. *Analytica Chimica Acta*, 456, 263–269. Retrieved December 11, 2012, from Web of Science database.
- Irena, V.D., Dubravko, D., & Slavica, Č., (1997). Spectrofluorometric method for determination of the total mercury content in sediment and soil. *Analytica Chimica Acta*, 355, 151-156. Retrieved November 15, 2012, from Web of Science database.
- James, N. G., Byrne, S. L., & Mason, A. B. (2009). Incorporation of 5 hydroxytryptophan into transferrin and its receptor allows assignment of the pH induced changes in intrinsic fluorescence when iron is released. *Biochimica et Biophysica Acta*, 1794, 532–540. Retrieved November 28, 2012, from Web of Science database.
- Jenny, R. (2000). *Fundamentals of fiber optics: An introduction for beginners*. New York: Volpi Manufacturing USA Co.
- Jones, D. (1998). *Introduction to fiber optics*. Naval education and training professional development and technology center.

- Jourquin, G., Mahedero, M.C., Paredes, S., Vire, J.C., & Kauffmann, J.M. (1996). Fluorimetric determination of tin and organotin compounds in hydroorganic and micellar media in the presence of 8-hydroxyquinoline-5-sulfonic acid. *Journal of Pharmaceutical and Biomedical Analysis*, *14*, 967–975. Retrieved December 10, 2012, from Web of Science database.
- Jung, H. J., Singh, N., & Jang, D.O. (2008). Highly Fe<sup>3+</sup> selective ratiometric fluorescent probe based on imine-linked benzimidazole. *Tetrahedron Letters*, *49*, 2960–2964. Retrieved December 02, 2012, from Web of Science database.
- Kacmaz, S., Ertekin, K., Suslu, A., Ergun, Y., Celik, E., & Cocen, U. (2012). Sub-nanomolar sensing of ionic mercury with polymeric electrospun nanofibers. *Materials Chemistry and Physics Volume*, *133*, 547–552. Retrieved November 21, 2012, from Web of Science database.
- Kamps, A.P.S., Tuma, D., Xia, J., & Maurer, G. (2003). Solubility of CO<sub>2</sub> in the ionic liquid. *Journal of Chemical & Engineering Data*, *48*, 746–749. Retrieved December 12, 2012, from Web of Science database.
- Kim, H.S., & Choi, H.S. (2001). Spectrofluorimetric determination of copper(II) by its static quenching effect on the fluorescence of 4,5-dihydroxy-1,3-benzenedisulfonic acid. *Talanta*, *55*, 163–169. Retrieved October 02, 2012, from Web of Science database.
- Korotcenkov, G. (2010). *Chemical Sensors Fundamentals of Sensing Materials: Volume 2 Nanostructured Materials*. Retrieved November 05, 2012, from <http://www.momentumpress.net/books/chemical-sensors-fundamentals-sensing-materials-vol-2-nanostructured-materials>

- Kovacs, M., Nagy, M.H., Borsze'ki, J., & Halmos P. (2009). Indirect determination of fluoride in aqueous samples by inductively coupled plasma atomic emission spectrometry following precipitation of  $CeF_3$ . *Journal of Fluorine Chemistry*, 130, 562-566. Retrieved November 08, 2012, from Web of Science database.
- Kozono, S., & Haraguchi, H. (2003). Determination of trace iron in indium phosphide wafer by on-line matrix separation and inductively coupled plasma mass spectrometry. *Analytica Chimica Acta*, 482, 189–196. Retrieved November 16, 2012, from Web of Science database.
- Lae's, A., Vuillemin, R., Leilde, B., Sarthou,G., Bournot-Marec, C., & Blain, S. (2005). Impact of environmental factors on in situ determination of iron in seawater by flow injection analysis. *Marine Chemistry*, 97, 347– 356. Retrieved November 14, 2012, from Web of Science database.
- Lai, S., Chang, X., & Fu, C. (2009). Cadmium sulfide quantum dots modified by chitosan as fluorescence probe for copper (II) ion determination. *Microchimica Acta*, 165, 39–44. Retrieved October 15, 2012, from Web of Science database.
- Lakowicz, J. R. (1983). *Principles of fluorescence spectroscopy*, (1st ed.). NewYork and London: Plenum Press.
- Lakowicz, J.R. (2006). *Principles of fluorescence spectroscopy*, (3rd ed.). NewYork: Springer.
- Lakowicz, J. R. (2006). Mechanisms and dynamics of fluorescence quenching. *principles of fluorescence spectroscopy* (331-351). Springer: Verlag US.
- Lau, R.M., Van Rantwijk, F., Seddon, K.R., & Sheldon, R.A. (2000). Lipase catalyzed reactions in ionic liquids. *Organic Letters*, 2, 4189–4191. Retrieved October 27, 2012, from Web of Science database.

- Lee, S. H., Ku, B. C., Wang, X., Samuelson, L., & Kumar, A. J. (2002). Design, synthesis and electrospinning of a novel fluorescent polymer for optical sensor applications. *Materials Research Society Symposium Proceedings*, 708, 403-408 . Retrieved October 29, 2012, from Web of Science database.
- Leermakers, M., Baeyens, W., Quevauviller, P., & Horvat M. (2005). Mercury in environmental samples: Speciation, artifacts and validation. *Trends in Analytical Chemistry*, 24, 383-393. Retrieved November 02, 2012, from Web of Science database.
- Li, Y.H., Long, H., & Zhou, F.Q. (2005). Determination of trace tin by catalytic adsorptive cathodic stripping voltammetry. *Analytica Chimica Acta*, 554, 86–91. Retrieved December 15, 2012, from Web of Science database.
- Liu, S.R., & Wu, S.P. (2012). New water-soluble highly selective fluorescent chemosensor for Fe (III) ions and its application to living cell imaging. *Sensors and Actuators B*, 171– 172, 1110– 1116. Retrieved October 14, 2012, from Web of Science database.
- Lobnik, A., Turel M., & Urek, Š. K. (2012). *Optical chemical sensors: Design and applications*. Retrieved October 05, 2012, from <http://www.intechopen.com/books/advances-in-chemical-sensors/optical-chemical-sensors-design-and-applications>
- López-García, I., Arnau-Jerez, I., & Campillo, N., Hernández-Córdoba M. (2004). Determination of tin and titanium in soils, sediments and sludges using electrothermal atomic absorption spectrometry with slurry sample introduction. *Talanta*, 62, 413–419. Retrieved December 12, 2012, from Web of Science database.

- Lu, N., Shao, C., & Deng, Z. (2009). Colorimetric Hg<sup>2+</sup> detection with a label-free and fully DNA-structured sensor assembly incorporating G-quadruplex halves. *Analyst*, *134*, 1822-1825. Retrieved October 27, 2012, from Web of Science database.
- Luo, Y., Li, Y., Lv, B., Zhou, Z., Xiao, D., & Choi, M.M.F. (2009). A new luminol derivative as a fluorescent probe for trace analysis of copper (II). *Microchimica Acta*, *164*, 411–417. Retrieved October 07, 2012, from Web of Science database.
- Ma, Y. M., & Hider, R. C. (2009). The selective quantification of iron by hexadentate fluorescent probes. *Bioorganic & Medicinal Chemistry*, *17*, 8093–8101. Retrieved November 08, 2012, from Web of Science database.
- Macdiarmid, A.G., Norris, I.D., Jones, W.E., El-sherif, M.A., Yuan, J., Han, B., & Ko, F.K. (2000). Polyaniline based chemical transducers with sub-micron dimensions. *Abstracts of Papers ACS 220th IEC 310*. Retrieved October 14, 2012, from Web of Science database.
- Major ions in water training module*. (n.d.). Retrieved October 21, 2012, from <http://www.hydrologyproject.gov.in/%5Cdownload%5Cmanuals%5CWaterQuality%5CWQManuals%5C28MajorIonsinWater.pdf>
- Manciulea, A., Baker, A., & Lead, J.R. (2009). A fluorescence quenching study of the interaction of Suwannee River fulvic acid with iron oxide nanoparticles. *Chemosphere*, *76*, 1023–1027. Retrieved November 04, 2012, from Web of Science database.
- Manesh, K.M., Kim, H.T., Santhosh, P. Gopalan, A.I., & Lee K.P. (2008). A novel glucose biosensor based on immobilization of glucose oxidase into multiwall carbon nanotubes–polyelectrolyte-loaded electrospun nanofibrous membrane. *Biosensors and Bioelectronics*, *23* (6), 771-779. Retrieved December 01, 2012, from Web of Science database.

- Manzoori, J. L., Amjadi, M., & Abolhasani, D. (2006). Spectrofluorimetric determination of tin in canned foods. *Journal of Hazardous Materials*, *137*, 1631–1635. Retrieved December 25, 2012, from Web of Science database.
- Manzoor, S., Shah, M.H., Shaheen, N., Khalique, A., & Jaffar, M. (2006). Multivariate analysis of trace metals in textile effluents in relation to soil and groundwater. *The Journal of Hazardous Materials* *137(1)*, 1-7. Retrieved October 05, 2012, from Web of Science database.
- Mao, J., He, Q., & Liu, W. (2010). An rhodamine-based fluorescence probe for iron(III) ion determination in aqueous solution. *Talanta*, *80*, 2093–2098. Retrieved November 10, 2012, from Web of Science database.
- Mayr, T. (2002). *Optical sensors for the determination of heavy metals*. Retrieved November 26, 2012, from <http://d-nb.info/964444569/34>.
- Measurement systems*. (n.d.). Retrieved October 09, 2012, from [http://old.iupac.org/publications/analytical\\_compendium/Cha07sec4.pdf](http://old.iupac.org/publications/analytical_compendium/Cha07sec4.pdf)
- Meng, F., Chen, Y., Liu, J., Jin, Z., Sun, Y., & Liu, J. (2010). Novel nanoparticle detection method using electrochemical device based on anodic aluminum oxide nanopore membrane. *Procedia Engineering*, *7*, 100–105. Retrieved November 11, 2012, from Web of Science database.
- Mercan, D., Çetinkaya, E., & Sahin, E. (2013). Ru(II)–arene complexes with N-substituted 3,4-dihydroquinazoline ligands and catalytic activity for transfer hydrogenation reaction. *Inorganica Chimica Acta*, *400*, 74–81. Retrieved November 27, 2012, from Web of Science database.
- Mills A., Chang Q., & McMurray N. (1992). Equilibrium studies on colorimetric plastic film sensors for carbon dioxide. *Analytical Chemistry*, *64*, 1383. Retrieved October 19, 2012, from Web of Science database.



- Mohr, G. J. (2002). *Materials and polymers in optical sensing*. Retrieved November 08, 2012, from <http://www2.uni-jena.de/~c1moge/Mohr/ASCOS2002.pdf>
- Mohr, G. J. (2006). Polymers for optical sensors. *Optical chemical sensors* (297-321). Netherlands: Springer Printed.
- Moreda-Piñeiro, J., López-Mahía, P., Muniategui-Lorenzo, S., Fernández-Fernández, E., & Prada-Rodríguez, D. (2002). Tin determination in marine sediment, soil, coal fly ash and coal slurried samples by hydride generation-electrothermal atomic absorption spectrometry. *Analytica Chimica Acta*, *461*, 261–271. Retrieved December 17, 2012, from Web of Science database.
- Nano-enabled sensor technologies*. (n.d.). Retrieved October 28, 2012, from <http://www.epa.gov/radiation/docs/cleanup/nanotechnology/chapter-3-nano-enabled-sensor.pdf>
- Nanomaterials*. (n.d.). Retrieved October 22, 2012, from <http://en.wikipedia.org/wiki/Nanomaterials>.
- Nanoscience and nanotechnologies: opportunities and uncertainties*, (2004). Retrieved October 27, 2012, from [http://royalsociety.org/uploadedFiles/Royal\\_Society\\_Content/policy/publications/2004/9693.pdf](http://royalsociety.org/uploadedFiles/Royal_Society_Content/policy/publications/2004/9693.pdf)
- Narayanaswamy, N., & Govindaraju, T. (2012). Aldazine-based colorimetric sensors for Cu<sup>2+</sup> and Fe<sup>3+</sup>. *Sensors and Actuators B*, *161*, 304–310. Retrieved November 02, 2012, from Web of Science database.
- Niemelä, M., Perämäki, P., Kola, H., & Piispanen, J. (2003). Determination of arsenic, iron and selenium in moss samples using hexapole collision cell, inductively coupled plasma–mass spectrometry. *Analytica Chimica Acta*, *493*, 3–12. Retrieved November 04, 2012, from Web of Science database.

- Nuriman, N., Kuswandi B., & Verboom, W. (2011). Optical fiber chemical sensing of Hg (II) ions in aqueous samples using a microfluidic device containing a selective tripodal chromoionophore-PVC film. *Sensors and Actuators B*, 157, 438-443. Retrieved November 29, 2012, from Web of Science database.
- Ongun, M.Z., Ertekin, K., Gocmenturk, M., Ergun, Y., & Suslu, A. (2012). Copper ion sensing with fluorescent electrospun nanofibers. *Spectrochim Acta A Mol Biomol Spectrosc.* 90. 177-185. Retrieved October 02, 2012, from Web of Science database.
- Ongun, M. Z., Ertekin, K., Hizliates, C. G., Oter, O., Ergun, Y., & Celik E. (2013). Determination of Hg (II) at sub-nanomolar levels: A comparative study with nanofibrous materials and continuous thin films. *Sensors and Actuators B: Chemical*, 181, 244–250. Retrieved April 12, 2012, from Web of Science database.
- Oter, O., Ertekin, K., Kirilmis, C., & Koca, M. (2007). Spectral Characterization of a newly synthesized fluorescent semicarbazone derivative and its usage as a selective fiber optic sensor for copper (II). *Analytica Chimica Acta*, 584, 308-314. Retrieved November 13, 2012, from Web of Science database.
- Oter, O., Ertekin, K., Kirilmis, C., Koca, M., & Ahmedzade, M. (2007). Characterization of a newly synthesized fluorescent benzofuran derivative and usage as a selective fiber optic sensor for Fe (III). *Sensors and Actuators B*, 122, 450–456. Retrieved November 12, 2012, from Web of Science database.
- Oter, O., Ertekin, K., Kılınçarslan, R., Ulusoy, M., & Cetinkaya, B. (2007). Photocharacterization of a novel fluorescent Schiff Base and investigation of its utility as an optical Fe<sup>3+</sup> sensor in PVC matrix. *Dyes and Pigments*, 74, 730-735. Retrieved November 15, 2012, from Web of Science database.

- Oter, O. (2007). *Investigation of sensor characteristics of some chromoionophore structures in polymer and sol-gel matrices*. Retrieved October 28, 2012, from <http://www.belgeler.com/blg/17h7/investigation-of-sensor-characteristics-of-some-chromoionophore-structures-in-polymer-and-sol-gel-matrices-bazikromoiyonofor-yapilarin-polimer-ve-sol-jel-matrikslerde-sensr-zelliklerinin-inceleme>
- Ozcan, M., & Akman, S. (2000). Investigation of the effect of some inorganic salts on the determination of tin in graphite furnace atomic absorption spectrometry. *Spectrochimica Acta Part B: Atomic Spectroscopy*, 55, 509–515. Retrieved December 13, 2012, from Web of Science database.
- Parga, J.R., Cocke, D.L., Valenzuela, J.L., Gomes, J.A., Kesmez, M., Irwin, G., Moreno, H., & Weir, M. (2005). Arsenic removal via electro coagulation from heavy metal contaminated groundwater in La Comarca Lagunera México. *The Journal of Hazardous Materials* 124(1-3), 247-254. Retrieved November 05, 2012, from Web of Science database.
- Parker, C. A. (1968). *Photoluminescence of Solutions*. Amsterdam: Elsevier.
- Patra, S., Lo, R., Chakraborty, A., Gunupuru, R., Maity, D., Ganguly, B., & Paul, P. (2013). Calix [4] arene based fluorescent chemosensor bearing coumarin as fluorogenic unit: Synthesis, characterization, ion-binding property and molecular modeling. *Polyhedron*, 50, 592–601. Retrieved October 27, 2012, from Web of Science database.
- Pham, Q. P. Sharma, U., & Mikos, A. G. (2006). Electrospinning of polymeric nanofibers for tissue engineering applications: A review. *Tissue Engineering*, 12, 1197-1211. Retrieved November 26, 2012, from Web of Science database.

- Poiata, A., Creanga, D. E., Nadejde, C., Fifere, N., & Airinei, A. (2012). Chemically modified nanoparticles surface for sensing bacterial loading—experimental study based on fluorescence stimulation by iron ions. *Bioelectrochemistry, In Press*. Retrieved November 07, 2012, from Web of Science database.
- Prasanna, M.V. (2010). Speciation of ions in groundwater and its applications. *Groundwater Monitoring and Management through Hydrogeochemical Modeling Approach* (1 st ed.) (49-62). India: I.K. International Publishing House Ltd.
- Quaresma, M. C. B., Cassella, R. J., Guardia, M., & Santelli R. E. (2004). Rapid on-line sample dissolution assisted by focused microwave radiation for silicate analysis employing flame atomic absorption spectrometry: Iron determination. *Talanta*, 62, 807–811. Retrieved November 09, 2012, from Web of Science database.
- Rahimi, Y., Goulding, A., Shrestha, S., Mirpuri, S., & Deo, S.K. (2008). Mechanism of copper induced fluorescence quenching of red fluorescent protein, DsRed. *Biochemical and Biophysical Research Communications*, 370, 57–61. Retrieved October 07, 2012, from Web of Science database.
- Raoot, K.N., Raoot, S., & Kumari, L. (1983). Selective complexometric determination of mercury with thiocyanate as masking agent. *Talanta*, 30, 611–613. Retrieved November 12, 2012, from Web of Science database.
- Ratana-Ohpas, R., Kanatharana, P., Ratana-Ohpas, W., & Kongsawasdi, W. (1996). determination of tin in canned fruit juices by stripping potentiometry. *Analytica Chimica Acta*, 333, 115–118. Retrieved December 20, 2012, from Web of Science database.

- Reis, B.F., Knochen, M., Pignalosa, G., Cabrera, N., & Giglio, J. (2004). A multicommuted flow system for the determination of copper, chromium, iron and lead in lubricating oils with detection by flame AAS. *Talanta*, *64*, 1220–1225. Retrieved November 07, 2012, from Web of Science database.
- Reneker, D.H., & Chun, I. (1996). Nanometer diameter fibers of polymer, produced by electrospinning. *Nanotechnology*, *7*, 216–223. Retrieved October 22, 2012, from Web of Science database.
- Salem, A.A., (2006). Fluorimetric determinations of nucleic acids using iron, osmium and samarium complexes of 4,7-diphenyl-1,10-phenanthroline. *Spectrochimica Acta Part A*, *65*, 235–248. Retrieved November 10, 2012, from Web of Science database.
- San Vicente de la Riva, B., Costa-Fernandez, J.M., Jin, W.J., Pereiro, R., & Sanz-Medel, A. (2002). Determination of trace levels of Hg in water samples based on RTP energy transfer. *Analytica Chimica Acta*, *455*, 179-186. Retrieved December 07, 2012, from Web of Science database.
- Sasamoto, H., Yui, M., & Arthur, R.C. (2004). Hydrochemical characteristics and groundwater evolution modeling in sedimentary. *Physics and Chemistry of the Earth*, *29*, 43-54. Retrieved October 02, 2012, from Web of Science database.
- Scampicchio, M., Bulbarello, A., Arecchi, A., Cosio, M. S., Benedetti, S., & Mannino, S. (2012). Electrospun nonwoven nanofibrous membranes for sensors and biosensors. *Electroanalysis*, *24*, 719–725. Retrieved October 25, 2012, from Web of Science database. <http://onlinelibrary.wiley.com/doi/10.1002/elan.201200005/pdf>
- Schmidt, W. (1994). *Optische Spektroskopie*. Weinheim: VCH Verlagsgesellschaft.

- Schreuder-Gibson, H., Gibson, P., Senecal, K., Sennett, M., Samuelson, L., Walker, J., Yeomans, W., & et.al. (2001). Property Enhancements for Military Applications *Abstracts of Papers ACS 221st: IEC 288*. Retrieved October 06, 2012, from Web of Science database.
- Senecal, K., Ziegler, D., Auerbach, M., Schreuder-Gibson, H., & Samuelson, L. (2001). Nanofibrous composite membranes of semi-conducting and photoelectric materials. *Abstracts of Papers ACS 221st: IEC 358*. Retrieved November 14, 2012, from Web of Science database.
- Settheeworrit, T., Hartwell, S.K., Lapanatnoppakhun, S., Jakmunee, J., Christian, G. D., & Grudpan, K. (2005). Exploiting guava leaf extract as an alternative natural reagent for flow injection determination of iron. *Talanta*, *68*, 262–267 Retrieved November 12, 2012, from Web of Science database.
- Sharma, M., Saxena, R., & Gohil, N. K. (2009). Fluorescence assay of non-transferrin-bound iron in thalassemic sera using bacterial siderophore. *Analytical Biochemistry*, *394*, 186–191. Retrieved November 15, 2012, from Web of Science database.
- Sheldon, R. (2001). Catalytic reactions in ionic liquids. *Chemical Communications*, *23*, 2399–2407. Retrieved October 18, 2012, from Web of Science database.
- Silva, J.B.B., Giacomelli, M. B. O., De Souza, I. G., & Curtius, A. J. (1998). Automated determination of tin and nickel in brass by on-line anodic electrodisolution and electrothermal atomic absorption spectrometry. *Talanta*, *47*, 1191–1198. Retrieved December 16, 2012, from Web of Science database.
- Singh, N., Kaur, N., Dunn, J., MacKay, M., & Callan, J. F. (2009). A new fluorescent chemosensor for iron(III) based on the  $\beta$ -aminobisulfonate receptor. *Tetrahedron Letters*, *50*, 953–956 . Retrieved November 10, 2012, from Web of Science database.

- Shin, M.H., Wong, F. F., Lin, C.M., Chen W.Y. & Yeh, M.Y. (2006). New synthesis of highly potential efficient bluish-green electroluminescent materials based on 1,3,4-oxadiazole–triazolopyridinone–carbazole derivatives for single-layer devices. *Heteroatom Chemistry*, 17, 160-165. Retrieved December 03, 2012, from Web of Science database.
- Sinha, N., Jain, S., Tilekar, A., Upadhayaya, R. S., Kishore, N., Jana G. H. & Arora, S. K. (2005). Synthesis and antimycobacterial evaluation of nitroheterocyclic-based 1, 2,4-benzothiadiazines. *Bioorganic & Medicinal Chemistry Letters*, 15(6), 1573-1576. Retrieved November 04, 2012, from Web of Science database.
- Smith, K.C. (n.d.). *Basic photochemistry*. Retrieved December 01, 2012, from <http://www.photobiology.info/Photochem.html>
- Smith, M., Bisiar, T., Putra, T., & Blackwood, V. (n.d). *Geochemistry of Geothermal Fluids*. Retrieved January 12, 2013, from [http://www.ricocolorado.org/gov/geothermal/Geochemistry\\_of\\_Geothermal\\_Fluids\\_Rico\\_CO.pdf](http://www.ricocolorado.org/gov/geothermal/Geochemistry_of_Geothermal_Fluids_Rico_CO.pdf)
- Some information about the fiber optic sensors*, (2012). Retrieved October 22, 2012, from <http://www.chinaopticcable.com/News/386.html>
- Stetter, J. R., Penrose W. R., & Yao, S. (2003). Sensors, chemical sensors, electrochemical sensors, and ECS. *Journal of the Electrochemical Society*, 150 (2), 11-16. Retrieved October 14, 2012, from Web of Science database.
- Sumner, J.P., Westerberg, N.M., Stoddard, A.K., Fierke, C.A., & Kopelman, R. Cu<sup>+</sup> and Cu<sup>2+</sup> Sensitive PEBBLE Fluorescent Nanosensors using DsRed as the Recognition Element. *Sensors and Actuators B: Chemical*, 113, 760-767. Retrieved October 08, 2012, from Web of Science database.

- Sweeny, B.K., & Peters, D.G. (2001). Cyclic voltammetric study of the catalytic behavior of nickel (I) salen electrogenerated at a glassy carbon electrode in an ionic liquid (1-butyl-3-methylimidazolium tetrafluoroborate, BMIM<sup>+</sup>BF<sub>4</sub><sup>-</sup>). *Electrochemistry Communications*, 3, 712–715. Retrieved November 27, 2012, from Web of Science database.
- Tan, C., Wang, Q., & Zheng, Y. (2010). Anion/Cation (H<sub>2</sub>PO<sub>4</sub><sup>-</sup> and Fe<sup>3+</sup>) induced dual luminescence quenching effect based on terbium solid sensor. *Journal of Rare Earths*, 28, 888-892. Retrieved November 05, 2012, from Web of Science database.
- Teng, M., Wang, H., Li, F., & Zhang B. (2011). Thioether-functionalized mesoporous fiber membranes: Sol–gel combined electrospun fabrication and their applications for Hg<sup>2+</sup> removal. *Journal of Colloid and Interface Science*, 355, 23-28. Retrieved October 28, 2012, from Web of Science database.
- Time-resolved fluorescence spectroscopy*, (2001). Retrieved December 29, 2012, from [http://www.princetoninstruments.com/pdfs/casestudies/trf\\_spectroscopy.pdf](http://www.princetoninstruments.com/pdfs/casestudies/trf_spectroscopy.pdf)
- Topal, S.Z., Atilla, D., Ertekin, K., Tommasino, J.B., Luneau, D., & Gürek, A.G. (2012). Investigation of optical and electrochemical properties as well as metal ion sensitivities of different number of crown ether appended phthalocyanines. *Journal of Porphyrins and Phthalocyanines*; 16, 1–9. Retrieved October 10, 2012, from Web of Science database.
- Turel, M., Duerkop, A., Yegorova, A., Scripinets, Y., Lobnik, A., & Samec, N. (2009). Detection of nanomolar concentrations of copper(II) with a Tb-quinoline-2-one probe using luminescence quenching or luminescence decay time. *Analytica Chimica Acta*, 644, 53–60. Retrieved November 15, 2012, from Web of Science database.



Usharani, M., Akila E., & Rajavel, R. (2012). Mixed ligand schiff base complexes: synthesis, spectral characterization and antimicrobial activity. *Journal of Chemical and Pharmaceutical Research*, 4(1), 726-731. Retrieved November 28, 2012, from Web of Science database.

*UV-Vis luminescence spectroscopy theoretical principles*. (n.d.). Retrieved October 12, 2012, from <http://teaching.shu.ac.uk/hwb/chemistry/tutorials/molspec/lumin1.htm>

Uyar, T., Balan, A., Toppare, L., & Redenbacher, F. (2009). Electrospinning of cyclodextrin functionalized poly(methyl methacrylate) (PMMA) nanofibers. *Polymer*, 50, 2, 475–480. Retrieved November 17, 2012, from Web of Science database.

Valeur, B., & Leray, I. (2000). Design principles of fluorescent molecular sensors for cation recognition. *Coordination Chemistry Reviews*, 205, 1 3–40. Retrieved October 28, 2012, from Web of Science database.

Vasimalai, N., & Abraham, S. J. (2013). Micromolar Hg (II) induced the morphology of gold nanoparticles: a novel luminescent sensor for femtomolar Hg (II) using triazole capped gold nanoparticles as a fluorophore. *Journal of Materials Chemistry A*, 1, 4475-4482. Retrieved December 23, 2012, from Web of Science database.

Vázquez, P.P., Mughari, A.R., Galera, M.M. (2008). Application of solid-phase microextraction for determination of pyrethroids in groundwater using liquid chromatography with post-column photochemically induced fluorimetry derivatization and fluorescence detection. *Journal of Chromatography A*, 1188(2), 61-68. Retrieved November 04, 2012, from Web of Science database.

- Xia, Y.S., & Zhu, C.Q. (2008). Use of surface-modified CdTe quantum dots as fluorescent probes in sensing mercury (II). *Talanta*, 75, 215–221. Retrieved November 25, 2012, from Web of Science database.
- Wang, J., Wang, D., Moses, D., & Heeger, J. A. (2001). Dynamic quenching of 5-(2'-Ethyl-hexyloxy)-p-phenylene vinylene (MEH-PPV) by charge transfer to a C60 derivative in solution. *Journal of Applied Polymer Science*, 82, 2553–2557. Retrieved December 13, 2012, from Web of Science database.
- Wang, X., Drew, C., Lee, S.H., Senecal, K.J., Kumar, J., & Samuelson, L.A. (2002). Electrospun nanofibrous membranes for highly sensitive optical sensors. *Nano Letters*, 2, 1273–1275. Retrieved November 18, 2012, from Web of Science database.
- Wang, X., Drew, C., Lee, S.H., Senecal, K.J., Kumar, J., & Samuelson L.A. (2002). Electrospinning Technology: A novel approach to sensor application. *Journal of Macromolecular Science Part A Pure and Applied Chemistry*, 39, 1251-1258 Retrieved November 15, 2012, from Web of Science database.  
<http://nsrdec.natick.army.mil/LIBRARY/00-09/R02-113.pdf>
- Wang, X., Drew, C., Lee, S. H., Senecal, K. J., Kumar, J., & Samuelson, L. A. (2002). Electrospun nanofibrous membranes for highly sensitive optical sensors. *Nanoletters*, 2, 1273 1275. Retrieved December 17, 2012, from Web of Science database.
- Wang, Y.Q., Liu, Y., He X.W., Li, W.Y., & Zhang Y. K. (2012). Highly sensitive synchronous fluorescence determination of mercury (II) based on the denatured ovalbumin coated CdTe QDs. *Talanta*, 99, 69–74. Retrieved November 17, 2012, from Web of Science database.

- Welton, T. (1998). Room temperature ionic liquids, solvents for synthesis and catalysis. *Chemical Reviews*, 99, 2071–2083. Retrieved December 14, 2012, from Web of Science database.
- Welton, T. (1999). Room-temperature ionic liquids for synthesis and catalysis. *Chemical Reviews*, 99, 2071–2083. Retrieved October 16, 2012, from Web of Science database.
- Williams, A.T.R., Winfield, S.A., & Miller, J.N. (1983). Relative fluorescence quantum yields using a computer-controlled luminescence spectrometer. *Analyst*, 108, 1067–1071. Retrieved December 08, 2012, from Web of Science database.
- Wolfbeis, O. S. (2004). Fiber-optic chemical sensors and biosensors. *Analytical Chemistry*, 76, 3269-3284. Retrieved November 17, 2012, from Web of Science database.
- Wolfbeis, O. S. (1991). *Fiber optic chemical sensors and biosensors* (volume 2). The University of Michigan: CRC Press.
- Wolfbeis, O. S. (1997). Chemical Sensing Using Indicator Dyes. *Optical Fiber Sensors* (chapter 8) (53-107). Boston-London: Artech House
- Yaman, M., & Kaya, G. (2005). Speciation of iron (II) and (III) by using solvent extraction and flame atomic absorption spectrometry. *Analytica Chimica Acta*, 540, 77–81. Retrieved November 06, 2012, from Web of Science database.
- Yang, Z., & Pan, W. (2005). Ionic liquids: Green solvents for nonaqueous biocatalysis. *Enzyme and Microbial Technology*, 37, 19–28. Retrieved October 17, 2012, from Web of Science database.

Yari, A., & Afshari, N. (2006). An optical copper(II)-selective sensor based on a newly synthesized thioxanthone derivative, 1-hydroxy-3,4-dimethylthioxanthone. *Sensors and Actuators B: Chemical*, 119, 531–537. Retrieved October 17, 2012, from Web of Science database.

Zeyrek, M., Ertekin, K., Kacmaz, S., Seyis, C., & Inan, S. (2010). An ion chromatography method for the determination of major anions in geothermal water samples. *Geostandards and Geoanalytical Research*, 34 (1), 67-77. Retrieved October 09, 2012, from Web of Science database.

Zoriy, M., Ostapczuk, P., Halicz, L., Hille, R., & Becker, J.S. (2005). Determination of Sr-90 and Pu isotopes in contaminated ground water by ICP-MS. *International Journal of Mass Spectrometry*, 242, 203-210. Retrieved October 11, 2012, from Web of Science database.